Electrical properties of $BaTiO_3$, $CoFe_2O_4$ and $La_{1\ 2}(Ca, Sr)_{1\ 2}MnO_3$ thin films and their importance for active barriers in tunnel transport

Diego Fernando Gutiérrez Yatacue

Programa de Doctorat en Ciència de Materials-Departament de Física
Universitat Autònoma de Barcelona

Director: Prof. Josep Fontcuberta i Grinó

Tutor: Prof. Javier Rodríguez Viejo

Memòria presentada per l obtenció de la titulació de Doctor

Bellaterra December, 2014

Prof. Josep Fontcuberta i Grinó, Profesor de Investigación del Consejo Superior de Investigaciones Científicas y el **Prof. Javier Rodríguez viejo**, Catedrático de la Universidad Autónoma de Barcelona,

CERTIFICAN:

Que Diego Fernando Gutiérrez Yatacue, Licenciado en Física, ha realizado bajo su dirección el trabajo de investigación que lleva el título: **Electrical properties of $BaTiO_3$, $CoFe_2O_4$ and $La_{1/2}(Ca,Sr)_{1/2}MnO_3$ thin films and their importance for active barriers in tunnel transport** . Dicho trabajo ha sido desarrollado dentro del programa de doctorado de Ciencia de los Materiales de la Universidad Autónoma de Barcelona.

Y para que así conste, firman el presente certificado:

Prof. Josep Fontcuberta i Grinó　　　　Prof. Javier Rodríguez viejo

Bellaterra, 4 Diciembre de 2014

Acknowledgements

I would like to start expressing my acknowledgements to my family because they give me all the suport and motivation to enlarge my knowledge in spite of all the dificulties presented in our lives.

I would like to thank specially to my supervisor, Prof. Josep Fontcuberta, for all the expertise that he has provided to my work, and also to teach me how to work inexhaustibly. In this gratitude I should also include Prof. Florencio Sánchez and prof. Gervasi for their valuable comments during these almost five years.

Special acknowledgements to the german guys. Michael Foerster, who was my guide during my first year, and Nico Dix who through his efforts produced good samples to me. Here, I extent my gratitude to David Pesquera, Ignasi Fina for their comments about manganites and ferroelectrics. I also want to give my acknowledgements to Prof. Laukhin, Prof. Skumryev, Roque, Fanmao because their doubts enriched me. Equal importance was the successful collaboration with Greta and Prof. Bertacco. During several moths the interchange of knowledge between ICMAB and LNESS was incredible.

I recognize the support of the technicians of AFM, XRD, SEM. Special gratitude to Bernat who collaborated me a lot with the PPMS and SQUID.

I can not forget the frienship with my colegues at ICMAB. Thanks for your support. I appreciate the patience and collaboration of Mary during the writing of this thesis.

Support from Spanish goverment (Projects MAT 2008-067661-C03, MAT2011-29269-C03 and NANOSELECT CSD2007-00041) is acknowledged.

Abstract

Shrinking has been the relevant concept of silicon-based technology. However the scaling of its cornerstone (metal oxide semiconductor field efect transitor) will lead to the silicon oxide layer to the scale of $\sim 2\ nm$, where the efficiency of the devices is afected due to the increase of leakage current by tunnel effect. Therefore, the replacement of silicon oxides will be inminent.

The implementation of oxides materials with ferroic order can be seen as new avenue in the thechnology. For instance in random acceses memories (RAMs). Ferroelectric RAMs (FeRAMs), in wich information is encoded through the ferroelectric polarization, they are already commercially available. Ferrolectrics implemented in solar cells has been recently investigated. Magnetic insulators has been also attractive in spintronics. The control of magnetism by electric field also seems promising.

Here, leakage current associated to the tunnel transport is view not as a problem but as tool to read information in electric or magnetic devices and memories.

Nevertheless the physics of thin and ultrathin layers of some relevant ferroic oxides is not yet complete understood. This thesis is aimed to investigate oxides materials with ferroic character.

In the first block, magnetic materials as $CoFe_2O_4$ and $La_{0.5}A_{0.5}MnO_3$ (with A = Sr, Ca) have been investigated and the variation of their properties under strain has been monitored and explained. In the case of $CoFe_2O_4$ impedance measurements as a function of frequency and DC bias were done; the determined electrical permitivity is correlated with strain. Regarding $La_{0.5}A_{0.5}MnO_3$, nanometric films were grown on diffeerent substrates to impose different strain states by the coherent growth of the

films. The magnetic and electric character was monitored and explained in terms of orbital ordering.

The second block concern the description of some preliminary experiments on the effects of the visible light on the ferroelectric propoerties. Photocurrent is measured in $BaTiO_3$ films. It is found that polarization and coercive field can be depresed by illumination.

The last block is mainly devoted to the characterization of ferroelectric tunnel juctions (FTJs). $BaTiO_3$ is used as ferroelectric barrier while $La_{0.7}Sr_{0.3}MnO_3$ and Pt are the bottom and top electrode respectively. The electric field control of the remanent resistance states of large area FTJs displaying values of $3{\times}10^4\%$ tunnel electroresistance room temperature. Capacitance vs bias measurements in these juctions present similarities to those found in metal-oxide-semiconductor. Next, ultrathin layers of $La_{0.5}A_{0.5}MnO_3$ have been inserted between ferroelectric layer and metallic electrode aiming to explore possible metal-to-insulator transition in these layers as a way to enhance the tunnel electroresistance of the device. It is found that for some particular composition is seen that the room temperature electroresistance can increase up to five times. In relation to $CoFe_2O_4$ ultrathin films it has been observed tunnel and non-tunnel channels. A methodology to study the transport in ultrathin films of this type is proposed.

Resumen

La miniaturización ha sido el concepto relevante de la tecnología basada en silicio. No obstante, el escalamiento de su elemento pilar (el transistor de efecto de campo por apilamiento de metal/óxido/semiconductor) pronto llevará a la capa óxido de silicio a un espesor de $\sim 2\ nm$, donde la eficiencia de los dispositivos es afectada por el incremento de las corrientes de fuga debida al efecto túnel. Por lo tanto, la substutución del óxido de silicio parece inminente.

La implementacion óxidos que presentan orden ferroico pueden ser vistas como una nueva ruta a seguir en el campo técnologico. Por ejemplo, en memorias de acceso aleatorio (en ingles RAMs). Memorias ferroelectricas (RAMs), en las cuales la información es codificada a través de polarización ferroelectrica, ya estan siendo usadas en dispositivos comerciales. Materiales ferroelectricos estan siendo usados en investigaciones sobre celdas solares. Aislantes magnéticos han sido importantes en espintrónica. El control del magnétismo mediante campos électricos es otro tópico que parece prometedor.

Aquí, la corriente de fuga asociada al transporte túnel no es vista como un problema sino como una herramienta para leer información en dispositivos eléctricos o magnéticos y memorias.

No obstante la física de las capas delgadas y ultradelgadas de ciertos óxidos ferroícos aún no esta completamente entendida. Esta tesis esta encaminada a investigar en nanoescala, materiales con propiedades ferroicas.

En el primer bloque, materiales magnéticos como $CoFe_2O_4$ y $La_{0.5}A_{0.5}MnO_3$ (con A = Sr, Ca) han sido estudiados y la variación de sus propiedades bajo estrés han sido monitoreadas y explicadas. En el caso de $CoFe_2O_4$ medidas de impedancia en función

de la frecuencia y bias DC han sido realizadas. La constante dieléctrica hallada es correlacionada con el estrés. Con respecto a $La_{0.5}A_{0.5}MnO_3$, capas nanométricas has sido crecidas sobre diferentes substratos para imponer un estado de estrés mediante el crecimiento coherente de las películas. El orden magnético y el carácter eléctrico de las películas de $La_{0.5}A_{0.5}MnO_3$ es explicado en términos de ordenamiento orbital.

El segundo bloque trata sobre la descripción de algunos experimentos preliminares sobre el efecto de la luz en las propiedades ferroelectricas. Fotocorriente es medida en películas de $BaTiO_3$. También se ha encontrado que la polarización y campo coercitivo pueden ser reducidos mediante iluminación.

El último bloque es dedicado a la caracterización de junturas ferroelectricas de tunelamiento (en ingles FTJs). $BaTiO_3$ es usado como barrera ferroelectrica mientras que $La_{0.7}Sr_{0.3}MnO_3$ y Pt son usados como electrodos inferior y superior respectivamente. El control eléctrico de estados de resistencia de remanencia en FTJs de gran área muestran $3 \times 10^4\%$ electroresistencia túnel (en ingles TER) a temperatura ambiente. medidas de capacitancia en función del voltaje DC presentan similitud con aquellas encontradas en metal-óxido-semiconductor. Posteriormente, capas ultradelgadas de $La_{0.5}A_{0.5}MnO_3$ han sido insertadas entre el electrodo metálico y la capa ferroelectrica con el proposito de explorar una posible transición metal-aislante in estas capas como una forma de mejorar el valor de TER. Es encontrado que para una composición particular el valor de TER puede crecer hasta 5 veces. En relación a las capas ultradelgadas de $CoFe_2O_4$ se han observado contribución túnel y contribución tipo no tunnel. Una metodología para estudiar el transporte en este tipo de capas es propuesta.

Contents

I Fundamental aspects 1

1 Introduction 3

1.1 Background . . . 4

1.1.1 Metal-semiconductor contacts . . . 4

1.1.2 Tunnelling . . . 5

1.1.3 Spin filter . . . 8

1.2 $CoFe_2O_4$ structural characteristics . . . 10

1.3 Electroresistance in ferroelectric capacitors . . . 12

1.4 $BaTiO_3$ structural characteristics . . . 13

1.5 Manganite structure and double exchange . . . 14

1.6 The present thesis . . . 15

1.6.1 Objetives . . . 15

1.6.2 Thesis structure and chapter description . . . 16

2 State of the art 19

2.1 Properties of $CoFe_2O_4$ under strain . . . 19

2.2 Low efficiency in $CoFe_2O_4$-based spin filter . . . 24

2.3 Photoinduced effects on $BaTiO_3$ . . . 26

2.4 Diode and photocurrent effect in $BaTiO_{3-\delta}$ single crystal . . . 29

2.5 Ferroelectric tunnel junctions . . . 31

2.6 The interest in half-doped Manganites for Enhanced TER . . . 35

II Experimental 39

3 Experimental techniques 41

3.1 Introduction 41
3.2 Pulsed Laser Deposition 41
3.3 Sputtering 43
3.4 Scanning probe techniques 44
3.4.1 Scanning electron microscopy 44
3.4.2 Atomic force microscopy 45
3.4.3 Conducting atomic force microscopy 47
3.4.4 Piezoresponse force microscopy 49
3.4.5 Imaging at contact resonance 53
3.5 Structural characterization 53
3.5.1 X-Ray difracction 54
3.6 Magnetic characterization 58
3.7 Galvanomagnetic measurements 60
3.8 Contacts preparation 62
3.8.1 Contacts using micrometric mask 62
3.8.2 Electron beam litography 63
3.9 Dielectric and ferroelectric characterization 65
3.9.1 Measurement configuration 68

III Strain effects on magnetic thin films 69

4 Dielectric response of $CoFe_2O_4$ films 71

4.1 Introduction 73
4.2 Films preparation and morphology 73
4.3 Tetragonality and volume conservation 74
4.4 High dielectric constant at low frequency 77

4.5 Dependence of the intrinsic dielectric constant 82
4.6 Conclusions 86

5 Strain effects in $La_{0.5}A_{0.5}MnO_3$ 89

5.1 Introduction 91
5.2 Target preparation of $La_{0.5}A_{0.5}MnO_3$ (A = Sr, Ca) and bulk lattice parameters 91
5.3 Structural properties of $La_{0.5}A_{0.5}MnO_3$ (A = Sr, Ca) films 93
5.4 Magnetization, electrical transport and magnetotransport properties . . 101
5.5 Conclusions 112

IV Photoinduced effects in ferroelectrics 115

6 Photoinduced effects on $BaTiO_3$ films 117

6.1 Introduction 119
6.2 Thin film growth and structural characteristics 119
6.3 Top top measurements 122
6.3.1 Photocurrent 123
6.3.2 Polarization measurements 125
6.4 Top-bottom measurements 131
6.5 Discussion 133
6.6 Conclusions 133

V Tunnel transport 135

7 Electrical transport through nanometric $CoFe_2O_4$ barriers 137

7.1 Introduction 139
7.2 Description of the stacking 139
7.3 Results of transport characterization 139
7.4 Conclusions 148

8 Pt/$BaTiO_3$/$La_{0.7}Sr_{0.3}MnO_3$ junctions **149**

8.1 Introduction 151

8.2 Device fabrication and piezoresponse 151

8.3 Transport properites at low bias 153

8.4 Capacitance measurements 159

8.5 Conclusions 164

9 Pt/$La_{0.5}A_{0.5}MnO_3$/$BaTiO_3$/ $La_{0.7}Sr_{0.3}MnO_3$ junctions **167**

9.1 Introduction 169

9.2 Description of the stacking 169

9.3 TER measurements 170

9.4 Low temperature measurements 174

9.5 Preliminary conclusions 176

VI General conclusions **177**

Supplementary information **183**

Supplementary material 1: PFM characterization 183

Supplementary material 2: maximum measured TER 184

Supplementary material 3: Bias and Frequency dependence of the junction capacitance 185

Supplementary material 4: Extraction of tunnel barrier properties from $I-V$ characteristics. 187

List of publications and presentations **191**

Published works 191

Contributions to congress 192

Part I

Fundamental aspects

Chapter 1

Introduction

The continuing quest for higher storage density, higher speeds, and lower power consumption drives vigorous exploration of new materials, physical principles and operation schemes that could be exploited in non-volatile memories. A dramatic improvement in materials fabrication techniques, especially thin film deposition, also played an important role in this search for new memory/logic devices. For instance the memristor, was until recently considered to be the missing circuit element, but now much more close to be achievable thanks to ferroelectric materials. Other recent advances on the nanoscale properties of ferroic materials (such as ferromagnetism, antiferromagnetism and ferroelectricity) allow the coupling between these ferroic orders at the interfaces, offering much more versatile opportunities for next-generation nanoelectronics.

There are several characteristic of the physics of semiconductor that can be extended to the world of oxide materials. For instance, let s anticipate the rectifying or Schottky barriers formation (SB). On the other hand, for ultra thin films, it can be envisaged that oxides with richer properties than typical semiconductors can participate as active elements due to its ferroic order at room temperature.

At following, the ideas about rectifying or SB formation and tunneling transport will be mentioned. Then, the structural caracteristic of the oxides materials implemented in this thesis will be presented. Finally the objetive and the development of this thesis will be mentioned.

1.1 Background

1.1.1 Metal-semiconductor contacts

Dielectric oxide materials estudied in bulk present very well stablished insulating properties, but as the thickness is reduced at the nanoscale, it becomes more appropiate to treat they as semiconductors with a fairly large band gap [1]. When metal makes contact with a semiconductor, a barrier is formed at the metal-semiconductor interface. This barrier is responsable for controlling the current conduction as well as its capacitance behavior. For a metal with a high work function (Ψ_m) and n-type semiconductor, when they are put together the fermi energy of both materials are aligned and the formation of the barrier is established. The energy of the barrier Φ_B is given by

(1.1)

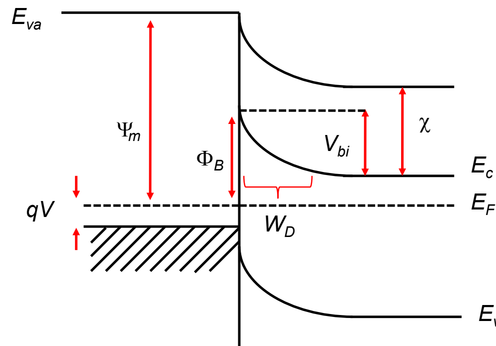

Figure 1.1: Band diagram for Schottky barrier between metal-semiconductor.

where λ is the electron affinity of the semiconductor. The aligment of the Fermi energy levels is accompanied by the formation of depleted layer (W_D) into the semiconductor

$$W_D = \sqrt{\frac{2\epsilon_s}{qN_D}\left(V_{bi} - V - k_B T \;\, q\right)} \tag{1.2}$$

where qN_D is density charge in the depletion region, ϵ_s is the dielectric contact of the semiconductor, V_{bi} is the built voltage (see the Fig. 1 1) and k_BT is the thermal energy. This insulating layer produces an interface capacitance C_D given by

$$C_D = \sqrt{\frac{q\epsilon_s N_D}{2\left(V_{bi} - V - k_BT \quad q\right)}} \tag{1.3}$$

.

When a positive bias is applied to the metal, then an unbalance between the electron coming from the metal and electrons coming from the semiconductor is established. The equation for the current density J is given by

$$J = J_0 \left[exp\left(\frac{qV}{\eta k_B T}\right) - 1\right] \tag{1.4}$$

.

For the ideal case of a perfect contact between the metal and the semiconductor $\eta = 1$. When the metal and the semiconductor is separated by a thin interfacial insulating layer (intentionally or intentionally) introduced before metal deposition, η increases due to the tickness of the oxide layer and interface traps [2 3].

1.1.2 Tunnelling

When two metals are separeted by very thin insulating material as Al_2O_3, MgO or vacuum, the transport properties are dominated by the quantum mechanism rules. Here, an electron is allowed to cross a potential barrier that exceeds its kinetic energy. The electron therefore has a finite probability of being found on the opposite side of the barrier. This is because the wave function of the electron does not disapear abruptly out of the metal but decays with the distance from the metal surface.

The theory of tunnelling can be refined in order to obtain a more realistic interpretation. For instance, the insulator and metal materials employ in elaboration of tunnel junctions presents a characteristic unavoidable in very thin films, this is roughness. For a given average insulator thickness t_0, it can be associated a given roughness (ϵ). For

simplicity it can be assume that the variation of the thicknesses t, follows a gaussian distribution as shown in equation 1 5

$$\rho = \frac{2}{\epsilon \quad \pi} exp\left(-\frac{(t_0 - t)^2}{\epsilon^{\ 2}}\right) \tag{1.5}$$

On the other hand the expresion of tunneling is given by

$$j = j_0 \cdot exp\left(-\frac{t}{\lambda(\Phi \ \ V)}\right) \tag{1.6}$$

where j_0, dependences on average energy barrier Φ, applied voltage V and t_0, and inside of the exponent the term $\lambda(\Phi \ \ V)$ which gives the decay rate of the wave function. Then the current density must be weighed by the gaussian probability as follow:

$$j_{avg} = \quad {}_{0} \quad j_0 \frac{2}{\epsilon \quad \pi} exp\left(-\frac{t}{\lambda(\Phi \ \ V)}\right) \times exp\left(-\frac{(t_0 - t)^2}{\epsilon^{\ 2}}\right) dt \tag{1.7}$$

or

$$j_{avg} = \frac{2j_0}{\epsilon \quad \pi} \cdot exp\left(\frac{-t_0^2}{\epsilon^{\ 2}}\right) \quad {}_{0} \quad exp\left(-\frac{t^2 - 2\beta t t_0}{\epsilon^{\ 2}}\right) \tag{1.8}$$

where β is defined by

$$\beta = 1 - \frac{\epsilon^{\ 2}}{2\lambda(\Phi \ \ V)t_0} \tag{1.9}$$

Knowing that

$$\frac{t^2 - 2\beta t t_0}{\epsilon^{\ 2}} = \frac{(t - \beta t_0)^2 - \beta^2 t_0^2}{\epsilon^{\ 2}} \tag{1.10}$$

then the integral presents the form

$$j_{avg} = \frac{2j_0}{\epsilon \quad \pi} \cdot exp\left(\frac{-t_0^2 + \beta^2 t_0^2}{\epsilon^{\ 2}}\right) \quad {}_{0} \quad exp\left(-\frac{(t - \beta t_0)^2}{\epsilon^{\ 2}}\right) dt \approx j_0 \cdot exp\left(\frac{-t_0^2 + \beta^2 t_0^2}{\epsilon^{\ 2}}\right) \tag{1.11}$$

Replacing β^2

$$j = j_0 \cdot exp\left\{-\frac{t_0}{\lambda(\Phi \ \ V)}\left[1 - \frac{\epsilon^{\ 2}}{4\lambda(\Phi \ \ V)t_0}\right]\right] \tag{1.12}$$

From 1 12 it can be defined the efffective thickness (t_{eff}) as

$$t_{eff} = t_0\left(1 - \frac{\epsilon^{\ 2}}{4\lambda(\Phi \ \ V)t_0}\right) \tag{1.13}$$

The effective thickness t_{eff} is smaller than the real thickness t_0. The result of equation 1 13 is better understood with the help of Fig. 1 2. The relation between ϵ and t_0 is quite obvious because $\epsilon\ \ t_0 < 1$ is needed to avoid short circuits. From Fig. 1 2 the effect of λ appears more evident because when the decay of λ is very low (violet curve), the variation of the amplitude of the wave function between $t_0 - \epsilon\ \ 2$ and $t_0 + \epsilon\ \ 2$ is not so strong as when λ decays very fast (orange curve). So, the comparison of ϵ and λ is also important. A numerical theorical work done by Miller et. al.[4] analyzes the roughness effect and shows the deviation of the barrier thickness and the energy barrier when the roughness increases.

In equation 1 6 the term $\lambda(\Phi\ \ V)$ is given by

$$\lambda^{-1} = \frac{2\ \ \overline{2m(\Phi - eV)}}{\ } \qquad (1.14)$$

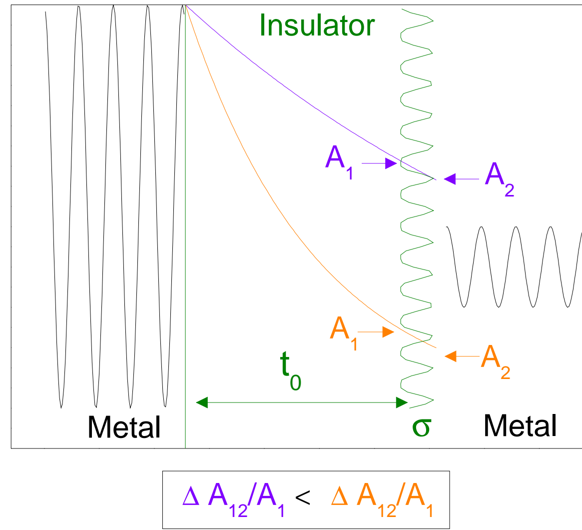

Figure 1.2: Sketch of the tunneling process in a roughly insulator surface.

In equation 1 14, m is the electron mass, the constant plack e, is the absolute value electron charge and V is the applied voltage. In this model the barrier Φ is fixed. Recently, it has been demostrated that the barrier can be modified either depending on the polarization direction of an ferroelectric barrier, or depending of the electron s spin orientation to tunnel if the barrier is a magnetic insulator.

1.1.3 Spin filter

Ferromagnetic spin filters consist in junctions where a non-magnetic electrode (NM) is used as electron injection: electrons tunnel across a ferromagnetic insulating layer and flow into a second electrode, the `analyzer , which is ferromagnetic. As the tunnel barrier is magnetic, the electronic states are splitted, so the barrier height encountered by spin up and spin down electrons is different. The electrons with different spin will experiment different probability of passing into the second electrode. It follows that the relative orientation of the magnetization between the magnetic electrode and the insulating barrier modulates the tunneling process because the density of states $N(E_F)$ into the magnetic metal depends on the magnetization state at the Fermi level ($N\ (E_F) = N\ (E_F)$) as sketched in Fig. 1 3. The variation of resistance R by the change of the relative orientation of the magnetic electrode and the magnetic barrier can be call Tunneling Magnetoresistance(TMR) as shown in eq. 1 15

$$TMR = \frac{R \quad - R}{R} \tag{1.15}$$

Assuming that the Jullière equation still is valid for spin filter (given a polarization P_{FM} for ferromagnetic metal and a P_{SF} for the ferromagnetic barrier), we have

$$TMR = \frac{2P_{FM}P_{SF}}{1 - P_{FM}P_{SF}} \tag{1.16}$$

Fig. 1 4 shows the case of parallel aligment: supposing that P_{FM} and P_{SF} are concordant in sign, electrons that tunnel the lower barrier height find a relative large density of states (DOS) available in the counter electrode, generating a low resistance state; the highest resistance occurs when the configuration is antiparallel. The difference of the barriers for spin up and spin down electrons can be expresed as $2\Delta E_{ex}$, where ΔE_{ex} is the exchange spliting of the electron states. The average of the two barriers can be call Φ_{avg}. A very small change of ΔE_{ex} can lead to very efficient spin filter, due to the exponential dependence.

The first material studied as spin filter candidates were the semiconductor Eu

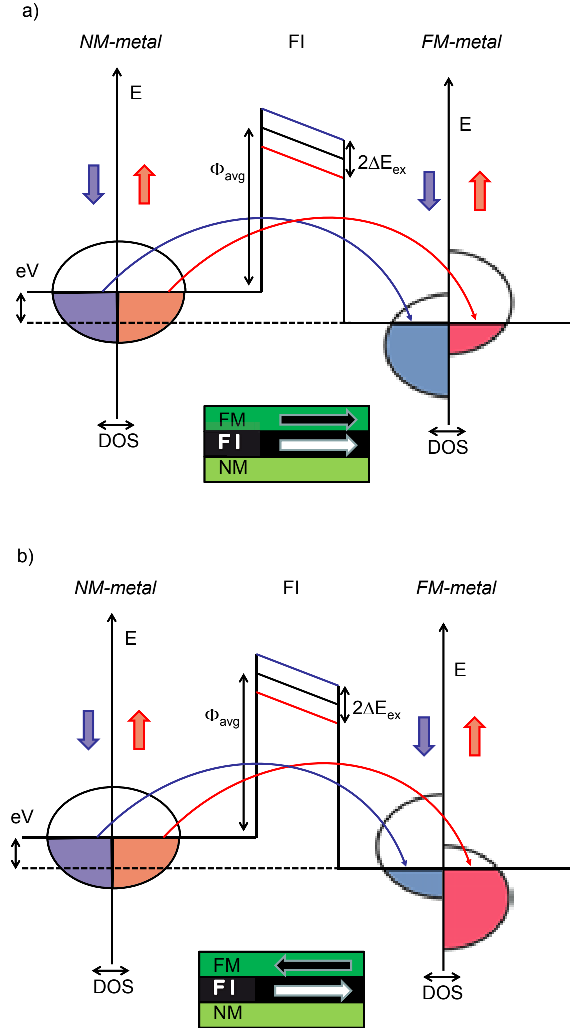

Figure 1.3: Schematic representationof the spin filter:ferromagnetic barrier(FI) and ferromagnetic electrode (FM) magnetized a) in parallel, or b) antiparallel directions.

chalcogenides. Early in the 60's, field-emission experiments were performed on junctions having EuS and EuSe as barriers [5], here the authors observed an increase of the field-emission current as the temperature was lowered below the temperature of magnetic ordering of the barrier ($T_c = 16.7\ K$), and conclude that a decrease of the barrier height is associated to the spin ordering. Similar field-emission experiments were performed on EuS-coated tungsten tips, showing a high degree of polarization of the field-emitted current below the Curie temperature of the barrier [6, 7] and

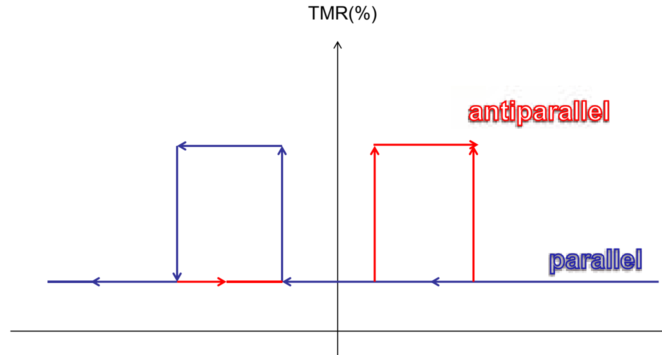

Figure 1.4: Sketch of the TMR response for an ideal spin-filter with P_{FM} and P_{SF}

these results were explained by the spin filter effect of the magnetically ordered EuS. Combining the accepted validity of the Meservey-Tedrow technique in evaluating spin polarization, with the mentioned studies on the Eu chalcogenides, in 1988 Moodera et. al. demostrated in Au/EuS/Al tunnel junction a polarization up 80% at 0.4 K. This work motivated a series of further studies aimed at investigating the role of the magnetic state of the barrier.

The spinel ferrites with chemical formula AFe_2O_4, show peculiar properties like a Curie temperature well above of room temperature, an insulating behavior due to the ionic character of their bonds and a large exchage splitting. Nevertheless the syntesis of high quality spinel ferrites films, with bulk-like properties, is made difficult by the relative emptiness of the crystal structure leaves the door open to the formation of structural defects than can modify the peculiar properties of the material.

1.2 $CoFe_2O_4$ structural characteristics

The ideal spinel crystal structure is a close-packed face centered cubic (fcc) lattice of oxygen anions, where divalent cations and trivalent cations ooccupy intersticial tetrahedral (A) and octahedral (B) sites (see Fig. 1.5). The unit cell contains 8 formula units, including 32 oxygen atoms, 64 thetrahedral sites occupied by 1/8 of the available

positions, and 32 octahedral sites, where the occupation fraction is 1/2. By definition, an A-site is surrounded by 4 nearest neighbors (NN) while a cation positioned in a B-site is surrounded by 6 NN. The lattice parameter is usually 8.0 and 8.4 $\mathring{A}$, and the smallest distance between cations is found for B-B neighbors (2.97$\mathring{A}$), for a lattice unit cell edge of 8.4 $\mathring{A}$, while the distance A-B is slightly larger (3.48$\mathring{A}$) and the A-A neighbors are even farther (3.65$\mathring{A}$). The main interaction acting between different cations is an exchange coupling meadieated by oxygen anions. The angle subtended by two adjacent B-sites and the involved oxygen B-O-B ion is 90°; in the case of adjacent A sites, the angle A-O-A is 80° for each intervening oxygen ions. The shortest superexchange path from A site to a B site subtends an angle A-O-B of 125°.

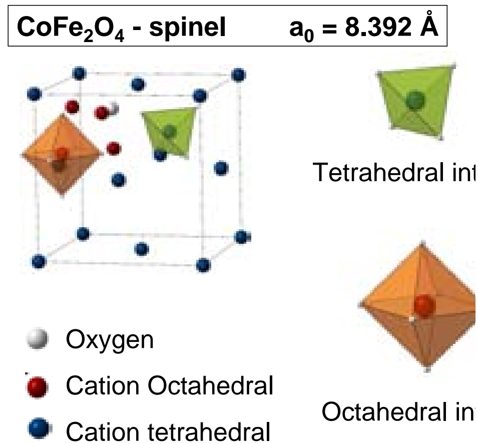

Figure 1.5: Schematic CFO unit cell with inverse spinel structure. All tetrahedral position and 50% of the octahedral positions are occupied by Fe^{3+}. The remaining 50% of the B-sites are occuppied by Co^{+2}.

In the unit cell, 8 divalent cations and 16 trivalent cations are found: considering the distribution of the cations over the two possible sites, three different spinel types can be distinguished, the normal , the inverse and the mixed structure. In the normal one, divalent cations M^{2+} are found onlly in the in the A-sites, while the trivalent ones N^{3+} are present only in B-site; The general formula $(M^{2+})^A\,[N^{3+}]_2^B\,O_4$ can be defined. The inverse structure is another extreme, where M^{2+} ions are found at B-sites and N^{3+} ions are equally distributed over A- and B sites (the general for-

mula) is for this case $(N^{3+})^{A}\left[M^{2+}N^{3+}\right]^{B}O_4$. The mixed structure can be expresed as $\left(M^{2+}_{1-x}N3+_{x}\right)^{A}\left[M^{2+}_{1-x}N^{3+}_{2-x}\right]^{B}O_4$ where x is the degree of inversion, $0 < x < 1$.

1.3 Electroresistance in ferroelectric capacitors

Up to now, the conventional semiconductor technology is based on charge storage. Recent advances on the nanoscale properties of ferroelectric materials appear as a link for the new advances and traditional technology. The existance of switchable spontaneous polarization in ultrathin ferroelectric films is the basis of design non-volatil random access memories (RAMs), where one bit of information can be stored by assigning one value of the Boolean algebra to each of the possible polarization states. Moreover the high dielectric permitivity of ferroelectrics makes them possible candidates to replace silica as the gate dielectric in metal-oxide-semiconductor-field effect transistor [8]. In addition, the coupling between ferroelectricity and ferromagnetism at the interfaces is also offering much more versatile opportunities for next-generation nanoelectronics.

The first and simple aproach is the use of a bare ferroelectric insulating material as a barrier for tunnel junctions (FTJ). Here, polarization reversal in a FTJ leads to a change in resistance of the junction, a phenomenon known as Tunnel Electroresistance (TER) effect. In FTJs, the information is stored in the FE polarization of the barrier which is mantained in the absence of an electrical field . The information ca be read by measuring the tunnnel electroresistance, which can be proved in a non-destructive way, overcoming the limitations of ferroelectric random access memories (FERAM) capacitors (read-destructive) and allowing faster and denser RAMs. However, the variation of the resistance by reversal polarization in leaky ferroelectric bulk-like capacitors appears as a recently extention inspired on the resulst obtained in FTJs.

1.4 $BaTiO_3$ structural characteristics

Bulk $BaTiO_3$ (BTO) in tetragonal phase presents an out-of-plane $c_0 = 4.038\mathring{A}$ and in plane lattice parameter $a_0 = 3.993\mathring{A}$ (see Fig. 1.6) . Because its Ti ion is off centering, the polarization can be switched in two different orientations along the c axis with a remanence polarization of 26 $\mu C/cm^2$.

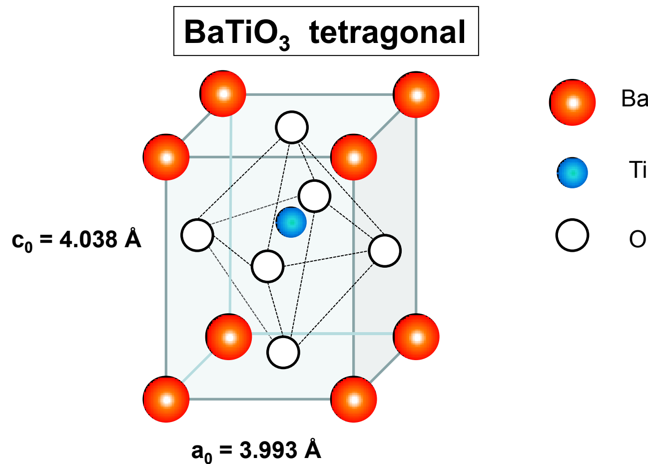

Figure 1.6: Schematic thetragonal BTO unit cell.

When BTO is grown epitxially on a substrate (i.e. $SrTiO_3$) the strain is imposed. The coupling between strain and polarization in perovskite oxides is known to be very strong; for instance, the enhancement of remanent polarization has been observed in BTO grown on $GaScO_3$ and $DyScO_3$ [9]. Another important factor than can play a role when the thickness of $BaTiO_3$ layer decreases is the depolarazing field. The depolarazing field is the field that appears when the surface polarization charges are not completely screening; then a electric field inside of the material try to reduce the polarization. Electrodes with high electron (hole) density can screen the surface polarization charges and thus reduce the effect of the depolarizing field. However, in ultra thin ferroelectric layers a competition between depolarizing field and epitaxial strain can give rise to new phases not observed in bulk [10, 11].

1.5 Manganite structure and double exchange

Among manganese perovskite oxides $La_{1-x}A_xMnO_3$ (where A= Ca, Sr) is very attractive due to the phoenomenon called Colossal Magnetoresistance (CMR). Fig. 1.7a) shows the basic $La_{1-x}A_xMnO_3$ perovskite crystal structure that, in a fisrt aproximation, can be viewed as a face centered cubic lattice with a Mn-site in the mixed-valence Mn^{3+} or Mn^{4+}, at the center surrounded by six oxygen anion sites forming an octahedral structure, and La, Sr and Ca, cations at the corners of a cube. More indeep, the structure of the manganites is altered by the tolerance factor $t_f = (r_{La}+r_O)/\left[\sqrt{2}(r_B)+r_O\right]$, where r_{La}, r_B and r_O are the atomic radii of the La, cation B and oxygen respectively. The prevoskite structure is stable for $0.89 < t_f < 1.02$. $t_f = 1$ corresponds to the perfect cubic [12].

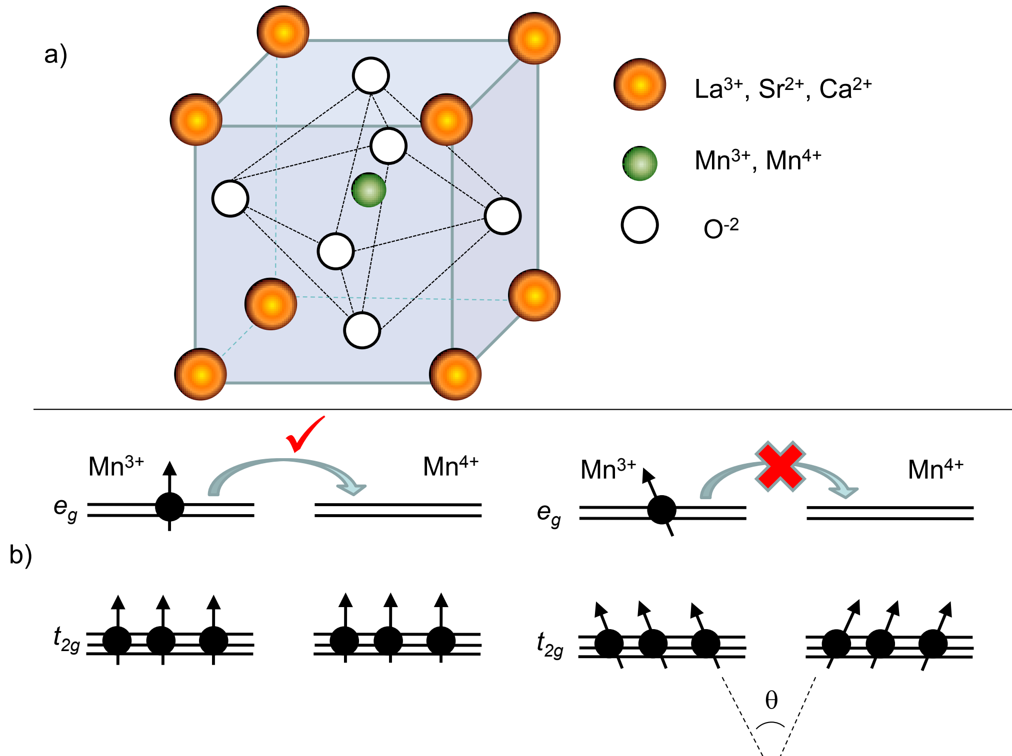

Figure 1.7: a) Schematic cubic $La_{1-x}B_xMnO_3$ unit cell. b) Scheme of DE model.

In this structure the six O^{2-} give rise to the crystal field in the Mn cation. Wave

functions pointing toward O^{2-} ions have higher energy in comparison with those pointing between them. The former wave functions, $d_{x^2-y^2}$ and $d_{3z^2-r^2}$, are called e_g orbitals, whereas the latter, d_{xy}, d_{yz}, and d_{zx}, are called t_{2g} orbitals. When electrons are put into these wave functions, the ground state is determined by the semiempirical Hunds rule. Taking into account that Mn^{3+} presents a d^4 configuration, Hunds rule produces a parallel alignment of all the spins, that is, $S = 2$, and three spins are put to t_{2g} orbitals and one spin occupies one of the e_g orbitals. For Mn^{4+} a d^3 is obtained and there is not electron in e_g levels. The magnetic properties of the manganites are governed by exchange interactions between the Mn ion spins. These interactions are relatively large between two Mn spins separated by an oxygen atom and are controlled by the overlap between the Mn d-orbitals and the O p-orbitals [13].

In the case of Mn^{3+}-O- Mn^{4+}, the Mn ions can exchange their valence by a simultaneous jump of the e_g electron of Mn^{3+} on the O p-orbital and from the O p-orbital to the empty e_g orbital of Mn^{4+}. This mechanism called *double exchange* (DE) originally proposed by Zener [14] ensures a strong ferromagnetic-type interaction. The kinetic energy gain of the e_g electron transfer from Mn^{3+} to neighbouring Mn^{4+} depends on $cos(\theta \;\, 2)$, θ being the angle between the Mn spins (Fig. 1 7 b)). The energy $t = t_0 cos(\theta \;\, 2)$ of the transfer integral of the parallel spin conguration, $\theta = 0$, maximizes t with respect to the antiparallel one, $\theta = \pi$. The kinetic energy gain for the carriers is maximized for parallel spins, which gives the ferromagnetic interaction between them.

1.6 The present thesis

1.6.1 Objetives

The goal of this thesis is to investigate the dielectrical or electrical poroperties of four different oxides which are $CoFe_2O_4$, $BaTiO_3$ and $La_{0.5}A_{0.5}MnO_3$ (with A = Sr or Ca). The investigation is divided in three brachs:

- ► I Characterization of the material in nanometric scale, where the properties known

in bulk can be different due to epitaxial strain. First, the dielectric constant of $CoFe_2O_4$ films is measured and correlated with its strain state. Second, the magnetic and electrical character in $La_{0.5}A_{0.5}MnO_3$ (with A = Sr or Ca) films grown on different subtrates is monitored.

▶ II Determine the impact of illumination on the ferroelectric properties of $BaTiO_3$ films.

▶ III Investigate the transport porperties in ultran-thin films. Verify the tunnel transport in $BaTiO_3$ and $CoFe_2O_4$ and explore the electric control of the resistance state in $BaTiO_3$-based tunnel juctions at room temeperature.

1.6.2 Thesis structure and chapter description

Chapter 2 contains a brief description of $CoFe_2O_4$, $BaTiO_3$ and $La_{0.5}A_{0.5}MnO_3$ (with A = Sr or Ca) materials and thin films. In the case of $CoFe_2O_4$, the elastic and magnetic properties under strain will be analyzed. Subsequently it will be mention the dificulties found in $CoFe_2O_4$ tunnel juctions. Then, regarding to photoinduced effects, some examples of reported data on $BaTiO_3$ will be overviewed. Next, the main results reported about the tunnel electroresistance (TER) will be reviewed. Finally, some reports about half-doped manganites ($La_{0.5}A_{0.5}MnO_3$) and its importance for hybrid tunnel juctions and enhanced TER will be also reviewed.

Chapter 3 contains a brief description of the experimental methods used in the thesis.

From chapter 4 to chapter 9, the results obtained in this thesis are presented. Chapter 4 describes the results corresponding to the $CoFe_2O_4$ films. In chapter 5 will be shown the results obtained in bare half-doped manganites films. Chapter 6 contains the here measured photoresponse of nanometric $BaTiO_3$. Chapter 7 collects thetunnel transport properties of ultrathin $CoFe_2O_4$films. The last two chapters (8 and 9) are dedicated to electroresistance effects on ferroelectric-based tunnel juctions. In chapter 8 the results of tunnel electroresistance (TER) in $Pt/BaTiO_3/La_{0.7}Sr_{0.3}MnO_3$ juctions

and capacitance measurements will be presented. In chapter 9 some preliminary results about the TER in Pt/$BaTiO_3$/Half-doped manganites hybrid tunnel juctions will be present.

The Thesis ends with a summary and conclusions (Part IV).

Chapter 2

State of the art

The aim of this chapter is to provide an account of the recent progress made in the understanding of the physics of the three different kind of materials studied in this thesis, which are spinel $CoFe_2O_4$, half-doped manganites and ferroelectric $BaTiO_3$. For $CoFe_2O_4$ this chapter collects the studies in thin films and the strain effect on its properties. On the other hand, the interes of new materials for solar cells has stimulated the research of ferroelectric materials in thin films and its interaction with the light.Some examples of photoinduced effects will be shown. Also the transport properties of the ferroelectric materials is an interest topic because can lead to a lower electric power consumption. Here, the studies on $BaTiO_3$ in crystal reveal interesting properties. The last part of this chapter ilustrates the recent advances in tunnel juctions where the barrier, fabricated with these materials, plays an important role for active barriers for tunneling transport.

2.1 Properties of $CoFe_2O_4$ under strain

The spinel AB_2X_4 is one of the most interesting and important families of crystalline compounds, with application in magnetic materials, catalysis etc. A, B and X denote a divalent cation, a trivalent cation and a divalent anion, respectively, in the stoichiometry formula of AB_2X_4, including oxides, sulfides, selenides and tellurides. For

example, spinel ferrite family has been studied for many years due to their performance in magnetostriction devices with corrosion resistance [15] .

Recently, research interest on spinel ferrites is increasing because their properties can be easily tuned due to the ability of AB_2X_4 structure to admit a large variety of ions at A, B and X sites and the complex anion-cation bond-netwok that AB_2X_4 structure forms connecting its tetrahedral (A) and octahedral (B) sublattices (see Fig. 1 5). In addition it has been observed that the mangetic properties of AB_2X_4 structure strongly depends on their composition, since the presence of magnetic cations provokes the aparition of competing mangetic interactions within and between each sublattice, as well as the existance of topological magnetic frustration as a consequence of the B-cations tetrahedral network. Furthermore, in the last few years, a number of uncommon phenomena, ranging from heavy-fermions [16] to the rare coexistence of ferroelectricity and ferromagnetism [17 16], or the existence of negative thermal expansion [18] have been discovered in materials from the spinel family, illustrating that in this structure the complex equilibrium between spin, charge, orbitals, and the lattice rivals with that of the better known perovskites.

Focusing on cobalt ferrite $CoFe_2O_4$ named by CFO, this material is used in magnetic delivery, microwave devices and high density information storage due to its wealth of magnetic and insulation properties, high coercitivity, moderate saturation magnetization and high Curie temperature T_C, [19 20 21]. On the other hand, it is important to point out that the main properties of spinel CFO (structural thermal optical and magnetic) have been determined in bulk and nanoparticles, while few data exist relating to their properties in spinel thin films. For example, it has not yet been sufficently explored the powerful route to tailor CFO unit cell dimension by substrate-induced epitaxial strain, which has been much more exploited in some oxides (i.e. binary oxide and perovskites) resulting in very interesting electrical properties. Indeed, it is believed that the open spinel structure (only a fraction of the tetrahedral (1/4) and octahedral (1/2) sites within the anionic scaffold are actually occupied by cations) can favor the strain accommodation in different ways, thus leaving opportunities for emerging prop-

erties. For example some effects of epitaxial strain on the properties of magnetic spinels have been reported [22]. Strain and Poisson ratio are related magnitudes which can offer a insight into the microstructure.

The Poisson ratio, defined by $\nu = -\epsilon_t \ \epsilon_l$, is related to the ratio of the longitudinal deformation ϵ_l by a load and a resulting transversal deformation ϵ_t. For $\nu > 0$ the material expands in a direction transverse to a load and the volume is preserved for $\nu = 1 \ 2$. The Poisson ratio collects fundamental characteristics of the material, either of the microstructure or the interatomic interactions and bonds in solids. For instance: whereas very dense and weakly compressible materials have $\nu \approx 1 \ 2$ more open structures such as zeolites or cork present negative Poisson ratio[23]. In addition, for an epitaxial film under 2D stress, the apparent poison ratio ν^* is given by $\nu^* = -\epsilon_{oop} \ \epsilon_{ip} = 2\nu \ (1 - \nu)$,[24] where ϵ_{oop} is the strain out-of-plane and ϵ_{ip} is the strain in-plane.

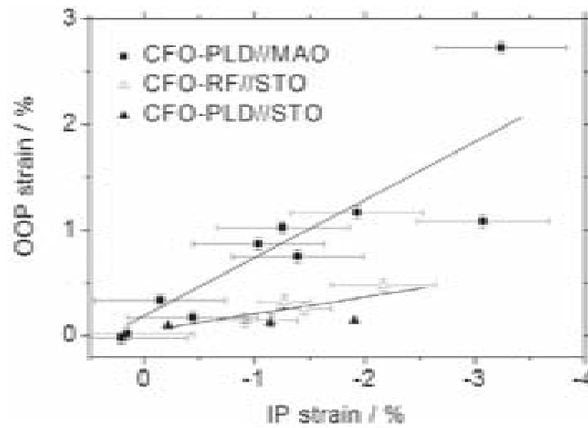

Figure 2.1: Strain diagram for epitaxially $CoFe_2O_4$ thin films: The out of plane strain vs. in-plane strain. The different apparent Poison ratios of samples grown on $MgAl_2O_4$ compared to those grown on $SrTiO_3$ are indicated by straight lines. PLD and RF refer to pulser laser deposition and sputtring deposition technics respectively. Extracted from [25].

In Fig. 2 1 Data for CFO on $SrTiO_3$ (STO) and CFO grown on $MgAl_2O_4$ (MAO), for films with different thickness (an indirect way to manage the strain) are shown. it can be observed that films grown on MAO or STO follow a roughly linear variation of ϵ_{oop} on ϵ_{in}. The positive ν^* reflects that under compressive in plane stress, the out-of-

plane cell parameter (c) doubtlessly expands, but not as much required to preserve the unit cell volume ($\nu^* = 2$ or $\nu = 0\ 5$); The Poisson ratio of CFO grown on STO $\nu \approx 0\ 12$ is found to be significantly smaller than CFO grown on MAO $\nu \approx 0\ 22$. These results are interesting because they can be correlated with phonon spectra.

In the Fig. 2 2 is plotted the A_{1g} vibrational mode at 712 - 695 cm^{-1}, measured by Raman Spectroscopy at room temperature with different wavelengths, in a function of films thickness (equivalent to strain). It is good to remark that the main atomic motions, as was studied by M. Foerster *et al.* [25], are neither purely in-plane nor purely along the c-axis but instead are in general along the cubic space diagonals. Here an unexpected red-shift is observed. This red-shift cannot be explained by variation of the tetragonallity $c\ \ a$, been a the in-plane lattice parameter. Instead, it has been observed that diagonal length d_D of the stressed unit cell given by $d_D = (2a^2 + c^2)^{1/2}$ or the equivalent edge of the volume of the unit cell $d_v = (a^2c)^{1/3}$, introduced in their model, can describe the observed red-shift. This is because in spite of strain produces high tetragonallity, the volume of the unit cell is reduced, producing a shorting in the bond length. This anomalous bond compressibility, as measured by the Poison ratio, should be reflected in funtional properties sensitive to interatomic bonds length and bond angles, particularly superexchage magnetic interactions or even dielectric response.

Others effects of epitaxial strain on the properties of magnetic spinels, most notably CFO, have been investigated [26 27 28 29 30 31 32 33]. For instance, Thang *et al.* [32] has explored the posiblity to inderectly control magnetic anisotropy by strain, varying the deposition temperature during the epitaxial growth. Fig. 2 3 represents the magnetization curves of CFO films grown on STO at different temperatures. As it can be observed for films grown at $T_s = 500°C$ the magnetic loop in-plane differs in shape of the magnetic loops done out-of-plane. This difference indicates a strong anisotropy. In contrast, for films grown at higher temperatures, the magnetic loops differences are less notably indicating that the anisotropy is reduced. Therefore, it was observed that when the substrate temperature increases, CFO lattice parameter is relaxed as shown by the comparable perpendicular hysteresis loops at $T_s = 700°C$.

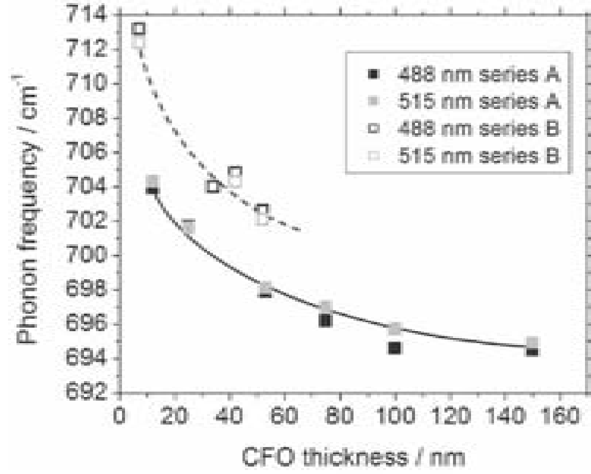

Figure 2.2: Extracted position of the peak close to 700 cm^{-1} in Raman spectra as a function of CFO thickness. the phonon frequency increases for thiner samples. The lines are guides to the eyes. Extracted from [25].

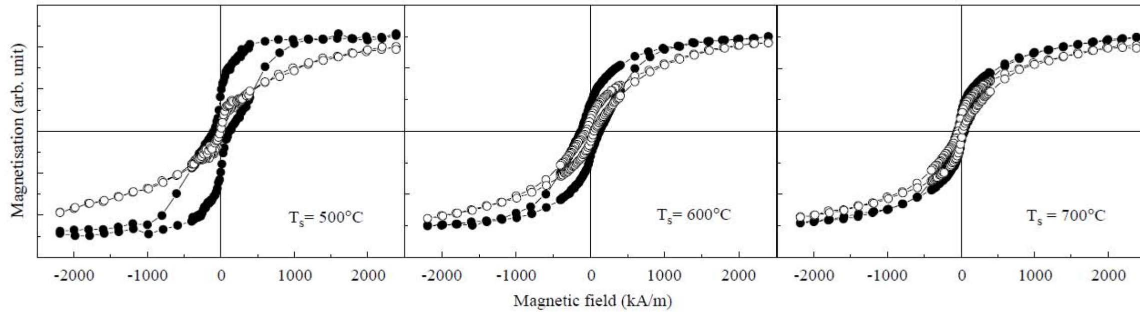

Figure 2.3: Mangetic loops for CFO films grown on $SrTiO_3$ at different temperatures. Filled points for in-plane and empty simbols for perpendicular applied magnetic field. Extracted from [32].

In summary, the few studies that have being performed in CFO thin films focus on the determination of their elastic and magnetic properties. Pioneering first principles studies have shown that CFO thin films under strain can provide opportunities for emerging properties [22]. Regarding to the dielectric properties of CFO there is a lack studies in thin films, in contrast with the several papers related to Perovskites [34 35 36 37 38].

2.2 Low efficiency in $CoFe_2O_4$-based spin filter

Tunneling phenomenon is observed in junctions of two metal layers separated by an insulator (or vacuum) of few nanometers. Here the wave nature of electrons manifests when a evanescent probability with the separation, but not zero, between the two metals allows electrons transport through the junction. Numerous useful electronic devices are based on this phenomenon. For example, The Josephson effect, based on the tunneling between two superconductors separated by an ultrathin insulator, allows measurements of magnetic field with extreme sensitivity. The scanning tunneling microscopy (STM), based in this principle, allows the studying of arrangement of individual atoms or molecules on a surface [39].

Significant interest in electronic tunneling has been risen up by the advent of spitronics, a technology that intends to exploit the the spin of the electron in addition to its electrical charge [40 41]. Highly spin-polarized current sources can be achieved by electron tunneling through a thin insulating barrier with spin dependent transmission probabilities (spin filter) [41 42]. Such spin filtering effect is expected for magnetic insulators due to the exchange split bandgap as sketched in Fig. 2 4. However, few materials with high enough transition temperature to operate at ambient conditions are known. Among them, spinel ferrite CFO appears a promising choice [41 42]. Although spin filtering through spinel thin films has been demonstrated,[43 44 45 46 47 48 49 50] up to now, the reported efficiencies are clearly below expectations derived from band structure calculations[51].

For instance, Takahashi *et. al.* [49] have studied the dependence of the resistance with the relative orientation between the magnetization of the CFO and the magnetization of a magnetic electrode, phenomenon known as tunnel magnetoresistance resistance (TMR). Here it has been observed that at low temperature the TMR is -30.5% and at room temperature is -3.4%, as shown in Fig. 2 5.

Based on the temperature dependence of the junction resistance, some authors [47 48 49] have proposed as a possible explanation the existence of a non-tunneling,

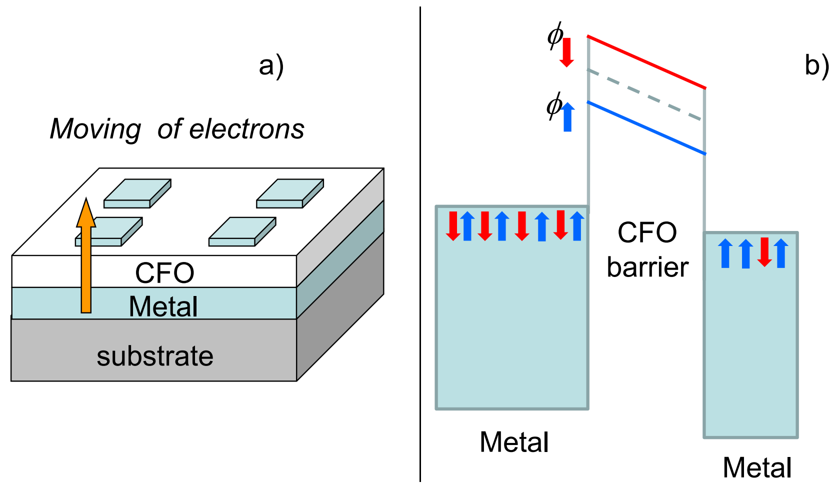

Figure 2.4: Schematic representation of a spin filter device. a) Sketch of device built from a stacking. b) Sketch of the mechanims of spin filter. The electrons with up polarization present higher probability to pass through the spin selected barrier.

non-spin conserving conductance channel through CFO thin films.

In addition, the nature of electric transport across tunnel barriers can be also inferred from the shape of the $I-V$ characteristics or the thickness dependence of the film resistance. For example, the exponential increase of resistance when increasing the insulating layer thickness is used as an indication that conduction is dominated by electron tunneling. To address the transport properties with high spatial resolution, atomic force microscopy (AFM) with a conducting tip [conducting AFM (CAFM)] [52, 53] is frequently used. However, quantitatively reliable data can be difficult to obtain, since the measured current depends critically on the tip-sample contact conditions [53], such as the contact force and the tip geometry and state, whose control is challenging.

In summary, low TMR at room temperature has been obtained using CFO-based spin filter. Tunnel process through CFO has been believed to take place. Studies of the real nature of the electrical transport of CFO ultra thin films are required to clarify its effect on TMR.

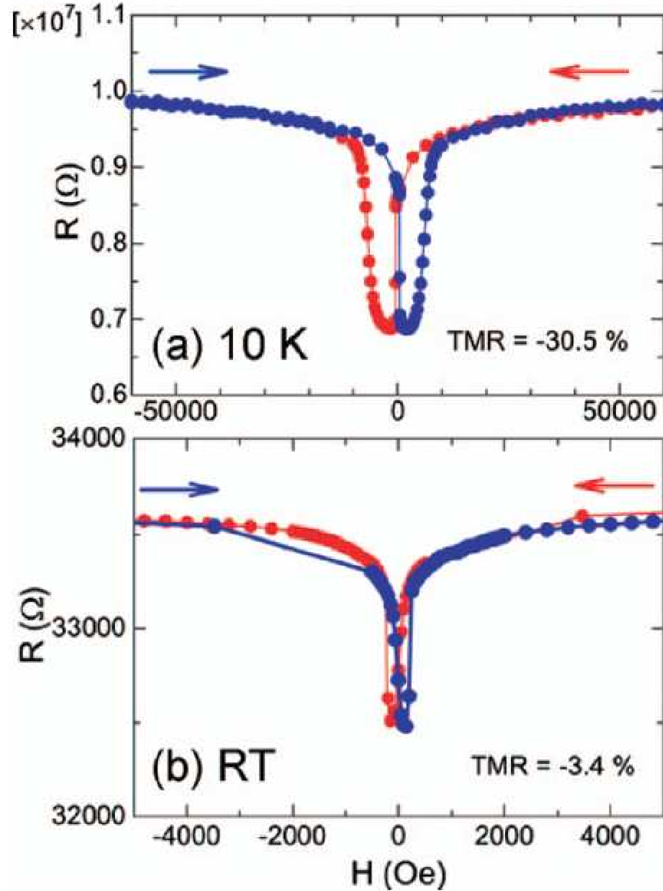

Figure 2.5: TMR curves of Pt/CFO/MgO/Co spin filter device at a) 10K and b) 300K. Extracted from [49].

2.3 Photoinduced effects on $BaTiO_3$

$BaTiO_3$ (BTO) is one of the most studied ferroelectric material due to its large band gap ($\sim 3\ 2\ eV$), high dielectric constant [54] and the posibility to acts as a optical storage medium [55]. The images stored are non-volatile and they are induced by a light of short wavelength ($< 400\ \ nm$) and applied bias combination [56]. Here, the photocarriers created can cause an enhancement of the conductivity, change of the dielectric constant or Curie temperature [57]. The underlying mechanism is the resdistribution of photoexited carriers that screening the polarization.

Pioneering works with BTO crystals were done by W. Warren and D. Dimos [55].

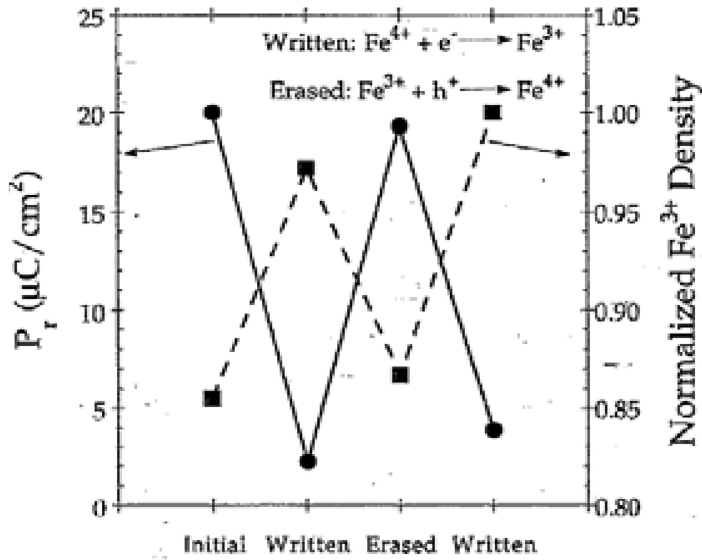

Figure 2.6: Plot of P_r and isolated Fe^{3+} signal intensities for varius UV-light/bias combinations. The written case was achieved by -6V/UV-light treatment (injection of electrons); the samples was erased by a +25V/UV-light combination (injection of holes) [55].

They analized a BTO crystal with a level of impurites of Fe 1 5 $\times$ $10^{18}/\text{cm}^3$. By electron paramagnetic resonance (EPR) measurements was determined the oxidation state of the Fe. They noticed that the Fe^{3+} EPR response is enhanced by ilumination. It is also demostrated that these impurites when excited by UV-light (Fe^{4+} + e^- Fe^{3+}) produce reduction on the remanence P_r in ferroelectric loops as shown in Fig. 2 6. This works appears as an interested way to enhance the photoinduced effect in a ferroelectric.

More recently, it has been developed new techniques that allows to investigate photoinduced effect on BTO in non-contact mode [58 59]. For instance scanning surface potential microscopy (SSPM) allows to detect the relative amount of surface charge on domains [58]. In Figs. 2 7 a) and b) are shown surface potential images showing a and c domains. The surface potential contrast is the largest between c^+ and c^-. In dark conditions the difference in potential $\Delta V_{c^+c^-}$ is $\sim$ 150-200 mV. Once the sample is illuminated by UV, a significant decreases in $\Delta V_{c^+c^-}$ $\sim$ 10 mV can observed

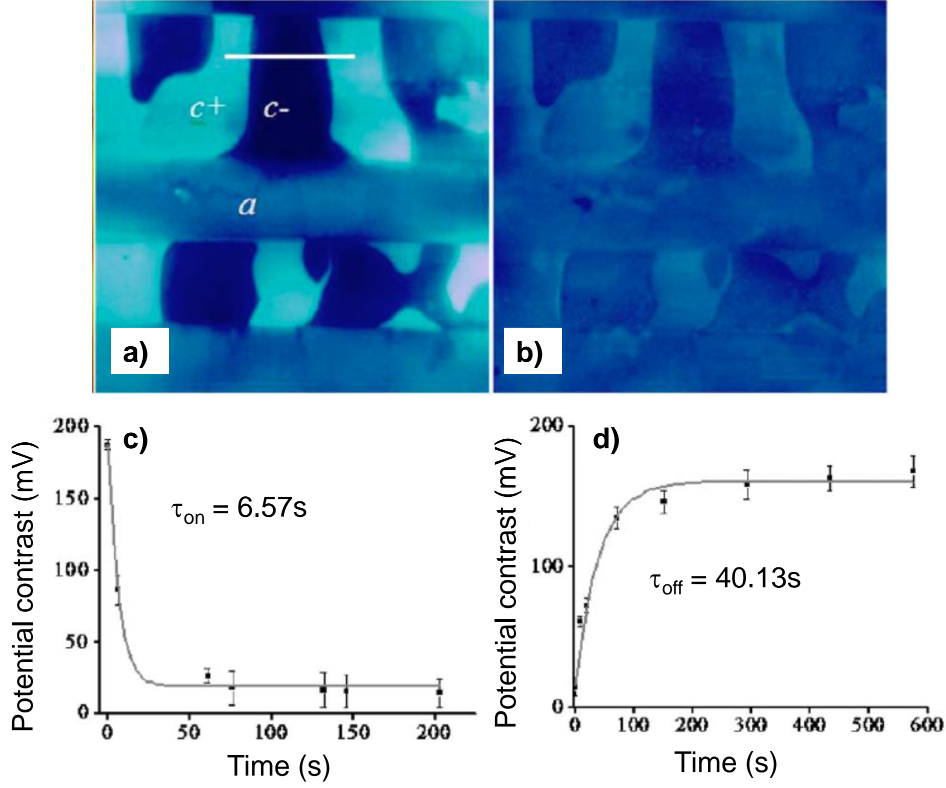

Figure 2.7: Surface potential image of an area showing the *a*-*c* domains a) in dark conditions and b) under iluminated conditions . The time dependence of the surface potential immediately after c) UV ilumination and d) turn-off. Extracted from [58].

in Fig. 2 7b). Clearly the surface potential contrast is influenced by UV ilumination. In Figs. 2 7c) and d) it is studied the time dependence of $\Delta V_{c^+c^-}$ when the UV is turn-on and turn-off respective. From an empirical relation between $\Delta V_{c^+c^-}$ and time (t) :

$$\Delta V_{c^+c^-} = A + B \cdot exp(-t \;\; \delta_{on}) \tag{2.1}$$

it can be determined that the time constant $\delta_{on} = 6.57\ s$. For turn-off, assuming a inverse process for $\Delta V_{c^+c^-}$, is obtained $\delta_{off} = 40.13\ s$. Longer time constants have been obtained by [59]. The creation of a large number of photocarriers screens the polarization. In a c^+ domain having a polarization vector out of the surface, the internal polarization drives positive charge away into the bulk while retaining the negative charges near of the surface. Some of the distributed photocarriers are trapped in

vacant trap states. Thus a space charge field opposing the polarization field increases until the space charge field equals the polarization field or electron-hole generation equals that of recombination. When the light is turn-off, the photocarriers decay but eventually some photocarriers are trapped. The release of the photocarriers is produced via thermally activated, giving longer constant times.

Other important ferroelectric material interesting for lighting applications is $BiFeO_3$ (BFO) due to its lower band gap ($\sim 2.7\ eV$). Here a photon of lower energy than UV radiation, creates photocarriers than can flow in different direction thanks to the polarization without external applied voltage. Another interesting application found it in this materials is the changing of the dimensions of a single crystal when it is subjected to light irradiation, opening a new posiblity to control the elasticity [60].

2.4 Diode and photocurrent effect in $BaTiO_{3-\delta}$ single crystal

Generally, a ferroelectric is defined as a material whose electric P can be switched by an external electric field (E). In order to apply high E larger than the coercive field and maintain the bound charge produced by the switched polarization, ferroelectrics in general should be highly insulating. Thus the leakage current in ferroelectrics had been one of the major obstacles that needed to be overcome. Recently, however, there have been studies on the relationship between electric transport properties and ferroelectric polarization, which include the polarization-dependent electric transport. In $BaTiO_{3-\delta}$ single crystal the oxygen deficiency produces a leakage ferroelectric.

The studies show diode like $I-V$ characteristics for leakage samples as reported for Won *et al.* [61] in $BaTiO_{3-\delta}$, and Choi *et al.* [62] in $BiFeO_3$. In the Fig. 2 8 it can observed the $I-V$ curves obtained in the work of Won *et al.* for $BaTiO_{3-\delta}$ Sandwiched between gold electrodes. Fig. 2 8 a), shows asymmetric $I-V$ characteristics irrespective of maximum applied voltages of 5, 7, and 10 V for a given polarization. The

striking effect of ferroelectric polarization on the $I-V$ characteristics is observed comparing the 2 8 a) and 2 8 b) where the polarization vector has been reversed. Diodelike $I-V$ characteristics which depend on the direction of ferroelectric polarization are clearly visible.

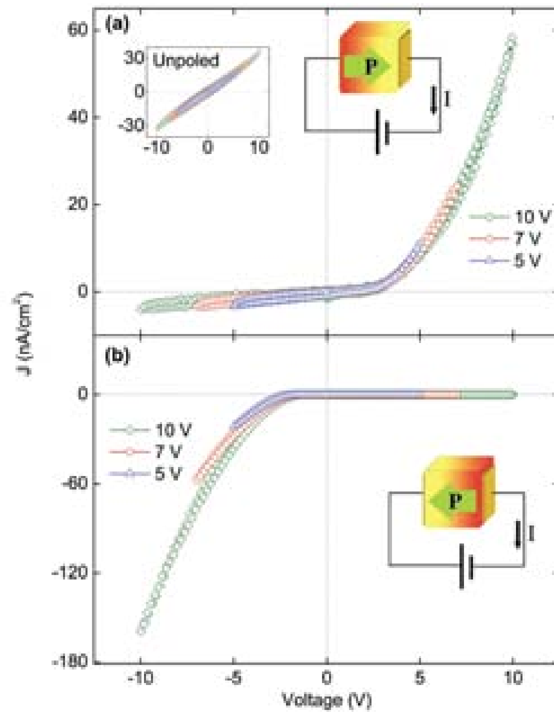

Figure 2.8: a) Current vs voltage curves for thin platelike $BaTiO_{3-\delta}$ single crystals with gold electrodes on both sides after forward poling. Maximum voltage for each curve is 5, 7, and 10 V. The $I-V$ curve for an unpoled $BaTiO_{3-\delta}$ single crystal is shown in the inset. b) $I-V$ curves after reverse poling. Extracted from [61].

The asymmetric contact potentials produced by ferroelectric polarization result in interesting photocurrent effects, which also depend on the direction of polarization. Fig. 2 9 a) shows the short-circuit photocurrent for $Au/BaTiO_{3-\delta}/Au$ structure measured as a function of photon energy of the illuminated light. For the case of ferroelectric polarization pointing to the right side of sample [right polarization, see the upper inset in Fig. 2 9 a)], it is observed positive photocurrent. The negative photocurrent measured for reversed ferroelectric polarization [left polarization, see the lower inset in Fig. 2 9 b)] confirms the dependence of the photocurrent on the direction of ferroelectric

polarization.

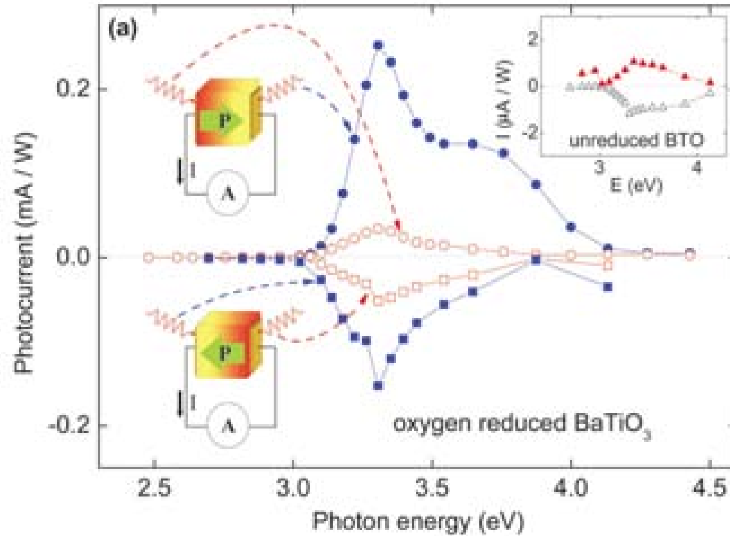

Figure 2.9: Photon energy dependence of the photocurrent for Au/$BaTiO_{3-\delta}$/Au structure with different polarization states and different directions of incident light. Inset displays the photon energy dependent photocurrent for Au/BTO/Au (unreduced BTO) structure with two different directions of incident light. Extracted from [61].

2.5 Ferroelectric tunnel junctions

Before to start the discussion about what is a ferroelectric tunnel junction (FTJ), it is necessary resolve a question; What is the critical thickness for ferroelectricity? It was believed that critical thickness for ferroelectricity in thin films was much larger than the thickness necessary for tunneling to take place. The discovery of ferroelectricity in ultrathin films achieved by Fong *et. al.* in 2004 was a very important step [63].

Now, imagine a capacitor of a ultra thin ferroelectric material sandwiched between two electrodes layers. The performance of these kind of capacitors will be reduced because the losses or leakage current become unavoidable due to the tunneling. So, how a ferroelectric ultrathin film sandwiched between two electrodes can be transformed in an useful device? Esaki in 1971 obtained the answer to this question proposing the concept of polar switching [64]. However, when Esaki proposed his idea there was

not experimental evidences of ferroelectricity in that scale due to the experimental limitation at that time.

As mention before, in a ferroelectric the polarization can be switched beween two stable orientations by applying an external electric field. In a FTJ, if the polarization is reversed, a change in resistance of the junction take place; This phenomenon is known as tunnel electroresistance (TER). The highest value of resistance is defined as R_{OFF} while the lowest value is defined as R_{ON}. Then TER is defined by:

$$TER = \frac{R_{OFF} - R_{ON}}{R_{ON}} \tag{2.2}$$

The physics behind of TER obeys at three different mechanisms [65]. The fisrt mechanism is the modification of the electrostatic potential across the junction, the second is the interface bonding strength and the third mechanism is the strain asso-

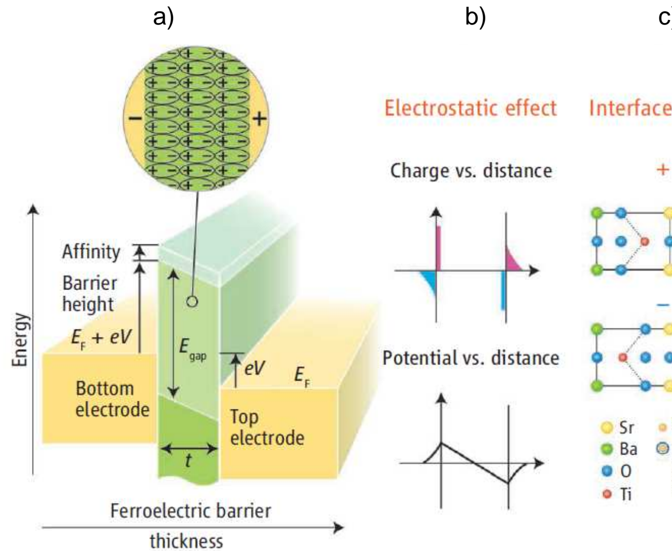

Figure 2.10: a) Sketch of a tunnel junction using a ultrathin ferroelectric sandwiched between two electrodes. E_{gap} is the energy gap, E_F is the Fermi energy, V is the applied voltage, V_c is the coercitive voltage, t is the thickness of the barrier, Δt is the variation of the barrier thickness under an applied electric field. b),c) and d) are the different mechanism affecting tunneling in FTJs: electrostatic potential, interface bonding and strain effect, respectively. Adapted from Tsymbal and Kohltedt [65]

ciated to the piezoelectric response. These mechanism for TER are ilustrated in Fig. 2 10.

The electrostatic effect results from the change of electrostatic potential profile induced by reversal of the electric polarization (P) into the ferroelectric. Here, the surface charges in the ferroelectric are only partially compensated by the electrodes, depending on the Thomas-Fermi screening length of the metal and therefore the depolarizing electric field in the ferroelectric is not zero [66]. This induces an asymmetric variation of the electrostatic potential across the tunnel barrier (fig. 2 10 b). When the ferroelectric is connected by two different electrodes, the screening and hence the electrostatic variation are different at the interfaces. This can be described as a shift of the barrier height when the ferroelectric polarization is switched [67 68].

The interface effect has been studied from atomistic calculations [69]. The polarization switching modifies the positions of the ions in the last atomic layer in the ferrolectric, as a consequence, the atomic orbital hybridization at the interface and therefore the interfacial DOS as well as the transmision probability is changed as showed in Fig. 2 10 c).

The piezoelectric response of the ferroelectric produced by an applied electric field produces a strain, sketched in Fig.2 10 d). Here, the length of the barrier is modified [68].

Polarization stability of ultra thin ferroelectric barriers in this case becomes a serious issue (See Fig.2 11). In the last years, different groups have fabricated FTJs with top nano-electrodes using BTO, PZT and BFO barriers and have demonstrated, by using SPM techniques, that in these devices it is posible to achieve giant room temperature TER. In particular, repetitive switching between two distinct resistance values (TER 100,000%), good data retention for up to 10 yr and the memory programing with short (10 ns) voltage pulses, just few volts in amplitude have been reported [70 71 72]. These results reveal the significant potential utility of FTJs in non-volatile memory applications with the advantages of non-destructive readout, simple device architecture, low power comsumption and high density data storage. Some authors also show that

changes in resistance scale with the nucleation and growth of ferroelectric domains in the ultra-thin barrier layer, thereby suggesting potential as multilevel memory cells and memristors [73 74].

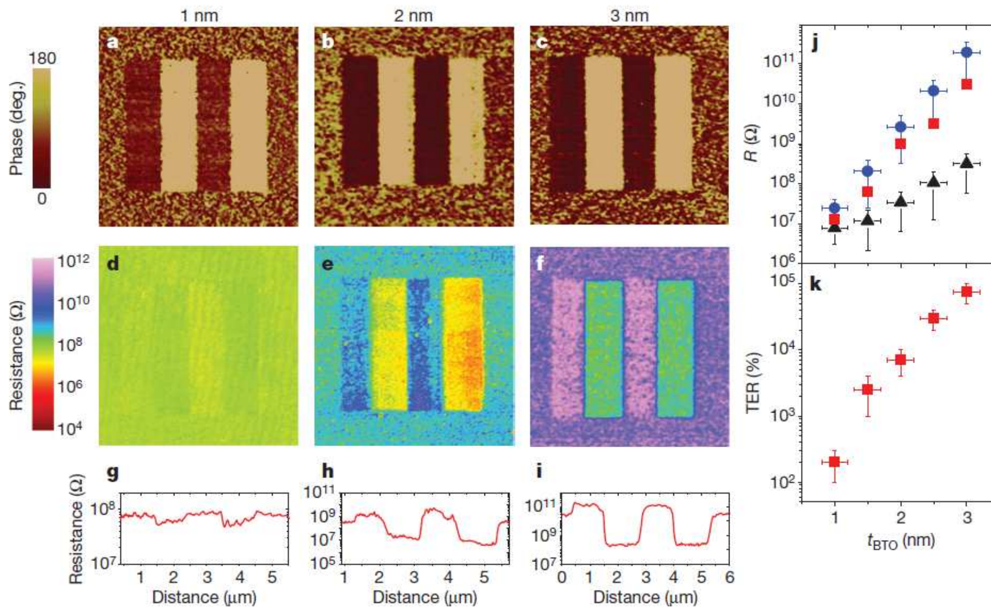

Figure 2.11: Observation of the giant TER effect in ultrathin BTO films. a-c) Piezoresponse force microscopy (PFM). (d-f) conducting atomic force microscopy resistance mapping for four written ferrolectric stripes. (g-i) Corresponding resistance profiles of the poled area. j) thickness dependence of the resistance of unpoled (red squares), positive (black squares) and negatively (blue circles) poled regions. The resistance increases exponentialy. k) dependence of TER on the thickness. Adapted from [75]

How non-tunnel transport affects the TER also have been studied for FTJs [76]. It has been observed that defects in ultrathin films deteriorate resistance switching properties. This problem appears more evident in large area devices. For instance, succesful demonstration of room temperature resistivite switching in junctions with TER ratio of $\sim$ 1000% and lateral dimensions in the range of $10^3 \mu m^2$ have been reported [77 76]. TER measured by SPM using the tip as a top electrode presents values $\geq$ of 10,000% [71].

2.6 The interest in half-doped Manganites for Enhanced TER

Before to disscuse how TER can be enhanced by half doped manganites, it is very interesiting to known how the properties of the manganites change by doping and strain.

The mixed-valence perovskites $La_{1-x}A_xMnO_3$, where A can be Ca, Sr or Ba and x is the doping level, were largely studied in monocrystal and polycrystalline samples. They show antiferromagnetic (AF) insulating behavior at low and high doping level and ferromagnetic (F) metallic behavior in a certain range of concentration centered around $x = 0.3$. For higher doping level $x = 0.7$ the manganite behaves antiferromagnetic and insulator. At x ∼0.5 it is expected a phase competition between AF and FM order as observed in Fig. 2 12. However, in thin half-doped manganites films, strain appers as a variable wich allows to lift the degeneration between the e_g levels, $3z^2 - r^2$ and the $x^2 - y^2$. For tensile strain $x^2 - y^2$ orbital presents lower energy than $3z^2 - r^2$, but for compresive strain $3z^2 - r^2$ is the orbital with lower energy, thus potentially leading to different properties than in bulk samples. This is called orbital degree of fredom (ODF) [13].

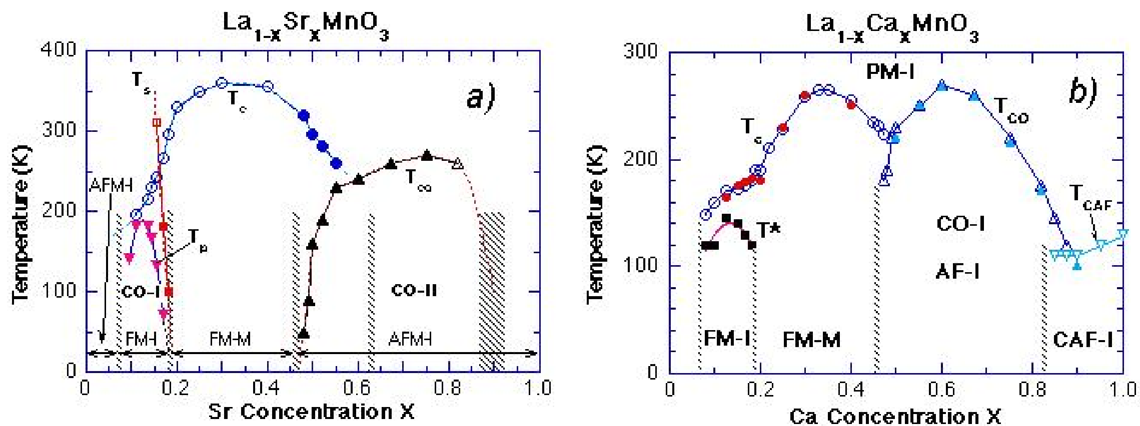

Figure 2.12: Phase diagram for a) $La_{1-x}Sr_xMnO_3$ and b) $La_{1-x}Ca_xMnO_3$ varing x. [78, 79]

A very interesting work was done by Konishi *et al.* [80]. It shows an experimental

way to control the magnetic and electric response of the $La_{0.5}Sr_{0.5}MnO_3$ by growing the films on subtrates with different lattice constants. The strain is measured in terms of tetragonality (c/a). For free strain, $c\ a = 1$ the e_g level are degenerates and the magnetic order is expected to be ferromagnetic (FM) and metallic. For tensile strain, $c/a < 1$, the magnetic order is ferromagnetic in plane but antiferromangetic between planes (A-AF), leading to a metallic in-plane electric response. For compresive strain $c/a > 1$, the spins align ferromagnetically along c-axis but antiferromagnetic (C-AF) coupling in the plane. Here, both out-of-plane and in-plane the transport must be insulating. The results obtained by Konishi was supported and expanded to other doping levels by the teoretical work of Fang *et. al.* [81]. The Fang s diagram is showed in the Fig. 2 13. In constrat to $La_{0.5}Sr_{0.5}MnO_3$, calculations of the effect of tetragonal distortion $c\ a$ on the phase diagram of narrower band with oxides such $La_{0.5}Ca_{0.5}MnO_3$, are not yet available, must likely due to the existance of charge ordering or electronic phase separation. Experimentally, strain effects on $La_{0.5}Ca_{0.5}MnO_3$ thin films are much less known[82 83].

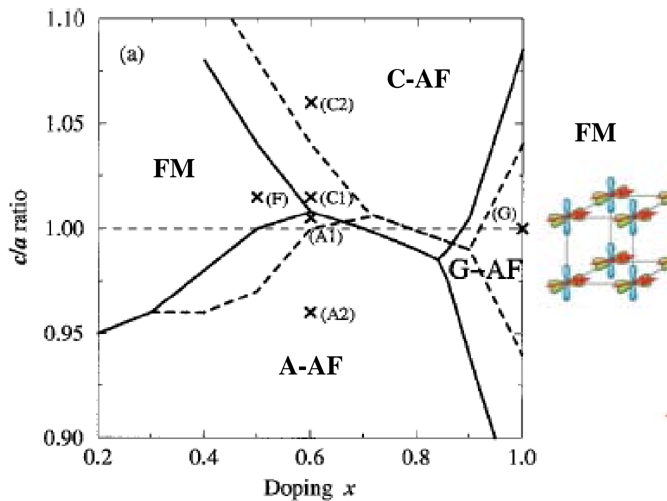

Figure 2.13: The Phase diagram of $La_{1-x}Sr_xMnO_3$. c/a and x are variables. FM, C-AF, A-AF magnetic order obtained from total energy calculations [81, 13].

The rich phase diagram of manganites has inspired important ideas pointing the posibility to control by field effect the metal or insulating behavior; The key for enhanced TER. An interesting prediction was made recently for the $La_{1-x}Sr_xMnO_3$/BTO interface with $x \sim 0.5$ [84]. First-principles calculations showed a possibility to switch a magnetic order at the interface, from ferromagnetic (FM) to anti-ferromagnetic (AFM), by reversing the polarization of the ferroelectric BTO. In a FTJ with such a magnetoelectrically active interface in the path of the tunneling current, switching of the ferroelectric barrier is expected to change the tunneling barrier thickness, thus leading to a giant change in conductance (enhanced TER) [85]. However no systematic TER measurements on tunnel structures BTO/HD layers involving different strained states are yet available.

Part II

Experimental

Chapter 3

Experimental techniques

3.1 Introduction

In this thesis we focus in two diferent areas of characterization thin films, the main is the dielectric characterization of insulator and/or ferroelectric materials and the second is the magnetic and transport characterization of manganites. The begining of this chapter will start explaning the method of sample obtention, moving to surface and structural characterization, then the measurements of magnetic and transport properties. Finally it will be described the experimental setup and procedures for dielectric and ferroelectric measurements.

3.2 Pulsed Laser Deposition

Epitaxial layers of $CoFe_2O_4/SrRuO_3$, $CoFe_2O_4/La_{0.7}Sr_{0.3}MnO_3$, $BaTiO_3$ /$La_{0.7}Sr_{0.3}MnO_3$, $La_{0.5}Sr_{0.5}MnO_3$, $La_{0.5}Ca_{0.5}MnO_3$, $La_{0.5}Sr_{0.5}MnO_3/BaTiO_3$ / $La_{0.7}Sr_{0.3}MnO_3$, and related heterostructures have been achieved by pulsed laser deposition (PLD) on (001), (110) (111)-oriented single-crystalline substrates at the service of thin film growth of ICMAB. Nico Dix Ms. and Dr. Florencio Sánchez took in charge of determine the growth conditions.

In this technique, a pulsed beam of an ultraviolet laser (excimer) is focused on

ceramic target placed in a vacuum chamber. Combining in a pulse, high photon energy, and high energy density, the material is ablated. Ablation refers to the etching and emision of material under conditions totally out of equilibrium. The created plasma expands fast along the perpendicular direction of the target. A substrate is placed in front of the target at certain distance, and an inert or reactive gases are usually introduced during the deposition process. A sketch ilustrating this process is shown in Fig. 3 1.

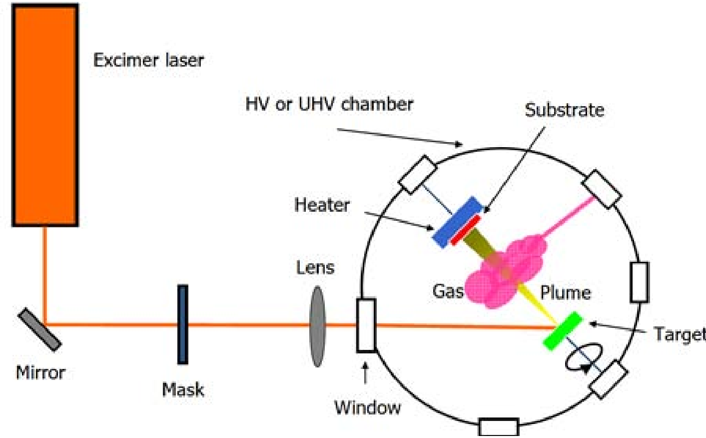

Figure 3.1: Sketch of PLD system located at the ICMAB.

The growth parameters are the gas pressure, substrate temperature, and laser frequency. During the deposition, oxygen gas is flowed in the chamber for obtaining the correct stoichiometry in the deposited film. Argon gas can be also used to obtain a stoichiometry low in oxygen. The gas flow is adjusted by a flowmeter. The temperature influences the kinetic energy of the species at the surface, allowing the atoms have a mobility to reach positions energetically propitious, favoring the crystallinity. Nevertheless, high temperature in excess produces a detrimental effect of the oxygen desorption. The frequency is related to the time of the adatoms that reach positions energetically propitious. If the frequency is high, the first atoms that arrive do not have enough time to find positions energetically propitious when the second atoms from the next pulse have already arrived, producing a detriment of crystalinity.

3.3 Sputtering

The sputtering proccess is defined as the ejection of material from a solid target due to the impact of energetic particles on its surface. The impact produces the detachment of material from the target. The target is set as a cathode and the sample is sets as anode in a vacuum chamber, which is previously evacuated to low pressure (10^{-6} $Torr$). Ionic bombardment of the target is obtained by a flux of gas (Argon in our case) which is ionized due to the potential difference between the target and the substrate; In rf sputtering, an alternating electric field is applied at a typical frequency of 13.56 MHz for generating plasma. To allow efficient targer erosion, magnetron sources are commonly used. to deposit the platinum, a `Plassys commercial sputtering system located at the ICMAB was used.

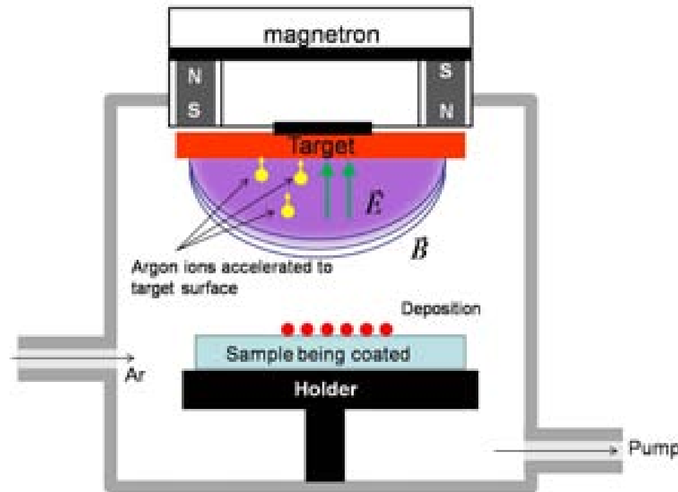

Figure 3.2: Sketch of sputtering system located at the ICMAB.

The important parameters for Pt deposition are the flux of Argon ($10sccm$) at room temperature, power ($20Watts$) and distance of the target-sample 6 cm. In these conditions the growth rate is around 7 nm min. Pt was chosen because it is a noble metal, easy to grow without impurities and difficult to be degradated, and have displayed to be appropiate as a top electrode for measuring ferroelectricity [86]. Previous to Pt deposition, the samples has been cleaned with acetone and ethanol, and sub-

sequent e: 't layers

$\leq< \sim 40$ arent is.

The Fig.

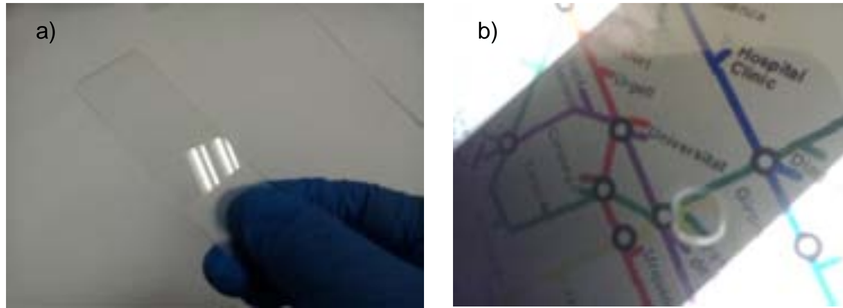

Figure 3.3: a) A glass slide without any deposition. b) The same glass slide after the platinum deposition ($\sim 40nm$). Here the Barcelona s metro map on a computer screen can be seen trough a glass coated by Pt.

3.4 Scanning probe techniques

3.4.1 Scanning electron microscopy

Scanning electron microscopy (SEM) produces images of the sample by using electrons. Here, using electron is posible to obtain wavelengths of 12 pm at 10 kV, allowing magnifications up to 9×10^5 times. In order to produce a sample image, a focused electron beam is scanned over the sample surface and several different interactions take place, whose its effects are detected. The easiest type of sample to be studied is a conducting material, because when the surface is insulating, like in the case of spinels the formation of charge accumulation causes deviations on the electron trajectories and the images appears distorted. In any case, several methods were developed in order to make the investigation of insulating materials possible, like coating them with a very thin flms of metallic layers (commonly Au, Au-Pd or carbon) deposited by sputtering or evaporation, or working in a low vacuum atmosphere (lower than 0.1 $Torr$). So positively charged ions generated by beam interactions with the gas help to neutralize the negative charge on the specimen surface. As pressure increases the electron mean

free path decreases, and a smaller focal distance has to be utilized in low vacuum SEM.

The imaging of the surface is achieved by the detection of reflected (backscattered) electrons, while the electrons emitted from the sample surface after the interaction with the material, called secondary electrons, are used to investigate the compositional homogeneity. When the microscope is equipped with a X-ray detector, the composition of the surface can be studied as well. The incidence electrons cause excitations in the sample atoms, which is relaxed by emiting X-rays with a wavelength specific for each element.

The results presented in this thesis were obtained in a QUANTA FEI 200 FEG-ESEM (Tungsten filment) located at the ICMAB.

3.4.2 Atomic force microscopy

Atomic force microscopy (AFM) is a scanning probe technique sensitive to the forces interacting between a sharp tip and sample surface placed below. It was developed by Binning, Quate and Gerber in 1986, with the objetive to resolve the failure of scaning tunneling microscopy (STM) for insulator and doped semicoductors [87]. The basic components of an AFM system consist of a cantilever, a photodetector which monitors the motion of the cantilever, and a scanner which controls the scanning the probe s position and consequently the distance between the probe and the sample(see fig. 3 4). When an AFM tip approaches to the surface, it undergoes an attractive or repulsive force. The attractive force causes a downward bending of the cantilever while the repulsive force causes an upward bending. The amplitude of the bending is related to the cantilever stiffness and the resonant frequency as well as the properties of the sample surface.

Topographical analysis at the nano-scale can be done. A cantilever, holding the tip at its extremity and moving over the sample, it is forced to deflect in response to the asperity of the surface as ilustrated in Fig. 3 4. the deflection is measured by an optical system. A laser beam, pointing to the cantilever reflects onto a photodiode detector;

the movement of the reflected beam over four detection pads gives information about the vertical displacement of the tip and about the lateral bending of the cantilever. There are two topographic imaging modes in AFM systems, tapping and contact mode.

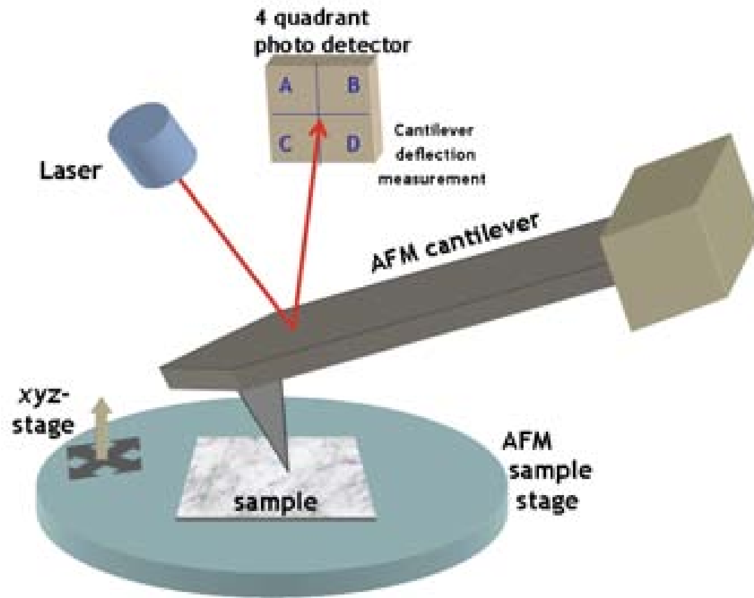

Figure 3.4: Sketch of atomic force microscope.

In tapping mode, the AFM probe keeps oscillating at a set frequency near its resonance ($300 \sim 400\ kHz$ lower than the resonance) driven by an oscillation piezo of the scanner. When the probe is scanning a surface and oscillating at a distance of hundreds of Angstroms from the sample, the resonance frequency of the tip is shifted from the set free oscillating frequency due to the force applied on the tip. The shift of oscillation frequency leads to a change in the oscillation amplitude of the tip. The height of the cantilever is adjusted by the scanner z piezo through a feed-back loop to maintain constant oscillation amplitude as specified by the set point value in the controlling software. When the topographic image is recorded, the phase image is also collected by recording the phase difference between the driven sine waves and the response of the cantilever. The phase signal is more sensitive to the variation of material components.

On the other hand, working in contact mode means the repulsion regime. Here the

signal of feedback is the normal force (vertical deflection of the cantilever). Variations on the friction between different areas suggest a change on the chemical properties, so information about relative chemical composition of the surface is also attainable.

3.4.3 Conducting atomic force microscopy

The use of coductive tips, in contact mode allows obtaining I-V curves or current maps on the surface of the samples.It is called Conducting atomic force microscopy (C-AFM). This technique is particularly useful and easily applicable for achieving qualitative analysis of the conductance homogenety of the samples, but its application for quantitative reliable interpreted values represents still a challenging issue. The current values obtained by C-AFM scan are subjected to the influence of many factors that do not depends on the the sample nature, but on the particular situation in which the measurement was taken, like the humidity of the enviroment or if the tip is wasted for previus experiments, limiting the repeatibility of the experiments. The I-V measurements for this thesis were done following a protocol previously established by Dr. Franco Rigato and Dr. Michael Foerster at the ICMAB. Here the critical point is maintaining a constant value of the force appplied at the tip in order to fix the contact area between the tip and the sample. The protocol is as following:

- The electronic offsets and gain of the applied voltage is corrected; a Ohmic resistance of 3 $M\Omega$ is connected in order to check the current detector and to correct the offset of the current.

- When samples had to be compared, they were all measured with new tips.

- The enviromental humidity can generate a water meniscus in the contact area, between the tip and the surface sample, which can alter the contact conductivity. In order to reduce this problem, a constant nitrogen flux was maintained inside of the AFM chamber.

- The force constant of the cantilever was measured folllowing the method known as Sader , which allows extracting the force-constant from a resonance frequency of the cantilever [88].

- The response of the laser beam detector to the cantilever deflection under an applied force was calibrated for every different scan on the sample surface, by means of $f(z)$ curve, where z represents the vertical displacement of the cantilever in the proximity of the surface and f is the voltage signal read by the detector, corresponding to the tip deflection. The Fig. 3 5 shows the typical response of the f with the distance. When the tip is approaching to the surface (*Forward*) the detector presents a constant value ($f = 0$) indicating that the tip is far away from the surface, but once the tip establishes contact with the surface f increases linearly with z. From the slope, the conversion of the applied voltage and the force can be achieved. When the tip is retracting (*Backward*) from the surface, the curve presents similar behavior as *Forward* except in a region where at the begining of the contact mode ($f = 0$); this difference is due to the cohesive forces.

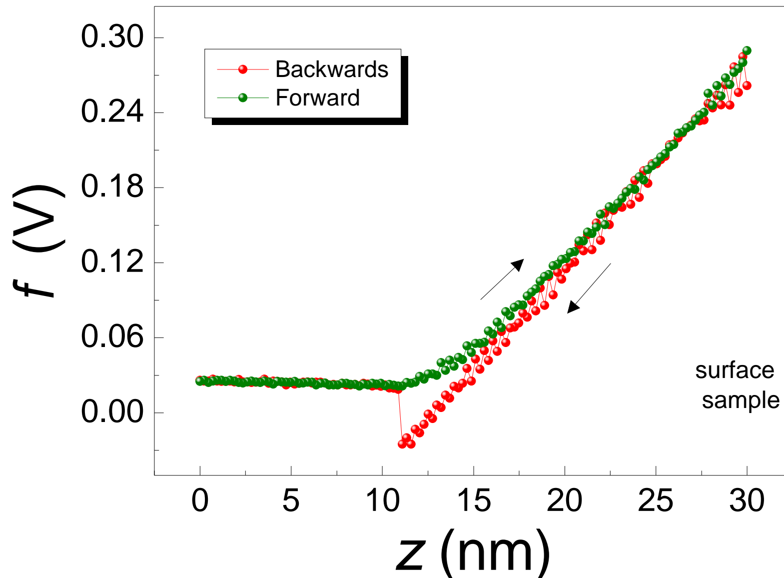

Figure 3.5: Normal force vs z. Green curve is *Forward* and red curve is *Backwards*.

The measurements of the films transport properties were performed at the ICMAB with a Nanotec Cervantes microscope, equipped with an I-V converter which alllows detecting currents at ranges from 100 nA, 1 μA and 10 μA. The sensitivity of the converter is $scale/10000$. The bias voltage can be varies from $-10V$ to $10V$ and it is applied to the bottom electrode while the tip is grounded. Si_3N_4 tip coated with boron doped polycrystalline diamond and with spring constant of $\sim 40\ N\ \ m$ were used. Nanosensor NCHR -CDT conductive tip have radius about 100 nm.

An extension of C-AFM were done in order to performace impedance espectrocopy and polarization measurements. Here, Pt or Au microcontacts contacts with a very well defined area were deposited on the samples surface. The conducting AFM tip was connected, via a coaxial wire, to one input channel of an impedance analyzer while the second input was connected to bottom electrode of the sample. The sample holder and the whole AFM setup were connected to the ground of the impedance analyzer. For contact force of $\sim 1\ \mu N$, it was observed that the electric contact between the tip and the metallic contact on the sample surface it is very well established given the highly reproducible data. Nevertheless, the series resistance (R_s) given by the tip ($\sim 10\ k\Omega$) has to be taking into account at the data analysis because it can be comparable to the impedance of the studied layer.

3.4.4 Piezoresponse force microscopy

From the necessity to observe the poled domains in ferroelectric materials, piezoresponse force microscopy (PFM) emerged in 1992 [89]. Since then, the PFM has become a standard technique for imaging ferroelectric domains [90 91 92]. Evenmore in ultra-thin ferroelectric films, where some other techniques for characterization fails, PFM has been used to demostrate that ferroelectricity persist in this ultra-thin regime[93].

PFM works necessarily in contact-mode. The conductive tip acts as a top electrode. An alternating voltage with a variable amplitud V_{ac} and frequency $\ \ 2\pi$ is applied to the tip by a function generation. The voltage-induced deformations of the sample lead

to a periodic vibrations of the sample surface and therefore transmitted to the tip. These periodic vibrations are sensed in the photodetector as variation in z direction:

$$z = z_0 + Acos(\quad t \ + \ \theta) \tag{3.1}$$

where A is an amplitude of the oscillation, is the angular frequency t is the time and θ is the phase. A Lock-in Amplifier (LIA) selects the response of the photodiode with same 2π as the excitation signal. PFM response will be in phase when the tip is located on a ferroelectric domain poiting up and consequenltly 0° phase shift related to the incoming signal V_{ac}. In contrast, when the tip is on the domains pointing down, PFM will detect a vibration out of phase with shift of 180°. A DC voltage can be used to p tern (see Fig. 3 6). Natural dom

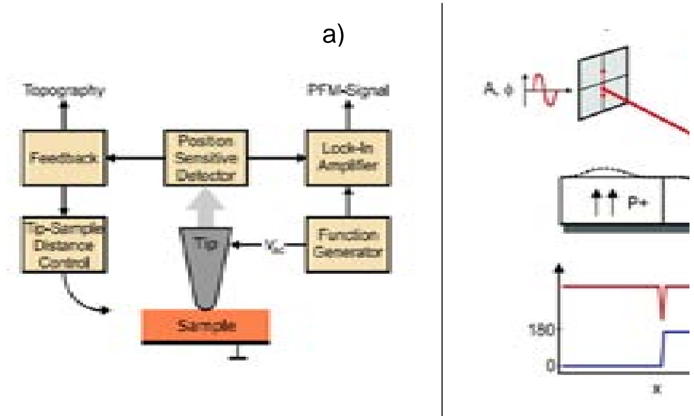

Figure 3.6: a) Diagram of signal adquisition in PFM. b) Schematic results obtained from the PFM. For colinear polarization the PFM amplitud must be constant but the phase has to change 180°. Fig. adapted from [92]

The dificulties to obtain absolute values with high accuracy, for example the piezoelectric coeficient, are inherited from the AFM where just relative values are important. But maybe the most important difficulty in PFM appears during the data adquisition where a inherent background is always present. A simple way to understand the role of the background is putting the incoming voltage signal in $X - Y$ representation. $X = A \cdot cos(\theta)$ and $Y = A \cdot sin(\theta)$ where A is the amplitud PFM signal and θ is the

PFM phase for a given polarization direction. Assume that the tip starts the scan in a domain point up with a $X \ = \text{A} \cdot cos(\theta \ )$ and $Y \ = A \cdot cos(\theta \ ) = 0$. When the tip during the scaning find a region with polarization pointing down it is expected a change in X axis but not in the Y. That means, $X \ = \text{A} \ \cdot cos(\theta \ )$ and $Y \ = Y \ $. The effect of the flotating voltage $Y \ \ = A \cdot cos(\theta \ \ ) = 0$ in determining the phase change between domain pointing up and domains pointing down is a phase change $\theta \ \ - \theta \ \ = 180°$ as observe round shift the origing of the reference s

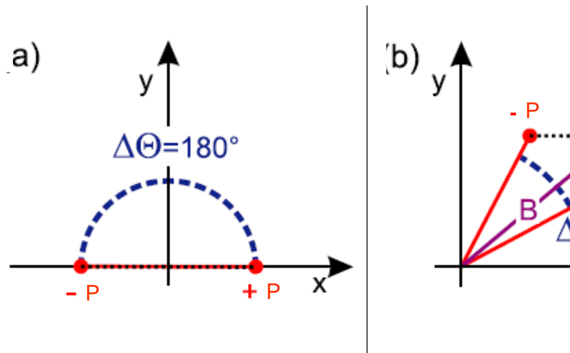

Figure 3.7: a) Ideal PFM response. b) Real PFM response due to the background. Fig. adapted from [92]

Another consequence of the background (B) is that the magnitude of the vector $-P$ and $+P$ are no longer equals, except when the B-vector coincides with the y axis.

An example of PFM measurements where the background affects the interpretation calculated phase is shown in Fig. 3 8. Here, PFM images of the surface of a poled $LiNbO_3$ crystal are shown. In these Figs., PFM response was adjusted by introducing a phase compensation in order to obtain the maximum variation signal in the X channel and minimize the variation in the Y channel, as can be observed in Figs. 3 8 a-b respectively. Although the Y channel does not present change of the contrast, the mean value is close to 30 mV. On the other hand, the amplitude of the PFM signal,(Fig. 3 8 c)), indicates not significant difference on the up or down domains, just the diagonal lines indicate a change of the polarization direction. The phase determined by the software indicates a change of phase of 23°. This kind of sample is reported to

present phase change of 180°. Such a big difference comes from the backgroung signal discused before. This indicates that in each experiment the background vector has to be determined and subtracted from the results obtained in a further data treatment.

An Agilent system 5500, located at the ICMAB, has been used for the experiments. Si_3N_4 tip coated with boron doped polycrystalline diamond and with spring constant of $\sim 40\ N\ m$ were used. The tip radius is about 100 nm. The maximum AC voltage and DC voltage is 10 V. The velocity of the tip was aproximately $10\mu\ s$. and the range of frequency used in this thesis goes from 10 kHz to 180 kHz. The tip force was maintained constant at a value aproximate of 500 nN.

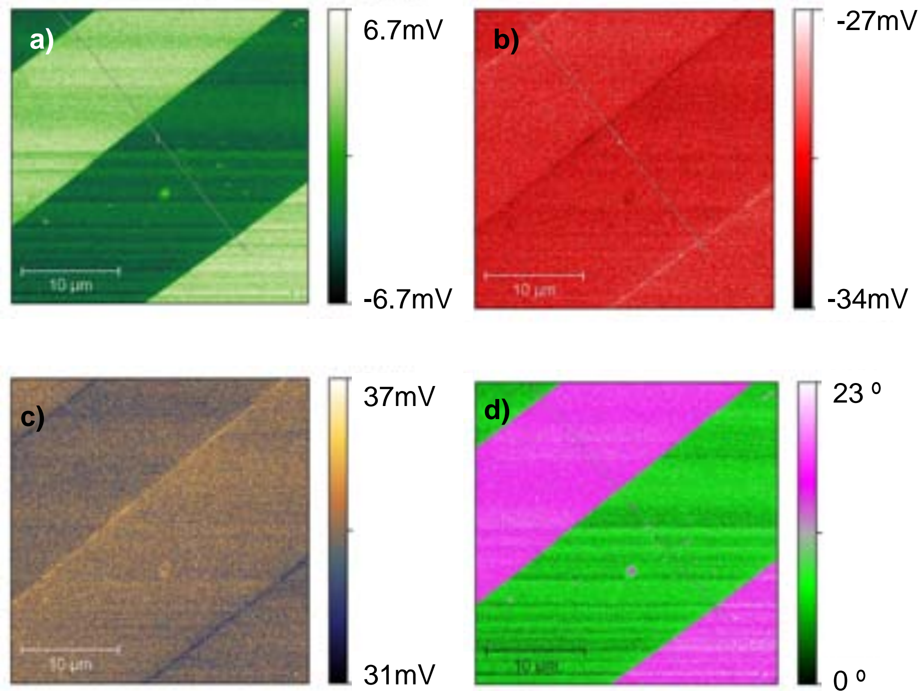

Figure 3.8: Data obtained from PFM for $LiNbO_3$. a) Signal of X-channel, b)Signal of Y-channel, c) Amplitude and d) Phase.

3.4.5 Imaging at contact resonance

For some samples, for example at very thin films, using a higher AC voltage is undesirable, because the AC magnitud can overcome the coercitive voltage of the thin film. New theorical advances in PFM suggest an alternative to high AC voltage. This concept is *PFM at resonance*. Here, the same model of Sader [88] working at the resonance frequency produces an amplitude A of the tip given by:

$$A = d_{33} V_{ac} Q \tag{3.2}$$

Where d_{33} is the piezoelectric coeficient, V_{ac} is the AC voltage applied and the Q is quality factor. Typical Q values range from 10-100, this implies that one can amplify a weak PFM signal by a factor of 10-100 by simply driven the tip voltage at the resonance frequency. It is good to remark that the resonance frequency in contact mode is not the same resonance frequency as in non-contact mode. A scan in frequency has to be done in contact mode to find the new resonance frequency.

A source of phase shifts no related to changes in polarization can come from irreversible changes to the cantilever itself. If the tip picks up a contaminant, the contact resonance can experience a sudden jump, the resonance jumps are typically of the order of few kHz. This causes large discontinuous changes in the measured phase. The high roughess can also produces a crosstalk between the topography and the PFM signal. Low roughness samples are the most indicates for PFM imaging at contact resonanse.

3.5 Structural characterization

In this section, it will be presented the analysis technique that provided information about the structural features of the films. While X-ray diffraction and reciprocal space maps analysis were performed at the *ICMAB* laboraries, X-ray difraction in grazing incidence was done at *ICN2*.

3.5.1 X-Ray difracction

X-Ray Difraction (XRD) is a non-destructive analysis which allows studying the crystal structure of materials. When X-ray striking a solid, the material produces secondary spherical waves with the same energy. If the solid presents a regular array of atoms, then the secondary waves, or scattered radiation, cancel out in most directions through destructive interference but they add constructively in a few specific directions. These specific direction are related with the interplanar distance $d_{\{hkl\}}$ of the crystal planes in the sample. Here $\{hkl\}$ is a vector proper to a family of the planes. Equation 3.3 is known as the Bragg's law that relates the angles and the distances between planes. Here λ is the wavelength of the radiation, and n is the order of the difraction. The Bragg's law implies also that the radiation incident on the surface of $\{hkl\}$ planes, with incident angle θ_i, will present the same angle between the outgoing radiation θ_r as observed in Fig. 3.9. The diffraction effect is relevant if λ is comparable to $d_{\{hkl\}}$, for this reason X-ray radiation is particularly indicated for the study of crystal structures.

$$sin(\theta_i) = \frac{n\lambda}{2d_{hkl}} \tag{3.3}$$

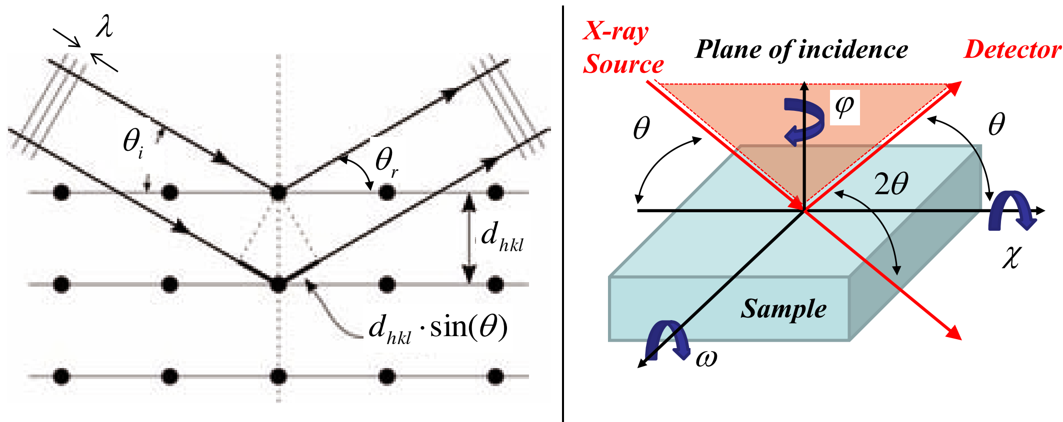

Figure 3.9: Scheme of Bragg condition.

In a conventional difractometer, the incident and reflected beams define the *plane of incidence* as described in Fig. 3.9. The X-ray source remains in a fixed position,

while the adjustment of four different angles allows establishing the geometry of the experiment. These four angles are:

θ: The angles defined by the direction of the imcoming radiation and the sample surface. This angle is modified by a rotation of a goniometer label around an axis normal vector of the sample plane.

2θ: The angle between the direction of the incoming radiation and the reflected beam. It is where the detector is placed.

: The rotation arround the axis defined by normal vector of the sample plane.

λ: The tilt obtained by rotating the sample plane arround a determined axis by intersection between the sample plane and the plane of incidence.

When diffraction planes are parallel to the film plane, symetric reflections are measured and incidence angle is equal to reflected angle ($= 2\theta$ 2).The asymetric reflections, associated to families of planes not parallel to the sample surface, can be studied by other methods: the first one consists on uncoupling the rotation from 2θ rotation, while the second posibility is to tilt the sample through a rotation of the λ angle.

Conventional X-ray techniques were applied in this work. Here they are briefly listed:

- $\theta - 2\theta$: the scan motion of the detector (2θ angle) and the rotation of the sample plane around the axis are coupled in the condition $= 2\theta$ 2. This configuration is used for symmetric reflections, and it allows to verify whether the film growth is textured and to obtain the out-of-plane lattice parameter.

- Rocking curves (-scan): the position of the detector is fixed at the diffraction condition of a particular reflection, whereas the angles is swept within a given range. The reflection intensity is a peak function of the angle, and the full with at half height of the peak characterize the crystalline quality of the sample.

- Reciprocal space maps: this procedure is important because it allows to compare the in-plane lattice parameters of the film and the substrate, in addition to the out-of-plane lattice parameter. The analysis is based on a series of standard $\theta - 2\theta$ configuration. First, an asymetric hkl family of planes must be selected. Once calculated the λ angle corresponding to the chosen reflection, i.e. the angle between the $[hkl]$ vector and the perpendicular to the film surface, the goniometer must be moved in order to locate the selected $[hkl]$ vector in the plane of incidence. As the reflection is asymetric, and 2θ goniometers have to be moved in order to achieve the new difraction condition, which is given by $= 2\theta\ 2 - \lambda$. Then, 2θ scans are adquired for several values, varying in a given range around the optimal condition. The result is a two-dimensional map $(2\theta, \ )$, displying intensity peaks, which can be converted in a map of the reciprocal space, expressed in terms of the reciprocal wave vectors q and q , respectively parallel and perpendicular to the surface, through the relations:

$$q \ = \frac{2}{\lambda} sin\left(\frac{2\theta}{2}\right) sin\left(\frac{2\theta}{2} - \ \right) \tag{3.4}$$

$$q \ = \frac{2}{\lambda} sin\left(\frac{2\theta}{2}\right) cos\left(\frac{2\theta}{2} - \ \right) \tag{3.5}$$

  Knowing the relationship between the reciprocal and real space lattices, it is posible to obtain the unit cell parameters from the q and q values: for example taking the $(h\ \ k\ \ l)$ reflection of a cubic (or pseudocubic) lattice, the in-plan a and the out-of-plane c lattice parameters can be extracted by the following relations:

$$a = \frac{\overline{h^2 + k^2}}{q} \tag{3.6}$$

$$c = \frac{l}{q} \tag{3.7}$$

Another utility of the X-ray technique extensively used for the work of this thesis was X-ray reflectivity(XRR). XRR measurements allow determining the thickness and

getting information about the roughness of films and heterostructures. Here, a $\theta - 2\theta$ scan is carried out for very low angles, from 0 3° to 7 0°. The Bragg s law (eq. 3 3) relates this angle range to interplanar spacings much larger than the crystal cell parameters. In fact, the diffraction effect is in this case achieved for the distance d of the film surface and the interface with the substrate, provided that they both are smooth enough. In contrast to standard X-ray diffraction experiments, now it is crucial to take into account the refractive effects, which are relevant at low incidence angle, but can be negleted at high angles involved in a standard XRD measurements.

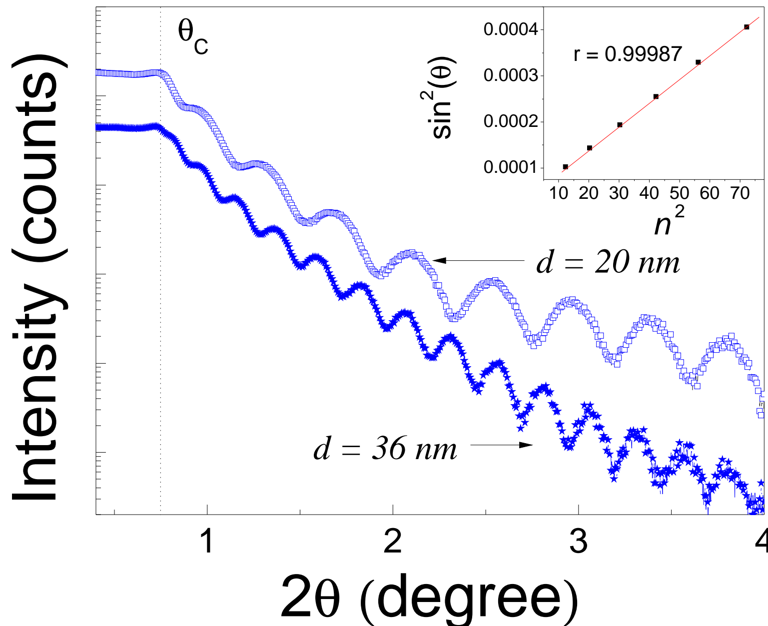

Figure 3.10: XRR data for a couple of $La_{0.5}Sr_{0.5}MnO_3$ films with diferent thickness grown on STO substrates. The inset presents the linear regresion explained in equation 3.8. The thickness is obtained from the slope.

A couple of examples of XRR analysis on $La_{0.5}Sr_{0.5}MnO_3$ films over STO substrate are shown in Fig. 3 10. The sample position is adjusted first by means of $\theta - 2\theta$ scan around a substrate diffraction peak at high angle, and then the low angle scan is performed. The resulting curve shows that bellow a threshold angle, the critical angle θ_C, all the incident radiation is reflected. Afterwards, the intensity measured by the

detector is oscillatory with respect to the 2θ angle. The period of these oscillations, called Kiessig fringes, depends inversely on the film thickness. Each peak corresponds to a different diffraction order n, and their position θ_M is determined by the relation:

$$sin^2(\theta_M) = sin^2(\theta_C) + \frac{\lambda^2}{4d^2}n^2 \tag{3.8}$$

From the slope of the $sin^2(\theta_M)$ vs n^2 plot, shown in the inset of Fig. 3 10, the thickness d can be extracted; Special care must be taken to indentify the exact order of the maxima, because at low angles the first orders can be hidden in the general trend. The resulting fit can be considered reliable when the linearity of the curve is maximixed. Moreover, the extracted θ_C value should correspond approximately to the maximum angle at which the total reflection is observed in the experimental curve.

The X-ray difraction at high angle were done at ICMAB using a Siemens D500-2 circle diffractometer and Bruker 1T8 Advance area detector. For XRR measurements a Rigaku rotaflex RU-200B was used. These difractometers works with Cu X-ray sources, with an emission spectrum characterized by two main lines: $k_{\alpha1}$ = 1.5406 $\AA$ and $k_{\alpha2}$ = 1.5444 $\AA$ with relative intensity 2:1. Appropiated Ni-filters are used to eliminated lower length emission lines (k_β) in the majority of the experiments. Grazing indicence (GIXRD) were performaced using a MRD X Pert Pro (Panalytical, Almelo) at *ICN2*.

3.6 Magnetic characterization

Magnetic characterization was performed at the ICMAB using a Superconducting Quantum Interference Device magnetometer (SQUID) from Quantum Desing. A maximum field of 7 T could be applied and the accesible temperature ranged between 5 K at 300 K. The measurements are carried out by displacing at low frequency ($\approx$ 0 5 Hz) the sample along a vertical axis, around which two coils detect the flux variations. The induced voltage is transmitted as electrical signal to a superconducting ring with two or more weak links, and the interference of the superconducting current flowing through the two halves of the rings is used to measure the magnetic field generated by

the sample, exploting the Josephson effect. The magnetization can be measured with a sensitivity up to 10^{-7} emu.

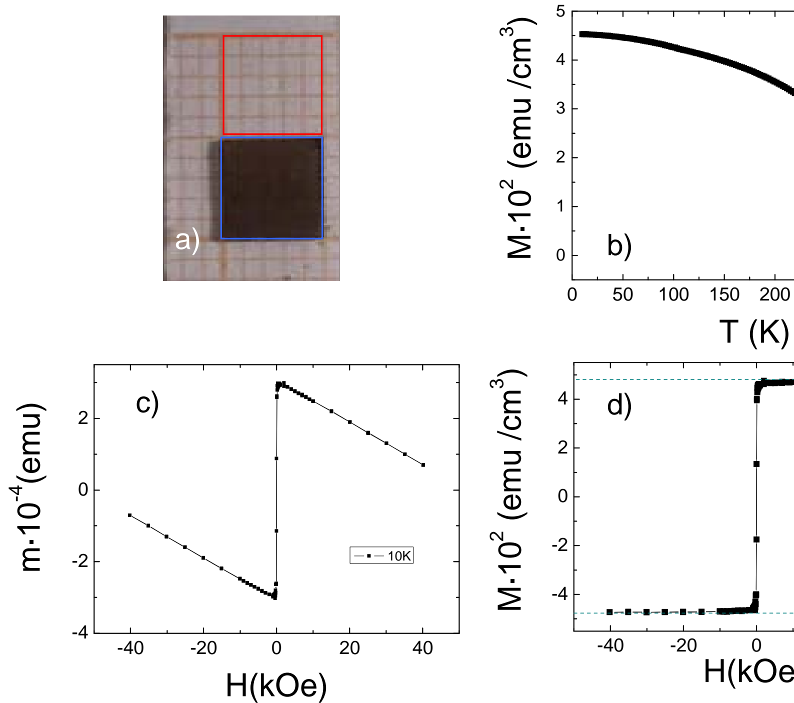

Figure 3.11: a) Picture of a sample positioned over a milimetric grid interspacing. The red line is defined area of 25 mm^2 and the blue line closes the area of the sample. b) Magnetization vs temperature to determine the T_c of a $La_{0.7}Sr_{0.3}MnO_3$ film on STO. The magnetic field (1 kOe) is applied in-plane. c) Raw data for magnetization vs applied magnetic field in-plane showing the strong diamagnetic contribution at high fields of a $La_{0.7}Sr_{0.3}MnO_3$ film on STO. d) Magnetic loop after removing the diamagnetic contribution of the sample and dividing by the volume of the $La_{0.7}Sr_{0.3}MnO_3$ layer on STO.

A Vibrating Sample Magnetometer (VSM) from Quantum Desing, also located at the ICMAB, was used for magnetic characterization. The basic measurements are achieved by oscillating the sample at high frequency ($\approx$ 40 Hz) and with a sinusoidal motion in proximity of a detection (pickup) coil, and the voltage induced is synchronously detected. The great advantage of this technique respect to SQUID is the high speed of the data adquisition, although the sensitivity is almost one order of magnitude lower.

A crucial paramater to determine the magnetization of the sample is the volume of the layer; to obtain this value it is nesessary obtain the thickness of the layer (by XRR) and the area of the sample. The area is determined by taking a digital photo of the sample over a paper with a milimetric grid interspacing, as can be seen in the Fig. 3 11 a); the sample area was calculated using a program called *Image J*, which compare the number of pixels contained in a region of the digital image with known area (red lines in the Fig.3 11 a)) and the region within the sample profile (blue line). The typical error associated to this method reaches values of 1%. The magnetization (M) of the samples was studied as a function of temperature $M(T)$ or an applied magnetic field [$M(H)$]. An exemplary $M(T)$ is shown in the Fig. 3 11 b), where it can be determined the Curie temperature for $La_{0.7}Sr_{0.3}MnO_3$. The raw data of [$M(H)$] is shown in Fig. 3 11 c). The negative slope at high fields comes indicates a dimagnetic contribution of the subtrate. In the Fig. 3 11d) the raw data has been corrected by substracting the diamagnetic contribution of the substrate, estimated from the linear high-field slope of the raw of the curve. This experimental aproach could understimate the film magnetization as any eventual high-field susceptibility is included in the substrate contribution. However, the value of the high-field slope of the raw data [$M(H)$] was always checked to be in good agreement with the measured susceptibility of the bare substrates, thus indicating full saturation of the film. For the calculation of the sample magnetization, the sample volume has to be determined from the layer thickness and the area of the film.

3.7 Galvanomagnetic measurements

The *I(V)* characteristic studies have been carried out in a two-contacts or four-contacts configuration. Four-probes method allows to overcome the problem of voltage drop at the contacts or cables, speciality when the sample to measure is expected to present low resistance (< 1 $kOhm$). The electric contacts were done by silver paint.

When two-probes were used, the electrical contacts were done in squared samples and the anchure of the electrical contact was the same of the sample width (see Fig.

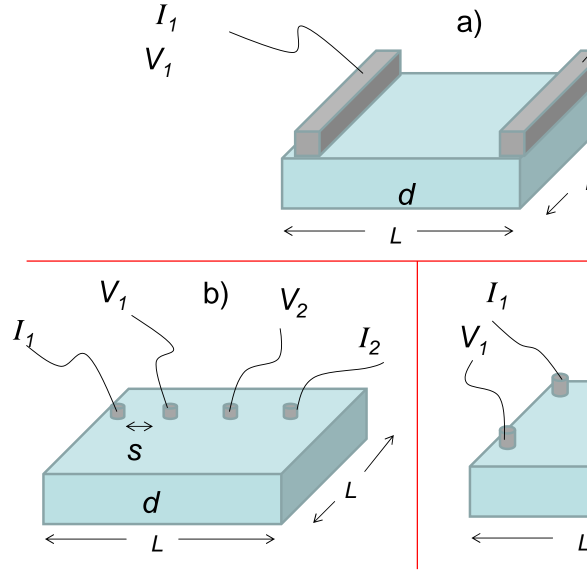

Figure 3.12: All the geometries for in-plane resistivity. a) Two points for samples with high resistance. b) and c) Four points measurements for low resistance measurements.

3 12). The relation between the resistance measured and the resistivity is $\rho = Rd$, where d is the sample thickness.

The four-probe method is divided in two different geometries, the collinear and the squared, as skecheted in the Fig. 3 12 b) and c). The squared geometry is ideal for samples with small areas. In a general way, the resistivity and the resistance are related by $\rho = CRd$ where C is a factor depending of the geometry. For squared geometry $C = 2\pi\ ln(2)$. For collinear geometry, C depends on the ratio of the lenght of the sample (L) and gap distance between the contacts (s) [94]. For the experiments in this thesis, in collinear geometry, the factor corresponds to $C = 3$.

A Physical Properties Measurement System (PPMS) from Quantum Design located at the ICMAB allows the option of AC current for resistance measurements. Resistance vs temperature measurements can be performace in the range of 2 K to 400 K. The maximum resistance that can be measure by the equipment is 20 $M\Omega$. Resistance vs applied magnetic field can be done at a given temperature. The maximum magnetic

field is 9 Teslas.

For tunnel trannsport *I(V)* characteristics were performed at the ICMAB and *L-NESS* in Milano. Room temperature measurements were done using a Keithley 2601 at the ICMAB and 2611 in *L-NESS*.

3.8 Contacts preparation

3.8.1 Contacts using micrometric mask

Plano-parallel capacitor is the most suitable geometry for the measurements of dielectric permitivity and polarization in bulk or thin films. The measured dielectric/ferroelectric material of thickness t sandwiched between two electrodes of defined area. These geometrical parameters determine the relation between permitivity ϵ or P and the measured magnitudes. A fast way to deposite a top electrode with a very well defined area on the dielectric/insulating material is using a mask. Here a *transmision electron microscopy grid* (TEM grid) is used as a mask where the squared areas are arround $\sim 60 \times 60 \mu m^2$ and separated by $\sim 20 \mu m$. For bigger areas, circles with diameters of $110 \mu m$ and $490 \mu m$ were done by a shadow mask. The materials used as top electrodes were Pt and Au, and they were deposited by sputering. The thickness of these electrodes materials goes from 20 nm to 40 nm, thin enough to allow part of the light to pass through it. Because the Pt and Au deposition by mask were *ex-situ* previous to metal deposition, the sample had been cleaned with a beam of acetone and ethanol, and subsequent exposition to an ozone atmosphere and ultraviolet light during 10 minutes. The Pt deposition were done at the ICMAB while the Au deposition were done at the *Servei de Microscopia de la UAB*. The TEM grid used were provided by Monocomp.

—

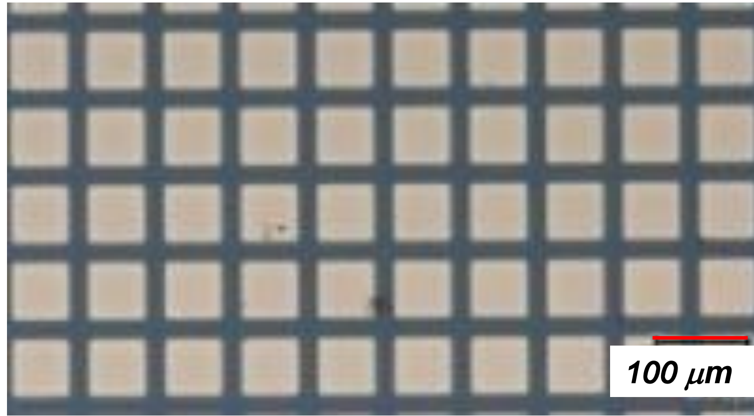

Figure 3.13: Exemplary Pt contacts using a TEM grid. The typical size of the contacts is $60 \times 60 \mu m^2$.

3.8.2 Electron beam litography

Au and Au-Pd contacts with areas $A < 400\mu m^2$ were also fabricated using electron beam litography. Here, an Au layer of 20 nm is deposited on the dielectric/ferrolectric layer, subsequently the samples are coated by a resin polymethyl methacrylate (PPMA). The resin is spread over the sample by means of a spinner during 45 seconds, reaching a velocity of rotation of 240 $rev\ min$. Then the sample with the resin is put in a hot plate at 180° during 1 minute. This heating process allows the resin to get hard.

The ELPHY program allows to create simple patterns, going from squares to circular shapes (more elaborated patterns can be imported). The same pattern has to be repeated several times in different position of the samples because some regions can presents defects producing an error in the litography process, but eventually some of the litographied areas are perfect. Afterward, the beam irradiation, which atacks some region of the resin, has to be defined in the program. Next, the spot of the beam is adjusted in order to obtained a current of 20 nA. Then, a maximum of work area (writing field) was defined. The writing field $200 \times 600\ \mu m^2$ is divided in small regions that define minimum the spatial step of the beam the (minimum step is 10 nm). Now the beam acts on the regions where the resin must be removed; if the time expended by the beam is very short the resine will not be removed completely. In this way the

time of the beam attacking (dwell time) is calculated from the settled current and takes some milliseconds.

Once all the patterns in the sample have been attacked by the beam, we proceed to reveal the patterns in the resin. The developer is a solution of isopropanol where the sample is immersed during 50 seconds and subsequently the sample is immersed in a bath of ethanol during 30 seconds.

Chemical etching using a IK solution is performed to lift off the metal without resin

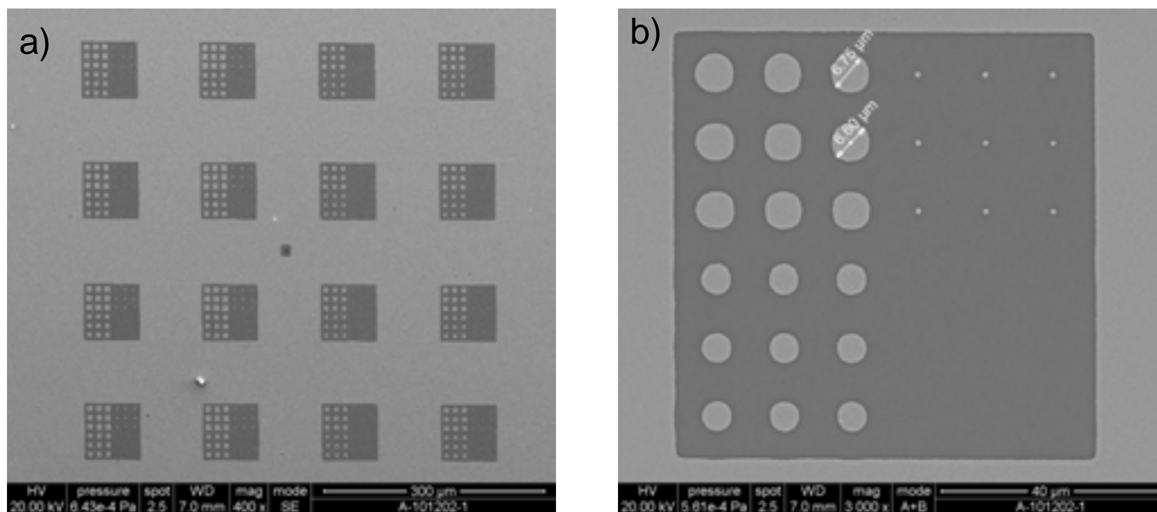

Figure 3.14: SEM images showing the Au contacts done by the electron beam litography. a) The pattern is repeated several times in different position with different dosis. b) Zoom of one of the repeated pattern. Microcontacts and nanocontacts can be observed more in detail.

Optical litography combined with Ar^+ bombardment were done by *Ph.D. Greta Radaelli* at the *L-NESS*. Some Pt contacts were deposited by FEBID at *Universitat de Barcelona* by *Josep Manuel Rebled*.

3.9 Dielectric and ferroelectric characterization

Dielectric characterization and/or impedance spectroscopy have been performed using a impedancemeter HP4192A LF (Agilent co.), which measure the impedance and the phase of the conected sample. The aviable measuring frequency ranges go from 5 Hz to 13 MHz and the oscillation voltage can be set between 50 mV to 1 V. In this thesis the tipical values of V_{ac} was between $50 - 200$ mV. The sinusoidal voltage (in complex representation) is given by $V(t) = V_0 exp(i \;\; t)$ where V_0 is the amplitude of the signal. The current generated by the ac field and the impedance $I(\;\;)$ and the impedance of the capacitor must give

$$V(t) = Z(\;\;)I(\;\;) \tag{3.9}$$

From this equation the real (Z)and the imaginary(Z) part of the impedance is determined at each frequency. The complex capacitance is determined by

$$C = \frac{1}{i \;\; Z} \tag{3.10}$$

Ferroelectric measurements consist on measuring the total current generated by a set of voltage pulses. From the integration of the current in time, the switched charge Q can be determined. Knowing the area A of the contact, the polarization P is determined from the $Q \;\; A$. The ferroelectric loops have been performed by a TFAnalizer2000(AIX-ACCT Systems GmbH. Co.). The maximum voltage applied is 25V in triangular or sinusoidal shape. The range of frequencies goes from 5×10^{-4} Hz to 2×10^{6} Hz.

Several methods can be implemented by the TFAnalizer2000 but in this thesis we focus in *Dynamic Hysteresis Mode* (DHM), *Dielectric Leakage Current Compensation*(DLCC) and *Posite-Up Negative-Down* (PUND) modes.

- DHM: Four bipolar triangular excitation signals of frequency ν_0 are applied with a delay time $\delta = 1$ s, as sketched in Fig. 3 15. The final *I*-*V* loop is obtained from

the combination of the currents measured while applying the negative voltage during the second pulse and the positive voltage during the fourth pulse. The fisrt and the second pulses are necesary in order to obtain the same measurement conditions

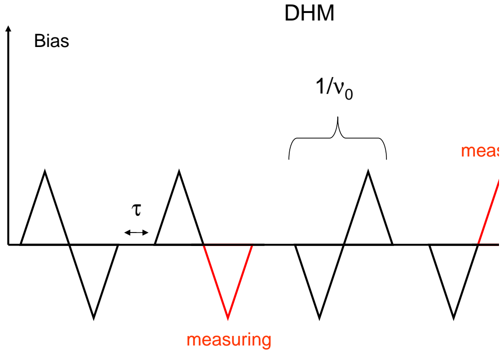

Figure 3.15: Voltage sequence that is applied in DHM. Red triangle indicates that moments that the curren

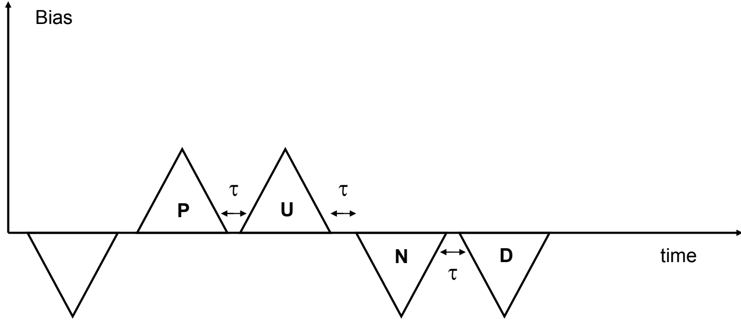

Figure 3.16: Voltage sequence that is applied in PUND.

- DLCC: This implementation is based on the DHM but instead of using one frequency ν_0, the DLCC works with ν_0 and $2\nu_0$. This method allows to substract the leakage current $I_{leakage}$ from the hysteresis loops, assuming that the displacemt current I varies linearly with the frequency and the DC current $I_{leakage}$ varies just by the voltage applied. From the substraction of the I-V loops at different frequencies the leakage cancel out and subssequently the I_ϵ is obtained [95].

- PUND: This technique has been implemented to obtain reliable values of polarization. Here five voltage pulses are applied to the sample. The first is negative and prepolarizes the sample to a negative polar state. The second and the third pulses are positive. The second (P) polarize the sample and therefore the corresponding current contains the ferroelectric and non-ferroelectric contributions; The third pulse (U) only has the non-ferroelectric contributions. then their substraction allows to obtain, in principle only the ferroelectric contribution. The same applies for the fourth(N) and the fifth (D), for negative state.

Another implementation that the TFAnalizer2000 allows is the measure currents in quasi-static mode. This method consist in to apply a step bias signal. Each value of bias is kept for 2 seconds while the measured current is avareged in this interval of time. The measurements can be done in unipolar configuration (from 0 to V_{final} to 0) unipolar unidirectional (from 0 V to V_{final}), and ambipolar (from $-V$ to V). An sketch of the applied bias is shown in Fig. 3 17. The leakage current in ferroelectric layers were measured by these methods.

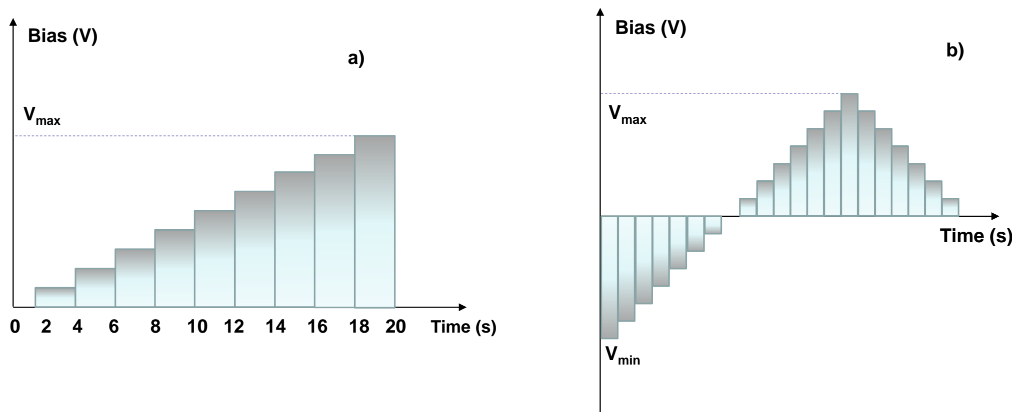

Figure 3.17: Sketch of the step bias implemented for leakage current measurements. a) Unipolar unidirectional. b) ambipolar.

3.9.1 Measurement configuration

Measurement configuration is the maner in which the dielectric or ferroelectric layer is electrically connected. We have used two measurements configurations called top-bottom and top-top. as observed in Figs. 3 18 a) and b) respectively.

In the top-bottom configuration, the bottom electrode is conected either by a drop of silver paint in the corner of the sample or by conecting one litographied contact which allows to reach electrically the bottom electrode. This is an asymmetric configuration, because the electrodes are different materials.

In the case of top-top configuration the measured capacitance should corresponds to a series of two identicals capacitors contacted through the bottom electrode (see Fig. 3 18 b). This is equivalent to the measurement of a single thin film capacitor with double thickness. Using this configuration, the asymmetries due to the different electrodes are compesated.

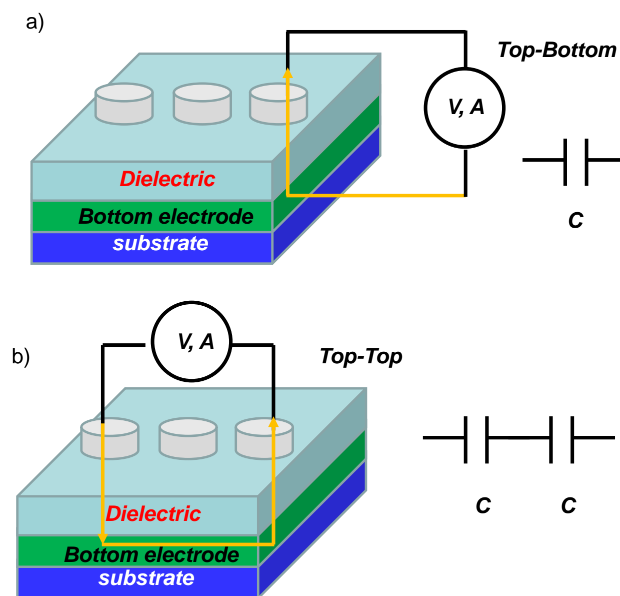

Figure 3.18: Sketch of the two different electrical configurations for impedance and ferroelectric measurements. a) top-bottom b) top-top.

Part III

Strain effects on magnetic thin films

Chapter 4

Dielectric response of $CoFe_2O_4$ films

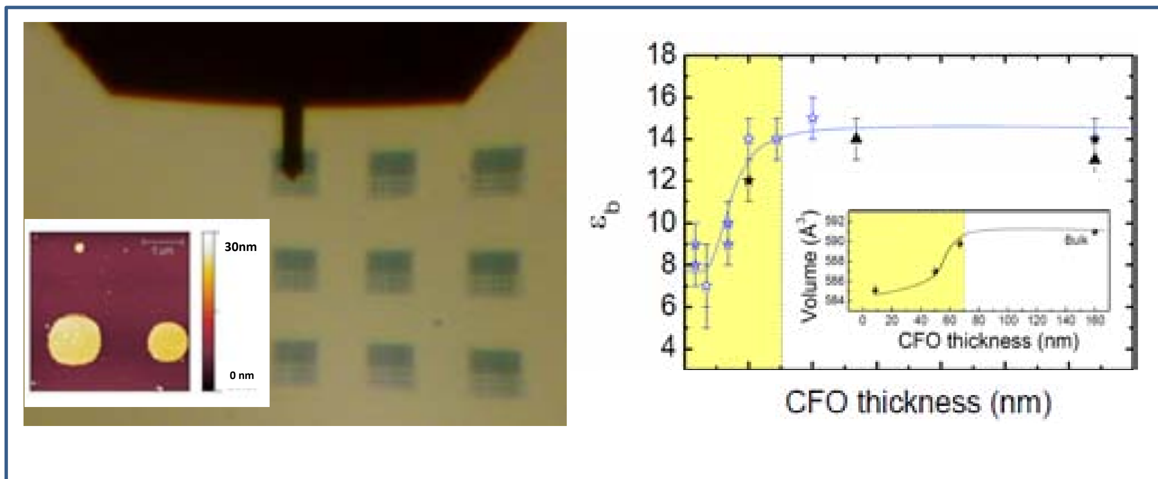

Part of the work discussed in this chapter is published in:

D. Gutiérrez, M. Foerster, I. Fina, D. Fritsch, C. Ederer and J. Fontcuberta, Dielectric response of epitalxially strained $CoFe_2O_4$ spinel thin films , Physics Review B, 86, 125309 (2012).

Abstract

Aiming to explore strain effects on the dielectric permittivity of ultra-thin films of oxides with spinel structure, epitaxial $CoFe_2O_4$ films with thickness between $4-160$ nm were grown on $La_{0.7}Sr_{0.3}MnO_3$ buffered $SrTiO_3$ (001) substrates. The strain state is tailored via thickness, where thicker samples are expected to be relaxed and thinner samples to be strained. It is found that films thicker than d $\approx$ 30 nm display bulk-like permittivity values ($\epsilon_r \approx 14$); however, a pronounced and gradual ϵ_r reduction is observed for thinner films when the in-plane compressive strain induced by the substrate increases. The experimental ϵ_r follows the same trend than the predicted ϵ_r (by first-principle calculations), however the theoretical values are substantially smaller than observed experimentally. A discussion about the possible mechanisms is done.

4.1 Introduction

The spinel crystal structure of $CoFe_2O_4$ (CFO) contains two inequivalent cation sites, the tetrahedrally coordinated A sites and the octahedrally coordinated B sites. The occupancy of these sites determines whether the normal or inverse structure is established. In practice, site occupancies vary between these two cases, depending on specific preparation conditions, and the inversion parameter x measures the fraction of less abundant cations on the B site sublattice, i.e. $x = 0$ for the normal spinel structure and $x = 1$ for complete inversion. According to that, the magnetization of CFO is dependent on x because the A and B sublattices are oriented antiparallel to each other. The band gap is also dependent on x.

Investigations about how to modify the inversion parameter have been done; For instance Daniel Fritsch *et al* [22] have signaled that epitaxial strain can influence the cation distribution in spinels. However, the strain also increase the tetragonality of the unit cell and such increase of tetragonality (in perovskites) lead to breakthrough discoveries such as induced or enhanced ferroelectricity [38 9]. Therefore, competition between different strain-based mechanism can be expected in CFO.

This chapter focuses on the dielectric properties of strained CFO films. The objective of this work is to determine if strain in CFO spinel oxide allows to significantly tune the dielectric response, that would indicate the proximity to a phase transition.

4.2 Films preparation and morphology

Samples were prepared by pulsed laser deposition on (001) $SrTiO_3$ (STO) single crystalline substrates. First, a metallic $La_{2/3}Sr_{1/3}MnO_3$ (LSMO) bottom electrode of thickness $d_{LSMO} \approx 25\ nm$ was deposited and a thin CFO dielectric layer of thickness d_{CFO} was subsequently grown on top. The thicknesses of CFO (d_{CFO}) and LSMO (d_{LSMO}) were determined by X-ray reflectometry (XRR) and found to agree with the number of laser pulses after appropriate CFO and LSMO growth-rate calibrations. The

CFO films reported here have thicknesses of 160 nm 67 nm 50 nm 25 nm 17 nm 8 5 nm *and* 4 2 nm CFO films were grown using 1 6 Jcm^{-2} laser fluence, a repetition rate of 5 at 500° C , and oxygen pressure of 0 1 $mbar$. After growth, the films *in situ* annealed at 450°C for 60 min under 200 $mbar$. The growth rate of CFO is $\sim$ 2 nm min Once the samples were grown, topography images confirmed the homogeneity and low roughness (from $\sim$ 0 2 nm for the 4 2 nm CFO layer to 2 nm for 50 nm) while no visible hot spots were detected in current maps, as showed in Fig. 4 1 a) and b) respectively.

Bulk STO, LSMO and CFO can be described using cubic unit cells of parameters: $a_{STO} = 3.905$ Å , $a_{LSMO} = 3.873$ Å and $a_{CFO} = 8.392$ Å, respectively. Consequently, it is expected that the substrate and buffer layer will induce an in-plane compressive

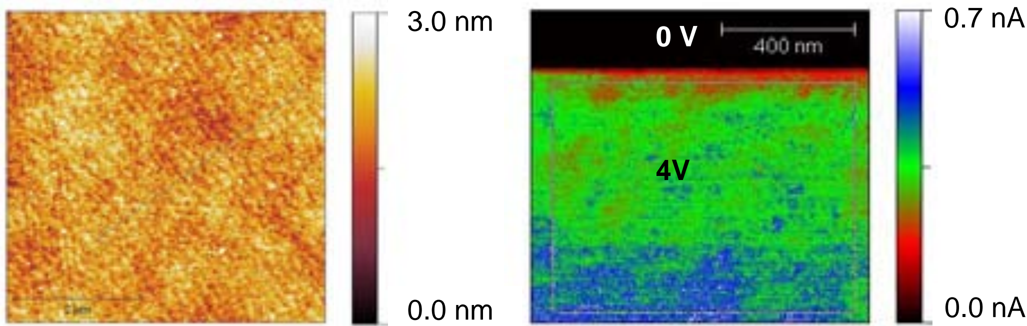

Figure 4.1: a) Topography image taken in dynamic mode for CFO 50 nm thick. b) Current map in CFO 17 nm thick. The lower part current were measure at 4 V; upper part of the map were done at 0 V in order to compare with the noise level.

4.3 Tetragonality and volume conservation

X-ray diffraction patterns in θ 2θ scans show only the (00l) reflections of CFO, LSMO and STO, indicating a textured growth along the c-axis for both layers. In Fig. 4 2 a) we show a region of the θ 2θ scan where the (004) reflection of CFO appears for

a number of films of various thicknesses. Inspection of this image reveals a gradual shift of the (004) reflection towards lower angles when reducing film thickness. This indicates an expansion of the out-of-plane c-parameter when reducing thickness, as expected for an in-plane compressed film.

It is noted in Fig. 4 2 a), that the c-axis of the 67 nm film is still larger than bulk

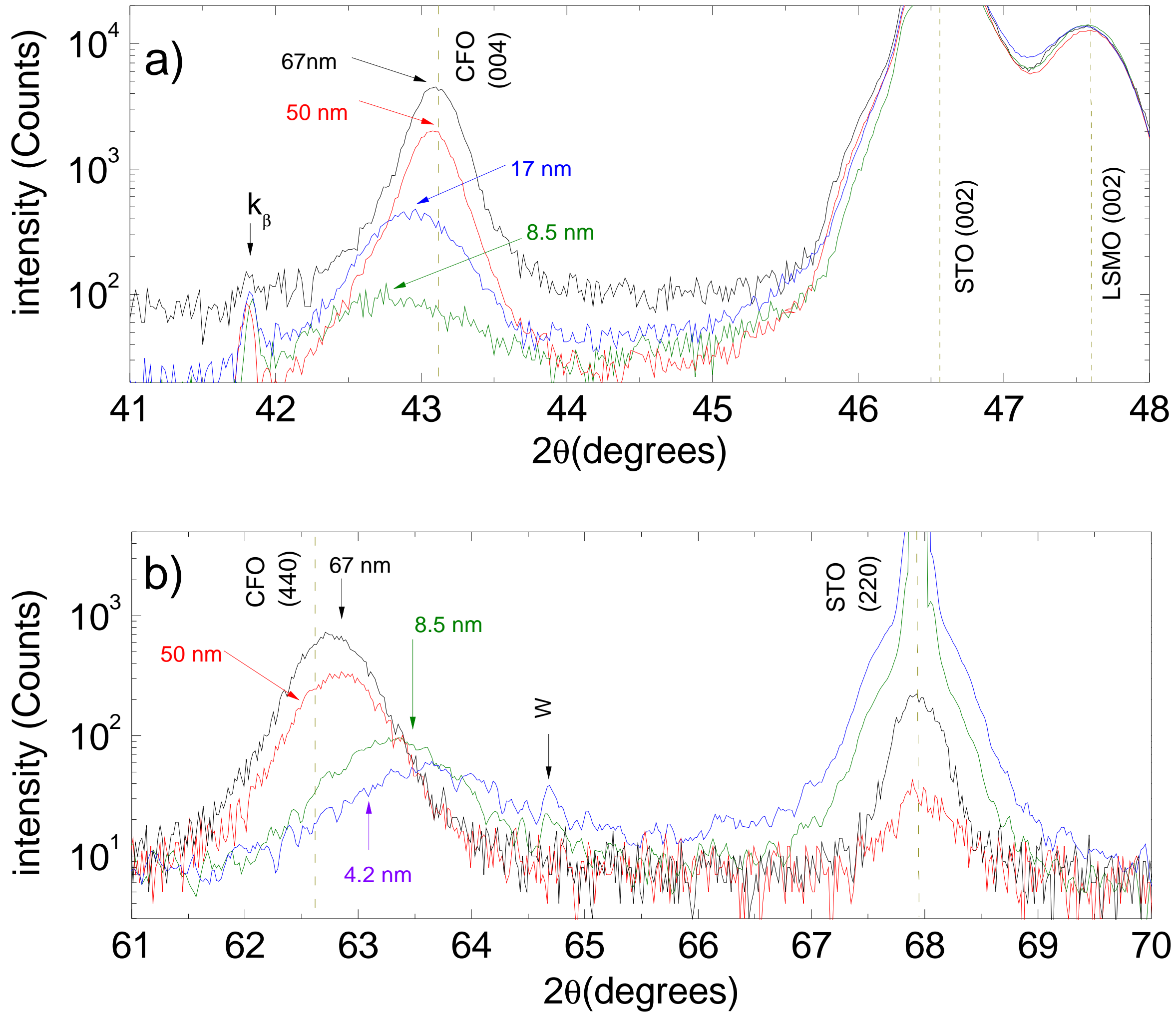

Figure 4.2: a) $\theta/2\theta$ scans around symmetric reflections of the CFO/LSMO//STO(001) heterostructures for different CFO thicknesses; dashed lines indicate the position of bulk (004) CFO and (002) STO and the position of the (002) reflection of LSMO bottom layer. The reflection of tungsten (W) comes from the equipment. b) Grazing incidence XRD (GIXRD) patterns around the (440) CFO reflection of some CFO/LSMO//STO(001) heterostructures; dashed lines indicate the position of the corresponding bulk reflections of (440) CFO and (220) STO.

CFO (dashed line) reflecting the presence of a minor strain. In contrast, the 160 nm film was found to be fully relaxed. The c-axis unit cell lengths evaluated from these θ 2θ plots, shown in Fig. 4 3 a), illustrate the gradual expansion of the c-axis for $d \leq 67nm$. A very similar trend had been found for CFO films grown on bare STO subtrates [25]. In Fig. 4 2a), can be observed that the position of the LSMO reflections of all films remains fixed and indicates a fully coherent growth of LSMO on STO.

In Fig.4 2 b) we show GIXRD of the thinnest films in the angular region where the (440) reflection of CFO occurs. The vertical dashed line indicates the position of the corresponding reflection of bulk CFO. Data in Fig.4 2 b) shows that the (440) reflections of these ultrathin films are shifted towards larger 2θ angles than bulk CFO when reducing thickness, thus reflecting an enhanced in-plane compression. Therefore, data in Fig. 4 2 a) and 4 2 b) show that CFO films on LSMO/STO(001) are in-plane

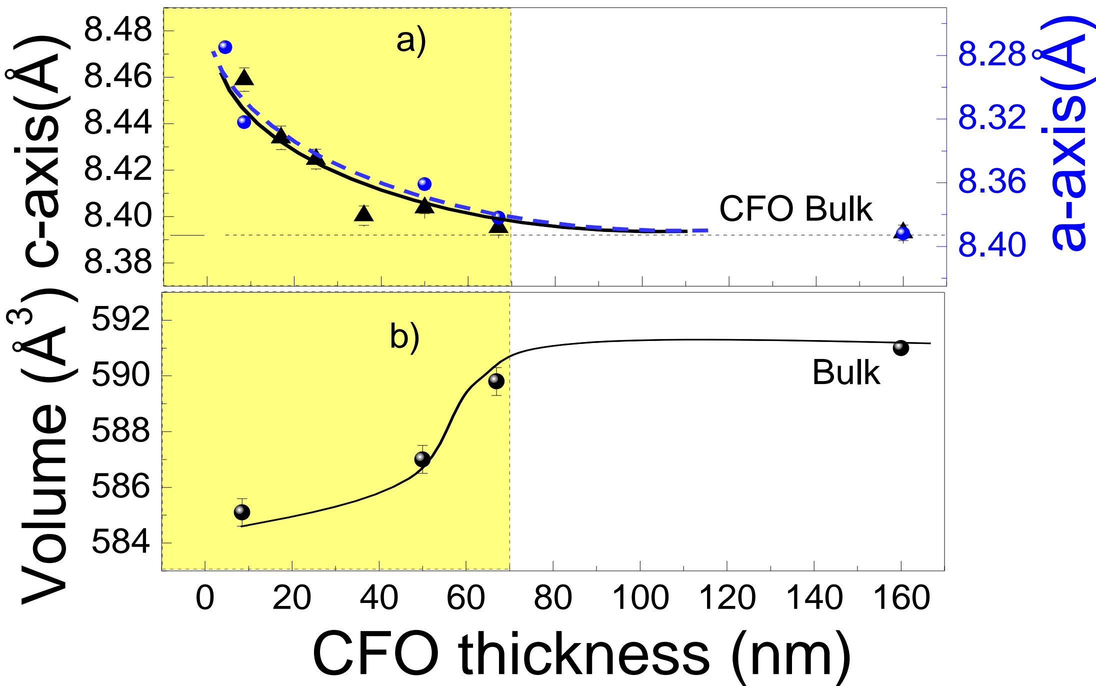

Figure 4.3: a) Thickness dependence of the out-of-plane (left axis) and in-plane (righ axis) parameters of CFO films, extracted from fits to the data in Fig. 4.2, using a gaussian profile. Dashed line indicates the unit cell volume of bulk CFO. b) unit cell volume of CFO films as a function of film thickness.

compressed and gradually relax towards bulk value when increasing thickness d (in round brackets): $a(4\ 2\ nm) = 8\ 255$ Å, $a(8\ 5\ nm) = 8\ 322$ Å, $a(50\ nm) = 8\ 361$ Å and $a(67\ nm) = 8\ 382$ Å. In Fig. 4 3 a) it is plotted the obtained c and a lattice parameter of the films as a fuction of the CFO thickness. Here, c and a lattice parameters tends to bulk values when the sample thickness increases. In Fig. 4 3 a) is is plotted the the unit cell volume determined from the data of Fig. 4 3 a).

4.4 High dielectric constant at low frequency

To performance dielectric measurement and to determine the dielectric constant of the material, metallic contacts on CFO surface has to be deposited. Two different types of circular electric contacts were used: a) Pt contacts with diameters from (490 μm to 112 μm) and b) Au contacts with diameters from (490 μm to 5 9 μm). Pt and Au contacts (with diameter larger than 112 μm) were used for thicker samples ($t > 50\ nm$). The metals were deposited by sputtering through suitable masks. On the other hand, It was also used smaller (diameter $< 112\ \mu m$) Au contacts made by electron beam lithography, for thinner films ($t < 50\ nm$). The use of smaller contact areas in such ultrathin films reduces the probability to encounter shortcircuits or large leakage currents in the contact region. By using this method, Au contacts with areas A from 88 μm^2 to 28 μm^2 were fabricated.

The contacts having areas smaller than 85 μm^2 were electrically connected by using a modified setup of the AFM. The conducting AFM tip was connected, via a coaxial wire, to one input channel of an impedance analyzer while the second input was connected to the LSMO bottom electrode. The impedance was measured by using an ac-driving voltage ($V_{ac} = 200\ mV$) at frequencies (f) within the 100 Hz $-$ 10 MHz range. When appropriate, a bias dc-voltage (V_{dc}) was applied. The sample holder and the whole AFM setup were connected to the ground of the impedance analyzer.

The dependence of the $C(f)$ on the ac frequency for the thickest CFO film (160 nm) is shown in Fig.4 4 a) (contact area 9800 μm^2). We include data obtained using Pt

contacts under different V_{dc} bias conditions. The first observation is that for $V_{dc} = 0$, the capacitance displays two well defined regions: a low-f region of high capacitance and a high-f region of smaller capacitance, weakly depending on frequency. In Fig.4 4 a) (right axis) we show the corresponding permittivity (ϵ^*) calculated using $C = \epsilon_0 \epsilon^* A \; d$ (ϵ_0 is the vacuum permittivity) and taking $d = d_{CFO}$ as the thickness of the dielectric CFO layer. It is clear that at low-f the permittivity ϵ^* values are exceedingly large, thus indicating that non-intrinsic contributions dominate the overall capacitance.

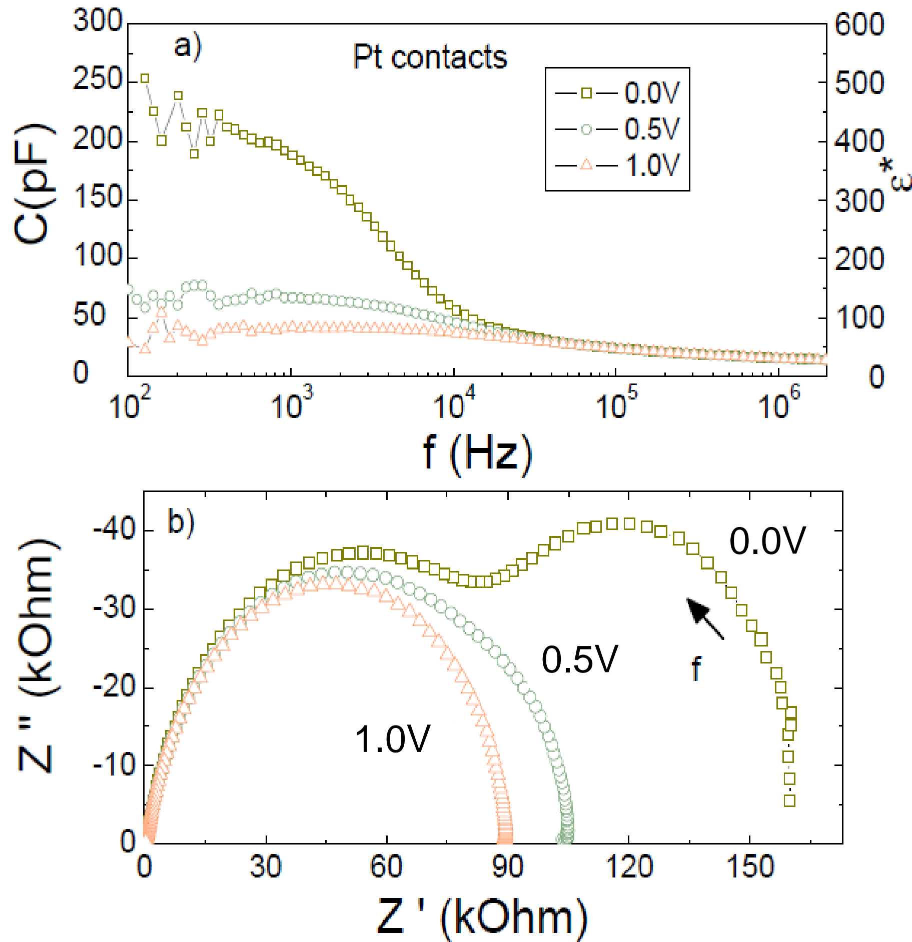

Figure 4.4: Dependence of the capacitance $C(f)$ and permittivity ϵ^* on the ac frequency (left and right axis) for a 160 nm thick CFO film, measured using different applied bias voltages $V_{dc} = 0$, 0.5 and 1.0 V (squares, circles and triangles, respectively). Inset: Imaginary part (Z) vs real part (Z) of the impedance Z for the same Pt contact measured under distinct V_{dc} bias.

In contrast, at high-f, ϵ^* is much reduced to $\epsilon^* < 25$, which is a more sound value. Most commonly, a low-f contribution to ϵ^* comes from Schottky barriers formed (SB) at the contact/insulator interface [34]. Under these circumstances, voltage drops at the thin SB (typically a few nm thick); therefore, in the presence of a leaky bulk contribution (as in the present case) a fake enhancement of the intrinsic permittivity is derived if d is used as the relevant thickness of the dielectric barrier [96 97]. This interpretation is corroborated by the reduction of the low-f capacitance when increasing bias V_{dc} as shown by data in Fig.4 4 a), where $C(f)$ data collected at $V_{dc} = 0 \quad 0\ 5\ V$ and $1\ 0\ V$ are displayed. The observation that at high-f, C (and ϵ^*) are independent of V_{dc} also signals that the intrinsic behavior dominates in this frequency region.

A common way to visualize the existence of distinct contributions in ac-conductivity experiments is by plotting the out-of-phase $Z\ (f)$ vs the in-phase component Z (f) of the frequency-dependent impedance $Z(f)$ as shown in the Fig.4 4 b). The observation of two quasi-circles in the $Z\ (Z\ )$ plot reflects the contribution of two RC-like circuits in the measured sample [98]. Consistently with data in Fig. 4 4 a), the low-frequency contribution is rapidly suppressed by the V_{dc} bias.

In Fig. 4 5 a), It is shown the capacitance measured using Pt and Au electrodes (square and triangle symbols, respectively) at $V_{dc} = 0$. The comparison of both sets of data confirms that the capacitance measured at the low-f region is largely dominated by the CFO-electrode interface. In contrast, the $C(f)$ values for $f > 100kHz$ are independent on the electrode, thus reflecting the intrinsic character. In agreement with discussion of Fig. 4 4, the equivalent circuit of the sample should contain, at least, two RC-like elements: $(RC)_i$ and $(RC)_b$ representing the interface and the bulk contribution respectively. $R_x(=G_x^{-1})$ and C_x stand for the dc-resistance (conductance) and capacitance of each element ($x = i\ \ b$). The permittivity drop at intermediate frequencies reflects the frequency-region where the interface contribution starts to vanish. Moreover, a detailed inspection of the high-f region of $C(f)$reveals the existence of a weak frequency dependence. This is a common observation in dielectrics and it is associated to an ac-conductivity term (G_{ac}) that accompanies the G_b and C_b [99 100].

This contribution is more clearly seen if the real part of the conductance measured is

ı this log-log plot,

re 3

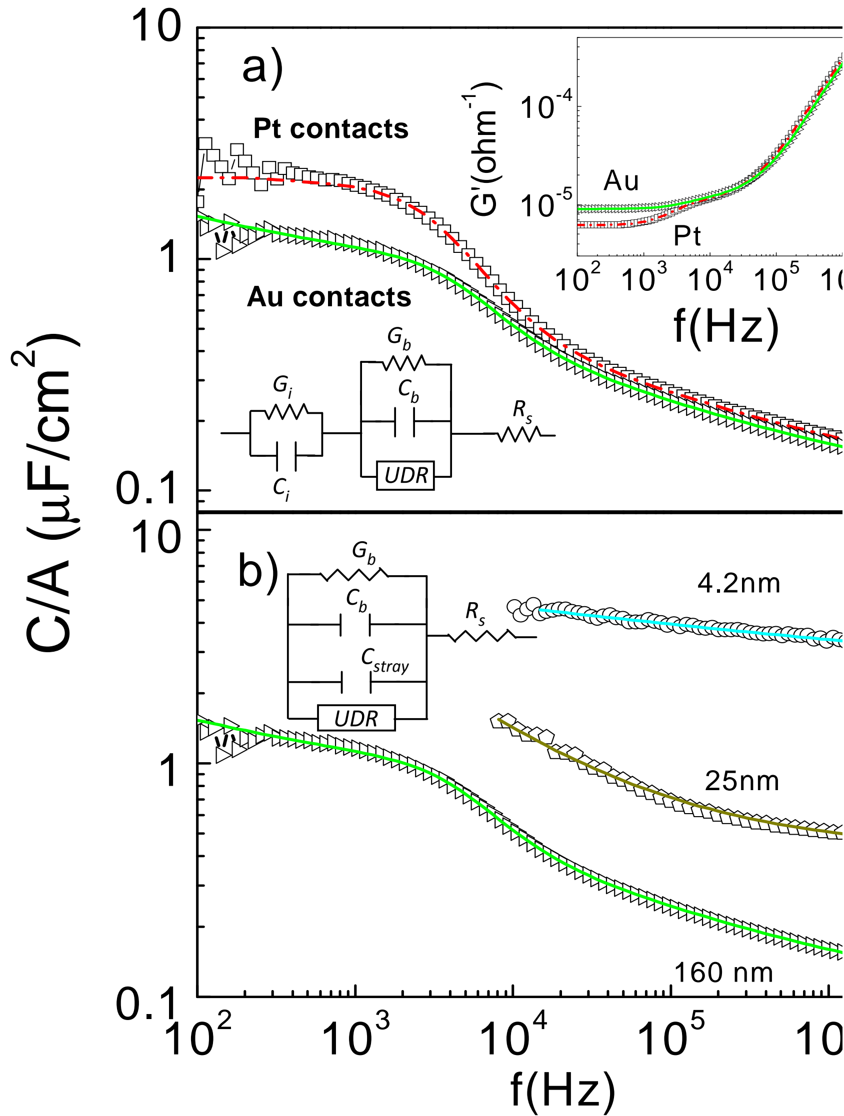

Figure 4.5: a) Capacitance vs frequency of a 160 *nm*-thick CFO film measured using Pt (squares) and Au (triangles) contacts and fits (lines) using the equivalent circuit as shown inthe schematic in the lower inset in a). Upper inset: dependence of the real part of conductance G (f) on the frequency of the same film using Pt and Au contacts as indicated. b)Frequency dependence of the capacitances of the 160-, 25-, and 4.2 *nm*-thick CFO films and fits (lines). The film with 160 *nm* thickness was measured using large contacts and needles, whereas films of 25 and 4.2 *nm* were measured by using e-beam lithographed smaller contacts and the AFM tip as described in the text. Inset in b): schematic of the equivalent measuring circuit for the AFM tip.

the almost-linear high-f region corresponds to the so called Universal Dielectric Relaxation (UDR) contribution which can be represented by $G_{ac} = G_{ac}^{0} \ \ ^{S}$ where is the angular frequency of the driving ac-field and S is some power smaller than 1; the UDR accounts for the frequency-dependence observed in the high-frequency region of $C(f)$ [99 100]. Therefore, the complete equivalent circuit, representing the bulk of the sample, the contact-interface and a series resistance corresponding to the wiring (R_S) is that shown in the sketch of Fig.4 5 a).

Using this circuit model, the $C(f)$ and $G\ (f)$ for the 160 nm sample measured by using either Au or Pt electrodes can be very well fitted as shown by the continuous lines through the data in Fig.4 5 a) (main panel and inset). The same circuit model has been used to fit the data for all films. The exceptions are the thinnest films, which as mentioned, had been measured using the AFM tip. In this case, a parallel capacitance (C_{stray}) representing the capacitor formed by the sample and the metallic cantilever must be included as indicated in equivalent circuit shown in the sketch in Fig.4 5b). C$_{stray}$ was determined by measuring C at a given frequency, as a function of the distance (z) between the tip and the sample. Using the slope of $C(z)$ vs z^{-1} and the z value at sample surface, we obtained C_{stray} (in the experimental conditions used $C_{stray} \approx 0\ 25\ pF$.) which is subsequently fixed when fitting $C(f)$. This simple model allows to obtain good fits of the $C(f)$ as illustrated in Fig. 4 5 b) where data for the 160 nm, 25 nm and 4 2 nm CFO films and the corresponding fits (solid lines through data) are shown. It can be noticed that for the thinnest films ($< 60\ nm$), for which small area electrodes have been used, at $f < 10\ kHz$ the impedance of the sample/electrode system exceeds the available measuring range of the impedance analyzer and thus data cannot be collected.

The fits described above, allow us to extract the parameters of the equivalent circuits for each CFO film. Of relevance here are the permittivity ϵ_b values (evaluated from C_b) and their thickness dependence collected in Fig.4 6 a).

4.5 Dependence of the intrinsic dielectric constant

In Fig. 4 6a two values of permittivity for a given thickness correspond to results from measurements using distinct contacts and/or using a different technique (AFM tip or needles) as indicated. We first note that for $d > 30\ nm$, $\epsilon_b = \epsilon_r \approx 14$, where ϵ_r denotes the relative permitivity of the film. This value is in good agreement with permitivity value reported for bulk CFO ($\epsilon_r \approx 12$) [101] and indicates that ϵ_r of relaxed CFO films is bulk-like. More interestingly, however, is the observation that for thinner films ($d < 30\ nm$) the permittivity decays rather abruptly by about 40 %; for instance for $d = 8\ 5\ nm$, $\epsilon_b \approx 8$. We note that if the permittivity data is plotted as $d\ d\epsilon_b$ vs d, as typically done to evidence the presence of dead layers in ferroelectric capacitors [34], it turns out that data for $d > 30$ follows a straight line (see inset in Fig.4 5a) that extrapolates to $d = 0$ thus excluding that a dead layer, at least one of constant thickness, could be responsible for the observed variation of permittivity. We strengthen that, to our knowledge, a systematic measurement of permittivity of CFO epitaxial thin films had not been reported earlier.

To get some insight into the microscopic mechanism of the observed reduction of permittivity, we show in Fig. 4 6 b) the measured variation of the strain along c-axis ($\epsilon_c = [c(d) - c_0]\ c_0$ where $c(d)$ and c_0 are the out-of-plane cell parameters of the films and bulk CFO respectively) resulting from the epitaxial compressive in-plane strain. It follows from data in Fig. 4 6 b) that the strain observed in the thinnest films, is rapidly reduced for $d > 30\ nm$. Therefore, from the comparison of data in Figs. 4 6 a) and 4 6 b), a direct connection between the decrease of the permittivity and the expansion of the c-axis, can be clearly appreciated. However, the effect of the in-plane compressive strain on the c-axis permittivity of CFO films is at odds with first expectations based on simple grounds, that is: a c-axis expansion should be accompanied by an enhancement of the corresponding permittivity due to the enlargement of the ionic bonds along that axis. Indeed, this is the observed behavior of some perovskite oxides, such as STO, where it has been shown that compressive

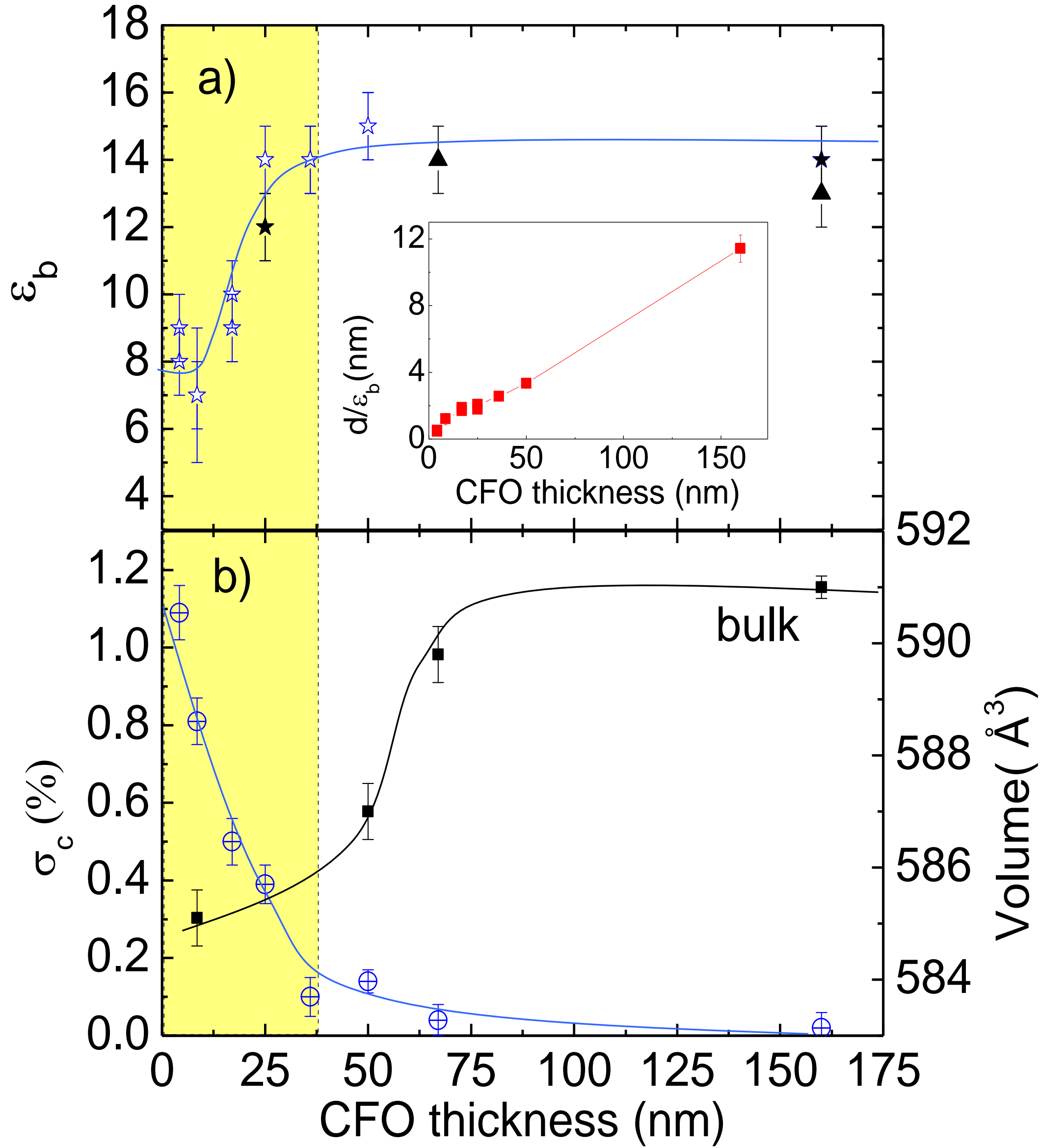

Figure 4.6: Dependence of the permittivity ϵ_b of CFO films on thickness. Distinct permittivity ϵ_b values plotted for a given thickness correspond to results obtained using distinct contacts or different techniques (empty stars: AFM tip on Au contacts, empty triangle: probe station on Au contacts, solid triangles: needles on Pt contacts). Inset: inverse of capacitance (d_{CFO}/ϵ_b) vs. CFO thickness. (b) Out-of-plane strain (circles, left axis) and unit cell volume (squares, right axis) of CFO films as a function of film thickness.

strain increases permittivity, eventually promoting the occurrence of a polar state [38]. Therefore, the observed reduction of c-axis permittivity cannot be simply explained on

the basis of the c-axis variation resulting from the compressive in-plane epitaxial strain. However, some recent reports on structural data and Raman spectroscopy of strained CFO could be inspiring. Indeed, it has been shown by Raman spectroscopy that in compressively strained CFO films grown on $MgAl_2O_4$ and STO substrates [102 25] phonon modes shift to higher frequencies upon strain-induced c-axis expansion. This striking observation was rationalized by noticing that the measured overall unit cell volume compression is the dominating factor, thus explaining the observed Raman blue shift. The structural data shown in Fig. 4 3 also follows the same trend, that is the CFO unit cell volume V_{CFO}, determined using measured in-plane and out-of-plane cell parameters of CFO films (Fig. 4 6 b) (solid squares, right axis)) clearly reduces when increasing compressive strain. Therefore, from the data in Fig. 4 6 a) it can be argued that the permittivity decreases when increasing compressive epitaxial strain as a result of the reduction of the unit cell volume, thus mimicking the results of Raman spectroscopy [102 25]. The reduction of permittivity upon reducing the unit cell volume is in agreement with results reported in related oxides under hydrostatic pressure (P_H) [103 104]. For MgO, for instance, $dln(\epsilon)\ dP_H \approx\ -0\ 3 \times 10 - 5\ bar^{-1}$ [101 105]. In the particular case of the CFO films described here, $dln\ dP_H$ can be estimated by using $dln(\epsilon)\ dP_H = (dln(\epsilon)\ dln(V_{CFO}))\ B$ where B is the bulk modulus. By using $B \approx 200\ GPa$ as reported for CFO [105] and $(dln(\epsilon)\ dlnV)$ from Fig.4 6 b), we obtain $dln(\epsilon)\ dP_H = -310 - 5\ bar^{-1}$. It thus follows that although the observed reduction of permittivity is in agreement with the expected trend upon unit volume compression, the measured variation is about one order of magnitude larger than the one found for oxides having rock-salt structure. As it could be argued that the more open structure of spinels could lead to a larger $dln(\epsilon)\ dln(V_{CFO})$ variation, a deeper insight is required.

To obtain a better understanding of strain effects on the dielectric properties of spinel films and aiming to disentangle the mechanisms for the observed reduction in permittivity, first principles calculations of the dielectric tensor under different epitaxial strain conditions were performed by *C. Ederrer*.

Table 4.1: Calculated values of the permitivity tensor. The upper row is calculated for the experimental lattice constants, whereas the lower rows correspond to theoretical lattice constants and strained configurations relative to the latter. $\epsilon_{x/y}$ and ϵ_z correspond to the in-plane(a) and out-of-plane (c) directions, respectively, whereas ϵ is averaged over all three Cartesian directions. Columns denoted Elect. and Ion. list the electronic ϵ and the ionic (phonon)contributions, respectively, to the dielectric constant. ϵ $_{total}$ is the total dielectric constant averaged over all three Cartesian directions.

			Elect.	Ion.	Elect.	Ion.	Elect.	Ion.	
a_0(Å)	a a_0	c c_0	$\epsilon_{x/y}$	$\epsilon_{x/y}$	ϵ_z	ϵ_z	ϵ	ϵ	ϵ $_{total}$
8.392	1.00	1.00	7.62	8.31	7.56	8.74	7.60	8.45	16.05
8.464	1.00	1.00	7.52	8.94	7.44	9.54	7.50	9.14	16.64
8.464	0.99	1.0113	7.55	8.37	7.54	10.01	7.55	8.92	16.46
8.464	0.98	1.00	7.69	7.81	7.72	8.77	7.70	8.13	15.83

The calculated permittivity values are listed in Table 4 1. It can be seen that the calculated permittivity averaged over all three Cartesian directions is very close to the value measured for the thicker, i.e. bulk-like films. The increase of the calculated permittivity is due to the increase of the ionic contribution to ϵ, whereas the electronic contribution (ϵ) is in fact decreasing slightly (due to a small increase in the band-gap). If the lattice constants in the $x-y$ plane are compressed by -1% to simulate the effect of epitaxial strain, the out-of-plane lattice constant along the z direction expands by +1.13% [106 107]. This leads to a reduction of the in-plane permittivity by -0.54 and an increase of the c-axis permittivity by +0.57. This is again in agreement with the simple expectation described in the previous paragraph, but it is at odds with the experimental observations. As discussed in [25] the observed out-of-plane relaxation in the CFO films is much weaker than what would be expected both from the calculated two-dimensional Poisson ratio and from the measured bulk elastic constants. The reason for this is currently unclear. To assess the effect of different out-of-plane strain on the permittivity, we also calculate the permittivity for a compressive in-plane strain

of -2% while keeping the out-of-plane lattice parameter fixed to the theoretical bulk value, i.e., we completely suppress any out-of-plane relaxation. It can be seen from Table I that in this case the permittivity along the z direction is indeed reduced by -0.49. This shows that the permittivity along a certain direction is not only affected by the strain along the same direction but also by strain in the perpendicular directions and by the overall change in volume. This is consistent with the fact that not all nearest neighbor bonds within the spinel structure are oriented parallel to the Cartesian axes and thus the corresponding bond lengths and force constants depend on the global strain state of the structure. However, while the calculated change in permittivity for suppressed c-axis expansion agrees qualitatively with the observed reduction in the thinner CFO films, there is a clear quantitative discrepancy, since the calculated strain-induced changes in ϵ are significantly smaller than the ones observed experimentally. As density functional theory (DFT) calculations incorporate all characteristics features of the spinel structure, namely its open character, as far it can be described by the used $P4_122$ space group, it follows that other factors, which are currently not included in the first principles calculation, are responsible for the strongly reduced permittivity in the thinner films. Such factors could involve strain-induced changes in stochiometry [108 109], defect concentration, microstructural features of the films and a thickness-dependent depletion layer in CFO.

4.6 Conclusions

In summary, a systematic study has been performed on the effect of epitaxial strain on the dielectric properties of spinel ($CoFe_2O_4$) thin films. It has been shown that CFO films on $La_{2/3}Sr_{1/3}MnO_3$//$SrTiO_3$, when grown strain-free, have a dielectric permittivity ($\epsilon_b \approx 14$) similar to the one reported for bulk materials. Interestingly, it is observed that the permittivity is largely reduced when increasing the in-plane compressive strain. It can be argued that this remarkable effect can be qualitatively described as resulting from the observed unit cell volume reduction under epitaxial compressive

strain. DFT calculation of epitaxial strain effects on dielectric permittivity shows that there is a competition between a permittivity enhancement along the out-of-plane direction due to its strain-induced cell expansion and a reduction of overall permittivity due to the shrinking of the CFO unit cell volume under compressive strain. The DFT calculations and estimates based on available elastic constants both predict a reduction of permittivity with increasing compressive strain if the out-of-plane expansion along c is partially suppressed, as observed. However, the measured variation appears to be about one order of magnitude larger than predicted, thus indicating that other effects, such as plastic defects or changes of stoichiometry of the film either as a response to elastic strain, as typically found in perovskites, or due to the growth should be considered. Possibly, the open structure of spinel oxides, allowing more complex patterns of lattice deformations under compressive strain and eventually modifying the film symmetry, may also play an important role.

Chapter 5

Strain effects in $La_{0.5}A_{0.5}MnO_3$

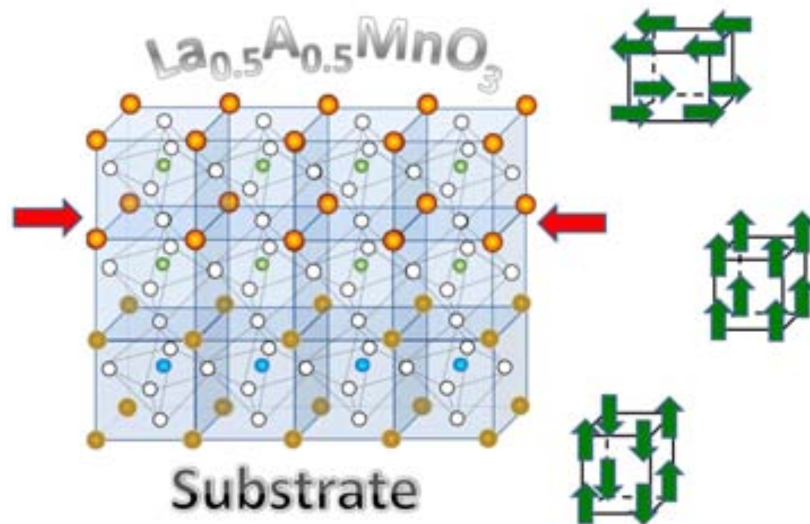

Part of the work discussed in this chapter is publushed in:

D. Gutiérrez, G. Radaelli, F. Sanchez R. Bertacco and J.Fontcuberta, Bandwidth-limited control of orbital and magnetic orders in half-doped manganitesz by epitaxial strain , Physics Review B, 89, 075107 (2014).

Abstract

The magnetotransport phase diagram of half-doped manganites $Ln_{0.5}A_{0.5}MnO_3$ *(*$Ln = La^{3+}$*,* Nd^{3+}*, etc., and* $A = Sr^{2+}$*,* Ca^{2+}*, etc.) is primarily dictated by the bare conduction bandwith (*W_0*), which itself is controlled by the Mn-O-Mn bond angle, and the carrier concentration. In thin films, epitaxial strain provides an additional tool to tune* W_0 *at fixed carrier concentration. Here, we will show that compressive or tensile epitaxial strain on half-doped manganite can have a tremendous and distinct effect on* $La_{0.5}Sr_{0.5}MnO_3$ and $La_{0.5}Ca_{0.5}MnO_3$ *thin films, having a broad or narrow bandwith, respectively. It is found that in* $La_{0.5}Sr_{0.5}MnO_3$*, large compressive strain triggers a change from a ferromagnetic and metallic ground state to an insulating and antiferromagnetic state whereas a tensile strain produces as antiferromagnetic but metallic state. In contrast, under strain,*$La_{0.5}Ca_{0.5}MnO_3$ *remains an antiferromagnetic insulator irrespectively of the strain state. These results illustrate that orbital ordering largely depends on the interplay between* W_0 *and strain providing a guideline towards responsive manganite layers.*

5.1 Introduction

Manganites of $La_{1-x}A_xMnO_3$ (A = Sr,Ca) with dopin level $x \approx 0$ 5 have recently attracted renewed attention because their ground state (ferromagnetic (FM) or antiferromagnetic (AF), metallic (M) or insulator (I)) can be easily modified by engineering the bandwidth (W_0). This property makes half-doped manganites ideal materials to be integrated in reconfigurable tunnel junctions with potentially large electroresistance[84]. Indeed, recent reports showed record tunnel electroresistance (TER) values where half-doped manganites are combined with ferroelectric tunneling [85]. In these heterostructures, the piezoresponse and polarization surface-charges of the ferroelectric layer both can contribute to modify the properties of the adjacent manganite layer and thus those of the tunnel barrier. Progress in this direction and discrimination between strain and field-effects in ferroelectric/half-doped heterostructures require detailed understanding of the epitaxial strain effects on the properties of half-doped manganite ultrathin films.

Here, it has been achieved a systematic investigation of the magnetic and transport properties of $La_{0.5}Sr_{0.5}MnO_3$(LSMO5) and $La_{0.5}Ca_{0.5}MnO_3$(LCMO5) thin films of different thicknesses and grown on different substrates which allow to explore a wide range of structural mismatch and subsequent strain state of the films. Furthermore, the use of two compounds with different conduction bandwidth (W_0 (LSMO5) > W_0 (LCMO5)) allows to study the impact of this parameter on the evolution of the magnetic and transport phase diagram vs. strain.

5.2 Target preparation of $La_{0\ 5}A_{0\ 5}MnO_3$ (A = Sr, Ca) and bulk lattice parameters

Previous to thin film deposition, targets of $La_{0.5}Sr_{0.5}MnO_3$ and $La_{0.5}Ca_{0.5}MnO_3$ were prepared. The targets of one inch of diameter were submitted to five tons of pressure during the 4th (last) treatment and heated up to 1350°C for 18 h. Fig. 5 1 the X-ray diffraction (XRD) analysis of the final targets of LSMO5 and LCMO5. In order to

know if the desired phase is obtained and discard the presence of spurious materials we compare the peaks of the XRD of the measured targets with the results of Spooren

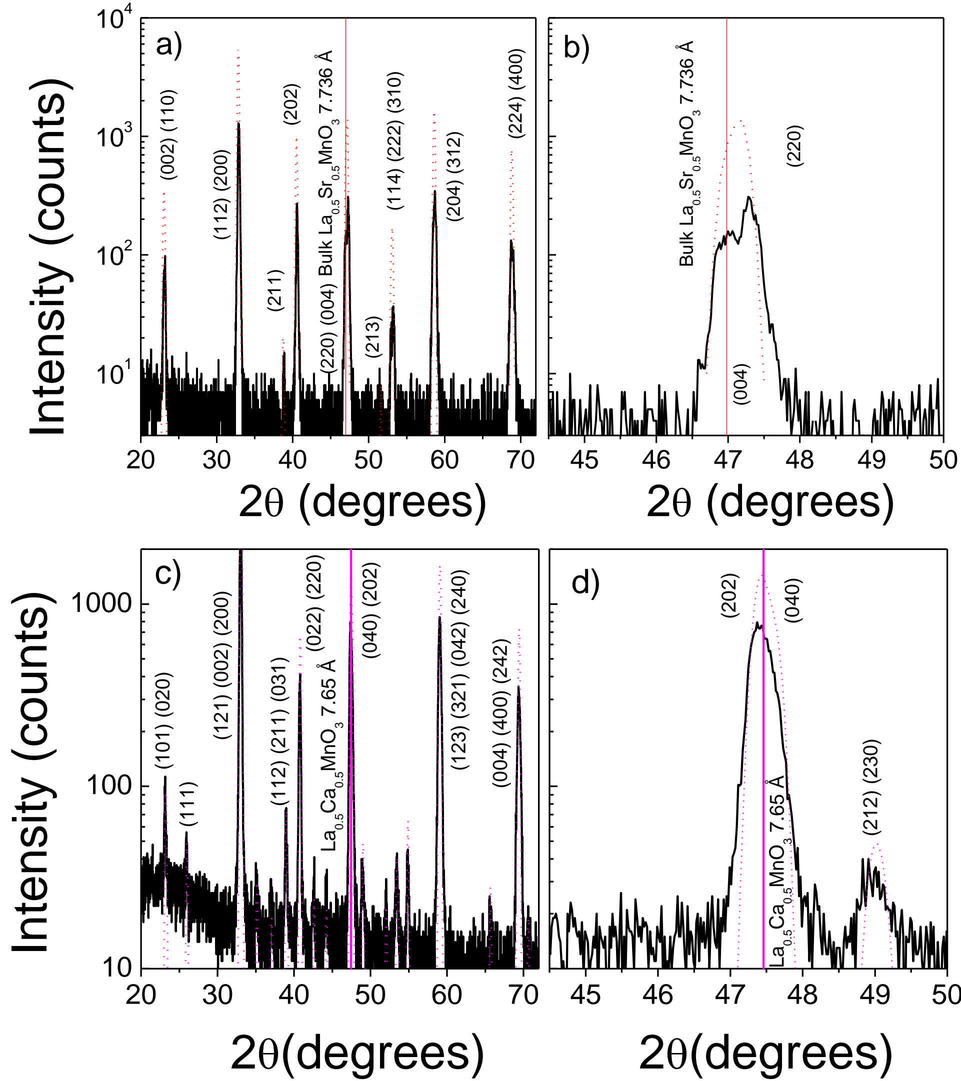

Figure 5.1: a) and c) XRD pattern for LSMO5 and LCMO5 target (continuous line), and the pattern for the same composition reported by J. Spooren [110]) (dashed line). b) and d) zoom of the reflection (004).

The results obtained on our targets (continuous black line) coincide with the results reported in the literature [110] (dashed red line), indicating that the desired phases are obtained in both targets. In the case of LSMO5 and LCMO5 an orthorhombic phase is

obtained. Note that peaks (004) and (220) can be distinguished in the case of LSMO5, but the peaks (202) and (040) cannot be distinguished in LCMO5, producing a less accuracy in lattice parameter determination in the last case. The average of the lattice parameters of pseudocubic phase of LSMO5 and LCMO5 are 3.858 $\AA$ and 3.83 $\AA$ respectively. Subsequently, we proceeded to grow nanometric layers of LSMO5 and LCMO5 on different substrates and characterize them in order to determine the role of strain in their electrical and magnetic properties.

5.3 Structural properties of $La_{0\ 5}A_{0\ 5}MnO_3$ (A = Sr, Ca) films

Thin films of LSMO5 and LCMO5 of different thickness, were epitaxially grown by pulsed laser deposition (PLD) on (001)-oriented single-crystalline substrates (a pseudo-cubic notation is used for those which are not cubic): (a) $DyScO_3$ (abbreviated hereafter as DSO, lattice constant of 3.940 $\AA$), (b) $SrTiO_3$ (STO, 3.905 $\AA$), (c) $(La,Sr)(Al,Ta)O_3$ (LSAT, 3.870 $\AA$), (d) $LaAlO_3$ (LAO, 3.792 $\AA$), (e) $YAlO_3$ (YAO, 3.720 $\AA$). For LSMO5 (3.858 $\AA$ [110]) the mismatch values referred to bulk coompounds, $\delta = (a_{substrate} - a_{manganite})\ a_{manganite}$ x 100%, are: +2.13% (DSO), +1.22% (STO), +0.31% (LSAT), -1.71% (LAO) and -3.58% (YAO). For LCMO5 films (3.830 $\AA$) the mismatch values δ are: +2.87% (DSO), +1.96% (STO), +1.04% (LSAT), -0.99% (LAO) and -2.87% (YAO). Mismatch values for LSMO5 and LCMO5 on different substrates are summarized in Table 5 1. The films have been deposited at 725°C in 0.2 *mbar* oxygen pressure with subsequent free cooling in 100 *mbar* oxygen pressure. The growth rate has been calibrated by measuring, by X-ray reflectivity (XRR), the thickness of some on-purpose prepared films. Subsquently, the number of laser pulses has been fixed and kept constant for all growth sequences. Laser fluence has been verified to be constant for all growth processes.

Fig. 5 2 a) shows the θ 2θ XRD pattern around the (002) reflections of LSMO5

films grown on all used substrates, respectively. The substrates (002) reflections are identified by vertical lines and by the corresponding name of the substrate. Solid vertical lines (purple) indicate the position of the (002) reflections of LSMO5 films and the dashed vertical lines indicate the position of the bulk (002) LSMO5 peaks. Broader angular range scans do not show any reflection different than (00l) thus indicating that films are fully *c*-axis textured. In most cases (except films on YAO) the Laue fringes are well visible indicating excellent films planarity and constant thickness. Horizontal arrows in Figs. 5 2 a) emphasize the shift between the measured position of the peaks of LSMO5 films and the corresponding bulk positions which reflects the strain state of the films. As shown in Fig. 5 2 a), LSMO5 on LAO film has the (002) reflections at lower 2θ angles than bulk LSMO5; this indicates an out-of-plane expansion as expected from the lattice mismatch ($\delta < 0$) imposing a compressive in-plane stress. On the contrary, in LSMO5 on STO and DSO, the (002) reflections occur at higher 2θ angles than bulk LSMO5; this indicates a shrinking of the out-of-plane cell parameter, in agreement with the lattice mismatch ($\delta > 0$) imposing a tensile in-plane stress. In the case of LSMO5 on LSAT, the (002) reflection of the film overlaps with the (002) reflection of the substrate as expected from their small mismatch. Note that the position of the (002) peak from LSMO5 film on YAO is very close to the bulk one, while from the mismatch value (δ = -3.58%) it should occur at lower angle than that of the film of LSMO5 on LAO (δ = -1.71%). This observation indicates that LSMO5 on YAO is almost relaxed. The data for LSMO5 on LSAT, which cannot be evaluated from the θ 2θ scan, has been estimated by assuming a full in-plane strain and assuming unit cell conservation.

In Fig. 5 2 b-e) it is shown the maps for the manganite films: LSMO5 films on STO and DSO substrates, with in-plane tensile stress, and on YAO and LAO substrates, with in-plane compressive stress.

In the cases of STO and DSO and LAO substrates (Fig. 5 2), it can be observed that the reflections from the films have $q_{[110]}$ values that roughly coincide with the ones of the substrate and are definitely far from the relaxed position (vertical line), while

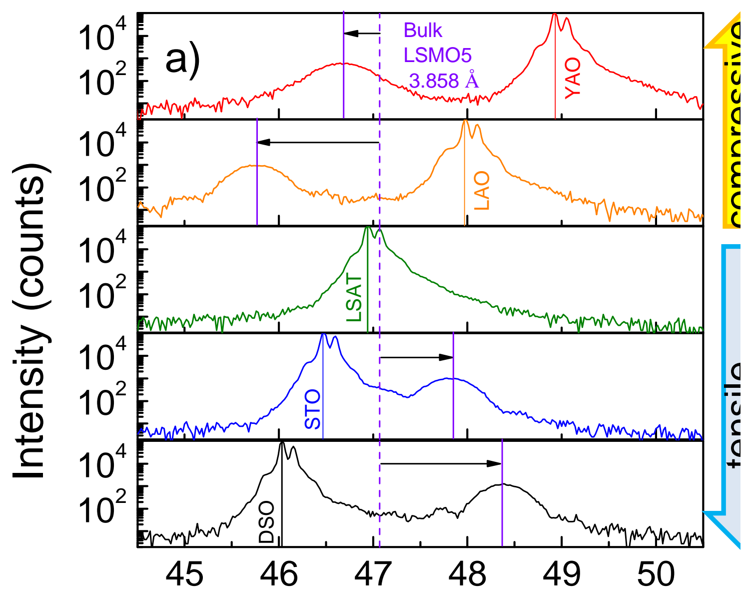

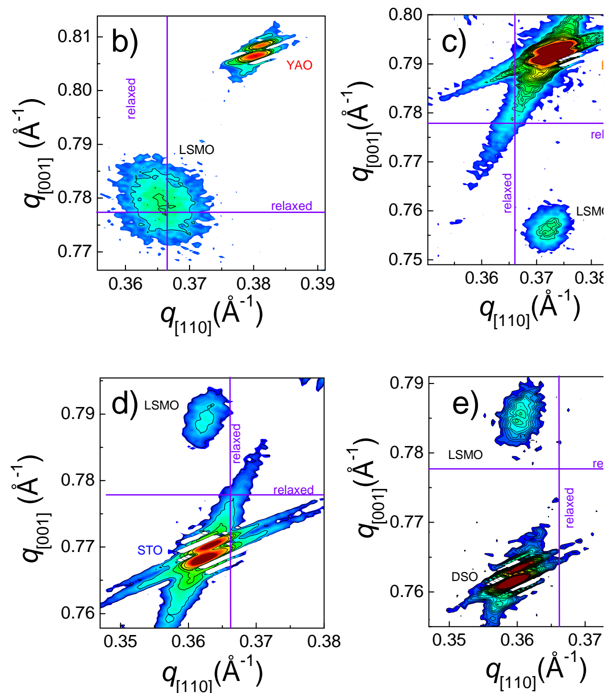

Figure 5.2: $\theta/2\theta$ XRD scan of the (002) reflections for LSMO5 films grown on different substrates(YAO, LAO, LSAT, STO and DSO). Reciprocal space maps arround (113) reflections for LSMO5 films on YAO, LAO, LSAT, STO and DSO. Lines indicates the position for LSMO5 bulk values.

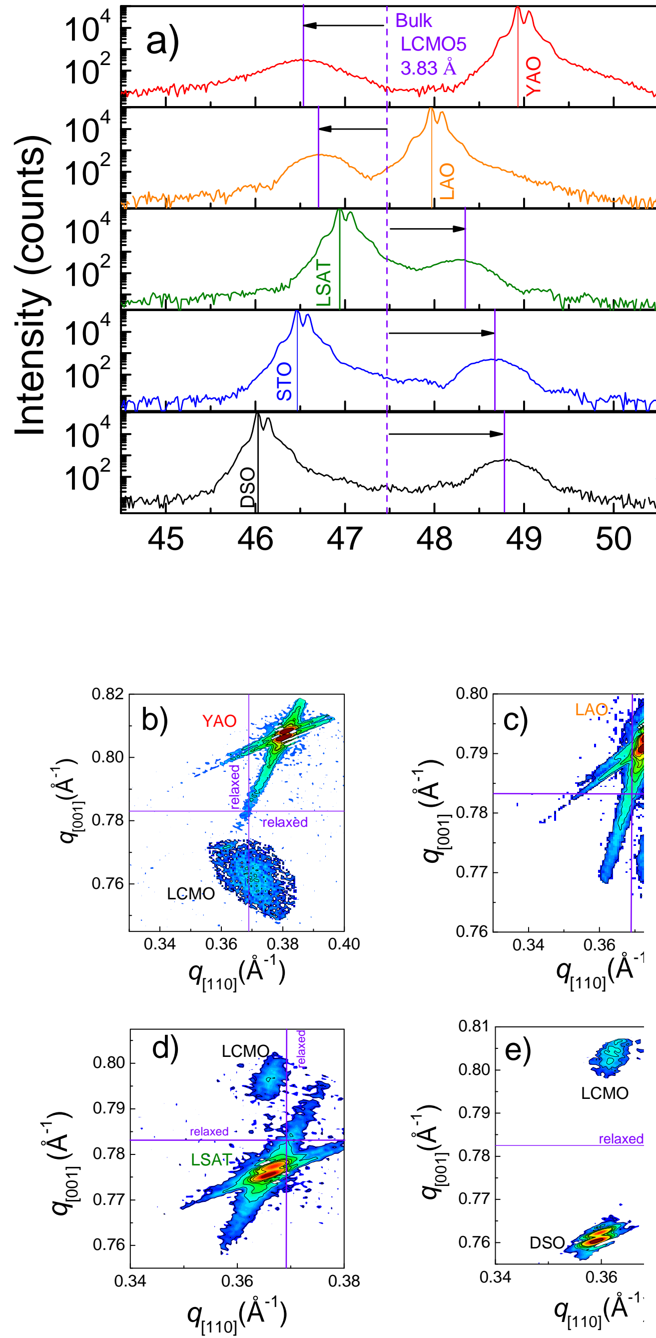

Figure 5.3: $\theta/2\theta$ XRD scan of the (002) reflections for LCMO5 films grown on different substrates (YAO, LAO, LSAT, STO and DSO). Reciprocal space maps arround (113) reflections for LCMO5 films on YAO, LAO, LSAT, STO and DSO. Lines indicates the position for LCMO5 bulk values.

the $q_{[001]}$ values of the spots from the films and the substrate are quite different. This means that the in-plane lattice constant (a) of the film matches that of the substrate, whereas the out-of-plane lattice constant (c) shrinks when is under tensile in-plane strain and expands when is under compresive in-plane strain. In the case of LSMO5 on YAO (fig. 5 2, respectively) the position of the spots of the films is closer to that of the corresponding bulk compounds, indicating lattice relaxation. From the position of the (113) films reflection we calculated the in-plane (a_{q-plot}) and out-of-plane (c_{q-plot}) lattice parameters. The a_{q-plot} data are included in Table 5 1, where we also show the c-parameter arising from $\theta/2\theta$ scans ($c_{\theta/2\theta}$). Since θ 2θ scans have higher resolution than q-plots in determining out-of-plane cell parameters, we used $c_{\theta/2\theta}$ and a_{q-plot} to calculate the tetragonality ratio c a and the unit cell volume values (V_{uc} = $(a_{q-plot})^2($ $c_{\theta/2\theta}$), shown in Fig. 5 4. These c a values reflect the actual strain state of the films and they will be used accordingly, in the following. Overall, data for LCMO5 films on the different substrates (Fig. 5 3 a-e) show the same trends. However, remarkable difference exists: as the unit cell of bulk LCMO5 is smaller than that of LSMO5, the stress-compressed films are less compressed and the tensile-stressed films are more tensile strained. The calculated out-of-plane lattice constants from these XRD data ($c_{\theta/2\theta}$) are included in Table 5 1.

In Fig. 5 4 a) we show the dependence of c a (left axis, solid symbols) and V_{uc} (right axis, empty symbols) of the epitaxial LSMO5 films on the mismatch with the substrates. The corresponding data for LCMO5 are shown in Fig. 5 4 b). We first note that in these 20 nm thick films, the c a ratio (solid symbols) can be changed from 0.958 to 1.043 for LSMO5 and from 0.954 to 1.023 for LCMO5 films, going, in both cases, from DSO to LAO substrate. Note that for LSMO5 films on YAO, the c a value is close to the bulk one (c $a \approx 1$, unstrained state) is expected from the high mismatch ($\delta \approx 3$ 58%), and in agreement with this, relaxation is observed in Figs. 5 2 b) 5 3 b). Very small tetragonality (c $a \sim 1$) also occurs when the mismatch is very small, as for LSMO5 on LSAT substrates. In the other cases, elongation (c $a > 1$) or contraction (c $a < 1$) is found when the mismatch is compressive or tensile, respectively.

Table 5.1: The calculated mismatch values (δ) and the in-plane a and out-of-plane c lattice parameters measured by q plots and $\theta/2\theta$ scan, respectively, for LSMO5 and LCMO5 films grown on five different substrates. Data for LSMO5 on LSAT, which cannot be evaluated from $\theta/2\theta$ scan, have been estimated by assuming a full in-plane strain and assuming unit cell conservation.

	LSMO5			LCMO5		
Substrate	$\delta(\%)$	a_{q-plot}	$c_{\theta/2\theta}$	$\delta(\%)$	a_{q-plot}	$c_{\theta/2\theta}$
DSO	+2.13	3.925	3.761	+2.87	3.91	3.733
STO	+1.22	3.907	3.803	+1.196	3.907	3.74
LSAT	+0.31	3.87	3.833	+1.04	3.865	3.77
LAO	-1.71	3.802	3.965	-0.99	3.793	3.88
YAO	-3.58	3.864	3.891	-2.87	3.833	3.90

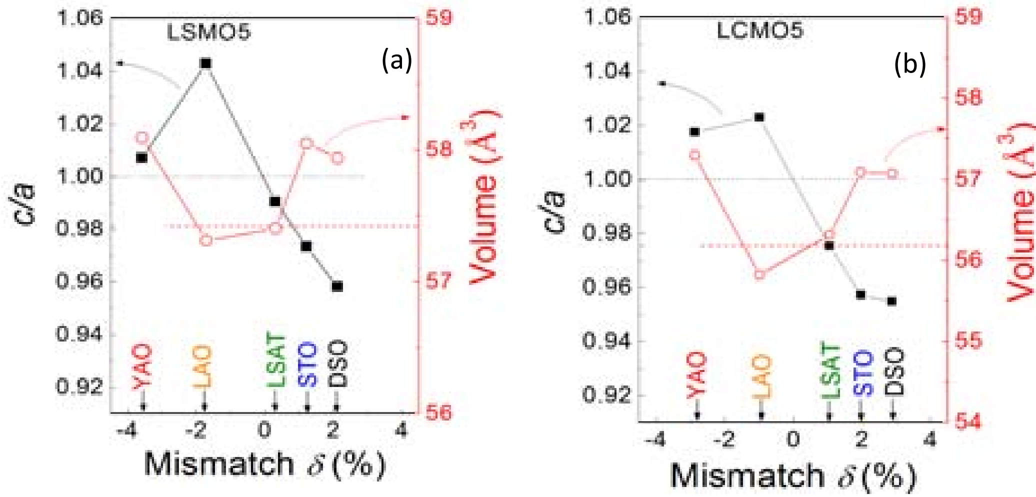

Figure 5.4: Dependence of tetragonality ratio c/a (left axis, solid squares) and unit cell volume (right axis, empty circles) values of the epitaxial LSMO5 (a) and LCMO5 (b) films on the structural mismatch imposed by various substrates (YAO, LAO, LSAT, STO, and DSO). Dotted and dashed horizontal lines indicate the corresponding bulk values of c/a and volume, respectively.

On the other hand, it can be also appreciated that neither for LSMO5 nor for LCMO5, the unit cell volume of the films (empty symbols) is preserved under strain (the corresponding bulk values are indicated by red dashed horizontal lines) but vary with the mismatch. V_{uc} is close to the bulk value for the films with smaller strain ($c\ \ a \approx 1$) but systematically enlarges upon tensile or compressive epitaxial strain. The very same trend is observed in LSMO5 (Fig.5 2 a)) and LCMO5 (Fig. 5 3 a)). These data do not allow to discriminate if this variation reflects a non-volume preserving pure elastic response of the LSMO5 and LCMO5 lattices under strain, or some sort of chemical self-adaptation (i.e. non-stoichiometry, to minimize the strain-related elastic energy), as reported in related oxides[109 111].

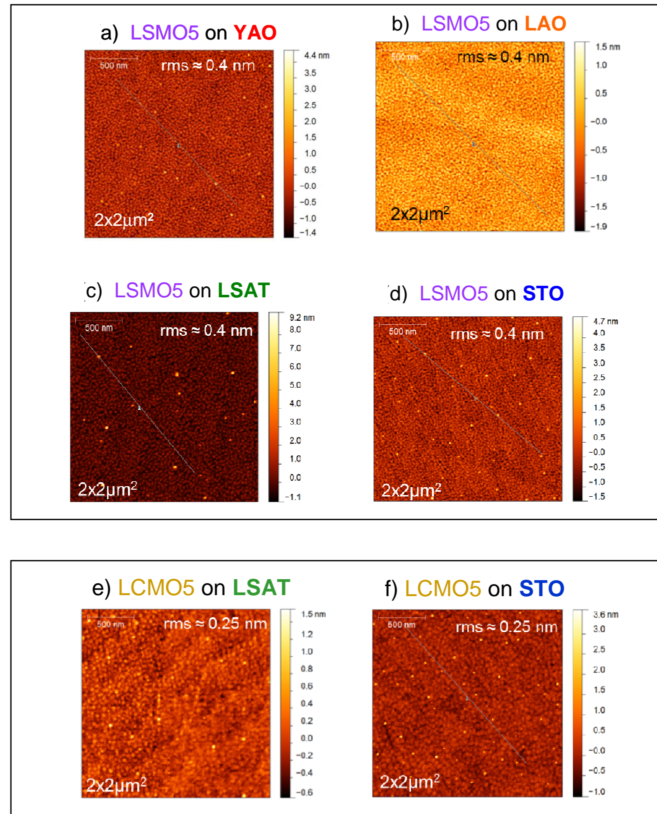

Figure 5.5: a-d)AFM images of a $2 \times 2\mu m^2$ area of the surface of LSMO5 films grown on YAO, LAO LSAT and STO substrates. The root mean square roughens (rms) is around 0.4 nm for all the samples. e-f) AFM images of a $2 \times 2\mu m^2$ area f the surface of LCMO5 films grown on LSAT and STO.

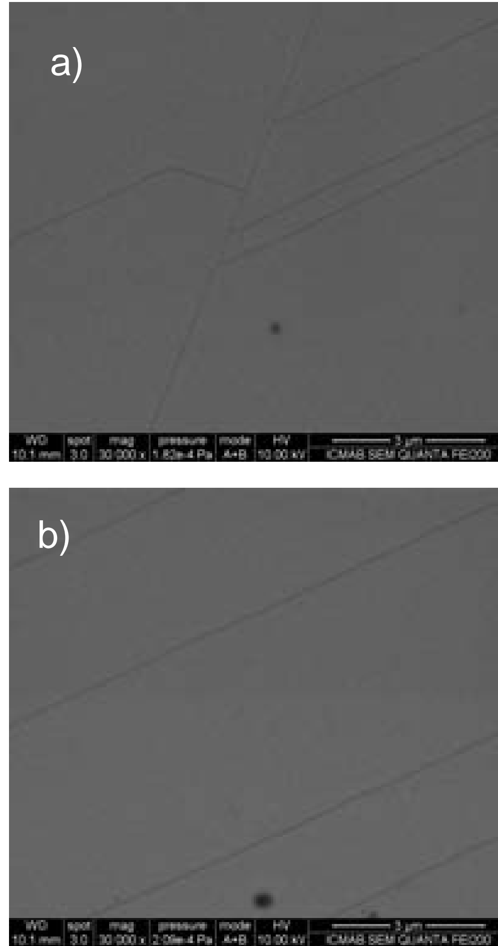

Figure 5.6: a) and b) SEM images of two different regions of the surface of LSMO5 films grown DSO substrate.

Surface morphology of all the samples has been characterized in order to study possible dependence on the lattice mismatch and the strain state of the films. The atomic force microscopy (AFM) images of the films indicate high quality morphology showing surface roughness around the perovskite unit cell. More in detail, LSMO5 films present surface roughness about 0.4 nm, while LCMO5 films present a lower surface roughness about 0.25 nm on a $2 \times 2 \mu m^2$ area. The topographic images of some of these samples are shown in Fig. 5 5. On the other hand, surface of LSMO5/DSO films were studied by SEM. In fig. 5 6, black lines indicate that cracks are presents

in these films. Note that straight dark line occur along specific directions; these lines correspond to fracture lines of the films. Similar fracture lines are observed wherever on the film surface. It can be anticipated that transport properties are dependent on this microstructure.

5.4 Magnetization, electrical transport and magnetotransport properties

Figs. 5 7 (a,b and c) display the temperature-dependent magnetization $M(T)$ (measured in field-cooling conditions (FC) using an in-plane field $H = 1\ kOe$), the field-dependent magnetization $M(H)$ (at 50 K) and the in-plane resistivity $\rho(T)$ of the LSMO5 films on different substrates, respectively. Figs. 5 7 (d,e and f) show the corresponding data for LCMO5. In these figs. the magnetic data for films on DSO are not show, because the strong paramagnetic nature of the substrate; the graphs are shown independent in further figures.

As shown in Fig. 5 7 a) the LSMO5 film grown on a matching substrate (LSAT ($c\ a = 0.990$, green circles)) displays a FM transition at the Curie temperature (T_C) around 345 K, and a large magnetization (about 400 $emu\ cm^3$) at the lowest temperature which is similar to that reported for bulk LSMO5 [112 78]. LSMO5 on YAO ($c\ a = 1.007$, red triangles), with a small compressive strain, also displays a similar FM behavior but with a somewhat reduced magnetization ($\approx 300\ emu\ cm^3$) and T_c decreased to about 335 K. The low temperature enhancement of magnetization is due to paramagnetic impurities in the YAO substrate. When increasing further the compressive strain, as in LSMO5/LAO ($c\ a = 1.043$, orange stars), the $M(T)$ data shows a severely depressed magnetization ($< 50\ emu\ cm^3$) and a peak at about 190 K, which indicates a transition from paramagnetic to antiferromagnetic AF state at the Neel temperature. The tensile strained LSMO5/STO ($c\ a = 0.973$, blue squares) film displays a much suppressed magnetization although a ferromagnetic contribution

rise below $T_C \approx 285\ K$. The $M(H)$ loops (Fig. 5 7 b)) (measurements have been performed at 50 K to minimize the paramagnetic contribution from the substrates) display the same trends as observed in the $M(T)$ data (Fig. 5 7 a)), namely a sharp suppression of ferromagnetism by strain.

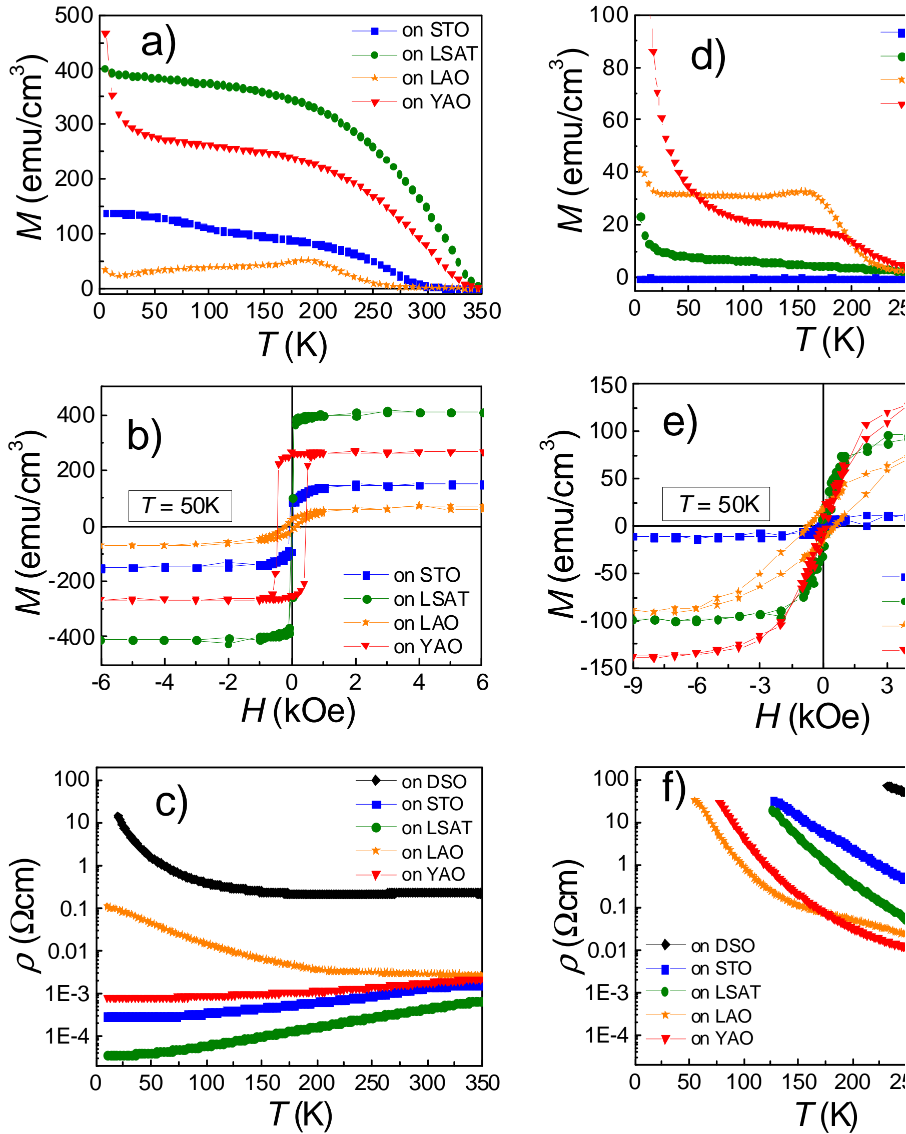

Figure 5.7: Temperature-dependent magnetization $M(T)$ (FC conditions; in-plane field $H = 1\ kOe$), field-dependent magnetization $M(H)$ loops (at 50 K, H in plane) and temperature-dependent resistivity $\rho(T)$ of the LSMO5 a)c) and LCMO5 d)f) films on different substrates (DSO, STO, LSAT, YAO, and LAO), respectively.

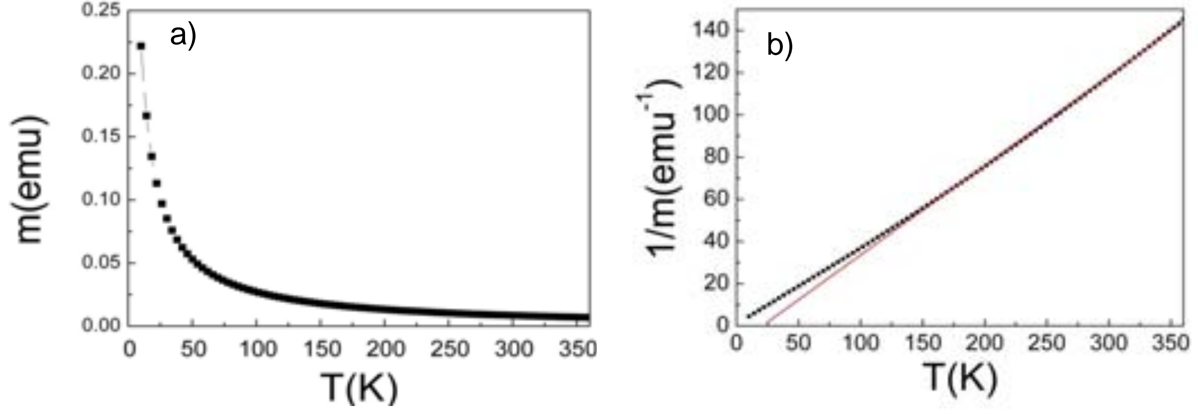

Figure 5.8: Magnetic moment (m) vs temperature of LSMO5/DSO film. b) Reciprocal magnetic moment ($1/m$) vs temperature. The straight line is a guide for the eye to the variation of magnetic moment with temperature in the high temperature region.

As shown in Fig. 5 7 c), the in-plane resistivity $\rho(T)$ is also reflecting the change of the magnetic ground state of LSMO5 under strain. It is clear that films grown on roughly matched substrates (LSMO5/LSAT ($c\ \ a = 0.990$, green circles)) or quasi-relaxed (LSMO5/YAO ($c\ \ a = 1.007$, red triangles)) are metallic: resistivity decreases as decreasing temperature. This is also true for the film grown on the moderately tensile stressing substrates LSMO5/STO ($c\ \ a = 0.973$, blue squares). In contrast, a compressive strain (LSMO5/LAO ($c\ \ a = 1.043$, orange stars)) drive the LSMO5 into an insulating phase, evidenced by the negative $\rho(T)$ slope at 300 K. By increasing further the tensile strain (LSMO5/DSO ($c\ \ a = 0.958$, black rhombi)), $\rho(T)$ displays a rather week temperature dependence, with a metallic-like slightly positive d$\rho(T)\ \ dT$ down to about 200 K, and a rapid increase at lower temperature. It can also be appreciated in Fig. 5 7 c) that the room-temperature resistivity of the LSMO5/DSO film is larger than that of the LSMO5/LAO film. This at first sight puzzling behavior is due to the presence of fracture microcraks due to the highly tensile stressed LSMO5/DSO film, as shown by SEM images in fig. 5 6. The dependencies of the remanent magnetization (at 50 K) and resistivity (at 230 K) of LSMO5 films on the tetragonality ratio $c\ \ a$ are collected in Figs. 5 9 a-b) (black solid squares).

The temperature dependent magnetic moment of a thin film of LSMO5 grown on

DSO is shown in Fig. 5 8 a). Data have been recorded with the magnetic field (500 Oe) applied in-plane and mesurements have been done under field-cooling conditions. It is clear that the overal magnetic moment is dominated by the large paramagnetic response of the substrate, thus making difficult to ascert the magnetic contribution from the thin LSMO5 layer. However, some hint can be inferred from data in Fig. 5 8 b), were the reciprocal magnetic moment is plotted versus temperature. The straight line thorough the data in the high temperature region indicates the expected paramagnetic contribution from substrate and film. At about 150 K, a clear deviation is visible, which indicates that at this temperature there is the onset of some reduction of magnetization. This is consistent with the onset of antiferromagnetism in the LSMO5 film.

Summarizing, LSMO5 films have FM ground state that shifts towards AF ordering when increasing the tetragonal distortion, either $c\ a > 1$ or $c\ a < 1$. However, it is clear in Figs. 5 7 a) and 5 7 b) that the transition from FM to AF does not produce a full suppression of magnetization but some ferromagnetic contribution persists in the films. This is fully consistent with a PS scenario where FM/AF phase coexistence is modulated by strain [113]. On the other hand, LSMO5 films, either unstrained or under tensile strain; a compressive strain, instead, produces an insulating ground state.

The LCMO5 films display a very different response. As shown by the $M(T)$ and $M(H)$ data in Fig. 5 7 d) and (e) respectively, all films have a very small magnetization signaling PS with predominant regions in the AF ground state, most noticeable in LCMO5/LAO film ($c\ a = 1.023$, orange stars) where a peak in the magnetization (Fig. 3(d)) at about 170 K suggests a paramagnetic to AF phase transition; the $M(T)$ plateau at lower temperatures signals the presence of a small FM contribution (about 30 $emu\ cm^3$) while the increase of $M(T)$ for very low temperature is due to the paramagnetic contribution of the LAO substrate. A similar behavior is displayed by LCMO5/YAO ($c\ a = 1.017$, red triangles) in Fig. 5 7 d) where we observe a very weak magnetic contribution (about 20 $emu\ cm^3$) and the strong paramagnetic contribution of the YAO substrate. In contrast, the magnetization of LCMO5/STO ($c\ a = 0.957$, blue squares) is negligible indicating a pure AF phase. Fig. 5 7 e) shows the $M(H)$

loops measured at $T = 50$ K. These plots confirm the presence of a residual FM phase in the LCMO5 films although the strong paramagnetic substrate contribution does not permit to easily appreciate the trend of M vs strain which is more evident in $M(T)$ data in Fig. 5 7 d). In summary, all LCMO5 films are AF. Films compressively strained, such as LCMO5/LAO and LCMO5/YAO, display major residual FM contributions, indicative of PS, which are not appreciated in the magnetization response of the films with tensile strain. The $\rho(T)$ data in Fig. 5 7 f), show that LCMO5 films, irrespectively of the substrate, are insulating. Inspection of data in Fig. 5 7 f) indicates that the resistivity increases when decreasing c a: from LAO, c $a = 1.023$ in-plane compressive strain, to DSO, c $a = 0.955$ in-plane tensile strain.

The overall trends in magnetization (at 50 K) and resistivity (at 230 K) vs. tetragonality of LCMO5 films are better seen in Figs. 5 9 a) and 5 9 b) (red empty symbols). When comparing the magnetic and transport results obtained for LSMO5 films and for LCMO5 films we can observe that: a) for LSMO5 films a compressive strain drives its FM/M ground state towards a PS state with predominance of AF/I regions, whereas tensile strains promote the formation of AF/M regions, and b) for LCMO5 films, the ground state is AF/I and strain does not change it. The existence of FM PS-regions in LCMO5 films is more evident in films under compressive strain. Probably this is also the reason why the resistivity of these films is lower than that of their tensile-strained counterpartners.

The coexistence of AF/I and FM/M phases in these films can be monitored by the magnetic-field dependent resistivity reported in Fig. 5 10. During the measurement the magnetic field was increased from 0 Oe to 90 kOe and then decreased back to zero. Whereas for LSMO5, low-temperature (10 K) measurements were possible owing to the relative low-resistivity of this serie of samples, the insulating character of the LCMO5 films precluded measurements below 200 K. To compare results for films on different substrates, resistivity values were normalized to the values measured at H = 0 Oe at the beginning of the measurement (ρ_0). In Fig. 5 10 a) are shown the results obtained at 10 K for LSMO5 films on different substrates. All the samples

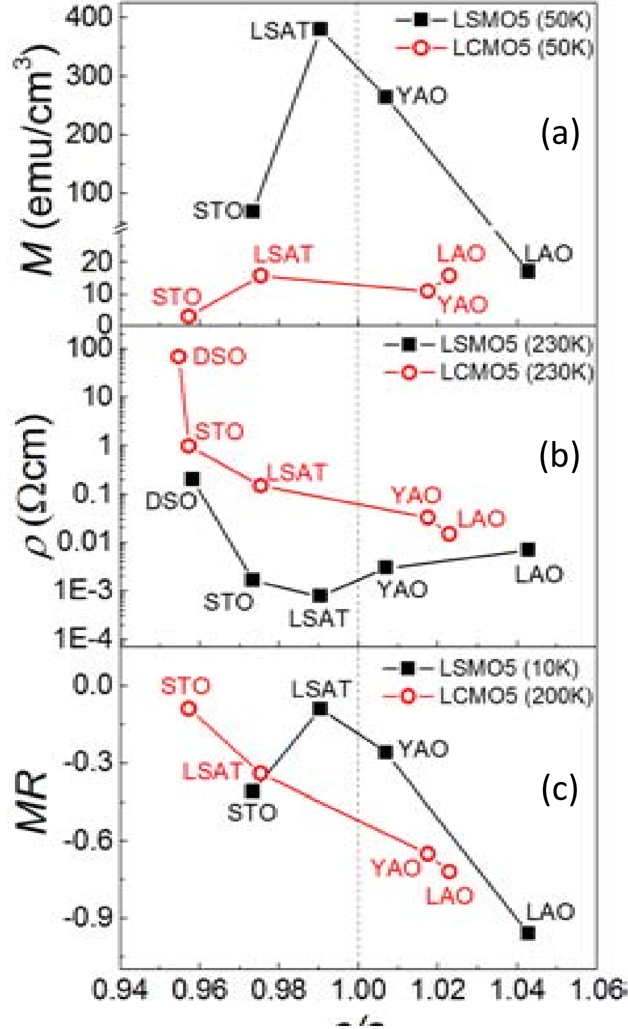

Figure 5.9: Dependencies of the a) remanent magnetization (at 50 K), extracted from $M(H)$ loops, b) resistivity (at 230 K), extracted from $\rho(T)$ curves, and c) magnetoresistance at 90 kOe (at 10 and 200 K) for LSMO5 (solid squares) and LCMO5 (empty circles) films, respectively, on the tetragonality ratio c/a.

present negative magnetoresistance (MR). It turns out that the MR clearly correlates with the $c\ a$ ratio, being minimal for $c\ a \approx 1$ and increasing when $c\ a$ departs from ≈ 1. For LSMO5/LSAT ($c\ a = 0.990$, green circles), LSMO5/YAO ($c\ a = 1.007$, red triangles), LSMO05/STO ($c\ a = 0.973$, blue squares) and LSMO05/LAO ($c\ a = 1.04$, orange stars) the corresponding MR values at 90 kOe are -10 %, -20%, -40% and -90%

respectively. In other words, MR is minimal for films that are ferromagnetic and display a metallic-like conductivity. This is the expected behavior, at low temperature, for an epitaxial film of a double exchange manganite presenting PS. Naturally, the presence of FM/M regions in the already metallic AF films (LSMO5/STO) makes the MR more pronounced. Finally, the MR gets even larger in insulating AF films containing FM/M patches such as LSMO5/LAO. Here field-induced magnetization orientation of FM/M clusters and its eventual expansion by charge-ordering suppression under magnetic field lead to a large MR[114]. The hysteretic $\rho(H)$ observed in LSMO5/LAO fully agrees with this picture. No hysteresis was observed in the other LSMO5 films.

The MR data of the LCMO5 films, shown in Fig. 5 10 b), follows a fully consistent trend. The MR is very small for films which are purely AF, without traces of FM regions (i.e. LCMO5/STO). The MR increases slightly in LCMO5/LSAT, where the FM contribution also increases. The larger increase of MR for LCMO5/YAO and LCMO5/LAO films is also in agreement with the presence of a larger fraction of FM/M regions. This also explains why the resistivity of these films is smaller than that of those films with smaller fraction of FM/M regions (LCMO5/STO, LSAT). In these measurements, there is no significant hysteresis probably due to relatively high temperature (200 K) used in the measurements.

In Fig. 5 11 the temperature dependence of the resistivity of all the samples measured at different magnetic fields($H = 0$ and 90 kOe).These data cleary show the presence significant negative magnetoresistance in most of the films. In fact, a detailed inspection of data shows that for films with a minor phase separation, LSMO5 films on LSAT is the clearest example [fig. 5 11 a)], a negative MR is seen close to the curie temperature, vanishing at lower temperature. This is the common colossal magnetoresiistance (CMR) in manganites, attributed to a complex percolative regime associated to nanoscale phase-separated phases occuring close to the Curie temperature. Incontrast, in the more strained films (such LSMO5 on LAO) an additional rapid increase of the negative MR is observed below about 200 K. This is the signature of the existance of the AF-FM phase separation occuring at this temperature. The stronger MR signal

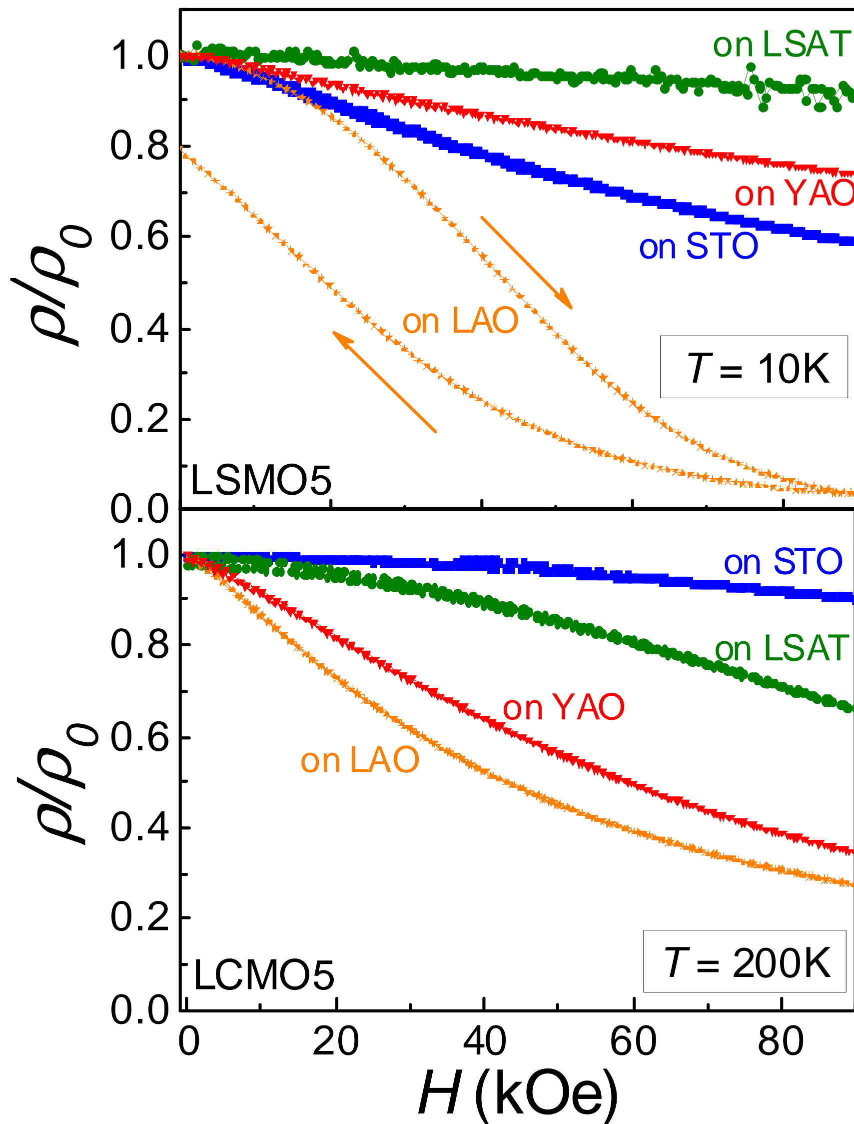

Figure 5.10: Magnetic-field-dependent resistivity of a) LSMO5 (at 10 K) and b) LCMO5 (at 200 K) films grown on different substrates. Data were recorded by increasing H from 0 Oe to 90 kOe and then decreasing back to zero. Except for LSMO5/LAO, hysteresis is negligible. Resistivity values were normalized to the value measured at 0 Oe at the beginning of the measurement (ρ_0).

the field-induced transition of some AF regions into FM under the magnetic field. The observation of these two different CMR effects are in full agreement with teorical predictions [115] and some early experiments on manganites single crystals [116]. Similar trends can be identified in LCMO5 films in fig 5 11 b).

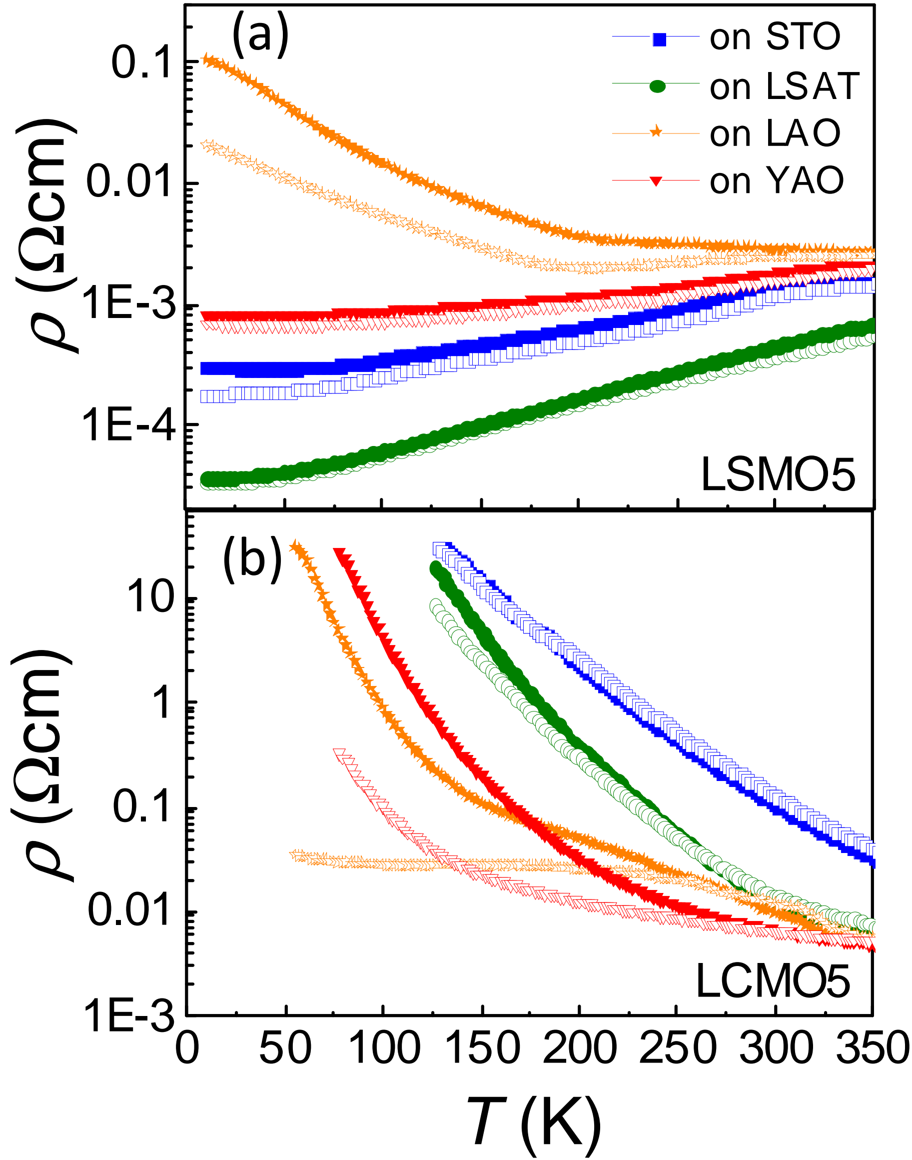

Figure 5.11: Temperature dependence of the resistivity of a) LSMO5 and b) LCMO5 films on different substrates (STO, LSAT, YAO, and LAO) measured at $H = 0$ Oe (full symbols) and $H = 90$ kOe (empty symbols).

Summarizing, the MR data are consistent with a distinctive PS in LSMO5 and LCMO5. In LSMO5, when increasing the strain, the M/FM state, characteristic of the unstrained condition, is gradually replaced by an AF/I (compressive) or AF/M (tensile) phase although patches of the M/FM phase remain. For LCMO5, although all films are AF and insulating, the magnetization and MR data also confirm the coexistence

of ferromagnetic and metallic regions.

The results presented above provide a comprehensive view of strain effects on wide-band (LSMO5) and narrow-band (LCMO5) half-doped manganites. Let me now discuss the magnetotransport phase control of LSMO5 and LCMO5 epitaxial films enabled by epitaxial strain. Let s focus first on LSMO5. As shown by data in Fig. 5 9 a), the weakly strained LSMO5 films are FM and the tetragonal distortion imposed by strain reduces the film magnetization and pushes the systems towards an AF ground state irrespectively of the sign of the strain. Transport data show that whereas compressive strain (as in LSMO5/LAO) induces insulating character, this is not the case for films under moderate tensile strain (LSMO5/STO) which are clearly metallic down to the lowest temperatures. On the basis of the similar inter-relation between the lattice strain and the magnetic and chargetransport properties obtained by Y. Konishi et al. [80] and based on the phase diagram of $La_{1-x}Sr_xMnO_3$ as a function of $c\ a$ [81 117], we assign the ground states of the respective films to FM/M (LSAT, YAO), *A*-type AF/M (STO), and *C*-type AF/I (LAO). It should be noted that the *A*-type AF state is metallic only in the lateral (in-plane) direction, whereas the *C*-type AF state is non-metallic. It is illustrated in the phase diagram of Fig. 5 12 a) that for films on LAO, YAO, LSAT, and STO, fully agrees with early predictions by Fang et al. [81] and Baena et al. [117]. In contrast, when LSMO5 is grown on DSO and has the largest strain-induced basal-plane expansion, the film is found to be metallic at high temperature, although with a remarkably small $d\rho(T)\ dT$, and shows a fast rise of $\rho(T)$ at lower temperature. Therefore, although this film could be labeled as an *A*-type AF/M, the $\rho(T)$ behavior is intriguing. Due to the stronger tensile strain of LSMO5/DSO film, it could be argued that the in-plane $d - d$ hopping integral is reduced by increasing the Mn-O-Mn bond length and, accordingly, this should lead to a reduction of the corresponding bandwidth and the FM double exchange term in the magnetic interaction, thus leaving behind only the antiferromagnetic superexchange term, and correspondingly an insulating antiferromagnetic state could be realized. However, LSMO5/STO and LSMO5/DSO films differ only modestly on tetragonality ($c\ a = 0.973$ and 0.955,

respectively) and therefore the difference in their low-temperature transport behavior (metallic vs insulating) does not seem directly related to the intrinsic band-narrowing effect produced by strain.

Therefore, either minute band narrowing drives the Fermi level below the mobility edge of the quasi-two-dimensional conducting band of $x^2 - y^2$ parentage or the conductivity is suppressed by extrinsic effects, such as dislocations or point defects that may be certainly more abundant in the most strained films. Measurements performed on four different LSMO/DSO films gave similar results. As mentioned above, in LSMO5/DSO films regular fracture lines have been clearly observed and it is likely that an even larger density of smaller cracks exists within the films thus giving rise to an extrinsic insulating-like behavior at low temperature. The narrowed bandwidth simply would amplify the impact of these microstructural defects on the measured $\rho(T)$.All LCMO5 films are found to be essentially AF and insulators, irrespectively of their strain state [Figs. 5 9 a) and 5 9 b)]. It is worth recall here that bulkLCMO5 commonly displays a FM phase with a $T_C \approx 250$ K and an antiferromagnetic charge-ordered state at $T_{CO} \approx 180$ K [113 79]; however, it has been shown that the LCMO5 ground state can be better described as a magnetically phase-separated system with ferromagnetic/metallic and antiferromagnetic/insulating phases coexisting in a wide temperature range, in amounts largely depending on measuring conditions and sample preparation [118 119 120]. Theoretical calculations suggest that in bulk LCMO5 the insulating charge-ordered state (CE-type) is the ground state which appears to be remarkably robust.In fact, CE is the ground state for unstrained and tensile-strained LCMO5, whereas the C-type AF can stabilize under large compressive strain [117]. In all cases and in agreement with the present experimental data, the insulating character of LCMO5 is preserved. Accordingly, we assign the ground states of the films having c $a > 1$ (i.e., LCMO5/LAO and LCMO5/YAO)to the C-type AF/I state, as depicted in Fig. 5 12 b). Regarding the tensile-strained regions (c $a < 1$), the results are compatible with the predicted CE-type ordering as observed at low temperature in bulk LCMO5 [113 79].

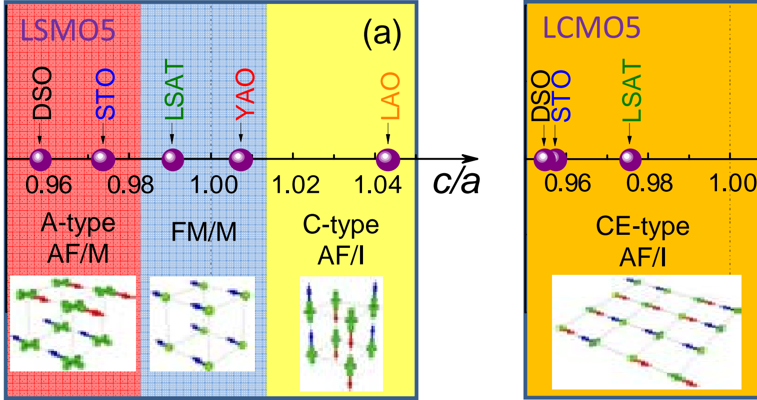

Figure 5.12: Experimentally obtained slice of the phase diagram of the $La_{1-x}Sr_xMnO_3$ (a) and $La_{1-x}Ca_xMnO_3$ b) in the plane of c/a and doping level x corresponding to $x = 0.5$. Yellow zones indicate C-type AF/I ground state, red zone indicates A-type AF/M ground state, blue zone indicates FM/M ground state, orange zone indicates CE-type AF/I ground state. Insets are adapted from Fig. 1 of Ref [117].

5.5 Conclusions

We have performed a comprehensive study of epitaxial strain on thin films of half-doped manganites $La_{0.5}Sr_{0.5}MnO_3$ (LSMO5) and $La_{0.5}Ca_{0.5}MnO_3$ (LCMO5) on a variety of substrates. It is found that epitaxial strain imposed by the substrates promotes pseudotetragonal cells with $c\ a$ ratio that can be largely tuned: $0.958 < c\ a < 1.04$ (LSMO5) and $0.954 < c\ a < 1.023$ (LCMO5). The metallic and ferromagnetic ground state of bulk LSMO5 is preserved in thin films grown on well matched substrates, and the corresponding thin films are ferromagnetic and metallic. In contrast, compressive biaxial strain leads to the emergence of an antiferromagnetic insulating state that we identify as C-type AF and tensile strain leads to an uncommon antiferromagnetic and metallic (in-plane) phase, reflecting an A-type AF spin ordering. The reduced metallicity of LSMO5 upon stronger tensile strain is attributed to the combined effect of conduction band narrowing and the ubiquitous presence of extended planar defects in

the film. In the narrower-bandwidth LCMO5 oxide, the epitaxial strain imposed by the substrates drives in all cases the films into an AF and insulating state, with minor effects on conductivity or magnetization. Coexistence of phase-separated AF and FM regions has been identified in strained LSMO5 films and, to a lesser extent, in LCMO5. It thus follows that strain has remarkably different effects on LSMO5 and LCMO5 that mainly arise from the difference in the electronic bandwidth and the corresponding ground state. Therefore It is anticipated that half-doped manganites, if integrated on piezoelectric stressors or tunnel junctions in conjunction with ferroelectric layers, will respond differently depending on their bandwidth. For instance, it is envisaged that any field effects should dominate in LCMO5-based barriers whereas piezo-induced strain may have a more prominentrole on LSMO5. Although more investigations are needed to definitely settle the microscopic nature of spin and orbital ordering in these films, the findings reported in this thesis should help to design more responsive devices, such as multifunctional tunnel barriers with improved response.

An extensive study of orbitals and spin ordering by X-ray difraction absortion of these layers has been reported in the Ph.D thesis of David Pesquera (UAB 2014, [121]) with fully agree with the phase diagram prosed here.

Part IV

Photoinduced effects in ferroelectrics

Chapter 6

Photoinduced effects on $BaTiO_3$ films

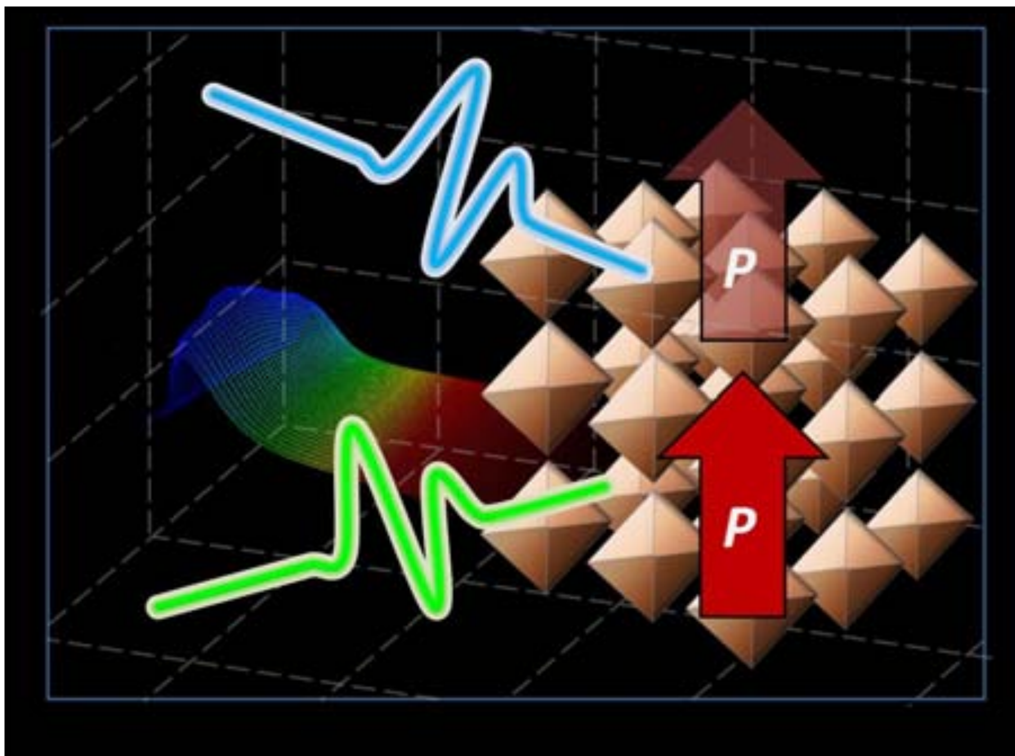

Abstract

Photosensitive ferroelectric materials exhibit various photoferroelectric phonomena due to the strong influence of nonequilibrium charge carriers on polarization. For $BaTiO_3$ a band-gap of 3 2 eV has been reported and typically UV radiation has been used to study the photoinduced effects. In this work we report on some preliminary experiments on the photoresponse of $BaTiO_3$ thin films and a) it dependence on illumination wavelenght, b) polarization state and c) contact configuration.

6.1 Introduction

While silicon-based diodes have been the dominant solar cell technology, novel photovoltaic mechanism due to ferroelectricity are being explored in pursuit of imporved efficiency [122]. Several works of photoinduced effects using ferroelectric materials in bulk have been reported [62 55 61 57 58 59], and others, more recently, focus on photoinduced effects in thin films [123 124 125 126] where polarization can be switched easily. In ferroelectric thin films, photoinduced phenomena are expected to be more pronounced because the light can be absorbed totally into the whole film. Nevertheless the nature of the electric transport understood in crystal-bulk ferroelectric would be completely different than in thin ferroelectric films due to defects or interface effects. In special, the influence of structural and charge defects on large bad-gap (3.2 $eV < E_g$) ferroelectrics thin films photoinduced properties have been less studied.

The objetive of this chapter is study the photoinduced effects on $BaTiO_3$ (BTO) films grown on pourpouse under not optimal conditions to induce large non-stoichiometric deffects. $La_{0.7}Sr_{0.3}MnO_3$ (LSMO) is used as bottom electrode and Pt as top electrode. Polarization and leakage current measurements in dark and under illumination were done using the different geometries (top-top and top-bottom as explaned in chapter 3).

6.2 Thin film growth and structural characteristics

The growth parameters as oxygen pressure and temperature play an important role in determining the crystalline and morphologic quality. Films following two different pulsed laser deposition growth conditions are studied. The methods are as follows:

- Bilayers of BTO/LSMO were grown on (001) $SrTiO_3$ (STO) substrates using a laser ($\lambda = 266nm$) with a fluence of $5.2Jcm^{-2}$ (for LSMO deposition process) or $2.2Jcm^{-2}$ (for BTO deposition process) and a repetition rate of $2Hz$. LSMO films (50 nm) were grown at a deposition temperature of 730°C and an oxygen pressure of 0.22 $Torr$. The subsequent growth of 150-nm-thick BTO, performed at 640°C

and with an oxygen pressure of 0.02 $Torr$, it was followed by 30 min annealing at 600°C in a high oxygen pressure (760 $Torr$). This method was successful to grow strained BTO of 17 nm thick [127], however is not straightforward that the same results will be obtained for thicker samples. These films were grown at LNESS by Ph.D C. Rinaldi.

- In the second method, bilayers of BTO/LSMO were grown on (001) $DyScO_3$ (DSO) (001) and $LaAlO_3$ (LAO), using a laser ($\lambda = 266nm$) with a fluence of $5.2Jcm^{-2}$ (for LSMO deposition process) or $2.2Jcm^{-2}$ (for BTO deposition process) and a repetition rate of $2Hz$. LSMO films (30 nm) were grown at a deposition temperature of 725°C and an oxygen pressure of 0.20 $Torr$. The subsequent growth of 50-nm-thick BTO, performed at 700°C and with an oxygen pressure of 0.02 $Torr$, it was followed by free cooling down without oxygen pressure. These films were grown at ICMAB by M.Sc. Nico Dix.

XRD around (002) reflection for each sample are plotted in Fig. 6 1. The highest intensity peak in each diffractogram corresponds to the substrate (002) reflection. For a bulk LSMO, the lattice parameter is expected to be 3 873 $\AA$, considering a pseudo-cubic structure, and its corresponding reflection should be placed at $2\theta = 46\ 91°$. In the case of DSO, the manganite peak is placed at higher angles if compared with its bulk position, indicating a reduction of the out-of-plane lattice parameter due to the tensile in-plane strain imposed by the substrate. In the case of STO, the manganite presents a slight strained state. LSMO on LAO is under a compresive strain.

On the other hand, BTO crystal has a tetragonal structure with an in-plane lattice parameter (a_{BTO}) of 3 993 $\AA$ and an out of plane lattice parameter (c_{BTO}) of 4 038 $\AA$. From the Fig. 6 1 a-d) it is observed that BTO reflections are placed at lower angles than the corresponding for bulk values. This indicates that there is a expansion of the out-of-plane lattice parameter of BTO films. The shape of BTO film peaks in Fig. 6 1 shows that for STO and DSO substrates, the BTO presents a non homogeneous lattice parameter. In the cases on BTO grown on LAO, the (002) reflection inticates that the

the lattice parameter of BTO film is close to the lattice paametro of bulk, problably because the expected compresive strain for BTO on LAO is very high (-5 3%) the relaxation occurs in the first layers with further relaxed growth. These characteristics of the samples make them interesting to study photoinduced effects since these puntual deffects (as oxygen deficiency) and planar deffects (as dislocations) can largely affect the

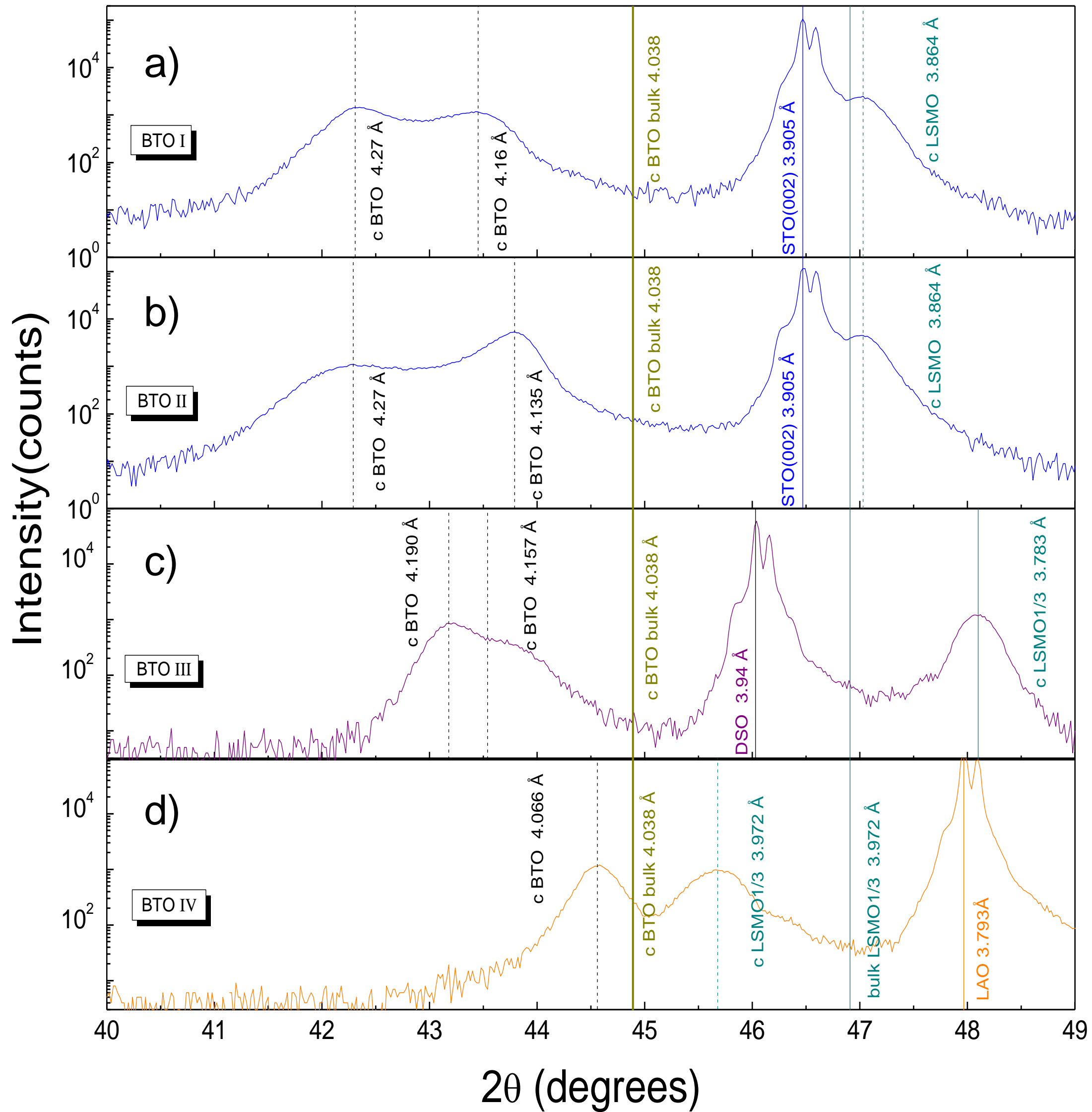

Figure 6.1: a- b) XRD profiles of the (002) reflection for BTO(150 *nm*)/ LSMO0.3(50 *nm*) on STO, c) on DSO and d) on LAO substrates.

photocarrier generation and recombination. The main characteristics of the samples are listed in table 6 1.

Table 6.1: Summary of the main characteristics of the samples. All the samples have Pt contacts of 40 *nm* thick.

Sample	Subs.	BTO (nm)	LSMO (nm)	c_{BTO} ($\mathring{A}$)	Annealing
BTO I	STO	150	50	4.27-4.135	yes
BTO II	STO	150	50	4.27-4.16	yes
BTO III	DSO	50	30	4.190-4.157	no
BTO IV	LAO	50	30	4.066	no

6.3 Top top measurements

Before to present the results of photocurrent at low bias in top-top geometry, it is worth to present the leakage current (quasi-static $I-V$) for negative and positive bias in dark conditions.

In top-top geometry the device can be considered as a two capacitors in series (Pt/BTO/LSMO/BTO/Pt) and symmetric $I-V$ curves are expected due to the symmetry of the stacking. Slight deviation of this behavior can be attributed to different quantity of defects under each Pt contact. This is observed in Fig. 6 2. The resistivity of the films at 1 V goes from $\sim 1{\times}10^{11}\ \Omega \cdot cm$ (for BTO III) to $\sim 3{\times}10^{11}\ \Omega \cdot cm$ (for BTO II). At 1 V the electric field is 66kV/cm for thicker BTO and 200 kV/cm for thinner samples. For these electric field the leakage current varies from 0.3 $\mu A\ \ cm^2$ to $1\mu A\ \ cm^2$ respectively. These values are comparable to the leakage current in $BaTiO_3$ and $Ba_{1-x}Sr_xTiO_3$ which present values of 2 $\mu A\ \ cm^2$ and 0.7 $\mu A\ \ cm^2$ in the same range of electric field [128 129].

Figure 6.2: Leakage current in top-top configuration for all BTO samples in dark conditions.

6.3.1 Photocurrent

Comparing the leakage current measurements in dark and illuminated conditions, it is a direct way to determine whether carriers are generated. In Fig. 6 3, representative leakage current measurements for all the samples are shown.

The leakage current measurements of Figs. 6 3 a-d) were performace using a blue laser with a wavelength of 405 nm and a power of 5 mW. Before to measure, the blue laser is ON for one minute; the measurements start and bias is applied while the leakage current is sensed during the experiment. When the bias reaches 0.4 V the laser is switched to OFF. Once the voltage reaches 0.7 V the laser is ON again, until the bias reaches 1 V. The decay in leakage current between 0.4 V and 0.7 V is due to the absence of photocurrent contribution. The leakage current values (at a given voltage when the laser is ON) in Figs. 6 3 a-c), are bigger than the leakage current values in Fig. 6 2. In the inset of Fig. 6 3 a) (in log scale) it can observed that photocurrent increases the leakage almost one hundred times. Only in Fig. 6 3 d)(BTO-IV sample) the photocurrent has a small contribution.

In the case of Figs. 6 3 e- h), the same method as explained before it is used, but here, a green laser of $\lambda = 532\ nm$ and a power of $6mW$ is used. The leakage current does not shows significant variations when the condition of illumination changes.

Fig. 6 3 clearly show that photocarriers are generated when the photon energy is very close to the energy band gap $E_g \approx 3\ 2\ eV$; using a blue laser ($\lambda = 405\ nm$, energy $= 3.10\ eV$) the photon energy is close to E_g. On the other hand using the green laser ($\lambda = 532\ nm$) the photon energy is 2.35 eV wich is much smaller than E_g

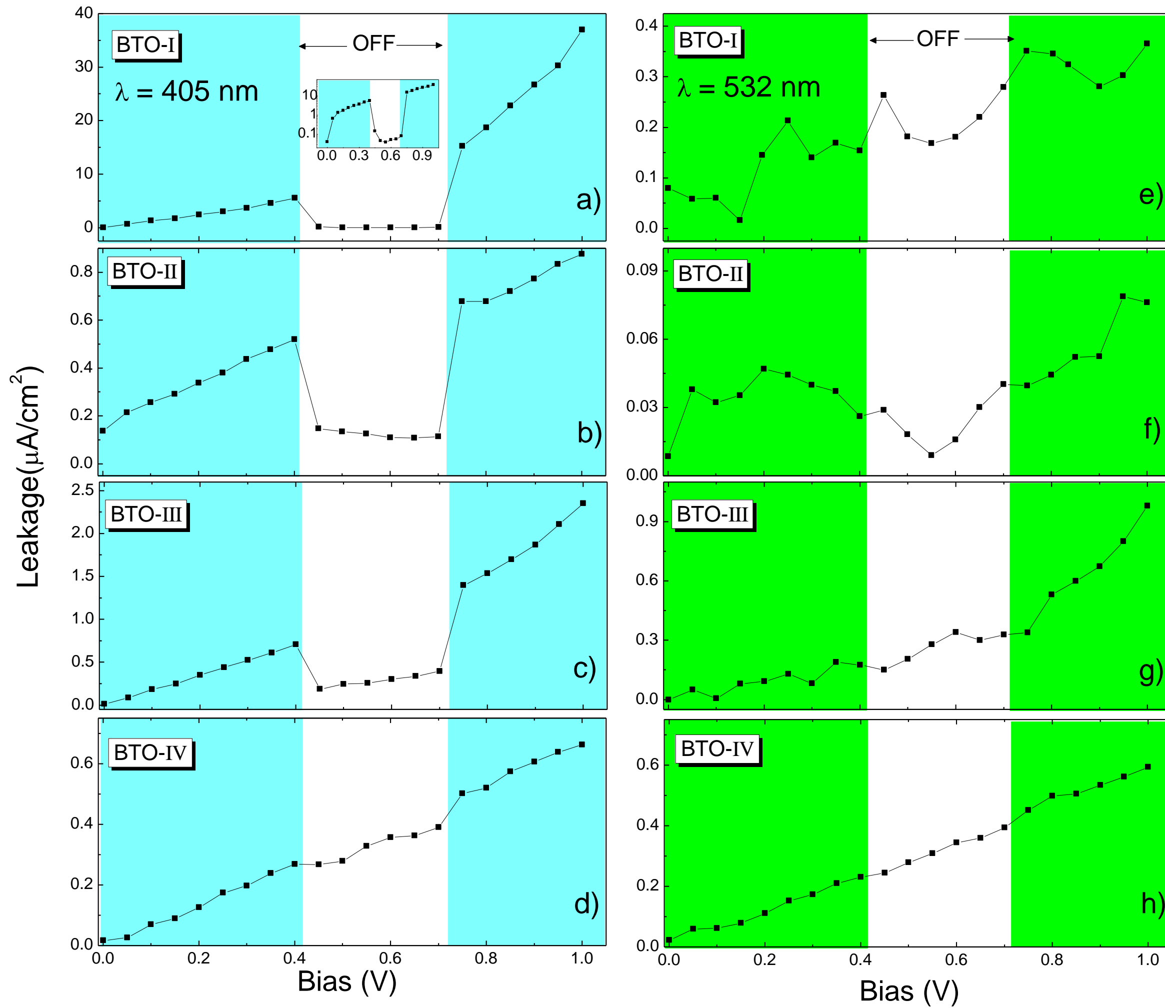

Figure 6.3: Photocurrent measurements for all samples. Figs. a-d): the current vs bias starts after applying the blue laser on ($\lambda = 405\ nm$). When the voltage reaches 0.4 V the blue laser is off. Once the bias reaches the 0.7 V, the blue laser is on again. Figs. e-h): represent the same experiments as the Figs. a) to d) but using a green laser ($\lambda = 532\ nm$). No photocurrent is observed with green laser.

6.3.2 Polarization measurements

The illumination of photosensitve ferroelectric materials results not only in an increase of their conductivity, but also in change on their ferroelectric properties. Below it will be shown the results obtained for current vs bias loops and their corresponding polarization loop in top-top configuration.

The effect of the illumination on the ferroelectric properties for sample BTO I is shown in Fig. 6 4. The black curve in the Fig. 6 4 a) corresponds to $I-V$ recorded in dark conditions. Here, a very well defined switching current is observed reaching a value of $\sim 80\ \mu A$ at a given frequency(2500 Hz). The other curves in Fig. 6 4 a) are $I-V$ loops under laser illumination ($\lambda = 405\ nm$): empty blue squares corresponds to $I-V$

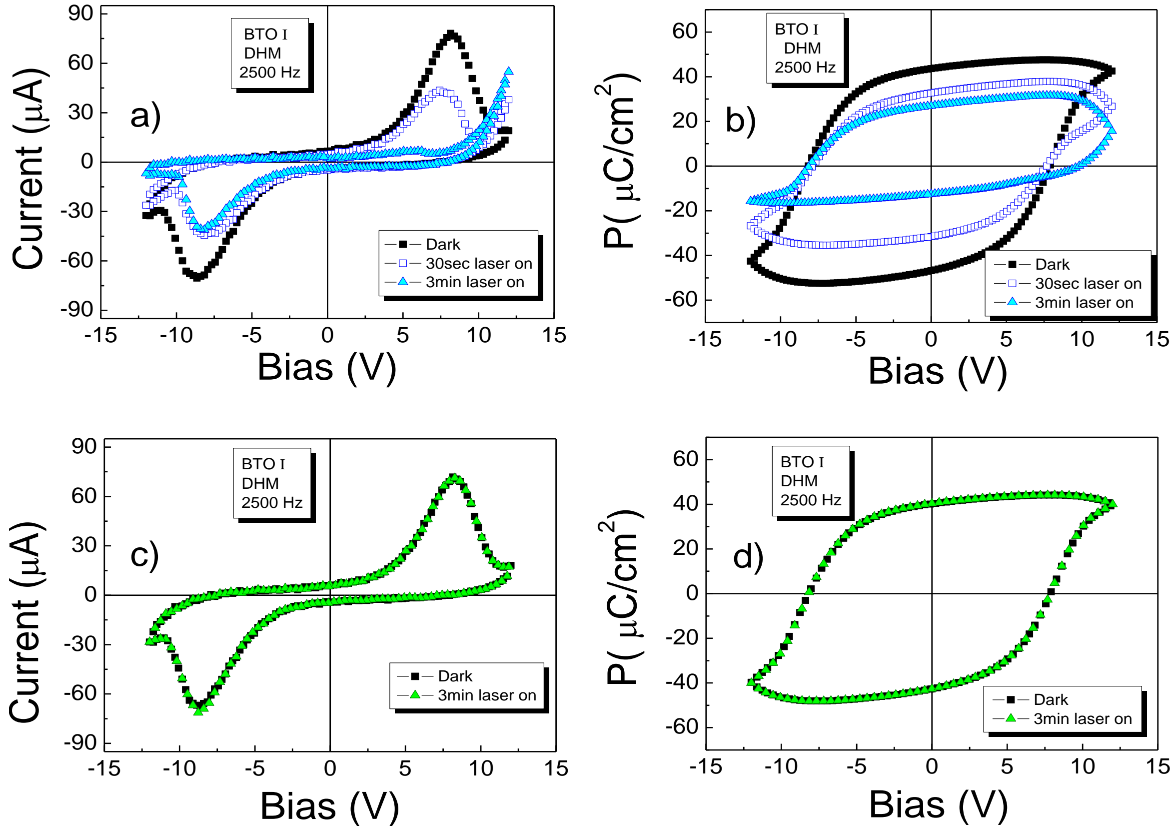

Figure 6.4: $I-V$ and P loops in dark and illuminated conditions for BTO I. a-b) Dark (black squares) and blue illuminated (empty square and triangles. c-d) Dark(black square) and green illuminated (triangles). Loops in Dark overlap the green illuminated loops.

curves recorded after 30 seconds of laser ON, while filled blue triangles corresponds to $I - V$ curves recorded after 3 minutes of laser ON. It is observed a notable progresive decreasing of switching current and also a shift of peaks towards 0 V for the positive and negative peaks indicating a reduction of the coercive bias. The corresponding polarization loops are presented in fig. 6 4 b). A progresive reduction of, for instance, remanence polarization (P_r) is observed under illumination with blue laser.

On the other hand, Figs. 6 4 c) and d) present a similar experiment as a) and b) but instead of a blue laser, a green laser is used ($\lambda = 532$ nm). No variations of switching current or polarization under green laser illumination are observed (curves

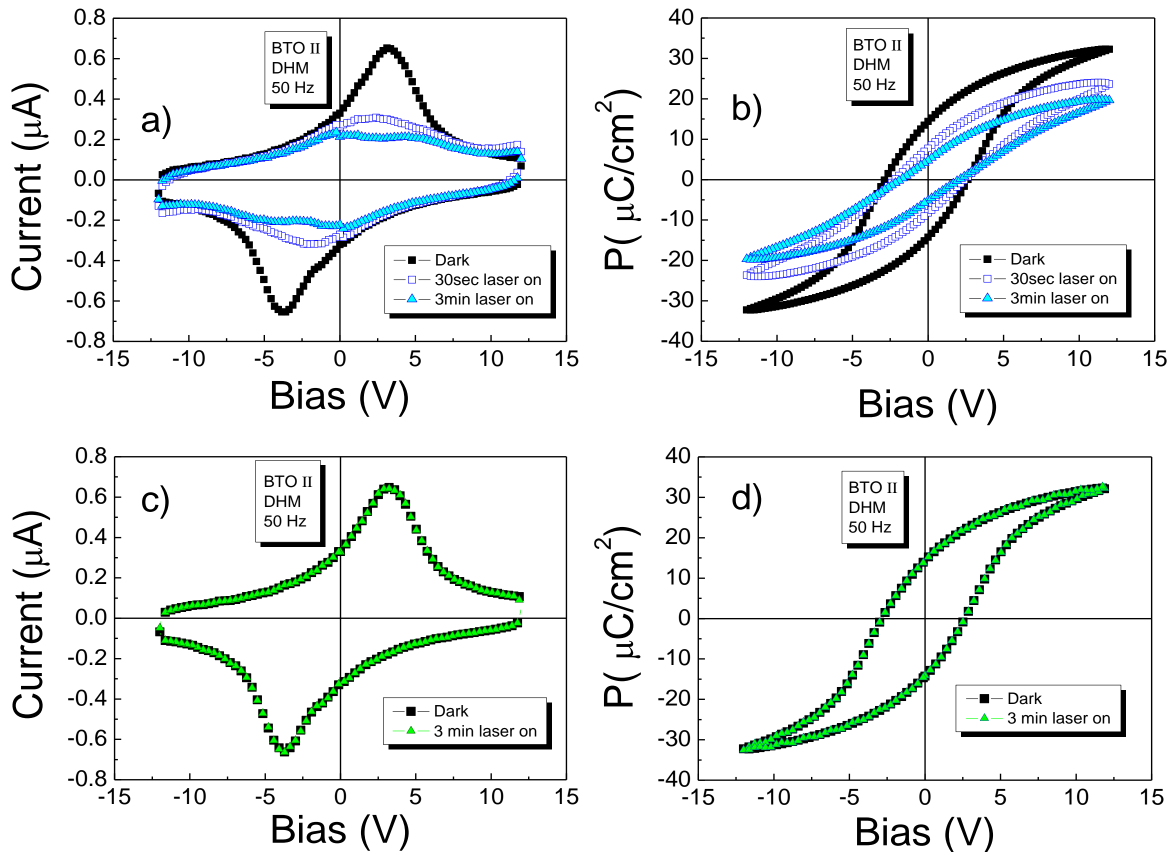

Figure 6.5: $I - V$ and P loops in dark and illuminated conditions for BTO II. a-b) Dark (black squares) and blue illuminated (empty square and triangles. c-d) Dark(black square) and green illuminated (triangles). Loops in Dark overlap the green illuminated loops.

These observations are in agreement with the observation of photocurrent shown in Fig. 6 3 e).

Figs. 6 5, 6 6 present the results of $I - V$ and polarization loops for samples BTO II and BTO III. The experiments were done exactly in the same way as in sample BTO I, using the same protocol but at different frequency (50 Hz for BTO II and 100 Hz for BTO III). The results here present similarities with the results in Fig. 6 4, where polarization is only sensitive to short wavelength illumination ($\lambda = 405$ nm). It is interesting to note that for BTO II and III, the $I - V$ curves under blue laser illumination do not show features of leaky capacitors, in spite of the photocurrent

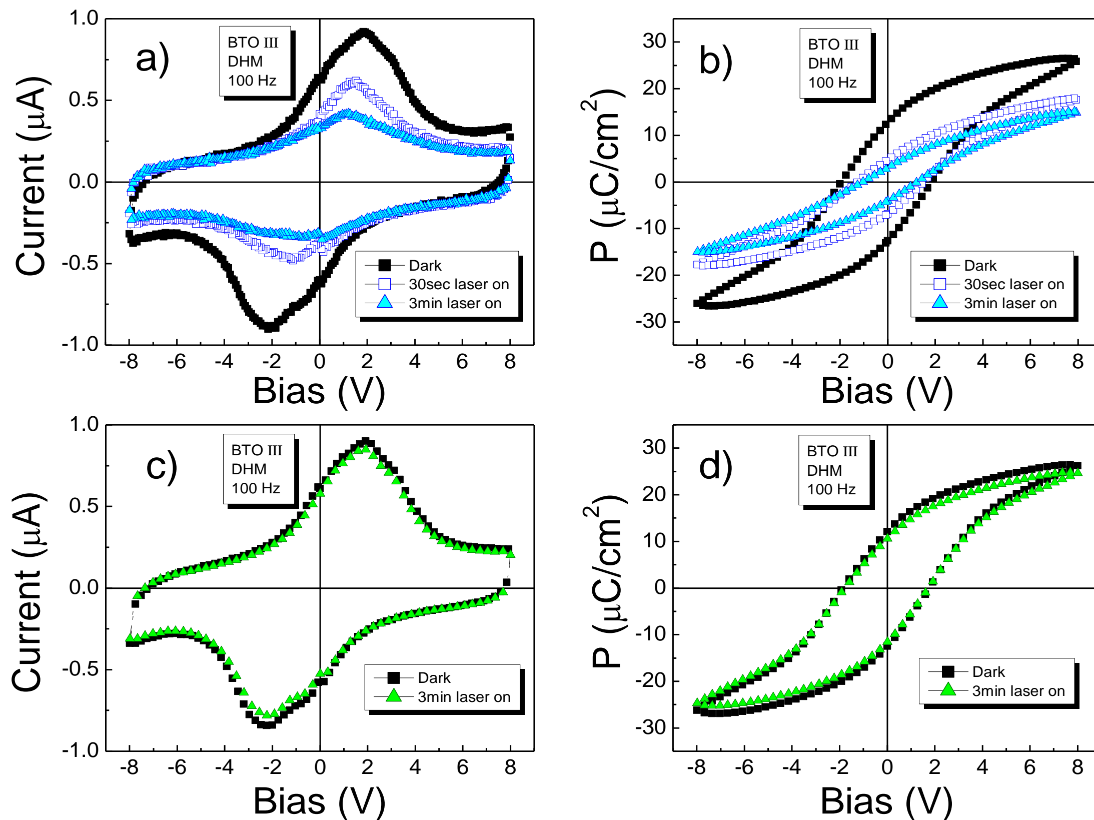

Figure 6.6: $I - V$ and P loops in dark and illuminated conditions for BTO III. a-b) Dark (black squares) and blue illuminated (empty square and triangles. c-d) Dark(black square) and green illuminated (triangles). Loops in Dark overlap the green illuminated loops.

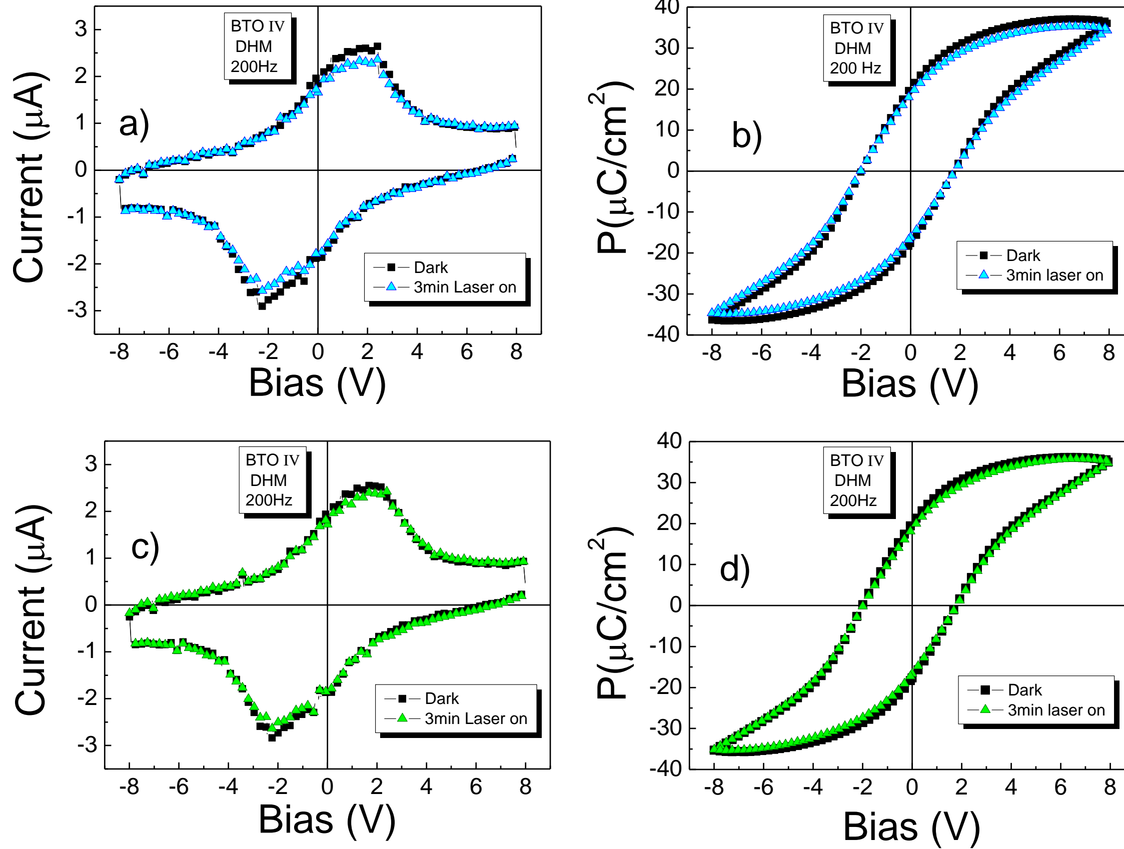

Figure 6.7: $I-V$ and P loops in dark and illuminated conditions for BTO IV. a-b) Dark (black squares) and blue illuminated (empty square and triangles. c-d) Dark(black square) and green illuminated (triangles). Loops in Dark overlap the green illuminated loops.

In the case of BTO IV (BTO on LAO), the photoinduced effects (using the laser of short wave length, $\lambda = 405\ nm$) are definitely smaller than in previous cases. Fig. 6 7 shows data of a precise pair of contacts where small although perceptible photoinduced effect is observable.

Up to now it has been shown that photocurrent is induced and polarization is depressed by blue light. Below it is shown and described the temporal dependence of the polarization in samples BTO I, BTO II and BTO III.

Figs. 6 8 a-c) show the polarization values of P_r and P_{max} while the Figs. 6 8 d-f) show the wide and the center of the loops (obtained from the coercive bias) for BTO

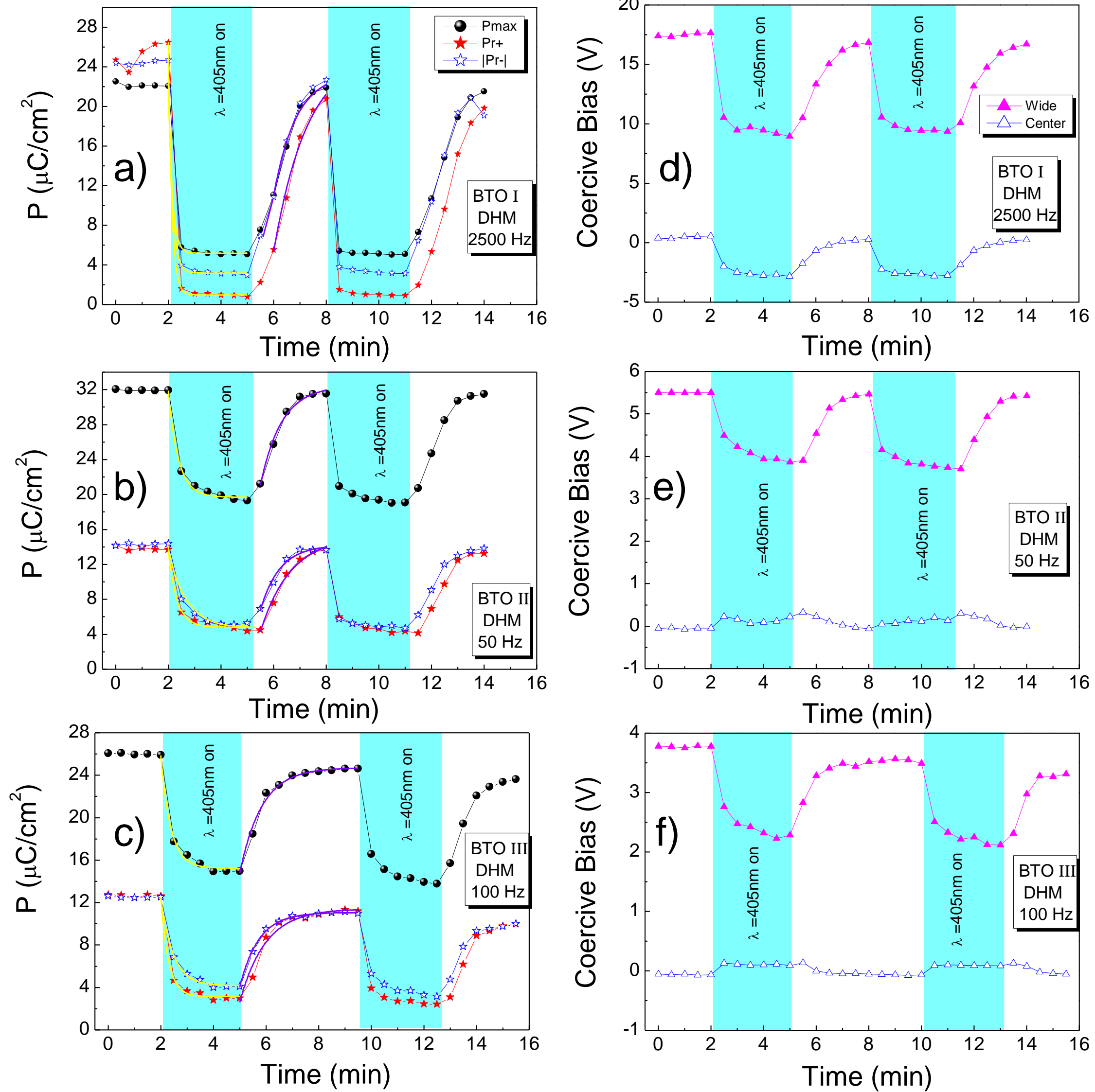

Figure 6.8: Time dependence in dark or illuminated condition. a) b) and c) present the P_{max}, $Pr+$ and $Pr-$. Figs. d) e) and f) show the time dependence in dark or illuminated condition of the wide of the hysteresis loop and the central point.

I, BTO II and BTO III. The first five measurements are taken in dark condition in order to check the reproducibility of the measurements and/or the noise level. Then, the light is switched ON and a decrease of polarization is observed until a minimum value is reached After that, when the light is switched OFF, a progressive recovery of polarization is observed. It can also be noticed that in Figs. 6 8 a) the time to

reach a minimum value of P is faster than in Figs. 6 8 b) and c). The data seem to be adjusted by a exponential decay under light and exponential recovery after turning OFF the light as follows:

$$P(t) = \Delta P e^{\frac{-t}{\tau_{on}}} + P_{min} \tag{6.1}$$

$$P(t) = \Delta P \left(1 - e^{\frac{-t}{\tau_{off}}}\right) + P_{min} \tag{6.2}$$

Table 6.2: fitted values of the decay δ_{on} and recovery time δ_{off} of polarization extracted from Fig. 6 8.

	$\delta_{on}(P+)$	$\delta_{on}(P-)$	$\delta_{on}(P_{max})$	$\delta_{off}(P+)$	$\delta_{off}(P-)$	$\delta_{off}(P_{max})$
BTO I	9 ± 2 s	10 ± 2 s	9 ± 2 s	51 ± 10 s	44 ± 3 s	62 ± 15 s
BTO II	20 ± 3 s	27 ± 2 s	23 ± 2 s	t0 ± 15 s	44 ± 9 s	48 ± 8 s
BTO III	20 ± 2 s	28 ± 2 s	23 ± 2 s	58 ± 9 s	43 ± 2 s	50 ± 5 s

where ΔP represents the variation of the polarization under light, P_{min} is the saturation polarization under light and $\delta_{on}(\delta_{off})$ represents the time constant in illuminated (or dark) conditions. The values of δ_{on}, δ_{off} are listed in Table 6 2. These values are comparable to time constant in the literature [58 59] . Direct band gap photoexcitation is believed to be a very fast process (below 0 1 *sec*, [60]), and longer times signal the contribution of defects [130 131 58 59]. On the other hand, Figs. 6 8 d-f) indicates that wide of the loop under light is always reduced indicating that the coercive field decreases with light. For Figs. 6 8 e- f) it can be noticed that center of the loops is not shifted significatively ($\sim 0.5\ V$) but in the case of the Fig. 6 8 d) it can be notice a strong shift ($\sim 2\ V$) in the loop under illuminated conditions. Similar changes on polarization and coercive bias under UV-light has ben observed in PZT films ($d \sim 2\mu m$) prepared by sol-gel [132 130].

6.4 Top-bottom measurements

Fig. 6 9 a) is a leakage current loop measured in step bias (as explained in section 3 9). This allows to avoid the contribution of the polarization (switching current) and only take the DC component. From Fig. 6 9 a) it can be observed a clear rectifying behavior in dark or illuminated conditions. This rectifying behavior indicates a Schottky barrier (SB) formation [133]. The application of high bias ($\sim 7\ V$) can polarize the sample

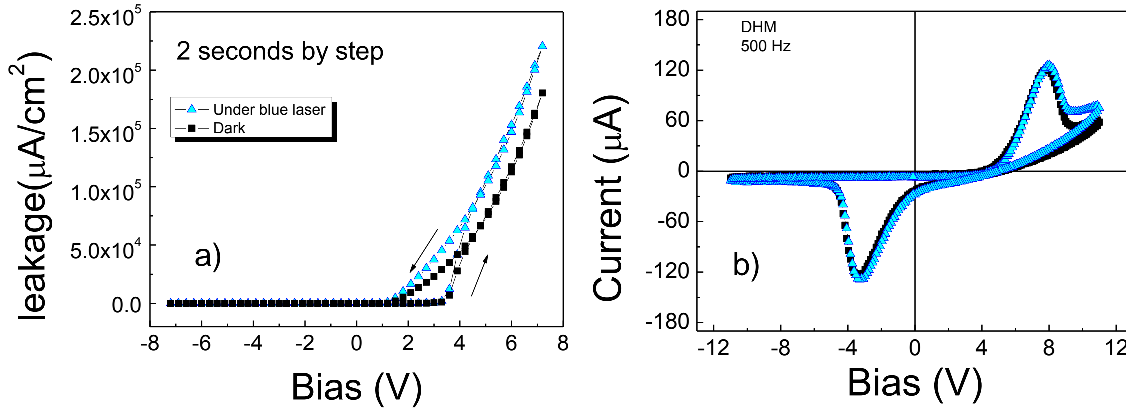

Figure 6.9: a) leakage current vs bias in dark and illuminated conditions for BTO I. b) $I-V$ loop at 500 Hz to observe to switching current and the DC contribution.

On the other hand, Fig. 6 9 b) was taken at 500 Hz in order to observe the switching current. This Fig. indicates a strong imprint in the ferroelectric loops. It can be notice that the loop is an overlapping of a rectifying behavior and the hysteresis loop without leakage. The effect of the light just increases the leakage current but there is no supression of the switching current peak by blue light, in contrast to the top-top geometry.

In order to investigate if the SB can be modulated by the polarization, measurements of $I-V$ in small range of voltage (0.5 V to 1.8 V) were done, after a pulse of voltage (V_{write}). V_{write} determine the polarization vector and the resistance is moni-

tored by the $I - V$ characteristics. Fig. 6 10 a) shows the $I - V$ curves for positive V_{write} (orange square) and negative V_{write} (violet squared) in dark conditions. Fig. 6 10 b) shows the $I - V$ curves for positive V_{write} (orange triangles) and negative V_{write} (violet triangle) under illuminated conditions. In both cases (dark and illuminated) there is a clear dependence of the current with the V_{write}, but in the cases of under illuminated conditions, the magnitud of the current is bigger than the current under dark conditions because there is a contribution of the photocarriers. Fig. 6 10 c) shows the current at 1.6 V as a function of the V_{write} under dark and illuminated conditions.

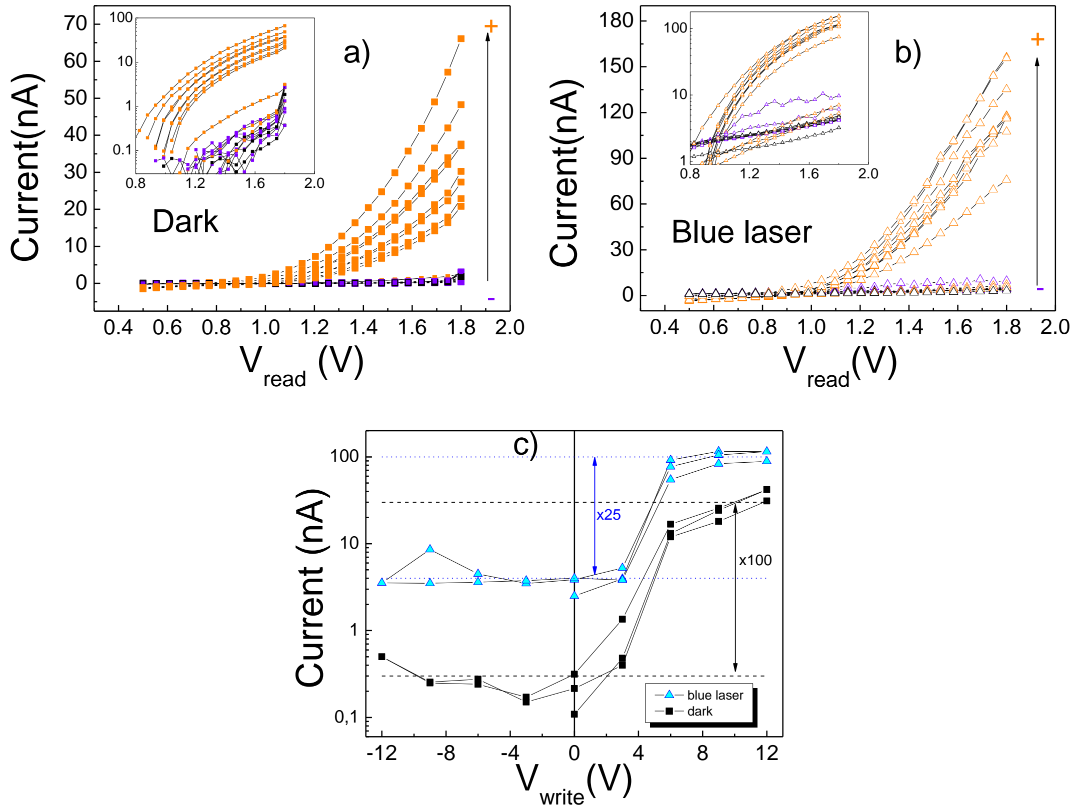

Figure 6.10: $I - V$ curves from 0.5 V to 1.8 V after positive V_{write} pulses(Orange squares) and negative V_{write} pulses (violet squares) in a) dark conditions, or b) illuminated conditions. c) current at 1.6 V vs V_{write} in dark (black squares) and illuminated conditions (blue trinagles).

Up to now there are experimental evidences of photoinduced effects on the ferroelec-

tric properties of BTO layers using a photon energy lower than the UV energy photon. In top-top geometry the polarization is affect directly by the short wavelenght ($\lambda = 405$ nm) whereas in top-bottom it is not, but the samples presents tuneable lekeage properties by polarization and light. At following, a discussion about the measurements in overall is offered.

6.5 Discussion

The results in Fig. 6 3 indicates photocurrent is induced when photon energy is close to the BTO band gap. Crystalline and/or stoichiometry defects in epitaxial films are expected to produce a smear of the edges of the valence band and the conduction band, introducing tails of the states in the forbidden band [135 126 136]. That allows subbandgap photon to be observed and photocarriers generated/recombined. On the other hand, in polarization measurements via $I-V$ loops, the photocurrent can adds to the switching current reducing the polarization and the coercive voltage (Fig. 6 8) when the ferroelectric is illuminated.

The question about why the polarization in top-top geometry is affect by short wavelength illumination whereas in top-bottom not, it is not yet clear. We can speculate that it appears to be related to the presence of strong imprint field.

In any case, this study shows that coercive field can be reduced under short wavelength illumination and polarization screened by photoinduced carriers.

6.6 Conclusions

Photoelectric effects have been studied on epitaxial $BaTiO_3$ films. This study had revealed the following:

Photocurrent enhancement and polarization reduction in top-top geometry is observed when using short wavelenght illumination (~ 405 nm) but not observed when using longer wavelength (e.g. 532 nm). Local microstructure affects the photoinduced

effects.

In top-top geometry, the coercive field is reduced under short wavelenght illumination. This phenomena and the polarization reduction by short wavelenght illumination, appears as interesting phenomenon for applications, like transforming a hard ferroelectric in soft ferroelectric temporally without the requirement of increasing the temperature; the reduction of polarization can be exploited for hidding information temporally in ferroelectric-based memories .

In top-bottom geometry the leakage current shows a rectifyng behavior in dark or short wavelenght illumination. The rectifying behavior cannot be switched neither suppressed but it can be modulated by the polarization direction. The high or low conductivity of this diode-type can be monitored at very small bias (between 0.5 V and 2.0 V).

In top-bottom configuration there is a a very strong imprint in the $I-V$ loops in dark or short wavelenght illumination. No significant suppresion of the ferroelectric switching current by short wavelenght illumination was detected, which dramatically contrast with top-top geometry results. It can be speculated that the imprint is the responsable of this difference.

Part V

Tunnel transport

Chapter 7

Electrical transport through nanometric $CoFe_2O_4$ barriers

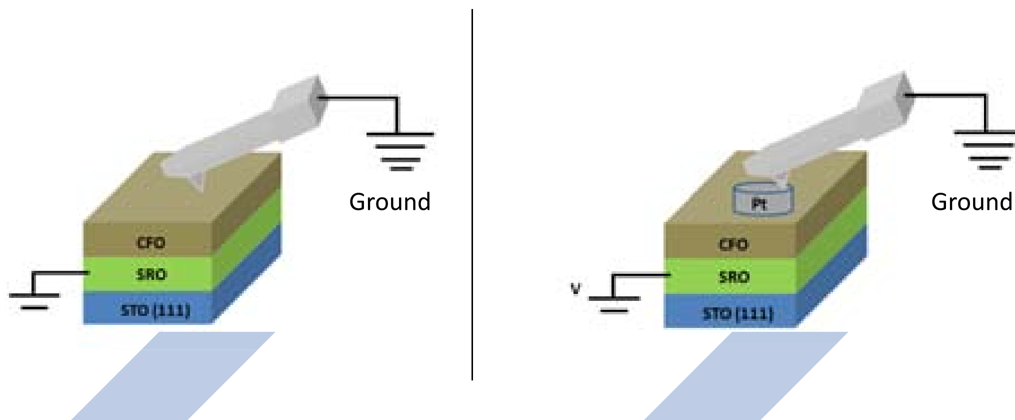

Part of the work discussed in this chapter is published in:

M. Foerster, D. Gutiérrez, J. M. Rebled, E. Arbelo, F. Rigato, M. Juordan, F. Peiró and J.Fontcuberta, "Electric transport through nanometric $CoFe_2O_4$ thin films investigated by conducting atomic force microscopy", Journal of Applied Physics, 111, 013904 (2012).

Abstract

Highly spin-polarized current sources can be achieved by electron tunneling through a thin ferromagnetic insulating barrier with spin dependent transmission probabilities (spin filter). $CoFe_2O_4$-based spin filters present high enough Tunnel Magnetoresistance for device application at low temperature ($\sim 30\%$), while at room temperature the eficiency is much below than expectations and requiriments for devices. So, the transport properties in ultrathin $CoFe_2O_4$ remained to be understood. Here, a systematic study of electric transport through thin ($2-8\ nm$) $CoFe_2O_4$ films deposited on epitaxial $SrRuO_3$ bottom electrodes was performed by conducting atomic force microscopy. Experimental procedures to investigate transport through thin insulating films by conducting atomic force microscopy are critically revised. It is concluded that a tunnel and non-tunnel transport channels coexist at room temperature. The potential of $CoFe_2O_4$ films for their use as spin-filtering barriers is assessed.

7.1 Introduction

As mention in the chapter 2, the experiments show a $CoFe_2O_4$ (CFO) based spin filter efficiency below the expectations at room temperature. Those results lead us to rethink about the nature of electric transport through CFO. In this chapter we present a study of electrical transport through CFO thin films(2-8 nm) using non-magnetic electrodes at room temperature. The thickness dependence of the transport properties was investigated using CAFM. Two methods of using CAFM for the characterization of thin insulating films are described and compared, and the potential advantages of using micrometric metallic electrodes on the surface of CFO are addressed.

7.2 Description of the stacking

A series of CFO thin films of thicknesses from 2-8 nm were grown by rf-sputtering on $SrRuO_3$(25 nm)-buffered $SrTiO_3$ (STO) substrates. CFO and $SrRuO_3$ (SRO) films of (111) texture were obtained by using (111)-oriented STO substrates. At room temperarture CFO must presents a ferromagnetic character while SRO is no magnetic.

7.3 Results of transport characterization

Typical maps of a CFO(3 5 nm)/ SRO/STO film are shown in Fig. 7 1. The topography image in Fig. 7 1 a) and the current map in Fig. 7 1 b) were recorded simultaneously using a contact force of $F_c \approx 600\ nN$ while applying a bias voltage of $V_{bias} = 1\ V$. The maps show a flat surface with homogenous transport properties and the absence of visible pinholes. The surface roughness (rms) measured in these conditions is only $\epsilon =\ 0\ 13\ nm$ and values below 0.3 nm are determined when using the AFM in dynamic mode.

The histogram of current values $P(I)$ extracted from the current map of Fig. 7 1 b) is shown in Fig. 7 2 a) (triangles). Fig. 7 2 a) illustrates that the $P(I)$ distribution, when measured on the bare CFO surface, is rather broad, as typically found in CAFM

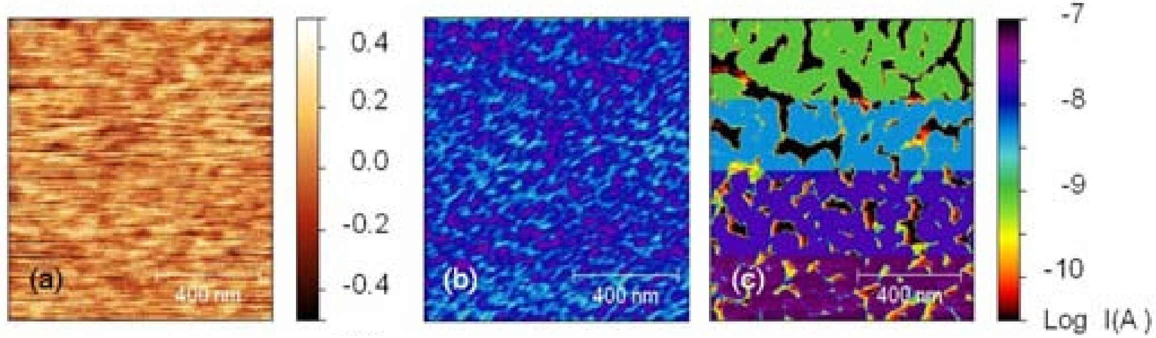

Figure 7.1: a) Flat surface topography of a CFO(3.5 nm)/SRO/STO multilayer. b) Current map ($F_c \approx 600\ nN$, $V_{bias} = 1$ V) obtained simultaneously with a); same logarithmic current scale as in c). c) Current maps measured on top of a Pt contact on a CFO(6 nm)/SRO/STO multilayer. Four different zones corresponding to different bias voltages are shown (from the top: 0.2 V; 0.4 V; 0.6 V; 0.8 V).

measurements on insulating films [137]. The current scale is defined by the typical current I_{typ}, which is the current value where the maximum of the $P(I)$ distribution is located. It can be seen in Fig. 7 2 b) (triangles), that I_{typ} increases exponentially when increasing the contact force,[138] implying that variations in the contact force will result in log-normal distribution of measured current values [137].

The typical current I_{typ} as a function of CFO layer thickness is shown in Fig. 7 3 (open circles) for current maps taken at $F_c \approx 300\ nN$ and V_{bias} =1 V. These values of I_{typ} from current maps can be compared with the corresponding current values determined directly from $I-V$ characteristics, obtained while keeping the tip on a point at the sample surface. With this aim, several sets of $I-V$ curves were recorded in different locations of the sample surface, using the same contact force ($F_c \approx 300$ nN) as for the current maps.

In Fig. 7 4(a), It is shown a series of $I-V$ measurements taken at different points of the surface of the 6 nm CFO film. For clarity, in Figs. 7 4 a) and 7 4 b), for each position on the sample, only one out of many consecutive $I-V$ curves is shown [7 4 a) on bare CFO surface and 7 4 b) on Pt]. The variations between consecutive $I-V$ curves recorded at the same point were much smaller than between different points.

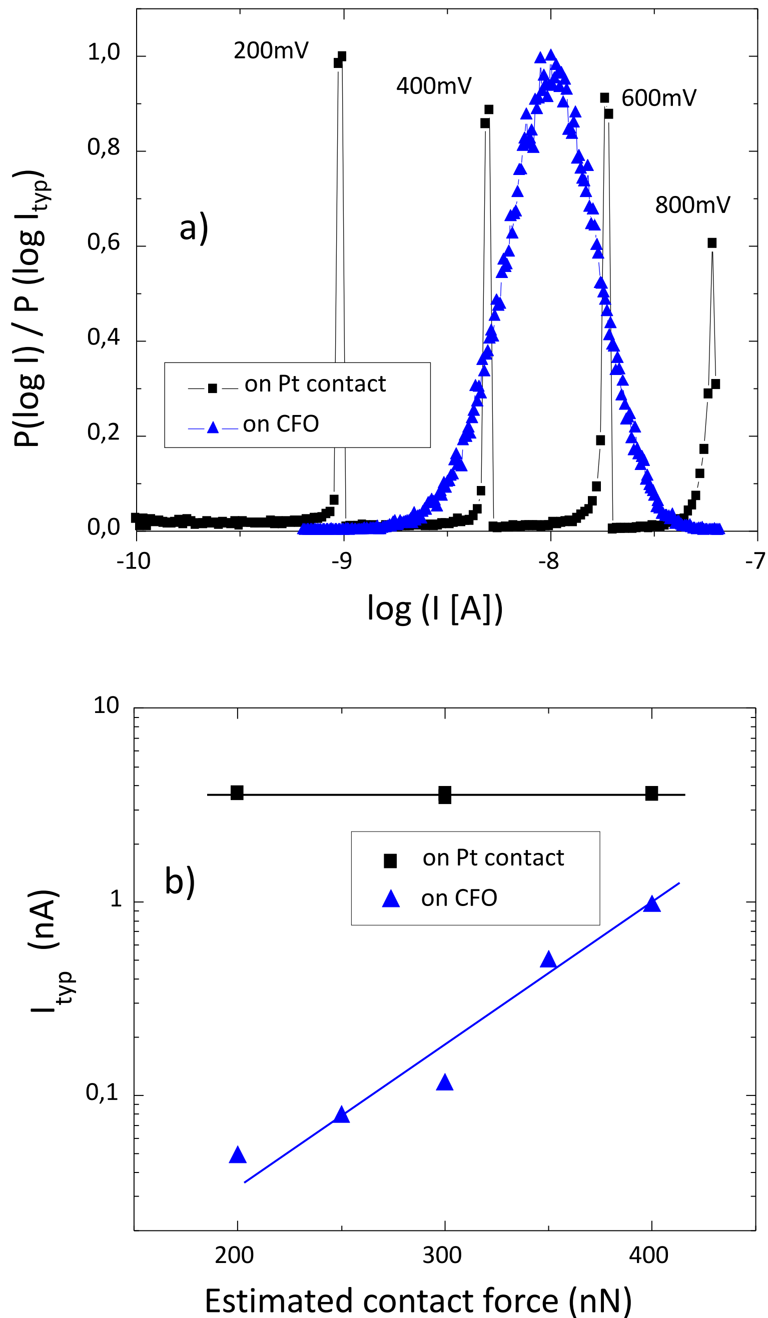

Figure 7.2: a) Distribution $P(I)$ of current values in the maps in Fig. 7.1-b) and Fig. 7.1-c). b) Dependence of the typical current I_{typ} vs the contact force for maps obtained on CFO (triangles) and Pt (squares).

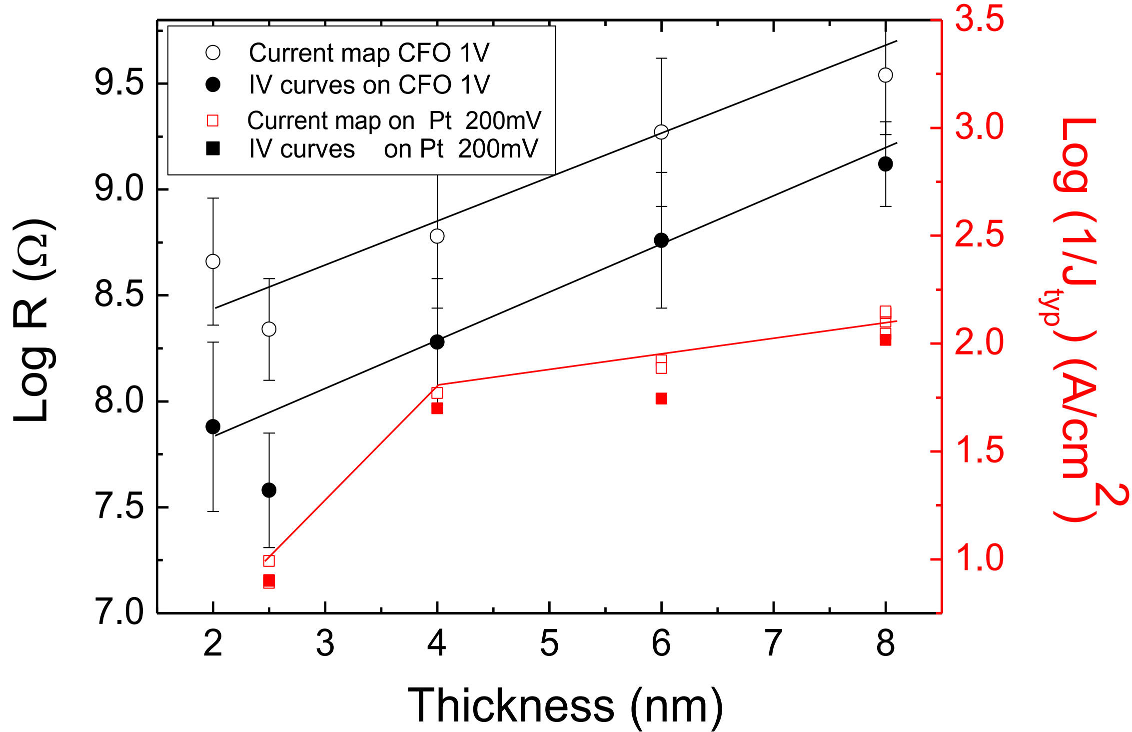

Figure 7.3: Current values measured in CAFM for CFO films of various thicknesses. Data measured on bare CFO is represented by circles and corresponds to the left axis. Open circles are typical current values I_{typ} of current maps; solid circles are values I_{avg} from $I-V$ curves obtained by logarithmical averaging. The respective current densities measured on Pt contacts J_{typ} and J_{avg} (open and solid squares) correspond to the right axis.

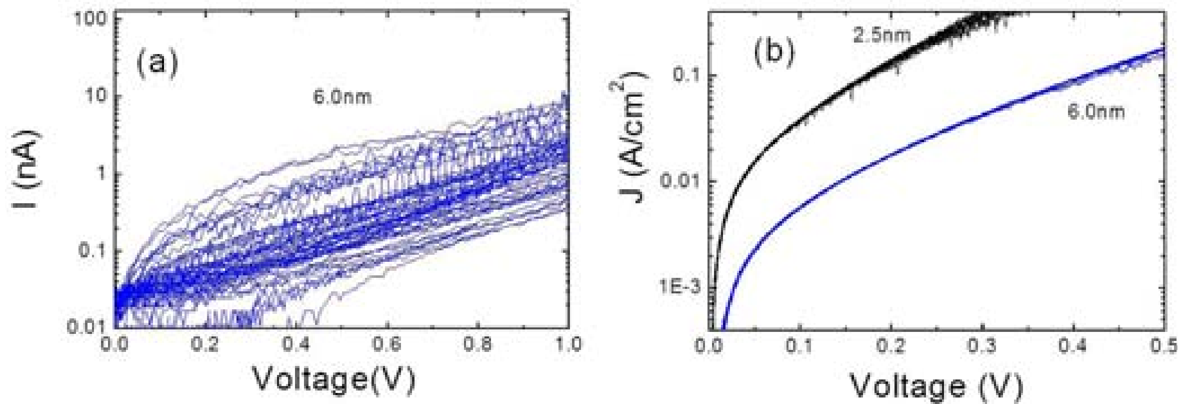

Figure 7.4: a) $I-V$ curves measured on a CFO(6 nm)/SRO/STO sample at 300 nN; each curve corresponds to a different location on the sample. b) $J-V$ curves measured on Pt contacts on CFO/SRO/STO samples with different CFO thicknesses.

The remarkable broad variation between individual $I-V$ curves raises the question of how these data can be properly analyzed and compared to current maps.

In a first step, the distribution of current values at a given voltage was determined. In Fig. 7 5, it is shown the current values at 1 V, as determined from the $I-V$ characteristics of Fig. 7 4 a). This distribution, shown in Fig. 7 5, follows roughly the same log-normal distribution as encountered in current maps[137 139].

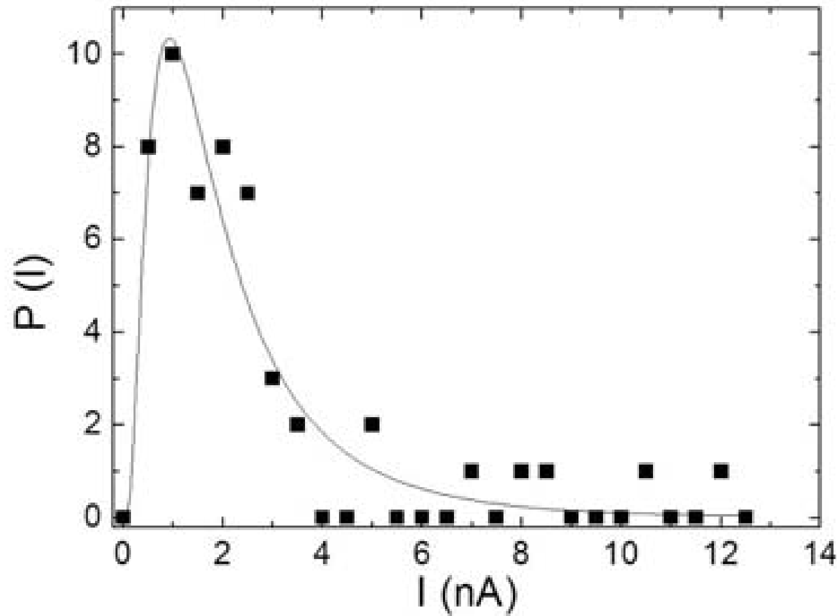

Figure 7.5: Distribution of current values at 1 V extracted from $I-V$ curves in Fig. 7.4 a), measured on a CFO(6 nm)/SRO/STO sample at 300 nN. The line corresponds to a fit with a log-normal distribution.

The reason for this distribution can be either spatial variations in the barrier properties or variations in the contact force. In any case, such distribution implies that data follows a normal (Gaussian) distribution on logarithmic scale. Thus, a meaningful statistical average should be done in logarithmic scale or the distribution should be fitted to a log-normal function (solid line in Fig. 7 5). Current values determined by fitting with a lognormal function (in the present example, $I_{fit} = 1.72\ nA$) or calculated by averaging $log(I)$ [here, $I_{avg} = 10^{<log(I)>} = 1.87\ nA$] are very similar, and so it will be used the latter in the following.

In a similar way it has been determined I_{avg} from a series of $I-V$ curves measured on CFO films of various thicknesses. It is clear from the results shown in Fig. 7 3 (solid circles) that data calculated in this way show a thickness dependence very similar to I_{typ} (open circles) obtained from current maps. This roughly exponential dependence will be discussed in more detail later on. Before, It is worth to comment on a few experimental observations. First, one notices that the difference between the absolute values of I_{typ} extracted from current maps and I_{avg} from $I-V$ curves is significant: the current measured in $I-V$ curves while keeping the tip at a fixed point is larger than the one measured when scanning the sample surface under nominally the same conditions. It was verified this difference to be reproducible and not related to any possible deterioration of the CFO film. Most likely, the contact between sample and tip is more stable and thus conductive when keeping the tip in one point than when the tip is pulled over the surface.

On the other hand, it can be appreciated, in Fig. 7 3, that the thinner films (2 nm and 2.5 nm) display a non-monotonic behavior of their resistance versus thickness, i.e., the fact that the current is higher for 2.5 nm than for 2 nm, which is unexpected. Clearly, this statement holds for data collected either using current maps (open circles) or $I-V$ curves (solid circles). This observation can be due to the intrinsic properties of the samples, but possible explanations related to the measurement have to be considered. It was used a fresh tip to measure each individual sample, because it had been previously observed that the conductance of the tip on the CFO decreased after several current maps. Thus, the most reproducible manner to measure was found to be the use of a new tip for each sample, which implies that, while the tip state is controlled well, the tip geometry can be slightly different from sample to sample. The data in Fig. 7 3 does not allow discriminating among these scenarios.

To eliminate the critical dependence on the tip-sample contact, small (diameter $\sim$ 1 μm) Pt contacts were deposited by FEBID on top of the samples, as it is known that metallic capping layers improve the stability of CAFM measurements [140]. Indeed, when current maps are conducted on the surface of the Pt-contact [Fig.7 2 c)] the

width of the $P(I)$ distribution shrinks drastically and the electrical contact between the tip and the Pt is found to be extremely stable. In Fig. 7 1 c), a combined current map for 4 different voltages (0 $2V$ 0 $4V$ 0 $6V$ and 0 $8V$) is shown. A well-defined current value for each voltage can be observed, independent of the tip position on top of the Pt contact. Areas with much smaller current (some dark (black) and bright (yellow) contrast regions black and yellow regions) reflect the granular structure of the Pt contact. The distribution of current values $P(I)$ extracted from Fig. 7 1 c) is also included in Fig. 7 2 a) (squares). It can be appreciated that the $P(I)$ distribution narrows and I_{typ} is better defined when current maps are recorded on the Pt contacts rather than on the bare CFO surface. This reduced variation is not only related to a more stable tip-sample contact, but also due to the averaging effect of the Pt-contacted area.

When using Pt/CFO top-contacts, the measured current level, represented by I_{typ}, is found to be contact-force independent [squares in In Fig. 7 2 b)]. In contrast, when the tip is directly placed on the CFO surface, the force has a crucial influence on the measured current value (triangles). Due to the good electrical contact between the tip and the Pt, measurements of $I-V$ characteristics are very stable and reproducible; see, e.g., Fig. 7 4 b), where $I-V$ curves recorded on different Pt contacts are shown. Since the current was found to scale with the area A of the Pt contact, the current density $J_{typ} = I_{typ}/\mathrm{A}$ is a well-defined parameter, allowing the fit of voltage-dependent current densities $J-V$ with standard expressions for tunnel conduction (see equation 1 6 at the introduction) [141 142].

In Fig. 7 3 (right axis), the values of J_{typ} (open squares) and J_{avg} (solid squares) determined using Pt contacts are included ($V = 200\ mV$). As described above, J_{typ} is determined from the $P(I)$ distributions of current maps (shown in In Fig. 7 2 a) after dividing by the Pt contact area and $J_{avg} = 10^{<logJ>}$ is calculated from $J-V$ curves. In Fig. 7 3, no data corresponding to the 2 nm film with Pt contacts are included, as it was found that Pt contacts deposited on the 2 nm CFO layer were short-circuited to the SRO bottom electrode, most likely due to pinholes in the thin 2 nm CFO film.

The strong increase of current observed for the 2.5 nm thick CFO sample compared with the 4-nm thick one may be still reminiscent of such pinholes. Interestingly, the difference between the current density values in maps (J_{typ}) and $J-V$ curves (J_{avg}) is only marginal when measured on Pt contacts (Fig. 7 3, squares), whereas significant differences were observed on the bare CFO film (circles). This observation is consistent with the picture that the scale difference on bare CFO between maps and $I-V$ curves is due to the poorer electrical contact established when scanning the tip over the CFO surface.

Now the discussion of the roughly exponential dependence of I_{typ} (J_{typ}) on the CFO layer thickness in Fig. 7 3 Will be retaken. As mentioned above, this exponential dependence is often taken as a signature of the tunnel nature of the transport. However, the data of Fig. 7 3 alone does not automatically guarantee that transport is dominated by the tunneling process. In fact, the thickness dependence of the current, as indicated by the slope in Fig. 7 3, is relatively small compared to the experimental error (error bars in Fig. 7 3 are taken as the width of the $P(I)$ distribution or from the standard deviation of $< logI >$). In fact, using the most simple approximation ($I \sim \exp \ \overline{\Phi}d\big)$ [141]), the slope observed in Fig. 7 3 would correspond to a small energy barrier Φ in the order of only some meV, which is much smaller than the voltages used in these experiments.

Since the thickness dependence of the resistance or current density of Fig. 7 3 does not allow unambiguous conclusions about the conduction process, the $J-V$ characteristics were studied in more detail by fitting appropriate expressions for tunnel transport. Exemplary $J-V$ fits are shown in Fig. 7 6 a). The agreement of the fits with experimental data is excellent. However, as reported elsewhere [143], the obtained fit parameters assuming tunnel transport (Brinkman [142] or Simmons[141] models) reveal important inconsistencies when comparing films of different thicknesses. These inconsistencies would remain hidden if only films of a single thickness were analyzed. Moreover, the comparison of the shape of $J-V$ curves for different CFO thicknesses provide conclusive indications for the existence of a non-tunnel transport channel [143].

Also, the observation that the slope of the log (J_{typ}) or log (J_{avg}) versus film thickness is substantially smaller when measured using the relatively large Pt contacts points in this direction.

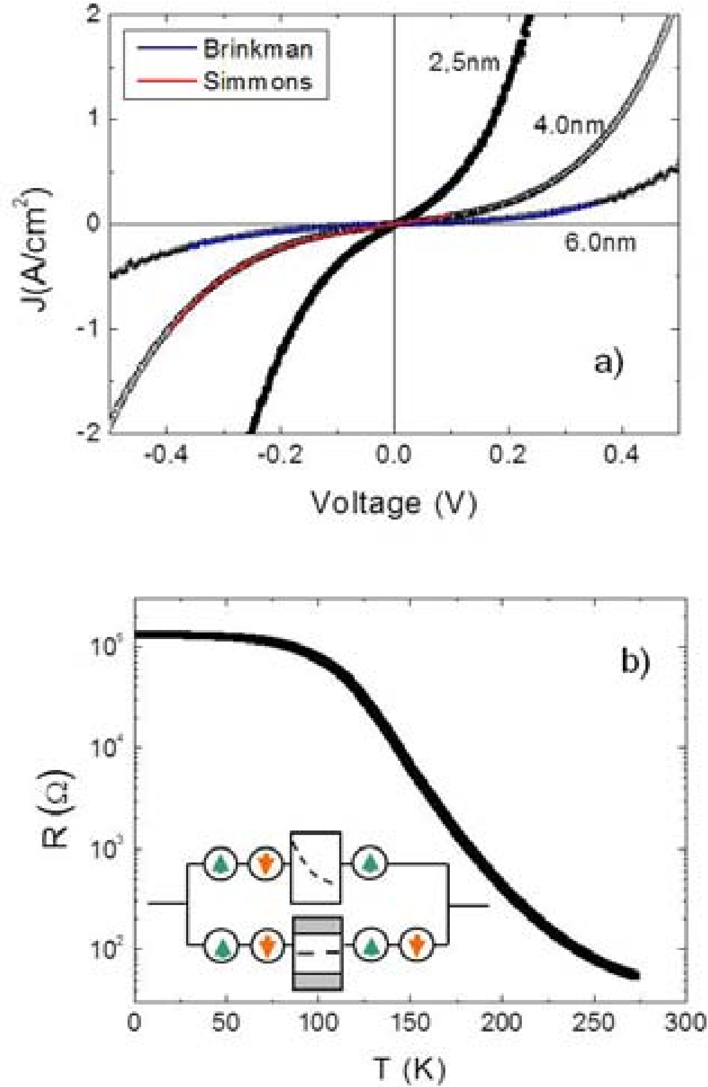

Figure 7.6: (Color online) (a) Exemplary fits of $J-V$ characteristics measured on Pt contacts on CFO/SRO/STO samples with different thicknesses, as indicated. Current density J is obtained by dividing the measured current by the Pt contact area, determined before by AFM in dynamic mode. A more detailed description of the fitting procedure and results is given in Ref. [143]. (b) Temperature dependence of the resistance of a Ag=CFO(8 nm)/SRO/STO contact prepared by optical lithography. Inset: schematic of the assumed conduction process: a channel with strongly decreasing resistance when increasing temperature in parallel to the tunneling process. Such a non-spin conserving channel can be the cause for low spin-filtering efficiency commonly observed in spinel ferrites.

Such a transport channel should also have an influence on the temperature dependent transport properties. In Fig. 7 6 b), it is shown the temperature dependence of the resistance of a Ag/CFO(8 nm)/SRO/STO junction (diameter 100 μm) prepared by a standard optical lithography process on an equivalent sample from the same series. It is observed that, below $\sim$ 100 K, the resistance varies little, as expected for electron tunneling. However, when increasing the temperature above 100 K, the resistance decreases over several orders of magnitude. This decrease can be explained by the existence of a parallel conductance channel with a strong temperature dependence, which does not contribute at low temperatures (see sketch in the inset of Fig. 7 6 b). A defect-assisted transport mechanism through the CFO layer is most likely the reason for such behavior. Qualitatively similar temperature dependencies have been observed for spin filtering CFO barriers[47 48 49] and have been related to the rapid decrease of the filtering efficiencies at elevated temperatures, since the non-tunneling conductance channel is not expected to be spin conserving.

7.4 Conclusions

It has been developed a metodology to efficiently use C-AFM to characterize tunnel transport in nanometric films.

It has been shown that in spite of data measured on CFO thin films showed the expected exponential thickness dependence of tunnel transport, indications for a non-tunnel conductance channel were found, with obvious detrimental effects on spin-polarized transport across the barrier. Although, from the present measurements, it cannot be inferred to what extent the non-tunnel transport at room-temperature stems from a relatively small energy gap in the insulator or is related to growth-induced defects in the barrier.

Chapter 8

$Pt/BaTiO_3/La_{0.7}Sr_{0.3}MnO_3$ junctions

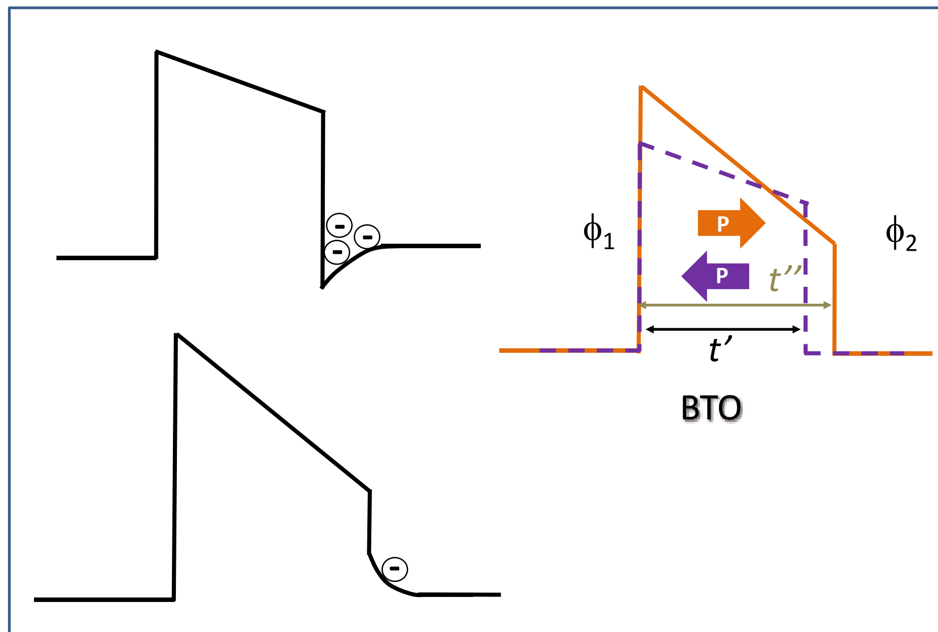

This work was done in colaboration with *Ph.D Greta Radaelli.* The details of litography process and some preliminary data and discussions are described in her tesis [144] . Part of the work discussed in this chapter is currently submitted for publication.

Abstract

The aim of this chapter is to investigate the electron transport through metal-ferroelectric-metal- juctions with ultrathin $BaTiO_3$ *barrier. Distinct to most of the earlier works, here, juctions were fabricated by optical litography method to obtain large area* $> 3\ \mu m^2$ *juctions, in order to determine the transport dependence on polarization state of the barrier. To that end, heteroepitaxial Pt* $BaTiO_3$(2-4 *nm*) $La_{0.7}Sr_{0.3}MnO_3$ *junctions have been fabricated on lattice-matched* $SrTiO_3$ *substrates. The current voltage characteristics of the juctions have been recorded at room temperature under different field-poling conditions to determine the tunnel electroresistance (TER). We have disclosed a significant change of the juction capacitance under bias and poling. The mechanism transport through these barriers are disscused.*

8.1 Introduction

Very large tunnel electroresistance (TER) were observed on $BaTiO_3$ (BTO) and $Pb_{1-x}Zr_xTiO_3$ (PZT) [75 71] ferroelectric thin films using scaning probe thechniques that allow direct correlation of the ferroelectric polarization orientation and tunnelling conductance. Functional ferroelectric tunnel junctions (FTJs) would be easier to implement in devices if top electrodes are patterned up to micro-size areas. However keeping high values of TER at room temperature and large areas still is a challenge. Here the first objetive of this chapter is to build Pt/BTO/$La_{0.7}Sr_{0.3}MnO_3$ junctions with areas from 4 to 900 μm^2 and measure its respective TER. Such areas allow to get insight view since capacitance measurements can be done. The second objective is by capacitance measurements determine whether the barrier width is preserved or not upon polarization reversal.

8.2 Device fabrication and piezoresponse

FTJs were fabricated on Pt(22 nm)/BTO(2-4 nm)/LSMO(30 nm) heterostructures grown on (001)-oriented-STO single crystal substrates. The oxide bilayers were epitaxially grown by pulsed laser deposition at ICMAB. LSMO films were deposited at 725°C in 0.2 $mbar$ oxygen pressure; Immediately after, BTO films at 700°C in 0.02 $mbar$ oxygen pressure. The growth rate, for both films, was calibrated by measuring, by X-ray Reflectivity (XRR), the thickness of some on-purpose prepared films. Laser fluence was verified to be constant for all growth processes. The metallic Pt layers were deposited on top of these bilayers ex-situ by sputtering at room temperature. The junctions were fabricated into a cross-strip geometry using photolithography and ion milling. A SiO_2 layer was deposited using sputtering to create an insulating layer to allow the fabrication of the final Au(300 nm)/Cr(7 nm) contacts, deposited by e-beam evaporation. On each sample, we have fabricated 36 junctions, with area A ranging from 4 to 900 μm^2. A schematic drawing of the FTJ structure, without showing the

SiO_2 layer, is illustrated in Fig. 8.1 a) together with an optical microscopy picture of a lithographed sample (Fig. 8.1b).

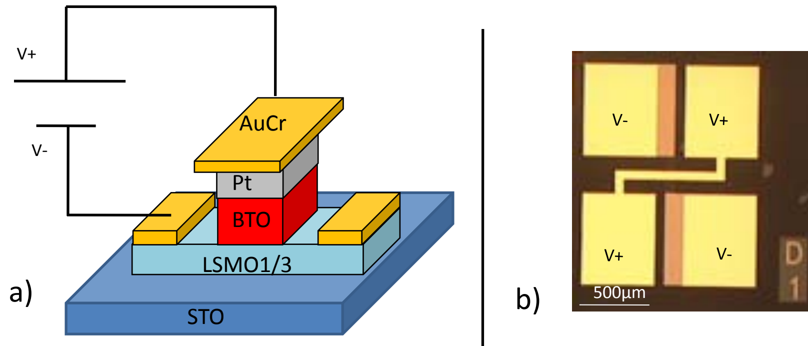

Figure 8.1: a) Sketch of the junction structure. b) Optical image (top view) of the device at the end of the litography process.

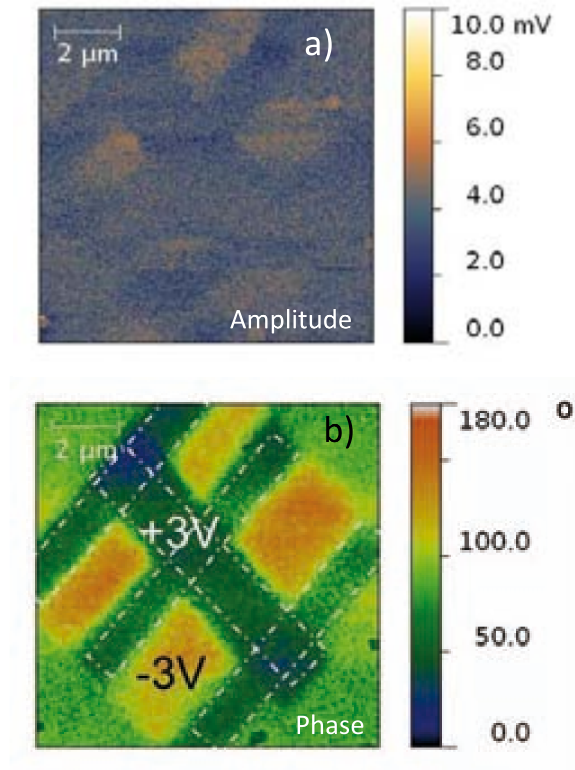

Figure 8.2: PFM image for BTO 4 *nm* shows a robust ferroelectricity.

Prior to deposition of the Pt, PFM was performed. The PFM images obtained from BTO surface (in Fig. 8 2) indicates the robust ferroelectric nature in BTO thin films. The poling voltages were +3 V and -3 V. In amplitude (Fig. 8 2 a)), the PFM image does not shown strong contrast between poled domains but in phase (Fig. 8 2 b)) the contrast between the poled domains is notable.

8.3 Transport properites at low bias

The electrical measuments were performace in two-probe geometry; top Pt electrode is biased and LSMO bottom is grounded. The ferroelectric polarization of BTO barrier was switched applying poling voltages V_{write} about 0.5 seconds duration; subsequenlty the pulse is removed and $I-V$ characteristics were performace from $-0\ 2V$ to $0\ 2V$. The TER values were obtained from the resistance at $0\ 1V$. All the measurements were obtained at room temperature. In Figs. 8 3 a) and b) it is showm illustrative $I-V$ curves obtained on junctions with BTO layers of 2 nm and 4 nm respectively, of areas A = 25 μm^2 and 60 μm^2 (denoted B5 and B2) respectively, after poling the samples with V+(orange line) and V-(violet dashed line) as indicated. The arrows in the Figs. 8 3 a) and b) indicate the direction of the written polarization in each case.

One first notice in Figs. 8 3 a) and b) that for the up-state (polarization pointing away from the LSMO bottom electrode) the conductance is larger (ON state) than for the down-state, where the polarization points towards the LSMO electrode (OFF state), as indicated in the sketches of Fig. 8 3 c). Similar measurements and results are obtained for the BTO film of 3 nm. In Fig. 8 3 d) we collect the resistance per area product ($R*A$) measured for the up- and down-states as a function of BTO film thickness. Note that $R*A$ values displayed in Fig. 8 3 d) are average values obtained considering all the measured junctions for each BTO thickness. Data in this plot shows an exponential dependence of the barrier resistance, as expected for tunnel transport, and distinctive values for up and down states illustrating the change of the energy barrier for tunneling upon polarization switching.

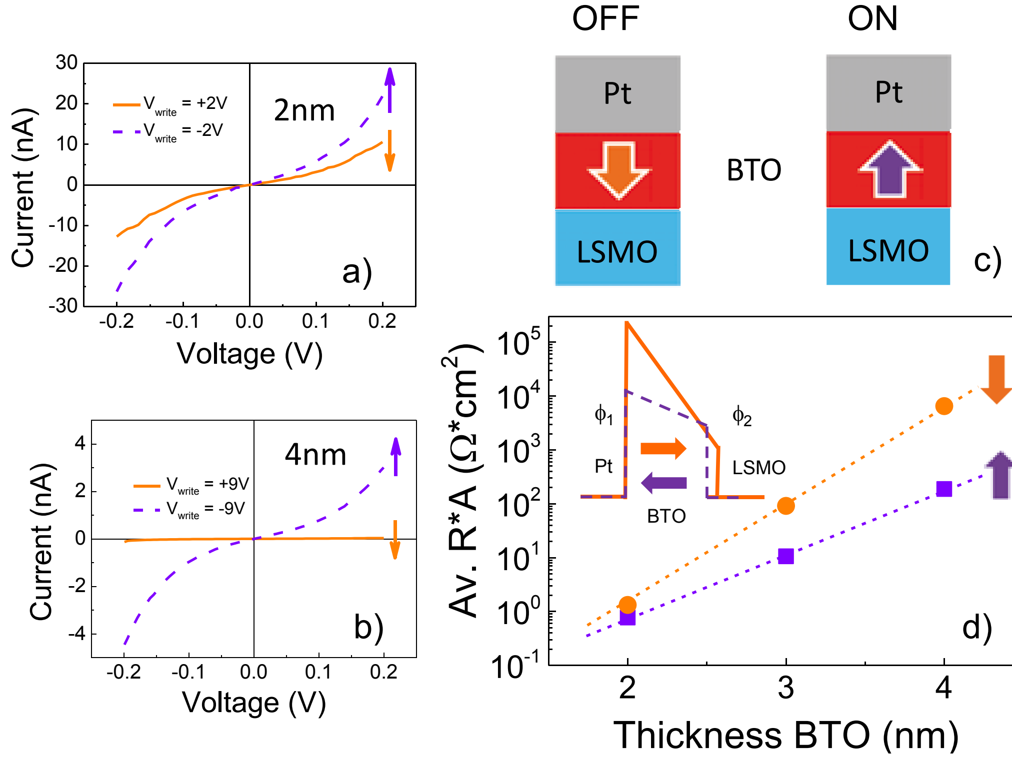

Figure 8.3: a) and b) ON and OFF room temperature $I-V$ characteristics (violet dashed and orange continuous lines, respectively) of representative Pt/BTO/LSMO FTJs with BTO thickness of 2 nm and 4 nm, and junction area A = 25 m^2 and 60 m^2 respectively. The sketch in c) illustrates the relative orientation of the polarization (arrow) of BTO in the LSMO/BTO/Pt hetetostructures at the ON and OFF states. d) Average junction resistance (at 100 mV) per area product $R*A$ as a function of BTO barrier thickness.

The $I-V$ curves of Fig. 8.3 a) and b) can be well fitted with the Brinkman model for tunnel transport across trapezoidal potential barriers in the WKB approximation[142]. For the particular case of the BTO barrier of 4 nm (data in Fig. 8.3 b) we obtain (see Supplementary material S4): $\phi_{av[ON]} = 0.48\ eV$ and $\Delta\phi_{[ON]} = 0.38\ eV$ for the ON state and $\phi_{av[OFF]} = 0.61\ eV$ and $\Delta\phi_{[ON]}$ =0.85 eV for the OFF state, where $\phi_{av[ON(OFF)]} = (\phi_{1[ON(OFF)]} + \phi_{2[ON(OFF)]})/2$ and $\Delta\phi_{av} = (\phi_{av[OFF]} - \phi_{av[ON]})$ are the average height of the barrier and its asymmetry respectively. These values are similar to earlier reports. For instance, Gruverman et al. [145] reported for a BTO barrier of 4.8 nm: $\phi_{av[ON]} = 0.72\ eV$ and , $\Delta\phi_{[ON]} = 0.48\ eV$, $\phi_{av[OFF]} = 0.88\ eV$ and$\Delta\phi_{[OFF]}$ 1.28 eV. Using our energy barrier data for a BTO barrier of 4 nm (data in Fig. 8.3 b), and a simple TER

estimate (ref.[145]):

$$TER = exp\left[\frac{\sqrt{2m}}{\hbar}\frac{(\phi_{av[OFF]} - \phi_{av[ON]})}{\sqrt{(\phi_{av[OFF]} + \phi_{av[ON]})/2}}t\right] \tag{8.1}$$

it is obtained $\approx$ 3300%. This is in agreement with direct measurements to be shown below.

Observation of ON state for polarization pointing away from the LSMO electrode in LSMO/ferroelectric layer(BTO or PZT)/metal junctions is in agreement with earlier observations [75, 77, 146, 147, 148, 73, 72, 149]. We notice however, that some few reports exist that the OFF state is obtained when the polarization points away from LSMO [71, 149, 150]. We note in passing that the observation that in the ON state the polarization is pointing away from the LSMO electrode is in streaking disagreement with what would be expected in a simple picture of a tunnel barrier where ON/OFF states are dictated by the relative direction of the polarization with respect to the asymmetric screening properties of the electrodes, if one would have assumed that the effective screening length of LSMO is larger than that of the metal electrode (Pt in the present case), i.e. δ/ϵ(LSMO) > δ/ϵ(Pt). Instead, as signaled above, most experimental results indicate the opposite. We will discuss below in more detail this issue.

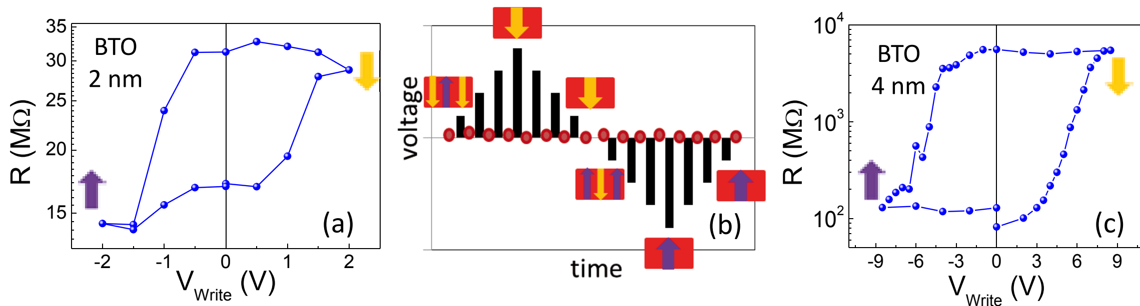

Figure 8.4: The measured poling-dependent resistance of LSMO/BTO/Pt junctions of: a) $2nm$ and c) 4 nm thick BTO barrier respectively. The sketch of the measuring protocol is shown in b).

In Figs. 8 4 a) and c) it is shown the polarization-dependent junction resistance for the same junctions (BTO barrier is 2 and 4 nm thick) as in Figs. 8 3 a) and b). In this set of experiments, consecutive poling (so-called writing pulses V$_{write}$) are applied and the junction resistance is subsequently determined by measuring $I-V$ curves and extracting the resistance at 100 mV, as indicated in the sketch in Fig. 8 4 b). Data in Fig. 8 4 a) and c) clearly show that the measured resistance follows a cycle that nicely mimics that of the ferroelectric polarization $P(V)$ (see Supplementary S1), thus fully confirming that the ON/OFF resistance values are dictated by the polarization state of the ferroelectric barrier. No significant imprint is observed. Data in Figs. 8 4 a) and c) allow a robust estimate of TER. It turns out that TER ≈ 100 % and 5x10^3 % for 2 nm and 4 nm BTO thickness, respectively. We note that direct measurement of TER for the 4 nm thick BTO junction shown in Fig. 8 4 c) (B2) is in good agreement with TER estimation obtained using eq. 8 1 from the fitting of the $I-V$ curves of the

Figure 4

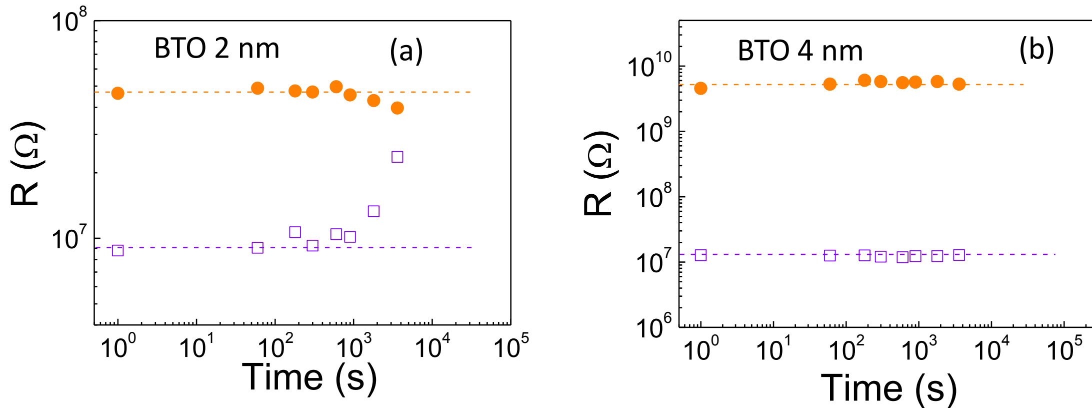

Figure 8.5: Retention of the ON and OFF states of the junctions with BTO barrier layer thickness of a) 2 nm and b) 4 nm.

In Fig. 8 6 a) it was collected TER results obtained for different junctions on the

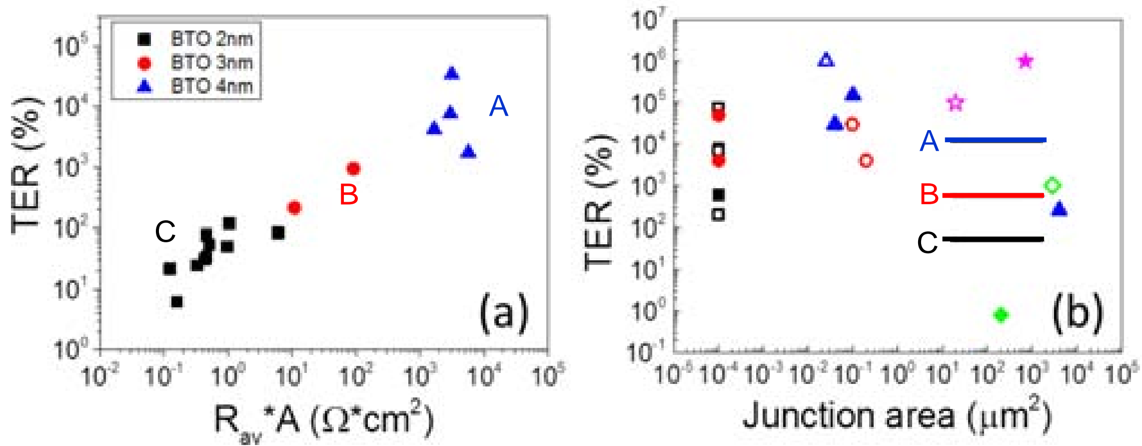

Figure 8.6: a) Dependence on the measured TER devices with thickness and area. b) Survey of room-temperature TER values reported here (A, B and C lines) with representative values reported in literature for junctions with different contact areas: BTO(2.4-4.8 nm)/SRO//STO (black full squares ■. Ref. [145]), BTO(3-2-1 nm)/LSMO//NGO (ref. [75], black empty square □), Au/Co/BTO(2 nm)/LSMO//NGO (ref. [73, 72], red empty circles ❍), Pt/BTO(4.8 nm)/SRO//DSO (ref. [76], green empty rhombus ◊), Pt/BTO/(3nm)//Nb:STO (ref. [151], pink full stars ★), Au/Co/BTO(1.6-2.8 nm)/LSMO//NGO (ref. [150], pink empty star ☆), PTO(3.6-1.6 nm)/SRO//STO (ref [152],red full circles ●), Co/PZT(9-3.2-1.5 nm)/LSMO//STO (ref. [71, 77],blue full triangles ▲), Pt/Co/BFO(4.6 nm)/CCMO (ref. [74] blue empty triangles), LSMO/BSTO(3.5 nm)/LSMO//STO (ref. [153], green full rhombus ◆).

same chip (nominally identical BTO film thickness) and different BTO thicknesses (2, 3 and 4 nm) as well as different junction areas. Data are plotted in terms of the measured $R_{av} \times A$ for each junction where A is the corresponding contact area and R_{av} the measured average($(R_{ON}+R_{OFF})/2$) resistance. Data in Fig. 8 6 a) shows that, in spite of the existence of some scattering of TER values in each chip, more pronounced in the thinnest films (2 nm), there is a clear exponential increase when increasing barrier thickness. This is in agreement with expectations based on the dominating tunnel character of the charge transport across the BTO barrier.

It is worth to compare the TER values reported here with representative data from available literature. In Fig. 8 6 b) we show a survey of TER data of ferroelectric junctions of different barrier thickness as a function of the contact area. Squares,

triangles and circles symbols correspond to data from literature obtained using FTJs including LSMO, SRO or CCMO as bottom electrode and/or BTO, PTO, PZT, BFO and BSTO as ferroelectric material. It is clear from this plot that the largest TER values are obtained using nanometric junctions most often made by using a conducting tip of an AFM microscope. The solid lines denoted by A, B and C in Fig. 8 6 b) represent the TER results presented here and show that they are record values for large junctions, at least for stacks non involving electrodes which are supposed to undergo a metal/insulator phase transition due to charge accumulation-depletion. Note that data indicated by stars refer to junctions where this kind of more complex interface-related phenomena can be involved [151 150].

Results presented so far, while providing records values for TER in large BTO junctions, indicate that there are good reasons to search towards even more efficient BTO junctions by improving materials properties. Still however, the results and their interpretation are based on the assumption of an asymmetric tunnel barrier whose height is modified by the ferroelectric polarization. However, as signaled above, the observation that the ON/OFF states are obtained for polarization directions that are just opposite to what could be expected in the, may be naif, picture of LSMO screening more poorly than Pt or other metals, indicates that the understanding of the role of the barrier and electrodes upon P reversal or under biasing is still limited. At least two ingredients should be considered. First, the previous picture assumes that the electrodes are robust metals with no significant changes of their properties upon polarization reversal. This is not the case of LSMO, which, even if optimally doped, charge depletion or accumulation at interface may lead, as indicated earlier, to a transformation into an insulating phase. Second, the standard picture also assumes that the ferroelectric barrier is a pure dielectric and the role of the Schottky barrier at metal/ferroelectric interface is neglected. Although it is unclear if these mechanisms could reverse the sign of what is ON/OFF states with respect to polarization, it is clear that they may induce variations of the barrier width.

8.4 Capacitance measurements

In the following it will be shown that upon voltage biasing, the LSMO/BTO/Pt junctions display features that indicate the presence of a semiconductor interface layer whose depletion/accumulation layer can be modulated by the applied bias and the ferroelectric polarization. As a consequence, the barrier properties, namely the barrier width is modulated, with subsequent impact on the measured TER.

In Fig. 8 7 a) and b) it is shown the specific capacitance C vs V_{bias} of two junctions (denoted B1 and B2) with 4 nm thick BTO barrier. In Fig. 8 7 a) the bias-dependence of the capacitance of a non-prepoled junction is measured at different frequencies. Data collected at different frequencies are normalized to the corresponding value at zero V_{bias}. It is observed that the capacitance is largely modified by the bias voltage. Indeed, for $V_{bias} < 0$, $C(V_{bias})$ displays a pronounced roll-off at about $V_{roll-off} \approx$ -0.4 V. At still lower (more negative) V_{bias} the capacitance develops either a plateau or recovers its initial larger value depending on the measuring frequency (high/low, respectively). This simple observation indicates that the LSMO/BTO/Pt heterostructure does not behave as expected for ideal metal-insulator-metal (M/I/M) capacitor but its response is characteristic of M/I/n-type semiconductor (n-SC) junctions. The roll-offin the $C(V_{bias})$ curve is associated to the formation of a depletion layer at the I/n-SC interface, the subsequent broadening of the dielectric layer and the accompanying reduction of the capacitance. As it is common in M/I/n-type semiconductor junctions, when measurements are performed at low frequency the capacitance recovers at lower (more negative) V_{bias} [2]. Therefore, the actual heterostructures could be viewed as a metal(Pt)/insulator/n-SC/metal(LSMO). As LSMO is a hole-type metal and BTO is commonly an n-type semiconductor, the most plausible structure compatible with the V_{bias} observed data would be: metal(Pt)/insulator (BTO)/n-type BTO /metal (LSMO).

A similar roll-off of $C(V_{bias})$ is observed in other junctions either having BTO barriers of 4 nm (another example is junction B2, shown in Fig. 8 7 b) or in junctions with

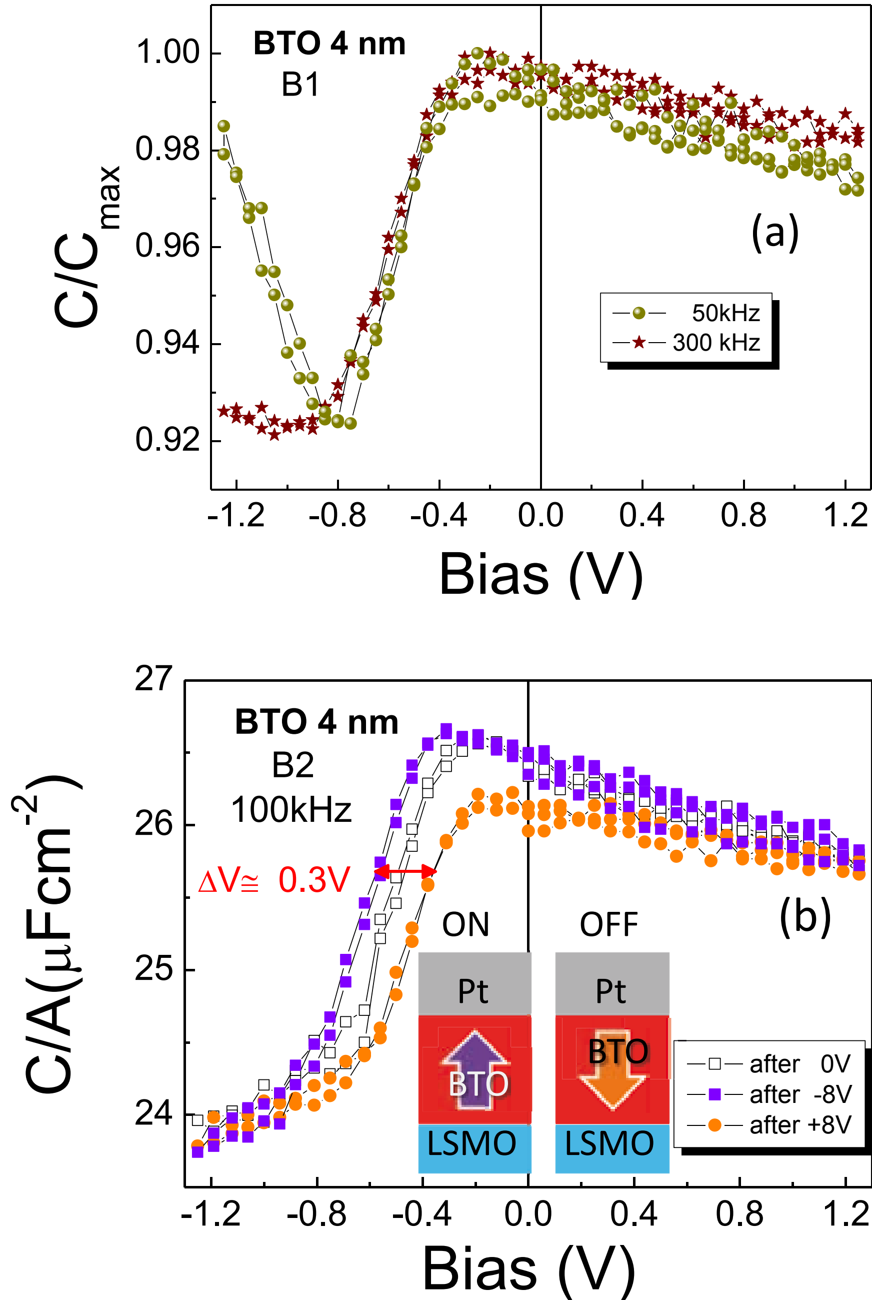

Figure 8.7: a) Differential capacitance vs V_{bias} curves of a junction (B1) on the Pt/BTO (4 nm)/LSMO heterostructure, measured at different frequencies in a non-prepoled state. b) Capacitance vs V_{bias} curves of a junction (B2) on the same Pt/BTO(4 nm)/LSMO heterostructure, measured at 100 kHz in the non-prepoled state (open symbols) and in poled-up (solid squares) and poled-down (solid circles) states.

barriers of 3 nm (see Supplementary material S3). Before proceeding it is worth to notice that the specific capacitance of a M/BTO/M capacitor is $C\ \ A \approx \epsilon_0\epsilon_r\ \ t$ where t is the thickness of a dielectric layer and ϵ_r its relative permittivity. If we use $\epsilon_r\ \approx\ 12$ and $t = 4\ nm$ (the BTO thickness of this junction) one gets: $C \approx 13.3\ \mu F\ \ cm^2$ which is comparable to the measured value ($C \approx 26\ \mu F\ \ cm^2$). As the actual value of the permittivity in this ultrathin layer is unknown, one cannot safely further elaborate on this difference of C s. However, the observation of a larger capacitance would be fully compatible with the presence of a degenerated n-type region of the BTO layer which is driven to accumulation for $V_{bias}\ \ > 0$. At the depletion state, the capacitance is reduced by about $\Delta(C\ \ A) \approx 2\ \mu F\ \ cm^2$, which for a barrier of $t \approx 4\ nm$ and $\epsilon_r = 60$ as above, leads to a depletion layer $W \approx \Delta(C\ \ A) * t^2\ \ (\epsilon_0\epsilon_r) \approx 0.6\ nm$.

In passing we note that for this junction, capacitance vs voltage measurements gave a doping of about $N_n \approx 4{\times}10^{21}\ cm^{-3}$ (see below and Supplementary information S3). According to experimental results on n-doped BTO single crystals, metallic behavior is obtained for $n > n_c \approx 1.0{\times}10^{20}\ cm^{-3}$ (ref. [154]) and ferroelectricity persists up to $\approx 2 \times 10^{21}\ cm^{-3}$ (ref. [155]) . Owing to the number of unknown parameters entering in the estimation of N_n (effective permittivity, etc) (see supplementary information S3), we conclude that the estimate of $N_n \approx 4 \times 10^{21}\ cm^{-3}$ is reasonable. This leads to a Debye screening length $L_D = \ \ \overline{\epsilon_0\epsilon k_B T\ \ (q^2 N_n)} \approx 0.14\ nm$ which is shorter than the estimated depletion width W ($\approx 0.6\ nm$), thus showing the consistency ($W > L_D$) of the evaluated data.

In Fig. 8 7 b) we show the $C(V_{bias})$ curves of a junction in the non-prepoled state (open symbols) and after poling with either a negative pulse ($V_{write} < 0$; violet solid squares) or with a positive pulse ($V_{write} > 0$; orange solid circles). As shown by data in Fig. 8 7 b) the capacitance in the depletion region ($V < V_{roll-off} \approx$ -0.4 V) depends on the polarization state of BTO. This indicates that the extent of the depletion layer varies with polarization and $C(V_{bias}\ \ P_{up}) > C_0(V_{bias}) > C(V_{bias}\ \ P_{down})$, where C_0 is the capacitance measured in the non-prepoled state. As in Fig. 8 7 b) no significant imprint was observed, it can be assumed that up and down ferroelectric domains under

the electrode produce a vanishing net polarization in the non-prepoled state. Therefore, $C_0(V_{bias}) \approx C_0(V_{bias}\ P \approx\ 0)$. No polarization dependence of the capacitance, i.e. $C(V_{bias}\ P_{up}) \approx C(V_{bias}\ P_{down})$, is visible in the accumulation state. This is fully expected in the accumulation regime as C is almost insensitive to V_{bias}.

Of the highest relevance for TER is the observation that $C(V_{roll-off}\ P_{up}) > C(V_{roll-off}\ P_{down})$, as this implies that the width of the dielectric layer for charge tunneling varies with P. From data in Fig. 8 7 b), the observed change of capacitance $\Delta C(P) = C(V_{roll-off}\ P_{up})$-$C(V_{roll-off}\ P_{down})$ in the depletion region is of about $1\mu F\ cm^2$. Using the same value of permittivity for BTO as above ($\epsilon \approx 60$), this change $\Delta C(P)$ indicates a depletion width variation upon P switching of about $\Delta W(P) \approx \Delta C(P) * t_{BTO}^2\ (\epsilon_0\epsilon_r) \approx 0.3\ nm$. Inserting this variation in the simplest TER expression of eq. [8 1], and using the same $\bar{\theta}_{av} = (\theta_{av(ON)} + \theta_{av(OFF)})/2$ and $\Delta\bar{\theta}_{av} = (\theta_{av(OFF)}$ - $\theta_{av(ON)})$ values (0.545 eV and 0.13 eV, respectively) as derived from the WKB fits of the $I - V$ curves, we obtain a relative variation of TER by about 25%, associated to the change of barrier width.

It would be tempting to use the $I - V$ data and its fit to the WKB model to explore if the corresponding barrier width in the ON and OFF states differ by about W. Unfortunately, although fits are still excellent when the barrier width is allowed to vary the set of fitting parameters is very broad so leading unreliable any further discussion(see Supplementary Information S4).

Finally, we note that whereas $V_{roll-off}$ in M/I/SC junctions is related to the built-in potential at the interface [2], the shift of the $V_{roll-off}$ upon polarization reversal should be related to the change of the Schottky barrier at the Pt/BTO interface upon switching of the polarization charges in the ferroelectric. Using $\Delta P \approx C \times \Delta V_{roll-off}$ [156], where C is the specific capacitance, $\Delta P \approx 0.3\ V \times 26\mu F\ cm^2 = 7.8\ \mu C\ cm^2$ which is the right order of magnitude for ultrathin BTO films. Alternatively, the overall SB shift when metal-ferroelectric junctions are switched up/down can be explicitly estimated using the models developed by Pintilie et al. [157] . It this case, $\Delta V_{roll-off} \approx \Delta\theta_{SB} = 2\ \overline{qP\ (4\pi\epsilon_0^2\epsilon_{opt}\epsilon_r)}$ where ϵ_{opt} is the high frequency dielectric constant ($\approx$ 5.4, ref.

[158]), q the elementary charge, ϵ_r, as above, is taken ≈ 60, and P is the switchable polarization. It turns out that $P \approx 4\ \mu C\ \ cm^2$, which is of the right order of magnitude. We note in passing that our measured change of Schottky barrier $\Delta\theta_{SB} \approx 0.3\ eV$ upon P reversal is somewhat smaller than that experimentally determined ($\sim\ 0\ 6-0\ 65eV$) by photoemission experiments in Pt/BTO junctions [158 159] . This difference may simply results from a smaller switchable polarization in these ultrathin BTO films (4 nm) compared with the 64 nm BTO films of ref. [158] . Anyhow all $\Delta\theta_{SB}$ reported experimental values are much larger than those predicted for ideal Pt/BaO interfaces in Pt/BTO ($\approx 30\ meV$) although it has been recognized that imperfect screening may lead to larger $\Delta\theta_{SB}$ variations .

In the depletion region ($V\ < 0$) the slope of the $1\ \ C^2$ vs V can be used to estimate the free carrier density in the n-type region and the build-in interface potential. As already suggested by data in Fig. 8 7 b), the slope of $1\ \ C^2$ vs V is different for P_{up} and P_{down} (see Supplementary information S3). Using $n = 2\ \ [q\epsilon_0\epsilon_{st}[\ \ (1\ \ C^2)\ \ \ (V)]$ (ref. [134]) it is estimated a change of carrier concentration upon P reversal of about $\Delta n\ \ 8\ 46 \times 10^{20} cm^{-3}$. This difference of Δn corresponds to the charge compensating P (ref. [160]), i.e. $2P \approx \Delta n \times t_{sc}$, where t_{sc} is the width of the semiconducting n-type BTO: $t_{sc}\ \approx\ W$ ($\approx 0.\ \ 6\ nm$) $<< 4\ nm$. Taking $t_{sc} \approx 1\ nm$, one gets: $P \approx 13$ $\mu C\ \ cm^2$. Again, polarization value is fully consistent with the estimates made above and comparable to the expected polarization of a BTO film.

In brief, data in Figs. 8 7 clearly show that the Pt/BTO/LSMO hetetostructure has to be viewed as a metal(Pt)/insulator (BTO)/n-type BTO /metal (LSMO) whose depletion layer is modulated by the polarization of the ferroelectric layer. It thus follow that the switching of the polarization has the dual effect of varying the tunnel barrier height and its depleted length, and consequently, the total tunnel barrier width. In Fig. 8 8 we sketch our view of the actual situation.

In Figs. 8 8 a) and b) the electron accumulation and the edges of depletion regions, respectively, are indicated. It is clear from this sketch that the capacitance is reduced in the depletion region ($V_{bias} < 0$) which is in agreement with experiments. In Figs

8 8 c) and d) we sketch the situation that is expected to occur when the polarization of the BTO, both in its insulating and n-type regions, is included and reversed. The capacitance when the polarization is pointing towards LSMO is smaller than when it is pointing away from LSMO. This is in agreement with the experimental data in Fig 8 7. According to the estimates obtained here from polarization-dependent $I - V$ curves and capacitance data: $\bar{\theta}_{av}$ and $\bar{\Delta}\theta_{av}$ values (0.545 eV and 0.13 eV, respectively) and t_{BTO} and $\Delta W(P)$ (4 nm and 0.3 nm, respectively), the width variation of the barrier accounts for up to 25% modulation of the TER signal.

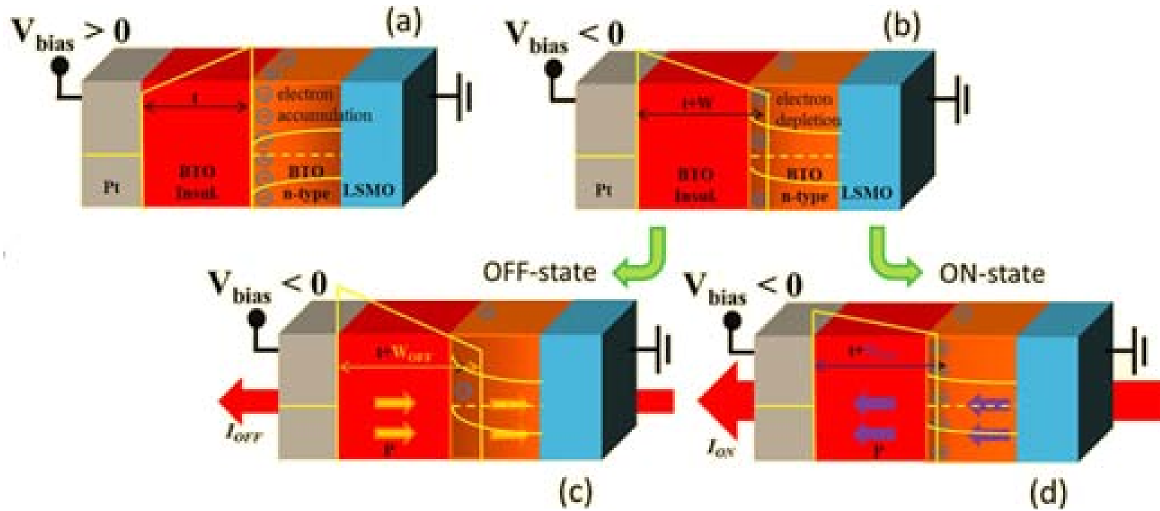

Figure 8.8: Schematic representation of Pt/BTO/LSMO Tjs and their energy band diagrams. a) and b): accumulation ($V_{bias} > 0$) and depletion ($V_{bias} < 0$) regions, respectively in the non-prepoled state. The extention of the depletion region, at negative external bias is controlled by the direction of the ferroelectric polarization, which yields either an increase c) or decrease d) of the width of the depletion region; the initial position of the depletion edge is indicated for reference (black arrow).

8.5 Conclusions

It has been shown that using appropriate growth conditions, Pt/BTO/LSMO tunnel junctions can be fabricated, by standard optical lithography techniques, displaying record room- temperature TER values reaching about 30000 % for 80 μm^2 juction size. By itself this record value is a hallmark that indicates that there is much room

for TER improvement in simple Pt/BTO/LSMO heterostructures. Moreover, we have shown that a proper description of the Pt/BTO/LSMO heterostructures shall include explicitly the presence of an n-type semiconducting region. Most likely, this should be related to a semiconducting BTO region. Importantly, upon biasing, the n-type region is driven to accumulation or depletion regimes with subsequent changes of the effective barrier width for tunnel transport across the junction. It has been seen that upon polarization reversal, not only the height but also the width of the dielectric barrier is modified, both contributing to the measured TER. As width of the depletion layer is controlled by both the doping level of the ferroelectric layer as well as by the Schottky barrier height, it is to be expected that there is much room for improvement of the relative change of both barrier height and width upon polarization reversal. On the other hand, it has been shown that measurements of capacitance in tunnel junctions have provided valuable information on the effective width of the tunnel junctions; probably, these results should stimulate a detailed revision of our understanding of ferroelectric tunnel junctions, and may be provide some clues for the understanding of the relationship between ON/OFF states and the relative direction of polarization with respect to the distinct electrodes.

Chapter 9

Pt/$La_{0\,5}A_{0\,5}MnO_3$/$BaTiO_3$/ $La_{0\,7}Sr_{0\,3}MnO_3$ junctions

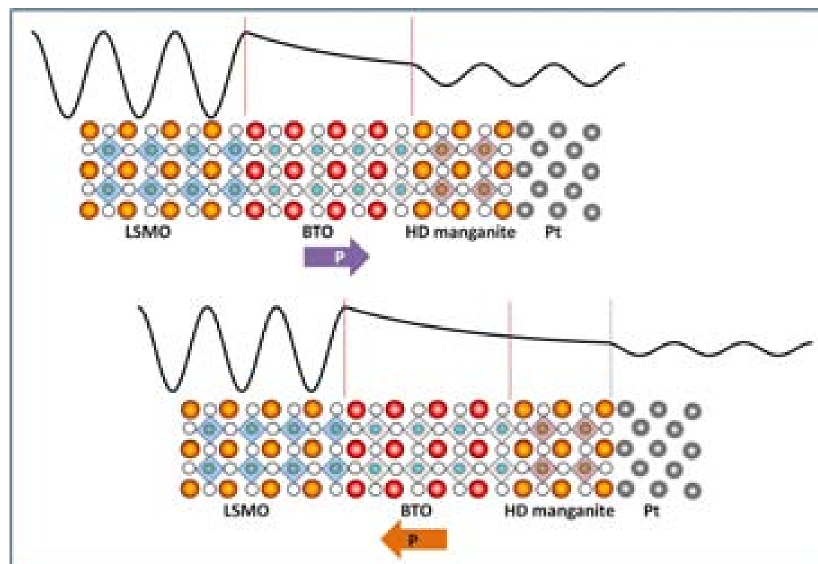

This work was done in colaboration with *Ph.D Greta Radaelli.* The litography process is described more in detail in her tesis [144].

Abstract

Recently, there have been efforts towards manipulating magnetization by electric fields. The incorporation of ferroelectric materials is specially helpful in this regard because their switchable polarization can induce a large magnetoelectric response at the interface with a magnetic material, specially with materials close to a magnetic phase transition. It has been shown that the electrical (and magnetic) character of $La_{0.5}A_{0.5}MnO_3$ (with A = Sr or Ca) is tunable. In this work we explore how the incorporation of ultrathin layer of $La_{0.5}A_{0.5}MnO_3$ beside of ferroelectric $BaTiO_3$ tunnel barrier affects the tunnel electroresistance (TER). Here, we present preliminary results on the transport properties upon polarization reversal.

9.1 Introduction

As tunnelling current is sensitive to electronic properties of the ferroelectric/electrode interfaces in FTJs, the electrode material can be specifically chosen to exhibit large modification of its electronic properties with the electric field provided by the ferroelectric as shown by Yin *et al* [85] and Jiang *et al* [147]. The objective of this study is to find out how a thin layer of $La_{0.5}Sr_{0.5}MnO_3$ or $La_{0.5}Ca_{0.5}MnO_3$ (HD) behaves when incorporated in BTO-based FTJs and if this could result in an increase in TER. $I-V$ curves at low bias will allow to determine the TER values in each samples. Temperature dependence of the resistance will be useful to determine if the transport is dominated by tunneling. Although the study is not yet fully accomplished some preliminary conclusions are drawn.

9.2 Description of the stacking

FTJs were fabricated on Pt (22 nm)/LSMO5(1-2 nm)/BTO(2-3 nm)/LSMO(30 nm), where LSMO5 stays for $La_{0.5}Sr_{0.5}MnO_3$, and Pt (22 nm)/LCMO5(1-2 nm)/BTO(2-3 nm)/LSMO(30 nm), where LCMO5 stays for $La_{0.5}Ca_{0.5}Mn_3$. Both type of FTJs where grown (001) oriented STO and $LaAlO_3$ (LAO) single crystal substrates. The oxide hetereostructure were epitaxially grown by PLD at ICMAB. HD films were deposited using the same conditions as mention in chapter 5. The BTO and LSMO(30 nm) were deposited with the same condition as metion in section 8. Samples were grown combining BTO barrier layer thickness 2 nm and 3 nm, LSMO5(or LCMO5) with thickness 1 and 2 nm, and STO or LAO substrates (see Fig. 9 1 a)).

Pt layer was deposited $ex-situ$ at room temperature by sputtering. After deposition of the stack, micrometric tunnel junctions, with areas from 4 μm^2 to 100 μm^2, were fabricated at LNESS using optical litography. An sketch of the staking and TFJ geometry is shown in Fig. 9 1 b) and c). Some of the samples could not be measured because the litography process was not succesful in all of them.

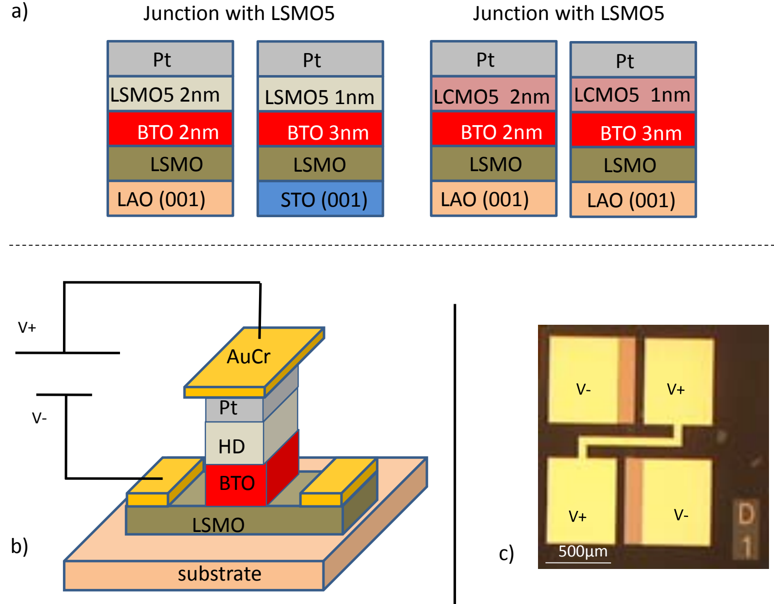

Figure 9.1: a) Sketch of the twelve samples grown for the fabrication of engineered interfaces FTJs. The heterostructures combine BTO thickness 2 nm and 3 nm, LSMO5 (LCMO5) thickness 1 nm and 2 nm, and STO and LAO substrates. b) A schematic diagram of the FTJ device geometry integrating HD manganite layers.c) Top view of the device.

9.3 TER measurements

The electrical measurements of the junctions were performed as in the case of Pt/BTO/LSMO junctions in section 8, in two probe geometry. the top electroded is biased. The ferroelectric polarization of BTO barrier was switched applying poling voltages V_{write} about 0.5 seconds duration; subsequenlty the pulse is removed and $I-V$ characteristics were performace from $-0\ 2V$ to $0\ 2V$. Below it is shown only preliminary results obtained at rooom temperature on the aviable Pt/HD/BTO/LSMO junctions.

$I-V$ curves of Pt/LSMO5/BTO/LSMO//LAO junctions were collected upon polarizing BTO barrier layer with positive or negative V_{write} pulses, corresponding to ferroelectric polarization of BTO P_{down} or P_{up} respectively. Fig. 9 2 a) shows $I-V$ curves in P_{up} and P_{down} states (violet and orange lines, respectively) of a representative FTJ with BTO ferroelectric barrier layer thickness 2 nm and LSMO5 thickness 2 nm. $I-V$ characteristics are highly nonlinear, as expected for tunneling transport regime,

and also clearly shows that the resistance of these junctions depend on the direction of the polarization. Positive pulses set the device to the high-resistance (OFF) state by driving the polarization to point to the LSMO bottom electrode, whereas negative

On LAO

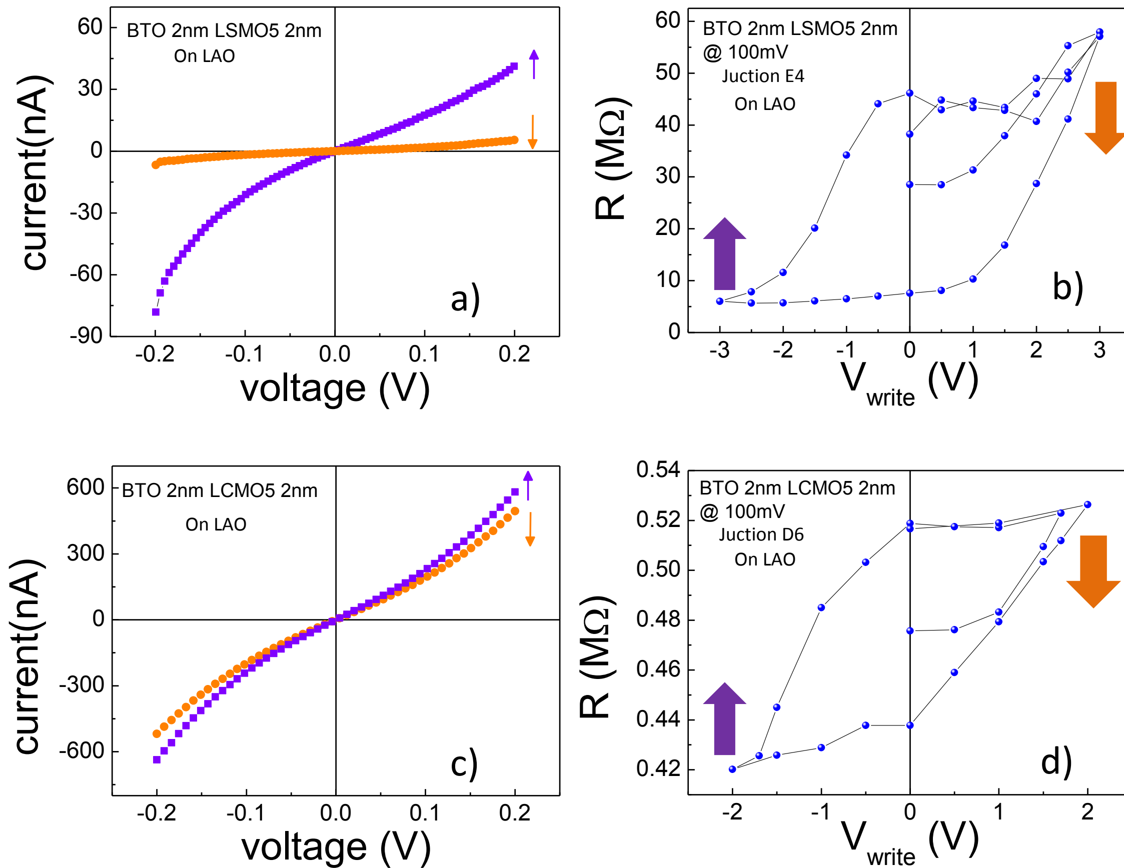

Figure 9.2: (a) ON and OFF room temperature $I-V$ curves (violet and orange lines, respectively) of a Pt/LSMO5/BTO/LSMO FTJ (shown in the inset) grown on LAO(001) substrate with BTO thickness 2 nm, LSMO5 thickness 2 nm and junction area $A = 8\ \mu m^2$. (b) Resistance hysteresis loop measured the same junction Pt/LSMO5/BTO/LSMO shown in a). c) ON and OFF room temperature $I-V$ curves (violet and orange lines, respectively) of a Pt/LCMO5/BTO/LSMO FTJ (shown in the inset) grown on LAO(001) substrate with BTO thickness 2 nm, LCMO5 thickness 2 nm and junction area $A = 60\ \mu m^2$. (d) Resistance hysteresis loop measured the same junction Pt/LCMO5/BTO/LSMO shown in c).

The same measurements were performed for Pt/LCMO5/BTO/LSMO FTJs grown on LAO substrates. Fig. 9 2 c) shows $I-V$ curves in P_{up} and P_{down} states (violet and

O5 1nm, BTO 3nm,
unction D1 (16µm²)

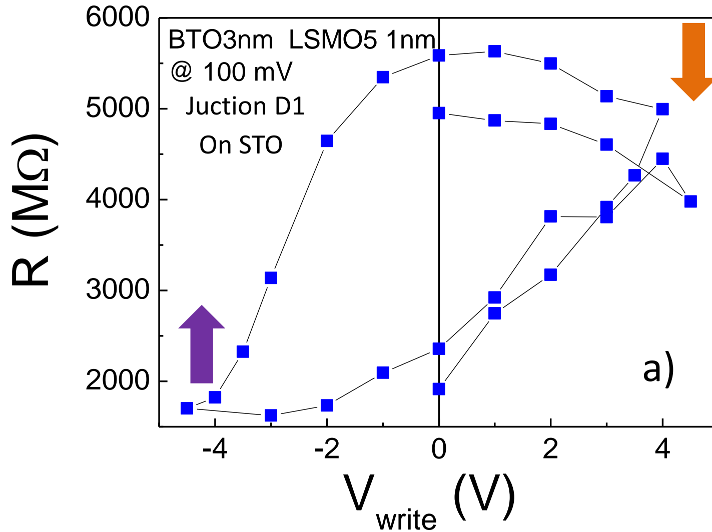

O 1nm, BTO 3nm,
nction F5 (80µm²)

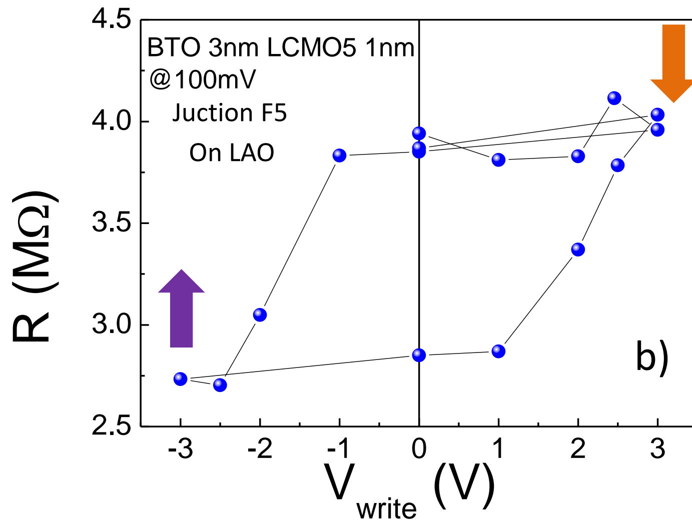

Figure 9.3: a) Resistance hysteresis loop measured in Pt/LSMO5((1 nm)/BTO(3 nm)/LSMO on STO. b) Resistance hysteresis loop measured in Pt/LCMO5(1 nm)/BTO(3 nm)/LSMO on LAO.

orange lines, respectively) of a representative FTJ with BTO ferroelectric barrier layer thickness 2 nm and LSMO5 thickness 2 nm. Fig. 9 2 d) shows a hysteretic resistance loops in this latter sample. The off states for both samples is with the P_{down} while ON state is P_{up}, similar to the results obtained in section 8. TER values obtained from the Figs. 9 2 b) and d) presents TER values of 500% and 23% respectively.

The Fig. 9 3 shows the resistance hysteresis loops of two different layers; the BTO thickness is 3 nm in both layers. for sample in Fig. 9 3 a) the HD consist on LSMO5

of 1 nm and using STO as a substrate while in Fig. b) HD consist on LCMO5 1 nm and using LAO as a substrate. In Fig. 9 3 a) the TER value is 150%, while in Fig. 9 3 b) the TER is 35%.

The specific resistance in sample BTO ($2nm$)/LCMO5 ($2nm$) on LAO in OFF states is $31M\Omega\mu m^2$ while for sample BTO ($3nm$)/LCMO5 ($1nm$) on LAO is $300M\Omega\mu m^2$. In both samples the total thickness is $4nm$. The increase in a factor 10 when the BTO increase $1nm$ indicates that the total resistance is given mainly by BTO layer.

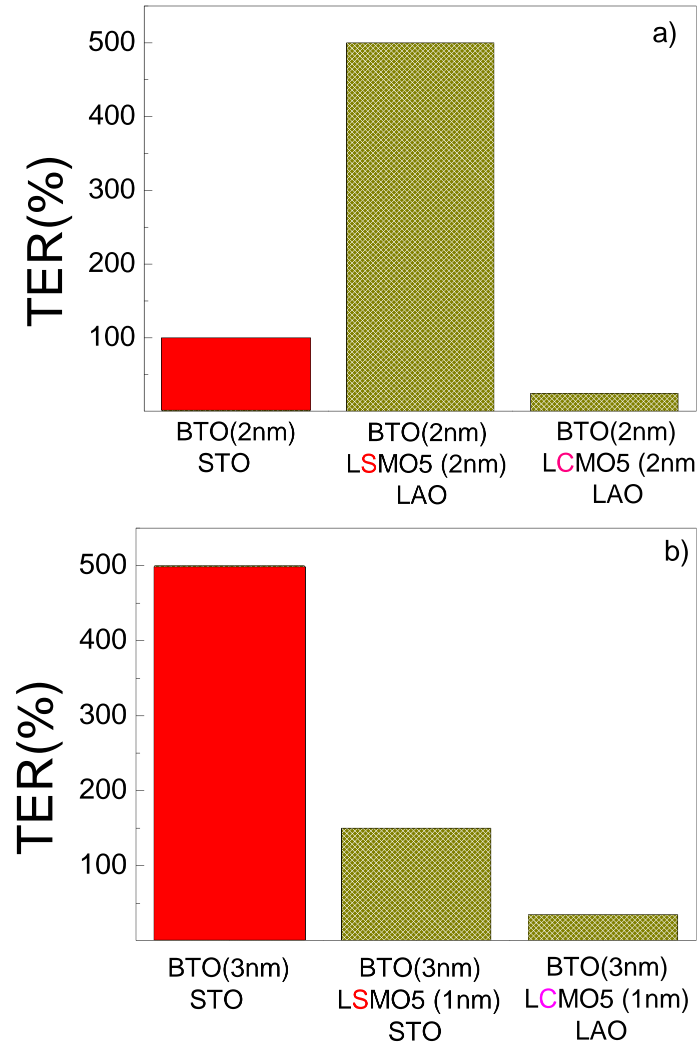

Figure 9.4: Comparison of the TER values in Bare BTO and BTO/La$_{0.5}$A$_{0.5}$MnO$_3$, a) for BTO thickness 2 nm and b) for BTO thickness 3 nm.

Now a comparison between the TER values obtained in chapter 8 and the TER values shown in Figs. 9 2 and 9 3 can be done. Fig. 9 4 a) compares the values obtained in bare BTO of 2 *nm* and TER values of samples with BTO (2 *nm*)/$La_{0.5}A_{0.5}MnO_3$(2 *nm*) while Fig. 9 4 b) compares the TER values corresponding to BTO 3 *nm*. Here the sample using LSMO5 (2 *nm*) on LAO as a substrate overcomes the TER values in bare BTO (2 *nm*). However in the case of BTO (3 *nm*) the samples with half-doped manganite does not overcome the values of the bare BTO (3 *nm*).

9.4 Low temperature measurements

Resistance vs temperature measurements (R vs T) was performanced in the sample BTO(3*nm*)/LCMO5(1*nm*) on LAO. The measurement was done in DC mode. A current of 2 nA was keep constant and the limit bias was $5V$. In Fig. 9 5 it can be noticed that the resistance increases when temperature decreases. From 300 K to 90 K the

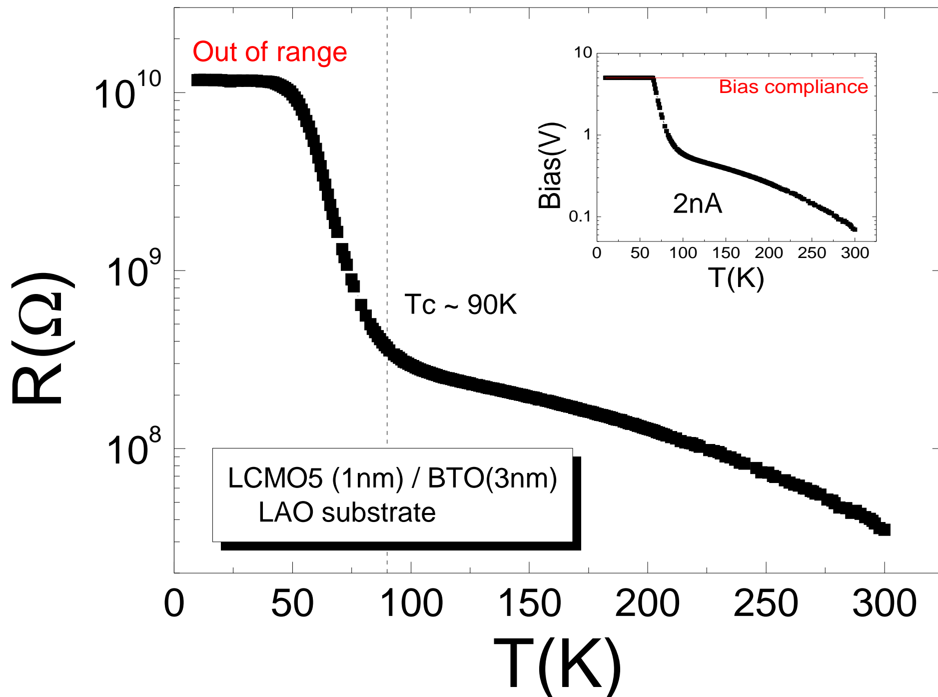

Figure 9.5: Resistance vs Temperature in Pt/LCMO5(1 *nm*)/BTO(3 *nm*)/LSMO on LAO in Juction F5.

resistance increses almost one order of magnitude, however, below 90 K the resistance experienced a big change. Such tempearuture variation between 300 K and 90 K suggest that in addition to the direct tunneling, a thermal activated transport occurs in parallel as reported by Yin *et al* [85]. Nevertheless the jump in resistance at $\sim 90\ K$ seems associated more probably to a transition.

Complementary $I - V$ curves at low temperature were performed. The results are shown in the Figs. 9 6 a) and b). $I - V$ curves from $-0\ 5\ V$ to $0\ 5\ V$ after a pulse of $+3$ and $-3\ V$ at 50 K present only for negative voltage read out difference in the conductivities but for positive voltage read out there is not difference (Figs. 9 6 a) and c)). However at 240 K (Fig. 9 6 b)) the conductivity increases either for positive or negative prepulse in comparison with the $I - V$ at 50 K. It is interesting to note that at 240 K TER increases with bias (Fig. 9 6 d)).

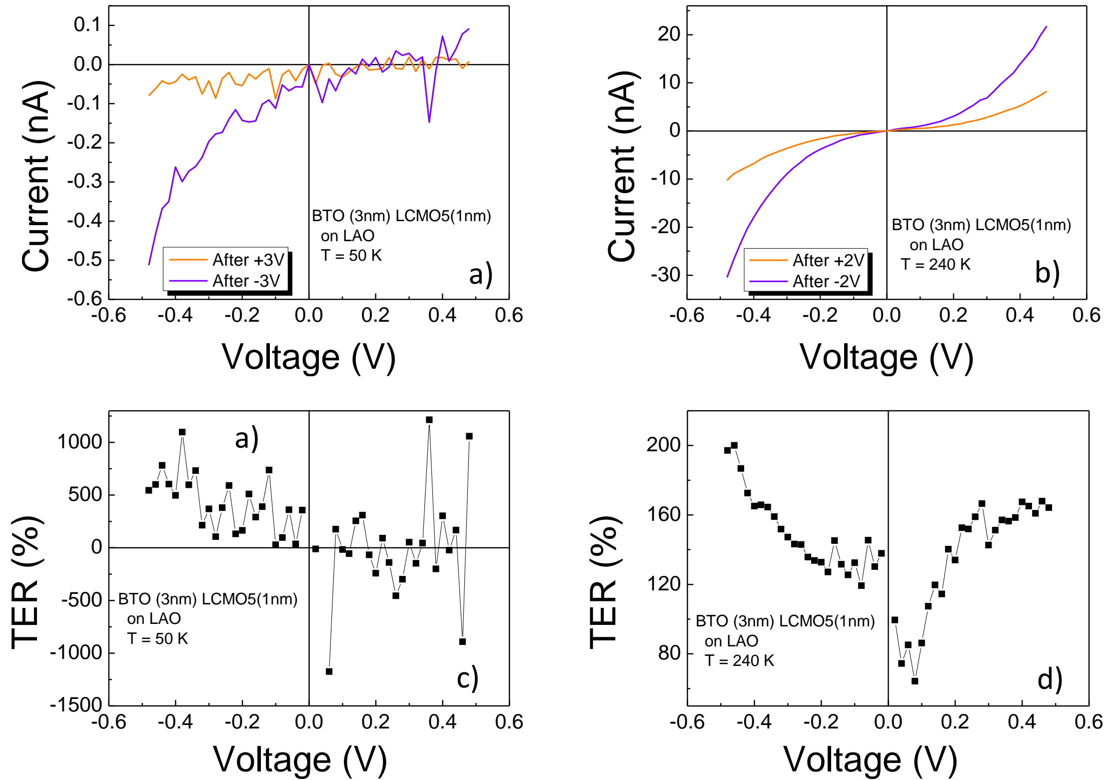

Figure 9.6: $I - V$ curves after a bias pulse in juction F5. a) at 50 and writing pulses of $+3\ V$ and $-\ 3V$. b)at 240 and writing pulses of $+2\ V$ and $-\ 2V$.

9.5 Preliminary conclusions

TER at room temperature has been measured in Pt/HD/BTO/LSMO/LAO and Pt/HD/BTO/LSMO/STO tunnel juctions. It has been observed that for some particular juctions [Pt/LSMO5(2 nm)/BTO(2 nm)/LSMO/LAO juction A3] the TER value exceed by a factor five the TER value measured in bare BTO (2 nm) (chapter 8) although the physics behind has not been clarified.

Part VI

General conclusions

General Conclusions

This thesis was developed to investigate the dielectric, transport and magnetic properties of some spinel and perovskite oxides which are $CoFe_2O_4$, $BaTiO_3$, $La_{0.5}Sr_{0.5}MnO_3$ and $La_{0.5}Ca_{0.5}MnO_3$. From one side, the materials were studied in a scale where strain can modify notably the known properties in bulk; on the other hand, it was also studied the electrical transport in films where the ferroic order afects the electrical response.

It was found that strain afects the properties of $CoFe_2O_4$ and $La_{0.5}A_{0.5}MnO_3$ (A = Sr, Ca) as explained below:

I-A It has observed that $CoFe_2O_4$ permitivity is largely reduced when increasing the in-plane compresive strain. From the structural data it was also observed that $CoFe_2O_4$ unit cell volume is reduced under compresive epitaxial strain. The reduction of the permitivity due to a reduction of the unit cell volume has been verfied by first principle calculations although the experimental observed reduction is found to be larger than predicted.

I-B $La_{0.5}Sr_{0.5}MnO_3$ films present magnetic and electric properties that largely depend on its strain state. For compresive strain an antiferromagnetism and insulating behavior has been observed while in the tensile strain a predominant antiferromagnetims but metallic state it was obtained. Quase-free strain films present robust ferromagnetic behavior and the highest metallicity.

I-C $La_{0.5}Ca_{0.5}MnO_3$ presents and insulating behavior either for compresive or tensile strain. The magnetoresistance measurements indicates that the nature of the insualting state under tensile strain is different than under compresive strain.

Regarding to photoinduced effects on $BaTiO_3$ it can be conclude that:

II-A $BaTiO_3$ films present a reduction of polarization under short wavelenght radiation (405 nm) in top-top geometry. Photocurrent has also been observed in this geometry. However in top-bottom geometry, when the imprint is present, the polarization is independent of short wavelenght radiation.

II-B The $I - V$ in top-bottom geometry in these films indicates that a rectifying behavior is be found. It was observed that the rectifying behavior can be modulated either by a polarization or by light.

In relation to the electrical transport throught $BaTiO_3$-based devices and $CoFe_2O_4$ it can be conclude that:

III-A In $Pt/BaTiO_3/La_{0.7}Sr_{0.3}MnO_3$ ferroelectric tunnel juctions display two remanent resistance states that can be controlled electrically by switching the ferroelectric polarization direction in the $BaTiO_3$ barrier. Despite these large area devices, transport at room temperature is dominated by tunneling. Tunnel electroresistace increases with barrier thickness and can reach a value of $3 \times 10^4\%$. Capacitance vs bias measurements in these junctions present similarities with the capacitance measured in metal-oxide-semiconductor (MOS). This observation suggests that in addition to the $BaTiO_3$ ferroelectric layer, a semiconducting n-type region exists and whose extention is modulated by the polarization. We have argue that this n-type region can be lead to accumulation or depletion regime with appropiate bias, and such variation upon polarization reversal can affect notably the TER measurements.

III-B In Pt/$La_{0.5}A_{0.5}MnO_3$/$BaTiO_3$/$La_{0.7}Sr_{0.3}MnO_3$ junctions (with ferroelectric and half-doped manganite) has been preliminary characterized. Two remanent resistance state have been obtained at room temperature. The values of tunnel electroresistance can exceed the values obtained when using of bare $BaTiO_3$ films as tunnel barrier.

III-C We have proposed a methodology to measure and analyze $I-V$ curves collected by using CAFM and to determine whether the transport is dominated by tunnel or not. Indications of non-tunnel transport through $CoFe_2O_4$ at room temperature has been obtained and it is suggested that this channel will be the responsable for the low spin filter efficiency observed at this temperature.

Supplementary information

Supplementary material 1: PFM characterization

S.1.1
Supplementary material 1: PFM characterization

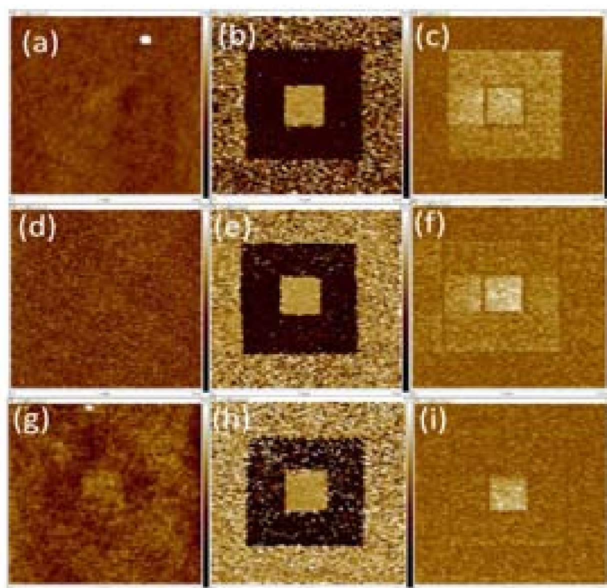

Figure S1-1: Demonstration of ferroelectricity of BTO ultrathin films (2, 3 and 4 nm thick) grown on top of a 30 nm thick LSMO electrode. (a,d,g) Topography (5 x 5 μm^2) and, (b-c,e-f, h-i) PFM out-of-plane (OOP) phase and amplitude images after writing a 3 x 3 μm^2 dark square with +3.5 V, and a 1 x 1 μm^2 white square with -3 V subsequently on top of that, for a 2 nm, 3 nm and 4 nm thick BTO film.

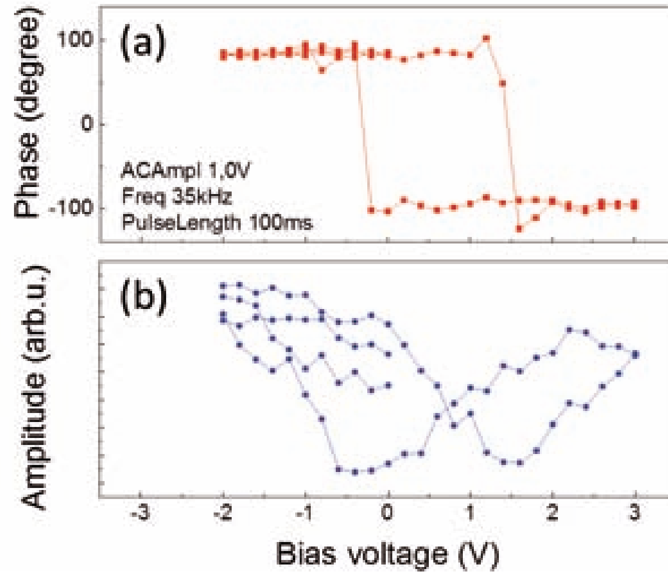

Figure S1-2: Local PFM hysteresis loops measured in the 4 *nm* thick BTO film (a) phase signal; b) amplitude signal

Supplementary material 2: maximum measured TER

Data in Figure S2-1 show the measured poling-dependent resistance of LSMO/BTO(4 *nm*)/Pt junction A2 (area 80 μm^2) following a cycle that nicely mimics that of the

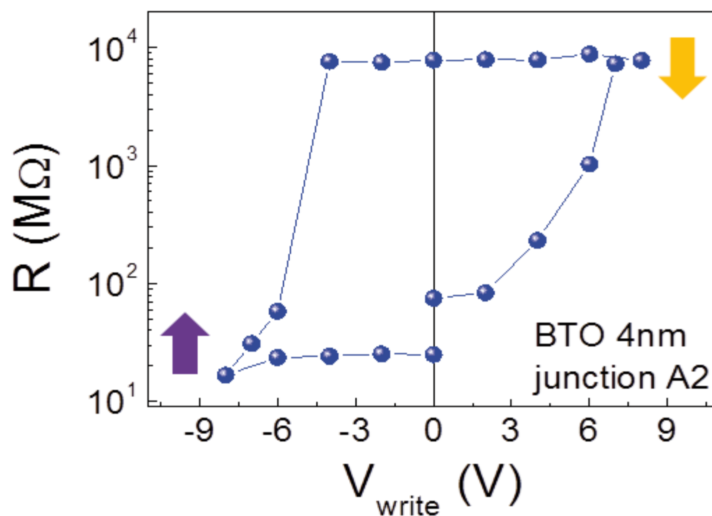

Figure S2-1: The measured poling-dependent resistance of LSMO/BTO(4 *nm*)/Pt junction A2 (area 80 m^2).

ferroelectric polarization $P(V)$, thus fully confirming that, also in this junction, the ON/OFF resistance values are dictated by the polarization state of the ferroelectric barrier. Data in Fig. S2-1 allow a robust estimate of TER. It turns out that TER $\approx 3 \times 10^4\%$, corresponding to the maximum TER value measured in the junctions.

S.2.1
Bias and Frequency dependence of the junction capacitance

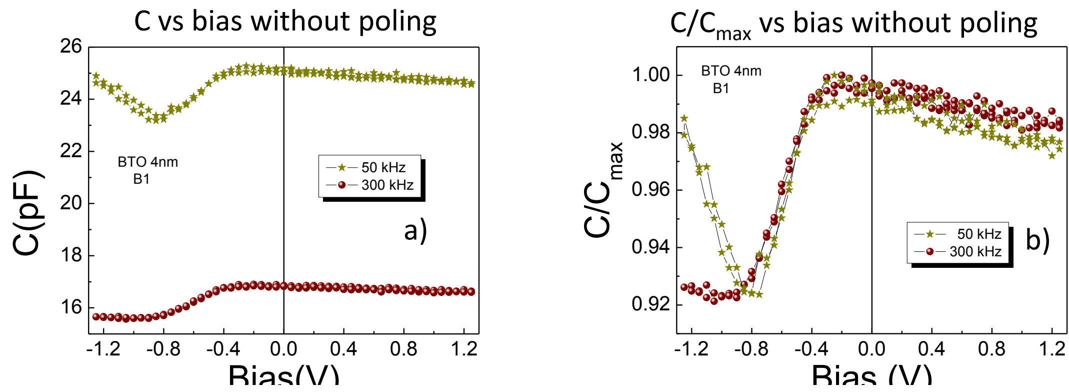

Fig **S.2.2** **Capacitance measurements on Pt/BTO (3 nm)/LSMO junctions (F1, and F2) at various frequencies**) The cap

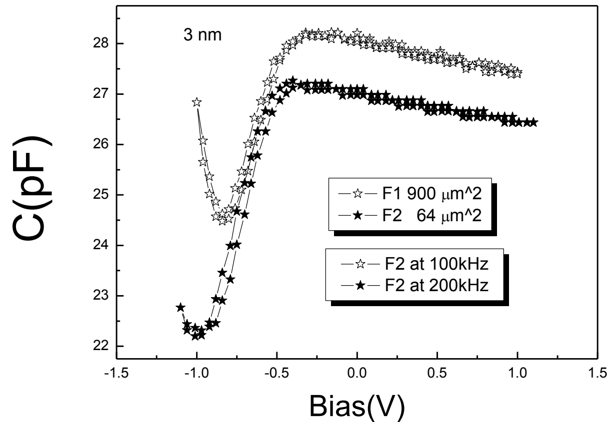

Figure S3-2: Capacitance measurements of different junctions on the junctions having a BTO 3 nm thick barrier. The measurements presents a strong frequency dependence similar to that observed for FTJs having BTO 4 nm thick barriers (figure S.3.1 a)).

Comparison of data in Figures S3-3 a) and b) indicates that the capacitance after poling down the BTO layer (+8 V) (orange stars and triangles) is independent on

S.3.3
Hysteresis of the Capacitance upon biasing and poling

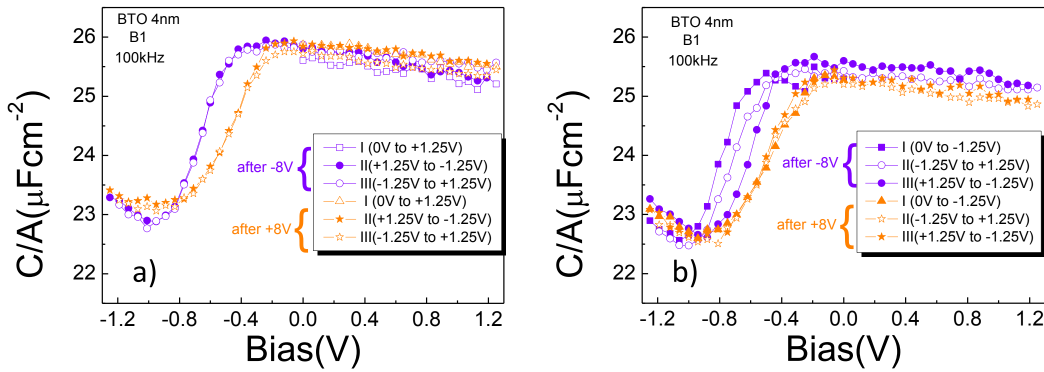

Figure S3-3: Capacitance vs bias. The Pt electrode is biased and the bottom electrode is grounded. The orange (stars and triangles) curves correspond to a prepulse of +8 V while the violet (squares and circles) ones correspond to a prepulse of -8 V. a) $C(V)$ measurements

S.3.4
Free carrier density variation estimation upon polarization reversal

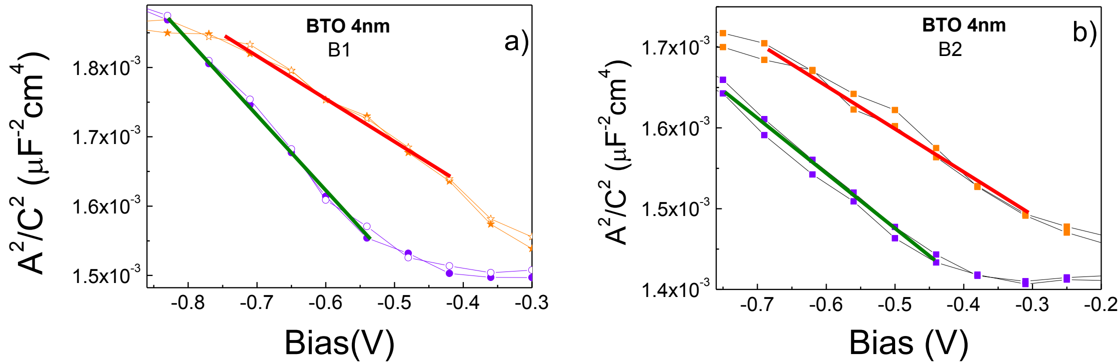

Figure S3-4:The inverse capacitance $(A/C)^2$ vs voltage dependence for junctions: a) B2 and b)B1 junctions on a BTO film 4 nm thick, in then ON state and OFF state as indicated.

From the slope of data in Figure S3.4 a) we estimate that the free carrier concen-

tration values are: $n(ON) = 4\ 36 \times 10^{21}\ cm^{-3}$ and $n(OFF) = 3\ 51 \times 10^{21}\ cm^{-3}$ and the corresponding difference $\Delta n = 8\ 46 \times 10^{20}\ cm^{-3}$. From data of junction B1 in Fig.S3-4 b) we estimate a corresponding change $\Delta n = 1\ 38 \times 10^{21}\ cm^{-3}$.

Supplementary material 4: Extraction of tunnel barrier properties from $I - V$ characteristics.

An estimate of the barrier properties, namely its average barrier height and its asymmetry, can be obtained from fits of the I-V data to a suitable model. For the present analysis we usethe current density J given by Gruverman et al. [145] for a trapezoidal potential barrier(Brinkman model [142]) using the WKB approximation,

$$J \cong C \frac{exp\ \ \alpha(V)\ \ \left(\theta_2 - \frac{eV}{2}\right)^{3/2} - \left(\theta_1 + \frac{eV}{2}\right)^{3/2}}{\alpha^2(V)\ \ \left(\theta_2 - \frac{eV}{2}\right)^{1/2} - \left(\theta_1 + \frac{eV}{2}\right)^{1/2}\ \ ^2} \times$$

$$\sinh\ \ \alpha(V)\ \ \left(\theta_2 - \frac{eV}{2}\right)^{1/2} - \left(\theta_1 + \frac{eV}{2}\right)^{1/2}\ \ \frac{eV}{2} \quad (9.1)$$

where $C = -\frac{4em^*}{9\pi^2\ \ 3}$, $\alpha \equiv \frac{4d(2m^*)^{1/2}}{3\ \ (\phi_1+eV-\phi_2)}$, m^* being the effective tunneling electron mass, d the barrier width andθ_1 and θ_2 the potential steps at the corresponding interfaces. For our fittings, which were performed using a Matlab code, we consider a metal(M)/ferroelectric(FE)/metal(M) heterostructure with bottom electrode M_1 made of LSMO, BTO as the ferroelectric, and Pt as the top electrode M_2 material. Data are fittedusing d, $\ _1$ and $\ _2$ as free parameters. Note that using expression (VI) we take into account only the direct tunneling mechanism [161], as in Gruverman et al. [145]. The other two possible transport mechanisms,thermoionic injection and Fowler-Nordheim tunneling, described in Pantel et al.[161] , have been neglected here for two reasons: i) Fowler-Nordheim is only valid at high voltage (larger than our barrier height) and thermoionic emission is considered for large barrier thickness [161], so our results can be explained well by considering only direct tunneling (in agreement

with our barrier thickness dependence of the resistance and with so our results can be explained well by considering only direct tunneling (in agreement with our barrier thickness dependence of the resistance and with Garcia et al [75] and Gruverman et al. [145]); ii) the transport equation considering all the three possible transport mechanisms gets extremely complex and includes many other parameters, as the spontaneous polarization and static permittivity of the BTO barrier and the screening lengths of

S3.1
I-V characteristics and WKB fitting

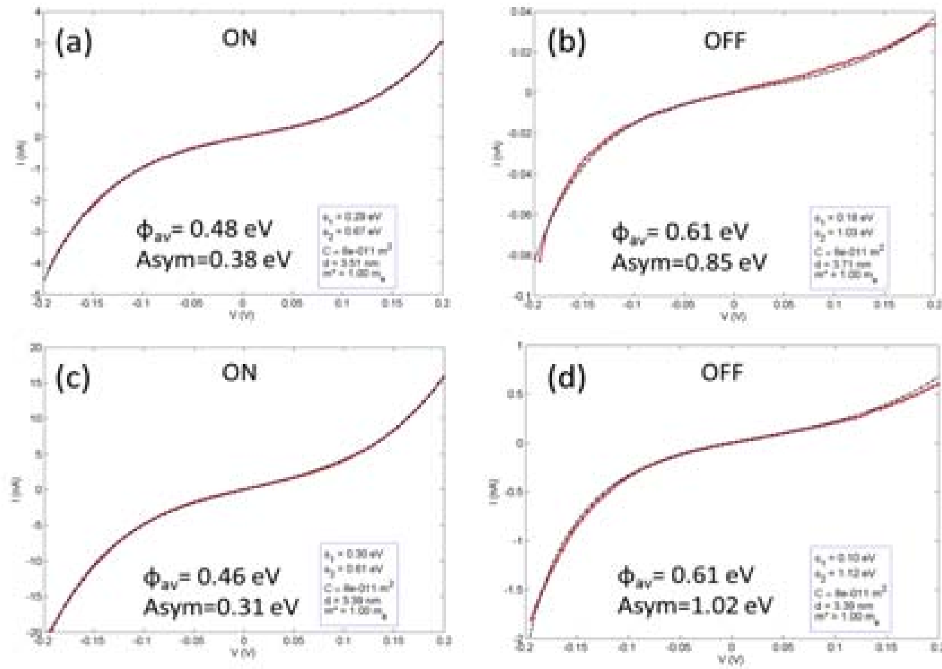

Figure S4-1: $I-V$ characteristics measured at room-temperature on junction B2 (a, b) and A2 (c, d) (on a BTO film 4 nm thick) of contact area 60 and 80 μm^2 respectively (red symbols) for: (a,c) ON and (b,d) OFF states, respectively. Dotted black lines across the experimental data are the results of the fits to eq. 1 above.

In Fig S4-1 (a,b) below we show the experimental data of junction B2 with d = 4 nm BTO barrier collected in the ON and OFF state (prepared as in Fig 1 of the manuscript) and the results obtained from the corresponding fits. When fitting, the contact area has been fixed to the nominal one (60 μm^2) and the effective electron

mass $m^* = m_e$ where m_e is the electron mass.

The results indicate a substantial rising of the average barrier height and its asymmetryand barrier thickness in the OFF state. For junction B2:

$$\text{ON state}: \theta_{av(ON)} = 0.48\ eV \text{ and } \Delta\theta_{ON} = 0.38\ eV$$

$$\text{OFF state}: \theta_{av(OFF)} = 0.61\ eV \text{ and } \Delta\theta_{OFF} = 0.85\ eV$$

It is interesting to note that very similar barrier properties are reported in literature. Indeed, Gruverman et al [145] reported for a BTO barrier of 4.8 nm: ON state $\theta_{av(ON)}$ = 0.72 eV and $\Delta\theta$ =0.48 eV, and for the OFF state $\theta_{av(OFF)} = 0.88\ eV$ and $\Delta\theta_(OFF)$ =1.28 eV.

In Fig S4-1 (c,d) we show the experimental data of another junction (A2) with d = 4 nm BTO barrier collected in the ON and OFF state (prepared as in Fig 1 of the manuscript) and the results obtained from the corresponding fits. When fitting, the contact area has been fixed to the nominal one (80 μm^2) and the effective electron mass $m^* = m_e$ where me is the electron mass.

The results indicate also in this case a substantial rising of the average barrier height and its asymmetry in the OFF state, but no variation of the barrier thickness.

S3.2
Extraction of tunnel barrier properties from WKB Fits

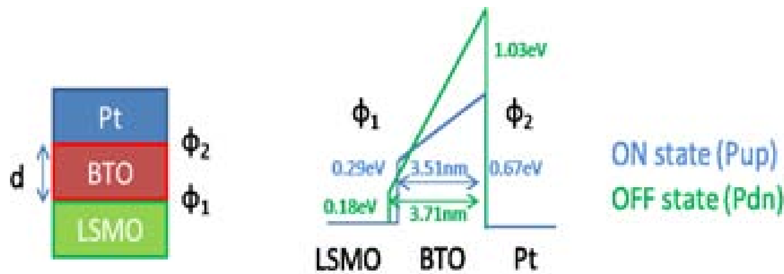

Figure S4-2: Sketch the resulting shape of the barrier in the BTO tunnel junction (energy barrier vales correspond to junction B2).

Although it would be tempting to discuss in detail the results of this fit, and particularly the implications of the extracted changes of the effective width, it turned out that fitting parameters ($\theta_{av(ON-OFF)}$, $\Delta\theta_{(ON-OFF)}$ and $d_(ON\ OFF)$) span a large range of values thus indicating that the particular set of ($\theta_{av(ON-OFF)}$, $\Delta\theta_{(ON-OFF)}$ and $d_(ON\ OFF)$) values given above may not be representative of the actual barrier properties.

List of publications and presentations

Published works

I) G. Radaelli, D. Petti, E. Plekhanov, I. Fina, P. Torelli, B. R.Salles, M. Cantoni, C. Rinaldi, ***D. F. Gutiérrez***, G. Panaccione, M. Varela, S. Picozzi, J. Fontcubeta and R. Bertacco. Electric control of magnetism at the Fe/$BaTiO_3$ interface, **Nature communication, 5, 3404, (2014)**.

II) ***D. F. Gutiérrez***, G. Radaelli, F. Sánchez, R. Bertacco and J. Fontcuberta, Bandwidth-limited control of orbital and magnetic orders in half-doped manganites by epitaxial strain, **Physics Review B. 89, 075107, (2014).**

III) ***D. F. Gutiérrez***, M. Foerster, I. Fina, D. Fritsch, C. Ederer and J. Fontcuberta. Dielectric response of epitaxially strained $CoFe_2O_4$ spinel thin films , **Physics Review B 86, 125309, (2012).**

IV) M. Foerster, ***D. F. Gutiérrez***, J. M. Rebled, E. Arbelo, F. Rigato, M. Jourdan, F. Peiró, and J. Fontcuberta. Electric transport through nanometric $CoFe_2O_4$ thin films investigated by conducting atomic force microscopy, **Journal of Applied physics 111, 013904, (2012).**

V) M. Foerster, ***D. F. Gutiérrez***, F. Rigato, J. M. Rebled, F. Peiró, and J. Fontcuberta. Non-tunnel trasport through $CoFe_2O_4$ nanometric barriers, **Journal of Applied physics letters 97, 242508, (2010.)**

Contributions to congress

- Workshop Nanoselect. Programa ingenio 2014.

  Strain effects on magnetic and electric phase diagrams of halfdoped manganite epitaxial thin films. *Diego F. Gutiérrez*, D. Pesquera, G. Radaelli, F. Sanchez and J. Fontcuberta.

  Sant Feliu de Guíxols-Catalonia-Spain, June, 2014. Oral presentation.

- Workshop Nanoselect. Programa ingenio 2013.

  Photoinduced effect on $BaTiO_3$ *Diego F. Gutiérrez*, Greta Radaelli, F. Sanchez and Josep Fontcuberta.

  Sant Feliu de Guíxols-Catalonia-Spain, July, 2013. Oral presentation.

- Pulsed laser deposition and sputtering workshop (Thin film laboratory ICMAB)

  Strain effects on half-doped $La_{0.5}Sr_{0.5}MnO_3$ and $La_{0.5}Ca_{0.5}MnO_2$ thin films. *Diego F. Gutiérrez*, J. Fontcuberta.

  ICMAB (Bellaterra -Catalonia- Spain). January 2013 Oral ppresentation.

- XXVIII Trobades Cientifiques de la Mediterranea.

  Dielectric response of epitaxially strained $CoFe_2O_4$ spinel thin films. *Diego F. Gutiérrez*, M. Foerster, M. Rubio, I. Fina, J. Fontcuberta.

  Menorca (Spain). October 2012. Oral presentation.

- Workshop Nanoselect. Programa ingenio 2012.

  Dielectric properties of $CoFe_2O_4$ nanometric films. *Diego F. Gutiérrez*, M. Foer-

ster, M. Rubio, I. Fina, J. Fontcuberta.

Sant Feliu de Guíxols-Catalonia-Spain, June, 2012. Oral presentation

- International School of Oxide Electronics (ISOE). Cargese (France). october 2011

  Poster.

- Workshop Nanoselect. Programa ingenio 2011.

  Dielectric properties and leakage through $CoFe_2O_4$. *Diego F. Gutiérrez*, M. Foerster, M. Rubio, I. Fina, J. Fontcuberta.

  Sant Feliu de Guíxols-Catalonia-Spain, June, 2011. Poster

- Functional Magnetoelectric Oxide Heterostructures. Physiczentrum,Bad Honnef (Germany).

  January 2011. Attendance.

- Fuerzas y tunel. Investigating the transport mechanism through $CoFe_2O_4$ thin films. *D.F.Gutiérrez*, M. Foerster, F. Rigato, J. M. Rebled, F. Peir, J. Fontcuberta.

  Tarragona-Spain, September 27-29, 2010. Oral presentation.

- Workshop nanoselect. Programa ingenio 2010.

  C-AFM Studies Of Electric Transport Through Nanometric Barriers: Tunnel Vs Hopping . *Diego F. Gutiérrez*, M. Foerster, F. Rigato, J. M. Rebled, J. Fontcuberta.

  Sant Feliu de Guíxols -Catalonia-Spain, July 14-16, 2010. Poster.

Bibliography

[1] M. Dawber, K. M. Rabe, and J. F. Scott, Physics of thin-film ferroelectric oxides, *Review of Modern Physics*, vol. 77, p. 1083, 2005.

[2] S. M. Sze, Physics of semiconductor and devices, *Wiley-Interscience Publication*, 2007.

[3] H. P. Maruska, F. Namavar, and N. M. Kalkhoran, Current injection mechanism for porous silicon transparent surface light emitting diodes, *Applied Physics Letters*, vol. 61, no. 11, 1992.

[4] C. W. Miller, Z.-P. Li, J. kerman, and I. K. Schuller, Impact of interfacial roughness on tunneling conductance and extracted barrier parameters, *Applied Physics Letters*, vol. 90, p. 043513, 2007.

[5] L. Esaki, P. J. Stiles, and S. v. Molnar, Magnetointernal field emission in junctions of magnetic insulators, *Physics Review Letters*, vol. 19, p. 852, 1967.

[6] N. Muller, W. Eckstein, W. Heiland, and W. Zinn, Electron spin polarization in field emission from eus-coated tungsten tips, *Physics Review Letters*, vol. 29, p. 1651, 1972.

[7] E. Kisker, G. Baum, A. H. Mahan, W. Raith, and K. Schroder, Conduction-band tunneling and electron-spin polarization in field emission from magnetically ordered europium sulfide on tungsten, *Physics Review Letters*, vol. 36, p. 982, 1976.

[8] N. Setter, D. Damjanovic, L. Eng, G. Fox, S. Gevorgian, S. Hong, A. Kingon, H. Kohlstedt, N. Y. Park, G. B. Stephenson, I. Stolitchnov, A. K. Taganstev, D. V. Taylor, T. Yamada, and S. Streiffer, Ferroelectric thin films: Review of materials, properties, and applications, *Journal of Applied Physics*, vol. 100, p. 051606, 2006.

[9] K. J. Choi, M. Biegalski, Y. L. Li, A. Sharan, J. Schubert, R. Uecker, P. Reiche, Y. B. Chen, X. Q. Pan, V. Gopalan, L.-Q. Chen, D. G. Schlom, and C. B. Eom, Enhancement of ferroelectricity in strained $BaTiO_3$ thin films, *Science*, vol. 306, p. 1005, 2004.

[10] P. Ghosez and J. Junquera, Handbook of theoretical and computational nanotechnology, vol. chap 134, 2006.

[11] V. Nagarajan, J. Junquera, J. Q. He, C. L. Jia, R. Waser, K. Lee, Y. K. Kim, S. Baik, T. Zhao, R. Ramesh, P. Ghosez, and K. M. Rabe, Scaling of structure and electrical properties in ultrathin epitaxial ferroelectric heterostructures, *Journal of Applied Physics*, vol. 100, p. 051609, 2006.

[12] A.-M. Haghiri-Gosnet and J.-P. Renard, CMR manganites: physics, thin films and devices, *Journal of Physics D: Applied Physics*, vol. 36, p. R127, 2003.

[13] Y. Tokura and N. Nagaosa, Orbital physics in transition-metal oxides, *Science*, vol. 288, p. 462, 2000.

[14] C. Zener, Interaction between the d shells in the transition metals, *Phys. Rev.*, vol. 81, p. 440, 1951.

[15] N. Mehmood, R. Grossinger, R. S. Turtelli, and M., A material with high magnetostriction produced by sol-gel method, *Advance materials research*, vol. 326, p. 157, 2011.

[16] A. Krimmel, A. Loidl, M. Klemm, S. Horn, and H. Schober, Dramatic change of the magnetic response in LiV_2O_4: Possible heavy fermion to itinerant d-metal transition, *Physics Review Letters*, vol. 82, p. 2919, 1999.

[17] Y. Yamasaki, S. Miyasaka, Y. Kaneko, J.-P. He, T. Arima, and Y. Tokura, Magnetic reversal of the ferroelectric polarization in a multiferroic spinel oxide, *Physics Review Letters*, vol. 96, p. 207204, 2006.

[18] J. Hemberger, H.-A. K. von Nidda, V. Tsurkan, and A. Loidl, Large magnetostriction and negative thermal expansion in the frustrated antiferromagnet $ZnCr_2Se_4$, *Physics Review Letters*, vol. 98, p. 147203, 2007.

[19] B. Hutchins, M. Platt, W. Hancock, and M. E. Williams, Directing transport of $CoFe_2O_4$-functionalized microtubules with magnetic fields, *Small*, vol. 3, p. 126, 2007.

[20] Y. H. Hou, Y. J. Zhao, Z. W. Liu, H. Y. Yu, X. C. Zhong, W. Q. Qiu, D. C. Zeng, and L. S. Wen, Structural, electronic and magnetic properties of partially inverse spinel $CoFe_2O_4$: a first-principles study, *Journal of Physics D: Applied Physics*, vol. 43, p. 445003, 2010.

[21] C. Chinnasamy, B. Jeyadevan, O. Perales-Perez, K. Shinoda, K. Tohji, and A. Kasuya, Growth dominant co-precipitation process to achieve high coercivity at room temperature in $CoFe_2O_4$ nanoparticles, *Magnetics, IEEE Transactions on*, vol. 38, pp. 2640 2642, 2002.

[22] D. Fritsch and C. Ederer, Effect of epitaxial strain on the cation distribution in spinel ferrites $CoFe_2O_4$ and $NiFe_2O_4$: A density functional theory study, *Applied Physics Letters*, vol. 99, p. 081916, 2011.

[23] J. N. Grima, R. Gatt, V. Zammit, J. J. Williams, K. E. Evans, A. Alderson, and R. I. Walton, Natrolite: A zeolite with negative poisson ratios, *Journal of Applied Physics*, vol. 101, p. 086102, 2007.

[24] J. Y. Tsao, Materials fundamentals of molecular beam epitaxy, *Academic Press, London*, 1993.

[25] M. Foerster, M. Iliev, N. Dix, X. Mart`, M. Barchuk, F. Sánchez, and J. Fontcuberta, The poisson ratio in $CoFe_2O_4$ spinel thin films, *Advanced Functional Materials*, vol. 22, p. 4344, 2012.

[26] Y. Suzuki, Epitaxial spinel ferrite thin films, *Annual Review of Materials Research*, vol. 31, p. 265, 2001.

[27] W. Huang, L. Zhou, H. Zeng, X. Wei, J. Zhu, Y. Zhang, and Y. Li, Epitaxial growth of the $CoFe_2O_4$ film on $SrTiO_3$ and its characterization, *Journal of Crystal Growth*, vol. 300, p. 426, 2007.

[28] M. Foerster, J. M. Rebled, S. Estradé, F. Sánchez, F. Peiró, and J. Fontcuberta, Distinct magnetism in ultrathin epitaxial $NiFe_2O_4$ films on $MgAl_2O_4$ and $SrTiO_3$ single crystalline substrates, *Physics Review B*, vol. 84, p. 144422, 2011.

[29] A. Lisfi, C. M. Williams, L. T. Nguyen, J. C. Lodder, A. Coleman, H. Corcoran, A. Johnson, P. Chang, A. Kumar, and W. Morgan, Reorientation of magnetic anisotropy in epitaxial cobalt ferrite thin films, *Physics Review B*, vol. 76, p. 054405, 2007.

[30] M. Pan, G. Bai, Y. Liu, S. Hong, V. P. Dravid, and A. K. Petford-Long, Effect of deposition temperature on surface morphology and magnetic properties in epitaxial $CoFe_2O_4$ thin films deposited by metal organic chemical vapor deposition, *Journal of Applied Physics*, vol. 107, p. 043908, 2010.

[31] J. A. Moyer, C. A. F. Vaz, E. Negusse, D. A. Arena, and V. E. Henrich, Controlling the electronic structure of $Co_{1-x}Fe_{2+x}O_4$ thin films through iron doping, *Physics Review B*, vol. 83, p. 035121, 2011.

[32] P. Thang, G. Rijnders, and D. Blank, Stress-induced magnetic anisotropy of $CoFe_2O_4$ thin films using pulsed laser deposition, *Journal of Magnetism and Magnetic Materials*, vol. 310, p. 2621, 2007.

[33] L. Horng, G. Chern, M. Chen, P. Kang, and D. Lee, Magnetic anisotropic properties in Fe_3O_4 and $CoFe_2O_4$ ferrite epitaxy thin films, *Journal of Magnetism and Magnetic Materials*, vol. 270, p. 389, 2004.

[34] L. Pintilie, I. Vrejoiu, D. Hesse, G. LeRhun, and M. Alexe, Extrinsic contributions to the apparent thickness dependence of the dielectric constant in epitaxial $Pb(Zr,Ti)O_3$ thin films, *Physics Review B*, vol. 75, p. 224113, 2007.

[35] N. A. Pertsev, R. Dittmann, R. Plonka, and R. Waser, Thickness dependence of intrinsic dielectric response and apparent interfacial capacitance in ferroelectric thin films, *Journal of Applied Physics*, vol. 101, p. 074102, 2007.

[36] L. J. Sinnamon, R. M. Bowman, and J. M. Gregg, Investigation of dead-layer thickness in $SrRuO_3/Ba_{0.5}Sr_{0.5}TiO_3/Au$ thin-film capacitors, *Applied Physics Letters*, vol. 78, p. 1724, 2001.

[37] L.-W. Chang, M. Alexe, J. F. Scott, and J. M. Gregg, Settling the dead layer debate in nanoscale capacitors, *Advanced Materials*, vol. 21, p. 4911, 2009.

[38] J. H. Haeni, P. Irvin, W. Chang, R. Uecker, P. Reiche, Y. L. Li, S. Choudhury, W. Tian, M. E. Hawley, B. Craigo, A. K. Tagantsev, X. Q. Pan, S. K. Streiffer, L. Q. Chen, S. W. Kirchoefer, J. Levy, and D. G. Schlom, Room-temperature ferroelectricity in strained $SrTiO_3$, *Nature*, vol. 430, p. 758, 2004.

[39] C. Day, Creating and characterizing individual molecular bonds with a scanning tunneling microscope, *Physics Today*, vol. 53, p. 17, 2000.

[40] F. Pulizzi, Spintronics, *Nature Materials*, vol. 11, no. 5, p. 367, 2012.

[41] G.-X. M. Jagadeesh S. Moodera and T. S. Santos, Frontiers in spin-polarized tunneling, *Physics Today*, vol. 63, p. 46, 2010.

[42] T. S. S. Jagadeesh S Moodera and T. Nagahama, The phenomena of spin-filter tunnelling, *Journal of Physics: Condensed Matter*, vol. 19, p. 165202, 2007.

[43] U. Luders, M. Bibes, K. Bouzehouane, E. Jacquet, J.-P. Contour, S. Fusil, J.-F. Bobo, J. Fontcuberta, A. Barthélémy, and A. Fert, Spin filtering through ferrimagnetic $NiFe_2O_4$ tunnel barriers, *Applied Physics Letters*, vol. 88, p. 082505, 2006.

[44] U. Luders, A. Barthélémy, M. Bibes, K. Bouzehouane, S. Fusil, E. Jacquet, J.-P. Contour, J.-F. Bobo, J. Fontcuberta, and A. Fert, $NiFe_2O_4$: A versatile spinel material brings new opportunities for spintronics, *Advanced Materials*, vol. 18, p. 1733, 2006.

[45] M. G. Chapline and S. X. Wang, Room-temperature spin filtering in a $CoFe_2O_4/MgAl_2O_4/Fe_3O_4$ magnetic tunnel barrier, *Physics Review B*, vol. 74, p. 014418, 2006.

[46] A. V. Ramos, M.-J. Guittet, J.-B. Moussy, R. Mattana, C. Deranlot, F. Petroff, and C. Gatel, Room temperature spin filtering in epitaxial cobalt-ferrite tunnel barriers, *Applied Physics Letters*, vol. 91, p. 122107, 2007.

[47] A. V. Ramos, T. S. Santos, G. X. Miao, M.-J. Guittet, J.-B. Moussy, and J. S. Moodera, Influence of oxidation on the spin-filtering properties of $CoFe_2O_4$ and the resultant spin polarization, *Physics Review B*, vol. 78, p. 180402, 2008.

[48] Y. F. Chen and M. Ziese, Spin filtering in $La_{0.7}Sr_{0.3}MnO_3/Fe_2O_4/Nb(0.5\%)$ $SrTiO_3$ heterostructures, *Physics Review B*, vol. 76, p. 014426, 2007.

[49] Y. K. Takahashi, S. Kasai, T. Furubayashi, S. Mitani, K. Inomata, and K. Hono, High spin-filter efficiency in a Co ferrite fabricated by a thermal oxidation, *Applied Physics Letters*, vol. 96, p. 072512, 2010.

[50] F. Rigato, S. Piano, M. Foerster, F. Giubileo, A. M. Cucolo, and J. Fontcuberta, Andreev reflection in ferrimagnetic $CoFe_2O_4$ spin filters, *Physics Review B*, vol. 81, p. 174415, 2010.

[51] Z. Szotek, W. M. Temmerman, D. Kodderitzsch, A. Svane, L. Petit, and H. Winter, Electronic structures of normal and inverse spinel ferrites from first principles, *Physics Review B*, vol. 74, p. 174431, 2006.

[52] L. Fumagalli, I. Casuso, G. Ferrari, and G. Gomilla, Probing electrical transport properties at the nanoscale by current-sensing atomic force microscopy, *Applied Scanning Probe Methods VIII, Springer New York*, vol. 8, p. 421, 2008.

[53] K. M. Lang, D. A. Hite, R. W. Simmonds, R. McDermott, D. P. Pappas, and J. M. Martinis, Conducting atomic force microscopy for nanoscale tunnel barrier characterization, *Review of Scientific Instruments*, vol. 75, p. 2726, 2004.

[54] G. C. Danielson, Dielectric behavior of single domain crystals of $BaTiO_3$, vol. 74, p. 986, 1948.

[55] W. L. Warren and D. Dimos, Photoinduced hysteresis changes and charge trapping in $BaTiO_3$ dielectrics, *Applied Physics Letters*, vol. 64, p. 866, 1994.

[56] J. Maldonado and A. Meitzler, Strain-biased ferroelectric-photoconductor image storage and display devices, *Proceedings of the IEEE*, vol. 59, p. 368, 1971.

[57] V. M. Fridkin, Photoferroelectrics, *Springer, Berlin*, 1979.

[58] R. Shao, Photoinduced charge dynamics on $BaTiO_3$ (001) surface characterized by scaning probe microscopy, *Applied Physics Letters*, vol. 89, p. 112904, 2006.

[59] J. L. Wang, Screning of ferroelectric domains on $BaTiO_3$ (001) surface by ultraviolet photo-induced charge and dissociative water adsortion, *Applied Physics Letters*, vol. 101, p. 092902, 2012.

[60] B. Kundys, M. Viret, D. Colson, and D. O. Kundys, Light-induced size changes in $BiFeO_3$ crystals, *Nature Materials*, vol. 9, p. 803, 2010.

[61] C. J. Won, Y. A. Park, K. D. Lee, H. Y. Ryu, and N. Hur, Diode and photocurrent effect in ferroelectric $BaTiO_{3-\delta}$, *Journal of Applied Physics*, vol. 109, p. 084108, 2011.

[62] T. Choi, S. Lee, Y. J. Choi, V. Kiryukhin, and S.-W. Cheong, Switchable ferroelectric diode and photovoltaic effect in $BiFeO_3$, *Science*, vol. 324, p. 63, 2009.

[63] D. D. Fong, G. B. Stephenson, S. K. Streiffer, J. A. Eastman, O. Auciello, P. H. Fouss, and C. Thompson, Ferroelectricity in ultrathin perovskite films, *Science*, vol. 304, p. 1650, 2004.

[64] L. Esaki, R. Laibowitz, and P. J. Stiles, Polar swith, *IBM Technical Disclosure Bulletin*, vol. 13, p. 2161, 1971.

[65] E. Y. Tsymbal and H. Kohlstedt, Tunneling across a ferroelectric, *Science*, vol. 313, p. 181, 2006.

[66] T. M. Shaw, S. Trolier-McKinstry, and P. C. McIntry, The properties of ferroelectric films at small dimensions, *Annual Review of Materials Science*, vol. 30, p. 263, 2000.

[67] S. J. M. Zhuravlev, R. Sabirianov and E. Tsymbal, Giant electroresistance in ferroelectric tunnel junctions, *Physical Review Letters*, vol. 94, p. 246802, 2005.

[68] H. Kohlstedt, N. Pertsev, J. R. Contretas, and R. Waser, Theoretical current-voltage characteristics of ferroelectric tunnel junctions, *Physical Review B*, vol. 72, p. 125341, 2005.

[69] J. Velev, C. G. Duan, K. Belashchenko, S. Jaswal, and E. Tsymbal, Effect of ferroelectricity on electron transport in $Pt/BaTiO_3/Pt$ tunnel junctions, *Physical Review Letters*, vol. 98, p. 137201, 2007.

[70] D. H. D. Pantel, S. Goetze and M. Alexe, Room temperature ferroelectric resistive swithing in ultrathin $Pb(Zr_{0.2}Ti_{0.8})O_3$ films, *ACS Nano*, vol. 5, p. 6032, 2011.

[71] D. Pantel, H. Lu, S. Goetze, P. Werner, D. J. Kim, A. Gruverman, D. Hesse, and M. Alexe, Tunnel electroresistance in junctions with ultrathin ferroelectric $Pb(Zr_{0.2}Ti_{0.8})O_3$ barriers, *Applied Physics Letters*, vol. 100, p. 232902, 2012.

[72] A. Chanthbouala, A. Crassous, V. Garcia, K. Bouzehouane, S. Fusil, X. Moya, J. Allibe, B. D. J. Grollier, S. Xavier, C. D. A. Moshar, R. Proksh, N. D. Mathurand, M. Bibes, and A. Barthélémy, Solid-state memories based on ferroelectric tunnel junctions, *Nature nanotechnology*, vol. 7, p. 101, 2012.

[73] A. Chanthbouala, V. Garcia, R. O. Cherifi, K. Bouzehouane, S. Fusil, X. Moya, S. Xavier, H. Yamada, C. Deranlot, N. D. Mathur, M. Bibes, A. Barthélémy, and J. Grollier, A ferroelectric memristor, *Nature Materials*, vol. 11, p. 860, 2012.

[74] H. Yamada, V. Garcia, S. Fusil, S. Boyn, M. Marinova, A. Gloter, S. Xavier, J. Grollier, E. Jacquet, C. Carrétéro, C. Deranlot, M. Bibes, and A. Barthélémy, Giant electroresistance of super-tetragonal $BiFeO_3$-based ferroelectric tunnel junctions, *ACS Nano*, vol. 7, p. 5385, 2013.

[75] V. Garcia, S. Fusil, K. Bouzehouane, S. Enouz-Vedrenne, N. D. Mathur, A. Barthélémy, and M. Bibes, Giant tunnel electroresistance for non-destructive readout of ferroelectrics states, *Nature*, vol. 460, p. 81, 2009.

[76] Z. Wen, L. You, J. Wang, A. Li, and D. Wu, Temperature-dependent tunneling electroresistance in $Pt/BaTiO_3/SrRuO_3$ ferroelectric tunnel junctions, *Applied Physics Letters*, vol. 103, p. 132913, 2013.

[77] D. Pantel, S. Goetze, D. Hesse, and M. Alexe, Reversible electrical switching of spin polarization in multiferroic tunnel junctions, *Nature Materials*, vol. 11, p. 289, 2012.

[78] Y. Tokura and Y. Tomioka, Colossal magnetoresistive manganites, *Journal of Magnetism and Magnetic Materials*, vol. 200, p. 1, 1999.

[79] P. Schiffer, A. P. Ramirez, W. Bao, and S.-W. Cheong, Low temperature magnetoresistance and the magnetic phase diagram of $La_{1-x}Ca_xMnO_3$, *Physics Review Letters*, vol. 75, p. 3336, 1995.

[80] Y. Konishi, Z. Fang, M. Izumi, T. Manako, M. Kasai, H. Kuwahara, M. Kawasaki, K. Terakura, and Y. Tokura, Orbital-state-meadiated phase-control of manganites, *Journal of the Physical Society of Japan*, vol. 68, p. 3790, 1999.

[81] Z. Fang, I. V. Solovyev, and K. Terakura, Phase diagram of tetragonal manganites, *Physics Review Letters*, vol. 84, p. 3169, 2000.

[82] J. Ma, H. Zhang, Q. Chen, and X. Liu, Effects of substrate-induced-strain on the electrical properties and laser induced voltages of tilted $La_{0.67}Ca_{0.33}MnO_3$ thin films, *Journal of Applied Physics*, vol. 114, p. 043708, 2013.

[83] M. Malfait, I. Gordon, V. V. Moshchalkov, Y. Bruynseraede, G. Borghs, and P. Wagner, Sign inversion of the high-field Hall slope in epitaxial $La_{0.5}Ca_{0.5}MnO_3$ thin films, *Physics Review B*, vol. 68, p. 132410, 2003.

[84] J. D. Burton and E. Y. Tsymbal, Giant tunneling electroresistance effect driven by an electrically controlled spin valve at a complex oxide interface, *Physics Review Letters*, vol. 106, p. 157203, 2011.

[85] Y. W. Yin, J. D. Burton, Y.-M. Kim, A. Y. Borisevich, S. J. Pennycook, S. M. Yang, T. W. Noh, A. Gruverman, X. G. Li, E. Y. Tsymbal, and Q. Li, Enhanced tunnelling electroresistance effect due to a ferroelectrically induced phase transition at a magnetic complex oxide interface, *Nature Materials*, vol. 12, p. 397, 2013.

[86] L. Pintilie, I. Vrejoiu, D. Hesse, and M. Alexe, The influence of the top-contact metal on the ferroelectric properties of epitaxial ferroelectric $Pb(Zr_{0.2}Ti_{0.8})O_3$ thin films, *Journal of Applied Physics*, vol. 104, p. 114101, 2008.

[87] G. Binnig, C. F. Quate, and C. Gerber, Atomic force microscope, *Physics Review Letters*, vol. 56, p. 930, 1986.

[88] J. E. Sander, J. M. chon, , and P. Mulvaney *Review of Scientific Instruments*, vol. 70, p. 3967, 1999.

[89] P. Guthner and K. Dransfeld, Local poling of ferroelectric polymers by scanning force microscopy, *Applied Physics Letters*, vol. 61, p. 1137, 1992.

[90] S. V. Kalinin and D. A. Bonnell, Imaging mechanism of piezoresponse force microscopy of ferroelectric surfaces, *Physics Review B*, vol. 65, p. 125408, 2002.

[91] A. Gruverman and S. Kalinin, Piezoresponse force microscopy and recent advances in nanoscale studies of ferroelectrics, *Journal of Materials Science*, vol. 41, p. 107, 2006.

[92] E. Soergel, Piezoresponse force microscopy pfm, *Jounal of Physics D: Applied physics*, vol. 44, p. 1, 2011.

[93] Y. H. Chu, T. Zhao, M. P. Cruz, Q. Zhan, P. L. Yang, L. W. Martin, M. Huijben, C. H. Yang, F. Zavaliche, H. Zheng, and R. Ramesh, Ferroelectric size effects in multiferroic bifeo3 thin films, *Applied Physics Letters*, vol. 90, p. 252906, 2007.

[94] H. Wieder, Laboratory notes on electrical and galvanomagnetic measurements, *ELSEVIER*, 1979.

[95] R. Meyer, R. Waser, K. Prume, T. Schmitz, and S. Tiedke, Dynamic leakage current compensation in ferroelectric thin-film capacitor structures, *Applied Physics Letters*, vol. 86, p. 142907, 2005.

[96] P. Lunkenheimer, V. Bobnar, A. V. Pronin, A. I. Ritus, A. A. Volkov, and A. Loidl, Origin of apparent colossal dielectric constants, *Physics Review B*, vol. 66, p. 052105, 2002.

[97] P. Lunkenheimer, S. Krohns, S. Riegg, S. Ebbinghaus, A. Reller, and A. Loidl, Colossal dielectric constants in transition-metal oxides, *The European Physical Journal Special Topics*, vol. 180, p. 61, 2009.

[98] N. Hirose and A. R. West, Impedance spectroscopy of undoped $BaTiO_3$ ceramics, *Journal of the American Ceramic Society*, vol. 79, p. 1633, 1996.

[99] A. K. Jonscher, The universal dielectric response, *Nature*, vol. 267, p. 673, 1977.

[100] A. K. Jonscher, Dielectric relaxation in solids, *Journal of Physics D: Applied Physics*, vol. 32, p. R57, 1999.

[101] M. Danilkevitch and I. Makoed, Dielectric properties of spinel, garnet and perovskite oxides, *physica status solidi (b)*, vol. 222, p. 541, 2000.

[102] M. N. Iliev, D. Mazumdar, J. X. Ma, A. Gupta, F. Rigato, and J. Fontcuberta, Monitoring B-site ordering and strain relaxation in $NiFe_2O_4$ epitaxial films by polarized Raman spectroscopy, *Physics Review B*, vol. 83, p. 014108, 2011.

[103] A. J. Bosman and E. E. Havinga, Temperature Dependence of Dielectric Constants of Cubic Ionic Compounds, *Physics Review*, vol. 129, p. 1593, 1963.

[104] V. G. Ivanov, M. V. Abrashev, M. N. Iliev, M. M. Gospodinov, J. Meen, and M. I. Aroyo, Short-range B-site ordering in the inverse spinel ferrite $NiFe_2O_4$, *Physics Review B*, vol. 82, p. 024104, 2010.

[105] F. Seitz, Note on the Theory of Resistance of a Cubic Semiconductor in a Magnetic Field, *Phys. Rev.*, vol. 79, p. 372, 1950.

[106] D. Fritsch and C. Ederer, Epitaxial strain effects in the spinel ferrites $CoFe_2O_4$ and $NiFe_2O_4$ from first principles, *Physics Review B*, vol. 82, p. 104117, 2010.

[107] D. Fritsch and C. Ederer, First-principles calculation of magnetoelastic coefficients and magnetostriction in the spinel ferrites $CoFe_2O_4$ and $NiFe_2O_4$, *Physics Review B*, vol. 86, p. 014406, 2012.

[108] S. Estradé, J. Arbiol, F. Peiró, I. C. Infante, F. Sánchez, J. Fontcuberta, F. de la Pena, M. Walls, and C. Colliex, Cationic and charge segregation in $La_{2/3}Ca_{1/3}MnO_3$ thin films grown on (001) and (110) $SrTiO_3$, *Applied Physics Letters*, vol. 93, p. 112505, 2008.

[109] S. Estradé, J. M. Rebled, J. Arbiol, F. Peiró, I. C. Infante, G. Herranz, F. Sánchez, J. Fontcuberta, R. Córdoba, B. G. Mendis, and A. L. Bleloch, Effects of thickness on the cation segregation in epitaxial (001) and (110) $La_{2/3}Ca_{1/3}MnO_3$ thin films, *Applied Physics Letters*, vol. 95, p. 072507, 2009.

[110] J. Spooren, R. I. Walton, and F. Millange, A study of the manganites $La_{0.5}M_{0.5}MnO_3$ (M = Ca, Sr, Ba) prepared by hydrothermal synthesis, *Journal Materials Chemistry*, vol. 15, p. 1542, 2005.

[111] J. Gazquez, S. Bose, M. Sharma, M. A. Torija, S. J. Pennycook, C. Leighton, and M. Varela, Lattice mismatch accommodation via oxygen vacancy ordering in epitaxial $la_{0.5}Sr_{0.5}CoO_{3-\delta}$ thin films, *Applied Physics Letters Materials*, p. 012105, 2013.

[112] Z. Jirák, J. Hejtmánek, K. Knížek, M. Maryško, V. Šíma, and R. Sonntag, Ferromagneticantiferromagnetic transition in tetragonal $La_{0.5}Sr_{0.5}MnO_3$, *Journal of Magnetism and Magnetic Materials*, vol. 217, p. 113, 2000.

[113] A. J. Millis, Lattice effects in magnetoresistive manganese perovskites, *Nature*, vol. 392, p. 147, 1998.

[114] H. Kuwahara, Y. Tomioka, A. Asamitsu, Y. Moritomo, and Y. Tokura, A first-order phase transition induced by a magnetic field, *Science*, vol. 270, p. 961, 1995.

[115] H. Aliaga, D. Magnoux, A. Moreo, D. Poilblanc, S. Yunoki, and E. Dagotto, Theoretical study of half-doped models for manganites: Fragility of ce phase with disorder, two types of colossal magnetoresistance, and charge-ordered states for electron-doped materials, *Physics Review B*, vol. 68, p. 104405, 2003.

[116] Y. Tokura, H. Kuwahara, Y. Moritomo, Y. Tomioka, and A. Asamitsu, Competing instabilities and metastable states in $(Nd,Sm)_{1/2}SrMnO_3$, *Physics Review Letters*, vol. 76, p. 3184, 1996.

[117] A. Baena, L. Brey, and M. J. Calderón, Effect of strain on the orbital and magnetic ordering of manganite thin films and their interface with an insulator, *Physics Review B*, vol. 83, p. 064424, 2011.

[118] J. C. Loudon, N. D. Mathur, and P. A. Midgley, Charge-ordered ferromagnetic phase in $La_{0.5}Ca_{0.5}MnO_3$, *Nature*, vol. 420, p. 797, 2002.

[119] P. Levy, F. Parisi, G. Polla, D. Vega, G. Leyva, H. Lanza, R. S. Freitas, and L. Ghivelder, Controlled phase separation in $La_{0.5}Ca_{0.5}MnO_3$, *Physics Review B*, vol. 62, p. 6437, 2000.

[120] G. Allodi, R. De Renzi, F. Licci, and M. W. Pieper, First order nucleation of charge ordered domains in $La_{0.5}Ca_{0.5}MnO_3$ detected by 139La 55Mn NMR, *Physics Review Letters*, vol. 81, p. 4736, 1998.

[121] D. Pesquera, Strain and interface-induced charge, spin and orbital ordering in transition metal oxide perovskite, *Ph.D. Tesis Universitat Autónoma de Barcelona*, ISBN 978-84-490-4735-0 de 2014.

[122] B. Y. Yongbo Yuan, Zhengguo Xiao and J. Huang, Arising application of ferroelectric materials in photovoltaic devices, *Journal of Materials chemistry A*, vol. 2, p. 6027, 2014.

[123] D. Cao, C. Wang, F. Zheng, L. Fang, W. Dong, and M. Shen, Understanding the nature of remnant polarization enhancement, coercive voltage offset and time-dependent photocurrent in ferroelectric films irradiated by ultraviolet light, *Journal Materials Chemistry*, vol. 22, p. 12592, 2012.

[124] Z. Peng, B. Liu, H. Zhu, Q. Zao, and Y. Wang, Effect of purple light on the ferroelectric and transport properties of epitaxial Mn-doped $BiFeO_3$ film, *Physics Status Solidi A*, vol. 209, p. 1451, 2012.

[125] Y. A. Park, K. D. Sung, C. J. Won, J. H. Jung, and N. Hur, Bipolar resistance switching and photocurrent in a $BaTio_{3-\delta}$; thin film, *Journal of Applied Physics*, vol. 114, p. 094101, 2013.

[126] J. Xing, K.-J. Jin, H. Lu, M. He, G. Liu, J. Qiu, and G. Yang, Photovoltaic effects and its oxygen content dependence in $BaTiO_{3-\delta}$ Si heterojunctions, *Applied Physics Letters*, vol. 92, p. 071113, 2008.

[127] S. Brivio, C. Rinaldi, D. Petti, R. Bertacco, and F. Sanchez, Epitaxial growth of Fe/$BaTiO_3$ heterostructures, *Thin Solid Films*, vol. 519, p. 5804, 2011.

[128] D. Roy and S. B. Krupanidhi, Pulsed excimer laser ablated barium titanate thin films, *Applied Physics Letters*, vol. 61, p. 2057, 1992.

[129] S. Zafar, R. E. Jones, B. Jiang, B. White, V. Kaushik, and S. Gillespie, The electronic conduction mechanism in barium strontium titanate thin films, *Applied Physics Letters*, vol. 73, p. 3533, 1998.

[130] A. L. Kholkin, S. O. Iakovlev, and J. L. Baptista, Direct effect of illumination on ferroelectric properties of lead zirconate titanate thin films, *Applied Physics Letters*, vol. 79, 2001.

[131] D. Schroder, Semiconductor material and device characterization, *Wiley-Interscience Publication*, 2006.

[132] T. Batirov, D. Dimos, E. Doubovik, R. Djalalov, and V. Fridkin, On the mechanism of the photodomain effect in ferroelectrics, *Journal of Experimental and Theoretical Physics Letters*, vol. 71, p. 318, 2000.

[133] A. Tsurumaki, H. Yamada, and A. Sawa, Impact of Bi deficiencies on ferroelectric resistive switching characteristics observed at p-type Schottky-like Pt $Bi_{1-\delta}FeO_3$ interfaces, *Advanced Functional Materials*, vol. 22, p. 1040, 2012.

[134] L. Pintilie and M. Alexe, Metal-ferroelectric-metal heterostructures with Schottky contacts. I. Influence of the ferroelectric properties, *Journal of Applied Physics*, vol. 98, p. 124103, 2005.

[135] F. Pontes, C. Pinheiro, E. Longo, E. Leite, S. de Lazaro, R. Magnani, P. Pizani, T. Boschi, and F. Lanciotti, Theoretical and experimental study on the photoluminescence in $BaTiO_3$ amorphous thin films prepared by the chemical route, *Journal of Luminescence*, vol. 104, p. 175, 2003.

[136] L. Pintilie, I. Vrejoiu, G. Le Rhun, and M. Alexe, Short-circuit photocurrent in epitaxial lead zirconate-titanate thin films, *Journal of Applied Physics*, vol. 101, p. 064109, 2007.

[137] M. Foerster, F. Rigato, K. Bouzehouane, and J. Fontcuberta, Tunnel transport through $CoFe_2O_4$ barriers investigated by conducting atomic force microscopy, *Journal of Physics D: Applied Physics*, vol. 43, p. 295001, 2010.

[138] K. M. Lang, D. A. Hite, R. W. Simmonds, R. McDermott, D. P. Pappas, and J. M. Martinis, Conducting atomic force microscopy for nanoscale tunnel barrier characterization, *Review of Scientific Instruments*, vol. 75, p. 2726, 2004.

[139] V. D. Costa, M. Romeo, and F. Bardou, Statistical properties of currents flowing through tunnel junctions, *Journal of Magnetism and Magnetic Materials*, vol. 258, p. 90, 2003.

[140] D. C. Worledge and D. W. Abraham, Conducting atomic-force-microscope electrical characterization of submicron magnetic tunnel junctions, *Applied Physics Letters*, vol. 82, p. 4522, 2003.

[141] J. Simmons, Conduction in thin dielectric films, *Journal of Physics D: Applied Physics*, vol. 4, p. 613, 1971.

[142] W. F. Brinkman, R. C. Dynes, and J. M. Rowell, Tunneling conductance of asymmetrical barriers, *Journal of Applied Physics*, vol. 41, p. 1915, 1970.

[143] M. Foerster, D. F. Gutiérrez, F. Rigato, J. M. Rebled, F. Peiro, and J. Fontcuberta, Nontunnel transport through $CoFe_2O_4$ nanometric barriers, *Applied Physics Letters*, vol. 97, p. 242508, 2010.

[144] G. Radaelli, Electric field control of remanent states in magnetic and ferroelectric tunnel junctions, *Ph.D. Tesis Politecnico Di Milano*, 2014.

[145] A. Gruverman, D. Wu, H. Lu, Y. Wang, H. W. Jang, C. M. Folkman, M. Y. Zhuravlev, D. Felker, M. Rzchowski, C.-B. Eom, and E. Y. Tsymbal, Tunneling electroresistance effect in ferroelectric tunnel junctions at the nanoscale, *Nano Letters*, vol. 9, p. 3539, 2009.

[146] P. Maksymovych, S. Jesse, P. Yu, R. Ramesh, A. P. Baddorf, and S. V. Kalinin, Polarization control of electron tunneling into ferroelectric surfaces, *Science*, vol. 324, p. 1421, 2009.

[147] L. Jiang, W. S. Choi, H. Jeen, S. Dong, Y. Kim, M.-G. Han, Y. Zhu, S. V. Kalinin, E. Dagotto, T. Egami, and H. N. Lee, Tunneling electroresistance induced by interfacial phase transitions in ultrathin oxide heterostructures, *Nano Letters*, vol. 13, p. 5837, 2013.

[148] V. Garcia, M. Bibes, L. Bocher, S. Valencia, F. Kronast, A. Crassous, X. Moya, S. Enouz-Vedrenne, A. Gloter, D. Imhoff, C. Deranlot, N. D. Mathur, S. Fusil, K. Bouzehouane, and A. Barthélémy, Ferroelectric control of spin polarization, *Science*, vol. 327, p. 1106, 2010.

[149] G. Kim, D. Mazumdar, and A. Gupta, Nanoscale electroresistance properties of all-oxide magneto-electric tunnel junction with ultra-thin barium titanate barrier, *Applied Physics Letters*, vol. 102, p. 052908, 2013.

[150] D. J. Kim, H. Lu, S. Ryu, C.-W. Bark, C.-B. Eom, E. Y. Tsymbal, and A. Gruverman, Ferroelectric tunnel memristor, *Nano Letters*, vol. 12, p. 5697, 2012.

[151] Z. Wen, C. Li, D. Wu, A. Li, and N. Ming, Ferroelectric-field-effect-enhanced electroresistance in metal/ferroelectric/semiconductor tunnel junctions, *Nature Materials*, vol. 12, p. 617, 2013.

[152] A. Crassous, V. Garcia, K. Bouzehouane, S. Fusil, A. H. G. Vlooswijk, G. Rispens, B. Noheda, M. Bibes, and A. Barthélémy, Giant tunnel electroresistance with $PbTiO_3$ ferroelectric tunnel barriers, *Applied Physics Letters*, vol. 96, p. 042901, 2010.

[153] Y. W. Yin, M. Raju, W. J. Hu, X. J. Weng, X. G. Li, and Q. Li, Coexistence of tunneling magnetoresistance and electroresistance at room temperature in $La_{0.7}Sr_{0.3}MnO_3$/(Ba, Sr)TiO_3/$La_{0.7}Sr_{0.3}MnO_3$ multiferroic tunnel junctions, *Journal of Applied Physics*, vol. 109, p. 07D915, 2011.

[154] T. Kolodiazhnyi, Insulator-metal transition and anomalous sign reversal of the dominant charge carriers in perovskite $BaTiO_{3-\delta}$, *Physics Review B*, vol. 78, p. 045107, 2008.

[155] T. Kolodiazhnyi, M. Tachibana, H. Kawaji, J. Hwang, and E. Takayama-Muromachi, Persistence of ferroelectricity in $BaTiO_3$ through the insulator-metal transition, *Physics Review Letters*, vol. 104, p. 147602, 2010.

[156] M. Liu, H. K. Kim, and J. Blachere, Lead-zirconate-titanate-based metal/ferroelectric/insulator/semiconductor structure for nonvolatile memories, *Journal of Applied Physics*, vol. 91, p. 5985, 2002.

[157] L. Pintilie, I. Vrejoiu, D. Hesse, G. LeRhun, and M. Alexe, Ferroelectric polarization-leakage current relation in high quality epitaxial Pb(Zr Ti)O_3 films, *Physics Review B*, vol. 75, p. 104103, 2007.

[158] J. E. Rault, G. Agnus, T. Maroutian, V. Pillard, P. Lecoeur, G. Niu, B. Vilquin, M. G. Silly, A. Bendounan, F. Sirotti, and N. Barrett, Interface electronic structure in a metal/ferroelectric heterostructure under applied bias, *Physics Review B*, vol. 87, p. 155146, 2013.

[159] F. Chen and A. Klein, Polarization dependence of Schottky barrier heights at interfaces of ferroelectrics determined by photoelectron spectroscopy, *Physics Review B*, vol. 86, p. 094105, 2012.

[160] H. Khassaf, G. A. Ibanescu, I. Pintilie, I. B. Misirlioglu, and L. Pintilie, Potential barrier increase due to gd doping of $BiFeO_3$ layers in Nb:$SrTiO_3$-$BiFeO_3$-Pt structures displaying diode-like behavior, *Applied Physics Letters*, vol. 100, p. 252903, 2012.

[161] D. Pantel and M. Alexe, Electroresistance effects in ferroelectric tunnel barriers, *Physics Review B*, vol. 82, p. 134105, 2010.